Investigation of creep age forming of high strength Al-Li alloy AA2060

by

Xi Wang

A Thesis submitted to the
Department of Mechanical Engineering
Imperial College London

In conformity with the requirements for the Degree of Doctor of Philosophy and for the Diploma of the Imperial College London

Oct 2022

Abstract

Panels are critical structural components for aircraft serving as the load-bearing structures and forming the aerodynamic shape. Creep-age forming (CAF), as a well-adopted technology specially invented for fabricating large-scale panels, has attracted much attention since its invention, especially in the recent two decades. Concurrently, continuous efforts have been made to create new generations of Al-Li alloys with advanced performances in strength and weight reduction. Characterised with superior synergy of strength, corrosion resistance, and weight reduction, as one of the newest 3rd generation Al-Li alloys, AA2060 is viewed as the ideal substitution for its predecessors. However, little study has been conducted regarding adopting this newly introduced Al-Li alloy in CAF. On the other hand, with the evident promotion of the strength of the material, the creep resistance of the high strength Al-Li alloys is increased especially in the T8 temper which is the mostly adopted finish temper for the Al-Li alloys. Hence, challenges exist in adopting AA2060-T8 in CAF and relative investigation is still lacking and urgently required.

Aiming at filling this research gap, this thesis presents a comprehensive investigation on adopting AA2060-T8 in CAF. A general review of the background and previous investigations regarding to the CAF and Al-Li alloys has been conducted. To fully understand the micro and macro material behaviours in CAF, a series of experiments have been systematically designed and conducted with corresponding results summarised and discussed. Based on the obtained experimental results, modelling works have been conducted including establishing a constitutive model for describing the stress-creep strain relationship in the uniaxial loading case, as well as extending the established model into the multiaxial case and implementing in the numerical simulations for the conducted CAF fabrication tests of four-point bending and adopting the flexible tool for verification. Lastly, a closed-form springback prediction solution and compensation method covering constitutive relations from elastic to plastic in CAF is developed and verified with the conducted CAF fabrication tests. With the conducted investigation works in this thesis, the basic knowledge of the material behaviours of AA2060-T8 in CAF has been gained and the subsequent forming issues induced by the high creep resistance of this alloy have been solved, which hopefully can shed a light on the future studies of adopting the high strength Al-Li alloys in CAF.

Copyright

The copyright of this thesis rests with the author. Unless otherwise indicated, its contents are licensed under a Creative Commons Attribution-Non Commercial-No Derivatives 4.0 International Licence (CC BY-NC-ND).

Under this licence, you may copy and redistribute the material in any medium or format on the condition that; you credit the author, do not use it for commercial purposes and do not distribute modified versions of the work.

When reusing or sharing this work, ensure you make the licence terms clear to others by naming the licence and linking to the licence text.

Please seek permission from the copyright holder for uses of this work that are not included in this licence or permitted under UK Copyright Law.

Declaration of originality

I herewith declare that I wrote this thesis on my own and did not use any unnamed sources or aid. Thus, to the best of my knowledge and belief, this thesis contains no material previously published or written by another person except where due reference is made by correct citation.

Xi Wang

Acknowledgements

I would like to firstly and foremostly express my deepest gratitude to my supervisors, Dr. Zhusheng Shi and Prof. Jianguo Lin, who selflessly guided me through my entire PhD journey with continuous encouragements and enlightening instructions. The brilliance of human nature and rigorous attitude toward the scientific research demonstrated by them have solidly inspired me and will always be the benchmark for me in the future. I would like to thank Prof. Lin, every time when I was stranded in the mist of my research, like a shining beacon he can always point out a direction. His profound knowledge in metal forming, passion and dedication to the research work, as well as the modesty and gently humorous in the normal life makes me deeply impressed. My most sincere gratitude also goes to Dr. Shi from the heart, who has helped and instructed me in every detail, ensuring that I received a qualified scientific PhD training and expecting me to benefit from it in future career. Each research work I produced during my PhD study is a witness of his exhaustive efforts for proofreading and penetrating comments and suggestions. It has been so fortunate to have guides like them so generously and diligently imparting their priceless academic and industrial experience to me and leading me to continuously progress on the way of pursuing my PhD.

Sincere thanks to Mr. Baoguo Chen and Prof. Yong Li, their kind understanding and timely assistance guaranteed the progress of the project during the special period of COVID. Thanks to the support of Mr. Suresh Viswamathan Chettiar, who devoted so much time and efforts helping me for the heavy lab work in the last stage. I would like to express my thanks to Dr. Qi Rong, Dr. Wenbin Zhou, and Dr. Jinghua Zheng, the constructive discussions and suggestions very much helped me regarding to my research work. Moreover, I should be gratitude to meet so many nice and excellent colleagues, Mr. Xiao Hu, Dr. Yun Hu, Dr. Shiming Liu, Miss. Jiaxin Lv, Dr. Xiaochen Lu, Dr. Jun Liu, Dr. Xiaochuan Liu, Dr. Qinmeng Luan, Dr. Shuai Jiang, and Dr. Dong Yang, their presences truly made my PhD journey more colorful and memorable.

Last but most importantly, I would like to thank for the support of my family. Pursuing a PhD degree will never be easy, only I knew what their supports and sacrifices mean to me when I looked back. Thanks again and I love you all.

Xi Wang

Contents

Abstract ..... **i**
Copyright ..... **ii**
Declaration of originality ..... **iii**
Acknowledgements ..... **iv**
Contents ..... **v**
List of Figures ..... **viii**
List of Tables ..... **xii**
Nomenclature ..... **xiii**
Publications related to this thesis ..... **xvi**
Chapter 1 ..... **1**
1.1 Methods for large panel fabrication 1
1.1.1 Peen forming 2
1.1.2 Creep age forming 4
1.2 Developments of aluminium alloys adopted in panel fabrication for aircraft 6
1.3 Aim and objectives 8
1.4 Thesis structure 10
Chapter 2 ..... **12**
2.1 Applications of CAF fabricated components 12
2.2 Creep behaviours of aluminium alloy 14
2.2.1 Characteristics of creep of aluminium alloy 14
2.2.2 Creep induced stress relaxation 16
2.3 Ageing behaviours of aluminium alloy 17
2.3.1 Age-hardenable aluminium alloy 17
2.3.2 Precipitation of Al-Cu based alloys 18
2.4 Hardening mechanisms in CAF 23
2.5 CAF of aluminium alloys in different series and treatments 27
2.6 Unified mechanism-based materials modelling for creep age forming 28
2.6.1 Development of constitutive models for CAF 29
2.6.2 Development of the sub models 33
2.7 CAF fabrication and springback 37
2.7.1 CAF fabrications of single and double curvature structures 37
2.7.2 Springback investigation in CAF 41
2.8 Summary 43
Chapter 3 ..... **45**
3.1 Introduction 45
3.2 Material and experimental overview 45
3.2.1 Material 45
3.2.2 Overall experimental plan for investigation of AA2060 in CAF 46
3.2.3 Test programme 47
3.3 Mechanical tests 51

3.3.1 Tensile tests 51
3.3.2 Hardness test for ageing specimens 55
3.4 Uniaxial creep-ageing test 56
3.4.1 Test specimen 57
3.4.2 Equipment and test setup 57
3.4.3 Experiment procedure 58
3.5 Microstructural investigation 59
3.5.1 Test specimen 59
3.5.2 Equipment and test setup 60
3.5.3 Test procedure 60
3.6 Four-point bending CAF test 61
3.6.1 Test specimen preparation 61
3.6.2 Equipment and test setup 61
3.6.3 Experiment procedure 63
3.7 Fabrication of CAF panel with a flexible tool 65
3.7.1 Test specimen 65
3.7.2 Equipment and setup 66
3.7.3 Experiment procedure 69
3.8 Summary 71
Chapter 4 72
4.1 Introduction 72
4.2 Mechanical properties of AA2060-T8 72
4.2.1 Tensile test results 72
4.2.2 Age hardening test results 73
4.2.3 Discussion of test results 74
4.3 Uniaxial creep-ageing and subsequent tensile tests 75
4.3.1 Creep-ageing test results 75
4.3.2 Subsequent tensile test results 76
4.3.3 Discussion of test results 77
4.4 Microstructural investigation results 78
4.4.1 TEM observation results 78
4.4.2 XRD test results 81
4.4.3 Discussion of test results 82
4.5 Four-point bending CAF test results 84
4.5.1 Results of four-point bending CAF test with same maximum surface stress 84
4.5.2 Results of four-point bending CAF test with target curvature 85
4.5.3 Discussion of test results 86
4.6 Multipoint CAF fabrication results 87
4.7 Summary 88
Chapter 5 89
5.1 Introduction 89
5.2 Effects of applied stress on creep deformation 89
5.3 Constitutive model development 91

5.3.1 Threshold stress determination 92
5.3.2 Microstructural constitutive equations 96
5.3.3 Strengthening constitutive equations 97
5.3.4 Stress-creep strain relationship 98
5.4 Model calibration, results and discussion 100
5.4.1 Determination of initial values and material constants 100
5.4.2 Stress-creep strain relationship 102
5.4.3 Microstructural evolution 103
5.4.4 Strength evolution 104
5.5 Summary 105
Chapter 6 106
6.1 Introduction 106
6.2 Implementation and verification of the proposed constitutive model in FE 106
6.2.1 Constitutive model extends to multiaxial condition 106
6.2.2 Constitutive model implementation and verification 107
6.3 Process modelling technique 110
6.3.1 Numerical simulation workflow 110
6.3.2 Simulation models setup 117
6.4 Simulation results 122
6.4.1 Simulation results of four-point bending CAF tests with the same maximum surface stress within elastic region 122
6.4.2 Simulation results of four-point bending CAF tests with target curvature 127
6.4.3 Simulation results of CAF adopting the multipoint flexible tool 132
6.5 Summary 134
Chapter 7 136
7.1 Introduction 136
7.2 Closed-form solution of CAF springback prediction 136
7.2.1 Geometric relation in CAF of single curvature sheet 136
7.2.2 Strain and stress determination in loading stage 139
7.2.3 Springback prediction after creep-ageing 145
7.3 Springback compensation method based on closed-form solution 146
7.4 Prediction solution and compensation method verification 149
7.4.1 Solution verification with four-point bending CAF experiment results 149
7.4.2 Compensation method verification with flexible tool CAF experiment results 152
7.5 Summary 153
Chapter 8 155
8.1 Conclusions 155
8.2 Future work 157
References 159

List of Figures

Figure 1-1. Applications of large panels in air and space crafts. (a) A380 in assembling with its outer panels being demonstrated [2]. (b) Fuel fuselage panels of space launch system for NASA's new rocket [3]. 2
Figure 1-2. Schematic of various types of peen forming. (a) standard peen forming for an integral sheet [7]. (b) Double sided peen forming [4]. (c) Laser-shock peen forming [8]. 3
Figure 1-3. Schematic of creep-age forming process [11]. 5
Figure 1-4. Developments of aluminium alloys for aerospace applications over time [12]. 8
Figure 1-5. Schematic of thesis structure. 11
Figure 2-1. Pictures demonstrating CAF related current and potential applications. (a) Largest CAF fabricated wing panel for A380 [11]. (b) CAF autoclave for fabrication of the A380 wing panel [17]. (c) Stiffened panels built up structural components for launching vehicles [22]. (d) CAF fabricated demonstrator of isogrid panel [19]. (e) CAF fabricated real size integral fuselage panel demonstrator with the length of 3670mm [16]. (f) Aluminium alloy skin panels of high-speed train head with streamline contour [20]. 13
Figure 2-2. Schematic of creep curves and effect of stress/temperature. (a) Creep curves demonstrating three stages in creep deformation [30]. (b) Creep curves under different stress/temperature conditions. 16
Figure 2-3. Schematic of creep induced stress relaxation. (a) Stress evolution curve along with time in stress relaxation. (b) Stress relaxation in constant deformation [11]. 17
Figure 2-4. HAADF-STEM images demonstrate the morphology and distribution of θ'' and θ' precipitates. Random distribution and parallel orientation with precipitate's habit plane can be both observed in (a) and (b) [46]. 20
Figure 2-5. Ternary Al–Cu–Mg phase diagram at 200°C (α = Al, θ = $CuAl_2$, S = Al_2CuMg, T = Al_6CuMg_4, β = $Al_{12}Mg_{17}$) [49]. 21
Figure 2-6. TEM images of precipitates: (a) TEM dark field micrograph of T_1 in a <110> zone axis for AA2198 alloy aged 500hr at 155°C [57]. (b) HAADF-STEM image of a sheared T_1 along a <110> zone axis [56]. 22
Figure 2-7. HAADF-STEM images of aged AA2198 at 18 h and 70 h. (a)-(d) shows sheared T1 precipitates below three T1 structure layers and (e) shows a shearing resisted four-layer T1 precipitate [66]. 24
Figure 2-8. The influence of precipitation on material strength and creep deformation. (a) The hardness evolution of AA2050-T34 in ageing [68]. (b) Double primary creep feature of AA2050-T34 in creep-ageing [68]. (c) Hardness evolution of Al-0.97wt.%Cu-3.08 wt.%Mg alloy in ageing with different temperatures [70]. 25
Figure 2-9. Schematic of contributions of solute hardening, age hardening and dislocation hardening to yield strength of AA7055 as a function of creep-ageing time [33]. 27
Figure 2-10. Evolution of creep strain and strength during CAF of AA7010-T3: (a) Creep strains from modelling (lines) and experiment (symbols) ; (b) Schematic of yield strength evolution and contributors [87]. 30
Figure 2-11. Evolution of creep strain and strength during CAF of AA7055. (a) Creep strain curves

from experiments (symbols) and modelling (lines). (b) Predicted evolution of yield strength and its components under 0 MPa (solid lines) and 250 MPa (dash lines), and corresponding experimental data (symbols) [33]. 31
Figure 2-12. Prediction of yield strength and creep strain. (a) Reversed hardening due to precipitates dissolving [88]. Comparison of experimental (symbols) and modelled (lines) creep strain curves for AA2050 under (b) tension and (c) compression during creep-ageing [74]..... 32
Figure 2-13. Schematic and picture illustrations of CAF devices. 37
Figure 2-14. Multipoint flexible forming tools for CAF. (a) Tool used for fabrication of AA7050 saddle shaped sheet [112]. (b) Tool used for fabrication of AA2050 sheet [113]..... 39
Figure 2-15. Schematic of two CAF FE numerical models..... 40
Figure 2-16. Schematic of DA method for springback compensation..... 42
Figure 3-1. Schematic of designed four-point bending test (dimension in mm). 48
Figure 3-2. Schematic of geometry relation between target curvature radius Rc and deformed deflection d_{tf} (CP stands for centre point of the curvature and L is the distance between supporting points). 50
Figure 3-3. Schematic of adopting multipoint flexible tool and geometry relation..... 51
Figure 3-4. Specimen geometry for room temperature (a) and elevated temperature (b) tensile test (dimension: mm)..... 52
Figure 3-5. Equipment setup for room temperature tensile test..... 53
Figure 3-6. Setup for elevated temperature tensile test..... 54
Figure 3-7. Hardness test equipment..... 56
Figure 3-8. Equipment and setup for uniaxial creep-ageing test. 58
Figure 3-9. Schematic of uniaxial creep-ageing test stages and heating curve..... 59
Figure 3-10. The equipment adopted for microstructural analysis in this research..... 60
Figure 3-11. Schematic of CAF specimen and the assigned local coordinate (dimension in mm). .. 61
Figure 3-12. Equipment and setup for the four-point bending CAF experiment..... 62
Figure 3-13. Measurement of deflections on the (a) first, (b) second, and (c) third mark..... 64
Figure 3-14. Experimental procedure for four-point bending CAF tests: (a) Initial state; (b) material is loaded and the tool was locked with locking bolts; (c) measurements of compressed height. (d) move the tool into the furnace for creep-ageing. 65
Figure 3-15.Schematic of specimen dimension and assigned local coordinates (dimension in mm). L'=335 and L''=17.5 for the 2 mm, L'=320 and L''=10 for the 4 mm..... 66
Figure 3-16. Demonstration of multipoint tool and pins layout for CAF fabrication..... 67
Figure 3-17. Test setup for multipoint tool CAF fabrication and setup of specimen with the tool. (a) Setup for loading and unloading of the tool. (b) Setup for the specimen with a multipoint tool. (c) Schematic of general setup in the $x' - y'$ section of the specimen (dimension in mm)..... 68
Figure 3-18. Adjustment of pin heights to derive designed tool surface. 70
Figure 3-19. General experiment procedure of CAF fabrication with a multipoint tool. (a) The compressing platen was lowered down to touch the metal cylinders. (b) The specimen was deformed to the designed curvature. (c) The tool was locked when deforming was completed. (d) The tool was moved to the furnace to start creep-ageing. 71
Figure 4-1. Stress-strain curves at room temperature (RT) and elevated temperature of 143 °C. (a) is the stress-strain curves of both conditions and (b) is the enlarged figure with a 0.2% offset line

to determine the yield strength. 73
Figure 4-2. Hardness evolution of AA2060-T8 at 143 °C 74
Figure 4-3. Results of uniaxial creep-ageing test. The dotted line in (b) indicates a strain rate of 1.0 x 10^{-8} s^{-1} which is treated as the upper limit of steady state. 75
Figure 4-4. Logarithm plot of steady state creep strain rate versus applied stress. 76
Figure 4-5. Strength evolution of AA2060-T8 in creep-ageing under different stress. 76
Figure 4-6. TEM bright field images along $[011]_{Al}$ zone axis under different stress and ageing time. 79
Figure 4-7. Statistical results of evolution of relative frequency of T_1 and θ' during creep-ageing. 80
Figure 4-8. T_1 precipitate size evolution under different stress. 81
Figure 4-9. Evolution of dislocation density with ageing time under different stresses. 82
Figure 4-10. Photo of the deformed specimens with target curvature in the four-point bending CAF tests. 85
Figure 4-11. Comparison of springback of four-point bending CAF with the same maximum surface stress and with target curvature. 87
Figure 5-1. Material deformation behaviour in the loading and creep-ageing stages (CA is the abbreviation for creep-ageing in the figures). 91
Figure 5-2. Determination of initial threshold stress with plots of ε against respectively $(\sigma - \sigma_{th0})$ and $(\sigma - \sigma_{th0})^n$. 93
Figure 5-3. Schematic of threshold stress σ_{th} variation with normalised dislocation density ρ_0 for the ramp function equation (RFE, Eq. (5-2)) and the reversed exponential equation (REE, Eq. (5-3)), showing the sudden turn for the former and smooth transition for the latter when σ_{th} approaches zero. 95
Figure 5-4. Schematic of the thermal history and the determination method for initial values of strength components. RT stands for room temperature. 101
Figure 5-5. Comparison of modelled (lines) and experimental (symbols) creep strain evolutions of the as-received materials under indicated stress levels. The triangle symbols are data used for verification. 103
Figure 5-6. Comparison of modelled (lines) and experimental (symbols) evolutions of the normalised dislocation density and normalised precipitate size with ageing time in material under the indicated applied stress levels. 104
Figure 5-7.Evolution of the yield strength and strength contributions with ageing time for the material. The experimental results are marked with symbols and modelling with lines. 105
Figure 6-1. Axisymmetric one element model established in ABAQUS under uniaxial stress. 109
Figure 6-2. ABAQUS simulation results (solid lines) of implemented stress-creep strain constitutive relation for 6 h creep-ageing under different stresses and comparison with MATLAB derived results (dashed lines). 109
Figure 6-3. Schematic of CAF numerical simulation workflow adopting VUMAT and UMAT subroutine. 111
Figure 6-4. Schematic of calculation flow of CREEP subroutine. 112
Figure 6-5. Schematic of calculation flow for VUMAT subroutine. 115
Figure 6-6. Schematic of calculation flow adopting UMAT subroutine to simulate unloading stage.

..... 117
Figure 6-7. Schematic of established FE model for single curvature four-point bending CAF test, dimension in mm. 118
Figure 6-8. Schematic of simulation model for flexible tool CAF of single curvature panel, dimension in mm. RP stands for the reference and centre point of the pin. 120
Figure 6-9. Simulation results of stress relaxation with the same maximum surface stress within elastic region (unit: MPa). 123
Figure 6-10. Simulation results of creep strain evolution with the same maximum surface stress within elastic region. 124
Figure 6-11. Deformed deflection simulation results of four-point bending CAF (unit: mm). 126
Figure 6-12. Comparison of the springback results of experiment and simulation (Exp stands for experiment and Sim stands for simulation). 127
Figure 6-13. Simulation results of stress relaxation with target curvature (unit: MPa). 128
Figure 6-14. Simulation results of creep strain evolution with target curvature. 129
Figure 6-15. Deformed deflection results of four-point bending CAF with target curvature (Unit: mm). 131
Figure 6-16. Comparison of the springback results of experiment and simulation. 132
Figure 6-17. Simulation results of stress relaxation from the beginning to the end of creep-ageing (unit: MPa). 132
Figure 6-18. Simulation results of deformed deflection (unit: mm). 134
Figure 7-1. Schematic of forming in CAF fabrication and two proposed loading models. 137
Figure 7-2. Schematic of deforming process in elastic loading and stress distribution through thickness. The labels in bracket in (b) are for the condition at the end of elastic loading. 139
Figure 7-3. Schematic of deforming process from elastic to plastic loading state in CAF and stress distribution through the thickness of the sheet. 141
Figure 7-4. Flow chart of bisection method. 144
Figure 7-5. Schematic of strain (x direction) distribution along thickness of the sheet (y direction) after completion of creep-ageing. ε is the bending strain along x direction. The dotted lines stand for neutral plane of the sheet. 146
Figure 7-6. Flowchart of closed-form solution-based springback compensation method. 149
Figure 7-7. Creep age forming behaviour for 2, 4 and 6 mm sheets, showing the predicted, FE simulated and experimental final deflection Δd_f vs loading displacement d_{lm}; the moment M_{end}, strain ε_c and plastic strain ε_p at the end of creep-ageing as a function of loading moment M_{load}.. 151
Figure 7-8. Photos of CAF iteration results of sheets with different thickness. 152
Figure 7-9. Evolution of adjustment factor and shape error with increased iterations. 153

List of Tables

Table 1-1. Comparison of fabrication methods between shot peen forming and creep-age forming. . 6
Table 2-1． Classification of strain-hardenable and age-hardenable aluminium alloys [35]..... 18
Table 2-2. Constitutive equations in different forms 29
Table 2-3. Unified mechanism-based constitutive model proposed by Ho et al. [85]. 30
Table 2-4. Unified mechanism-based constitutive model proposed by Zhan et al [31]..... 31
Table 2-5. Unified mechanism based constitutive model proposed by Li et al [13]..... 32
Table 3-1. Chemical composition of investigated AA2060. 45
Table 3-2. General experiment plan. 46
Table 3-3. Material property test programme. 47
Table 3-4. Uniaxial creep-ageing and subsequent RT tensile test programme. 47
Table 3-5. Samples selected for TEM and XRD tests. 48
Table 3-6. Experiment plan for four-point bending CAF with the same maximum surface stress within the elastic region 49
Table 3-7. Experimental plan for four-point bending CAF with the same target curvature. 50
Table 3-8. Experiments for multipoint tool CAF fabrication with target curvature. 51
Table 4-1. Summary of experiment results presented in each section. 72
Table 4-2. Material properties for AA2060-T8. 73
Table 4-3. Four-point bending CAF test results and corresponding springback with the same maximum surface stress of 430 MPa. 84
Table 4-4. Results of target curvature CAF four-point bending test and corresponding springback. 85
Table 4-5. Test results for 2 and 4 mm thickness specimen. 87
Table 5-1. Unified constitutive model including work hardening 99
Table 5-2. Determined initial values for the constitutive model. 101
Table 5-3. Determined material constants for the proposed constitutive model. 102
Table 6-1. Summary of dimensions of FE Model parts. 118
Table 6-2. Information of the material properties. 119
Table 6-3. FE model element information. 119
Table 6-4. Summary of setup of boundary conditions and surface contact. 119
Table 6-5. Summary of parts dimension. 121
Table 6-6. Information of material property. 121
Table 6-7. FE model element information. 121
Table 6-8. Summary of setup of boundary conditions and surface contact. 122

Nomenclature

C^i, C^{i+1}, C^j, C^{j+1},	Tool shape C in the i^{th} and $(i+1)^{th}$, j^{th} and $(j+1)^{th}$ iterations respectively for displacement adjustment and modified displacement adjustment methods.
C_{ijkl}	Components of the elasticity tensor.
D	Target shape to be formed.
d_{ave}, d_l	The measured deflection at the midpoint of the specimen and the measured loading displacement at the loading point.
d_{id}, d_{tf}, d_f	Initial deflection, target deflection, and final formed deflection at the midpoint of the specimen.
d_{ll}, d_{lm}	Loading displacements at the loading points (four-point bending) and at the midpoint.
$d_{rl,}$ d_{rm}	Springback recovered deflection at loading points (four-point bending) and at the midpoint.
k_1, k_2, k_3	Curvatures of sheet element in elastic loading, at the end of elastic loading, and in plastic loading, respectively.
L, L_1	Distance between the edge supporting points and distance between the supporting and loading points.
M_1, M_2, M_3	Moments generated in local yz plane for z axis in elastic loading, at the end of elastic loading, and in plastic loading.
M_{load}, M_{end}	Moments in yz plane for z axis at the end of loading stage and at the end of creep-ageing stage after stress relaxation before unloading.
O_a, O_b	Centre points of loaded curvature and CAFed, i.e. final deformed curvature of the sheet.
O_1, O_2, O_3	Centre points of sheet segment with the polar coordinate in elastic loading,

	at the end of elastic loading, in plastic loading.
$Q_a,\ R$	The activation energy of steady state creep and the gas constant.
$R_a,\ R_b,\ R_c$	Curvature radii of loaded shape, CAFed shape, and target shape.
$R_{n1},\ R_{n2}, R_{n3}$	Distances of the neutral plane to the origin point O_1 in elastic loading, and to the origin point O_2 at the end of elastic loading and in plastic loading, respectively.
RS^i	The value of the objective function in the i^{th} Newton-Raphson iteration
$r,\ r_i,\ r_o$	Distance of random specific plane to the origin point. Distances of the top and bottom elastic-plastic boundary to the origin point O_2.
$\bar{r}$	Normalised precipitate size.
$S^i,\ S^j$	Obtained formed shape S in i^{th} and j^{th} iterations.
S_p	The springback percentage.
T	The absolute temperature using the Kelvin degree.
$t_0,\ t_1,\ \Delta t$	The total accumulated time at the beginning and the end of the integration step; the time increment in the integration step.
$Tol_1,\ Tol_2$	Error tolerance for the modified springback compensation method; error tolerance for adopting the bisection method.
y_d	Distance of layer d of the sheet to the neutral plane.
$\alpha,\ \alpha'$	Compensation factor for modified displacement adjustment method and adjustment factor for the solution-based springback compensation method.
Δd_f	Deflection at midpoint of the CAFed sheet compared with its undeformed initial state.
$\Delta\sigma_{ij}$, $\Delta\varepsilon_{kl}^t$, $\Delta\varepsilon_{kl}^t$,	The increments of stress for the ij component, total strain, elastic strain, and

$\Delta\varepsilon_{kl}^{p}$	plastic strain for the kl component in the integration step.
$\varepsilon,\ \varepsilon_2,\ \varepsilon_y$	Strain generated along x direction in yz plane, accumulated strain at the end of elastic loading, and strain at 0.1% offset yielding point.
ε_c	Accumulated creep strain along x direction in yz plane.
ε_p	Plastic strain induced in loading stage.
$\varepsilon_{cr},\ \varepsilon_{ij}^{cr}$	The accumulated creep strain and creep strain components in ij direction.
$\theta,\ \theta_a,\ \theta_b$	Centre angle of the sheet segment. Centre angles of loaded curvature and CAFed curvature of the sheet.
$\theta_1,\ \theta_2,\ \theta_3$	Centre angles of deformed segment in elastic loading, at the end of elastic loading, and in plastic loading.
$\bar{\rho}_0,\ \bar{\rho}$	The normalised dislocation density in loading and creep-ageing stage.
$\sigma,\ \sigma_e,\ \sigma_p$	Stress along x direction in yz plane, stress at layer r along x direction in yz plane in elastic region and plastic region in plastic loading, respectively.
$\sigma_A,\ \sigma_B$	Strengthening by dislocation cutting through precipitate and by dislocation bypassing precipitate.
$\sigma_{dis},\ \sigma_{ppt},\ \sigma_i$	Dislocation hardening, precipitation hardening, and material intrinsic strength.
σ_{end}	Stress at the end of linear stress-strain relation.
σ_r	Relaxed stress along x direction in yz plane.
$\sigma_{th0},\ \sigma_{th}$	The initial threshold stress and threshold stress.
$\sigma_{vm},\ \sigma_{ij0},\ \sigma_{ij}$	Mises effective stress. The stress state components at the beginning and the stress components updated with $\Delta\sigma_{ij}$ in the integration step.

Publications related to this thesis

1. Wang X, Li Y, Chen B, Shi Z. Development and trend of unified mechanism-based materials modelling for creep age forming of aluminium alloys. IOP Conference Series: Materials Science and Engineering. 2021;1024:12021. DOI:10.1088/1757-899X/1024/1/012021.

2. Wang X, Rong Q, Shi Z, Li Y, Cao J, Chen B, et al. Investigation of stress effect on creep, precipitation and dislocation evolution of Al–Li alloy during creep age forming. Materials Science and Engineering: A. 2022;836:142723. DOI:10.1016/j.msea.2022.142723.

3. Wang X, Rong Q, Shi Z, Lin J. Improved creep behaviour for a high strength Al-Li alloy in creep age forming: experimental studies and constitutive modelling. International Journal of Plasticity. 2022:103447. DOI:10.1016/j.ijplas.2022.103447.

4. Wang X, Rong Q, Shi Z, Lin J. An efficient closed-form solution for springback prediction and compensation in elastic–plastic creep age forming. The International Journal of Advanced Manufacturing Technology. 2023. DOI:10.1007/s00170-022-10607-3.

Chapter 1

Introduction

1.1 Methods for large panel fabrication

Panels are critical structural components for aircrafts and launch vehicles, which are not only the key parts in forming the aerodynamic shape of the vehicles, but also are adopted in load-bearing structures for components such as wing and fuselage. On the other hand, in past decades, it has always been one of the main focuses of structural optimisation in the industry to achieve design and fabrication of lightweight structural components for air and space crafts to obtain superior mechanical performances in strength, durability, and corrosion resistance. Utilising large panels was one of the major optimisations and breakthroughs for modern space and air crafts: weight reduction and integral strength enhancement can be simultaneously achieved by much fewer rivets used for fastening compared with built-up components with riveted skin and stringers [1]. Additionally, significant cost savings associated with materials and manufacturing labour can be achieved. As a consequence, large panels are widely adopted as structural components for aircraft as the wing, fuel, and fuselage panels, and for spacecraft as fuel fuselage and bulkhead, as shown in Figure 1-1.

When fabricating large-scale panels, traditional cold forming methods such as rolling and stamping become inapplicable due to the size of forming panel. Alternatively, methods specialised in large-scale panel forming such as peen forming and creep age forming were introduced and proved their capability in fabricating large panel components. However, with the raising demands in fabricating extra-large panels with more complex contours and adopting newly invented high-strength aluminium alloys, challenges in fabricating large panels with reduced weight and higher strength are continuously being encountered. It is of significance to further explore and improve the fabrication of large panels with increased accuracy and cost efficiency to meet current demands.



(a) Assembling of A380



(b) Fuel fuselage panel

Figure 1-1. Applications of large panels in air and space crafts. (a) A380 in assembling with its outer panels being demonstrated [2]. (b) Fuel fuselage panels of space launch system for NASA's new rocket [3].

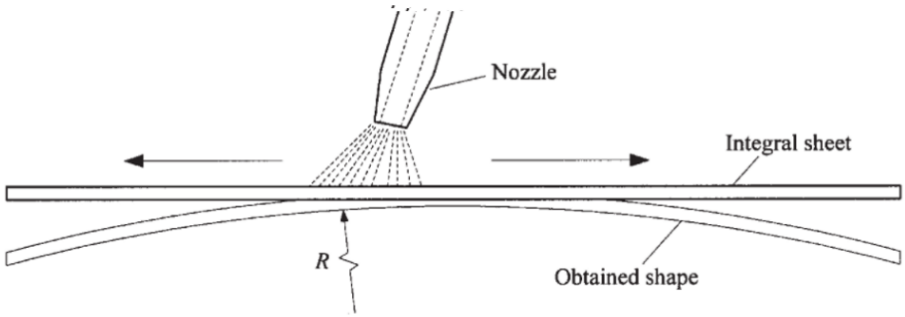
1.1.1 Peen forming

Peen forming was created as a forming method with combination of increasing fatigue resistance and shape forming. The schematic of peen forming is illustrated in Figure 1-2. By multiple shootings of high velocity moving mass towards the processing metal surface, plastic deformation is generated in the material's surface layers as a result of kinetic energy transformation, inducing compressive residual stress. With the existence of compressive stress, fatigue-induced crack propagating can be hindered and the fatigue life of the processed metal is increased. The ability of shape forming is accomplished by controlling the transferred kinetic energy through adjusting the shooting mass and velocity, hence different extents of plastic deformation can be generated to form corresponding forming curvatures.

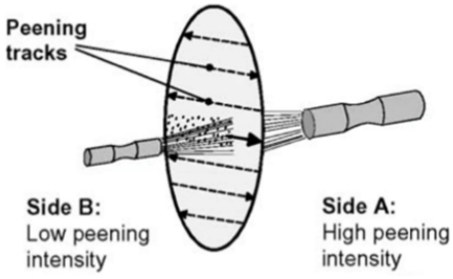
With the advancement of peen forming, this method has developed into various forms aiming at increasing efficiency and formability. Double-sided peen forming was developed in which two nozzles were used at two sides of the forming piece to increase its formability (shown in Figure 1-2b) [4]. By substituting the conventional nozzle with a more powerful laser launcher, laser-shock peen forming is capable of forming panels with higher curvatures when compared with the nozzle peen

forming methods (shown in Figure 1-2c) [5].

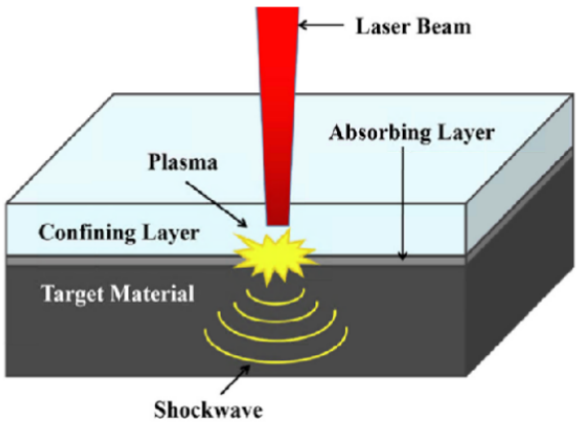
Peen forming does not have requirements for operating temperature and complex forming tools, beneficing its cost-efficiency and hence is widely adopted in the fabrication of large-scale panels. However, due to the limitation of energy transformation by shooting, conventional peen forming is limited in forming of higher curvature panels because of the observed peening saturation behaviour [6]. Additionally, the control of forming accuracy is also limited due to the disordered directions of the shooting mass after the shot. On the other hand, laser-shock peen forming can accomplish forming of a high curvature panel and with controllable direction but at much-elevated cost. It should also be noted that the surface roughness of the formed piece can cause undesirable stress concentration, hence additional surface fining process is required after peen forming by nozzle shooting or laser.



(a) Standard peen forming



(b) Double sided peen forming



(c) Laser-shock peen forming

Figure 1-2. Schematic of various types of peen forming. (a) standard peen forming for an integral sheet [7]. (b) Double sided peen forming [4]. (c) Laser-shock peen forming [8].

1.1.2 Creep age forming

In the mid of 1980s, a new integral large panel forming method named ‘creep-age forming (CAF)’, also named as autoclave forming or stress relaxation age forming, was developed and initially proved its capability in the fabrication of large aluminium alloy panels for military aircraft [9].

The dominant characteristic of CAF method is properly taking advantage of the creep and age-hardening phenomena of aluminium alloys when forming at elevated temperatures. The schematic of a complete CAF fabrication process is shown in Figure 1-3, containing three stages.

a. Loading stage. The undeformed aluminium alloy panel is placed on a forming tool with designed curvature. Then the load is exerted on the panel to deform it to the designed curvature. The load can be exerted in various ways such as curved or multipoint die, or pressure when formed in the vacuumed autoclave.

b. Creep-ageing stage. When the panel is reconfigured to the shape with the designed curvature, it is held in this shape and heated up in the furnace to the designed ageing temperature to start creep-ageing for a required time. During this stage, creep deformation induced stress relaxation and age hardening can happen and the former is counted as primary causes for deformation of the workpiece.

c. Unloading stage. After creep-aged with the designed period, the load exerted on the panel is released and the elevated temperature is reduced to room temperature, the workpiece can springback to a certain amount due to the existence of elastic strain. After springback, the final deformed panel is obtained.

Since the invention of CAF, it has drawn numerous research focusing on its mechanism and application, and more advantages of this forming method have been discovered. (i) When compared with traditional forming methods such as rolling and stamping, plastic deformation can be accomplished under the material’s yield strength in CAF, hence reducing the potential of plastic deformation induced damage to the material. (ii) Due to CAF requiring lower stress to be exerted in forming, less detrimental residual stress is induced in forming process, which can enhance the formed panel’s corrosion and fatigue resistance. (iii) Due to the adopted aluminium alloys in CAF are age-hardenable alloys, strengthening of the forming panel can simultaneously happen in creep-ageing if

processed with proper ageing time for corresponding alloy temper. These advantages lead to wide applications of CAF fabricated components on classical aircraft models such as the upper and lower wing skins of B1-B Long Range Combat Aircraft, and the wing panel assembled on Airbus A380 aircraft as the largest panel in service [10].

CAF also has its shortcomings in aspects of fabrication and forming accuracy control. (i) CAF needs forming tool with specific curvature to deform the panel in the loading stage and hold it in the creep-ageing stage under elevated temperature, increasing its fabrication cost for the complexity of both the tool and fabrication process. (ii) The final deformed shape is obtained after springback in the unloading stage, hence the springback prediction is critical to the forming accuracy. With the new generation of high strength aluminium alloys being introduced in the market, the springback of these high strength panels is significantly increased which can take up to more than 90% of the total deformation and in turn increase the prediction error. (iii) The CAF application is narrowed in the range of aluminium alloy. Also, for applying a new/different aluminium alloy in CAF, the specific stress-creep strain constitutive relation for the adopted alloy needs to be established through additional work including creep-ageing experiments and numerical simulation. A detailed comparison between large panel fabrication methods of peen shot forming and creep-age forming is given below in Table 1-1.

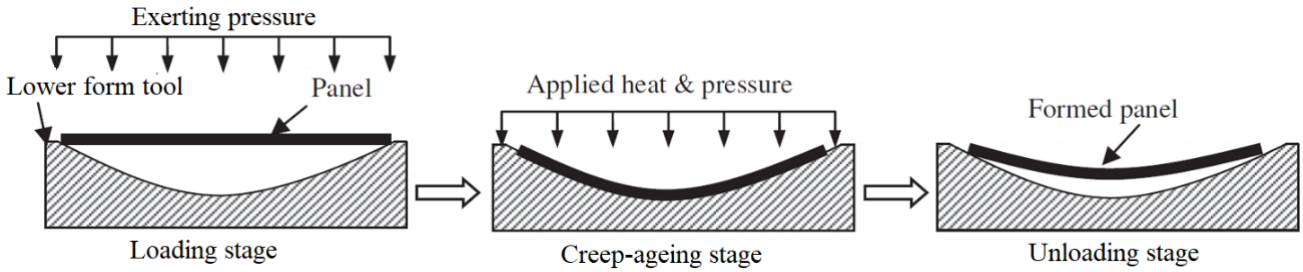


Figure 1-3. Schematic of creep-age forming process [11].

Table 1-1. Comparison of fabrication methods between shot peen forming and creep-age forming.

Method	Limitations	Characteristics of method	Characteristics of products
Shot peen forming	1. Material: metallic materials 2. Size: small / large / extra-large panels 3. Deformed curvature: Low curvature (High curvature can be achieved by laser-shock peen forming)	1. No need for complex forming tool and furnace 2. Low accuracy control in fabrication process (High accuracy control for laser-shock peen forming)	1. Rough surface (additional surface refining is required) 2. High compressive residual stress 3. High fatigue resistance 4. Low cost (High cost for laser-shock peen forming)
Creep-age forming	Material: Aluminium alloys 2. Size: small / large / extra-large panels 3. Deformed curvature: low to high curvature	1. Complex forming tool and furnace are required 2. High accuracy control in fabrication process 3. Additional experiments and simulation work is required for a new type of alloys	1. Little change on as-received material surface 2. Low residual stress 3. Higher yield strength 4. Fair cost

1.2 Developments of aluminium alloys adopted in panel fabrication for aircraft

With continuous progress being achieved in aircraft design and high strength aluminium alloy manufacturing, various advanced aluminium alloy products with optimised tempers are adopted in the fabrication of aircraft components, such as upper and lower wings, and fuselage panels [12]. Figure 1-4 illustrates the development of applications of various aluminium alloys over time. The

first application of aluminium alloy can be traced back before the 1910s, and since then various products in 2xxx and 7xxx series aluminium alloys have been adopted in the aerospace industry. 2xxx series as Al-Cu based alloys, for their superior performances in strength and fatigue resistance, are conventionally adopted for the fabrication of structural components as fuselage panel, lower wings, and stringers. 7xxx series as Al-Zn-Mg-Cu based aluminium alloys, also demonstrating the balanced synergy of strength and toughness, has been used as materials for fabrication of upper wings.

Additionally, the creation of Al-Li alloys was to fulfil the demands for further weight reduction of aircraft by decreasing the density of the adopted alloy. Li has a low density of 0.534 g / cm^3, a reduction of 3% of the alloy weight can be achieve by each adding of 1% weight percent Li into the alloy [13]. Al-Cu-Li alloy 2020 was invented as the first generation of Al-Li alloy in the 1950s. However, the application of 1st generation of Al-Li alloy was limited by its brittleness and poor ductility, leading to undesirable issues in the fabrication process.

In the 1970s, the 2nd generation Al-Li alloys were created in which Mn was replaced with Zr to induce finer Al_3Zr precipitates to improve the ductility and toughness of the alloy [14]. The AA7075 alloy used at the time was substituted with the 2nd generation Al-Li alloys such as AA2090 extrusions and AA2080 sheets. Even though the commercial applications of 2nd generation Al-Li alloys were proved to be successful, the alloys still possess a few undesirable characteristics such as high anisotropy of mechanical properties [12].

After the 1990s, the 3rd generation Al-Li alloys were invented with the characteristic of reduced Li concentration [14]. This generation of alloys was characterised by the balanced synergy of excellent corrosion resistance, high thermal stability, high strength and good toughness. The 3rd generation Al-Li alloys was successfully introduced to the market by substituting its predecessors for superior mechanical performances [12]: For fuselage skins, AA2060 was adopted as an advanced substitution for previously used AA2024 and AA2524; For panels and extruded stringers used in upper wings, Al-Li alloys like AA2055 plates and extrusions are replacing conventional AA7255 products with comparable performances and a reduced density of 6%; For materials used in lower wings, AA2060 and AA2099 extrusions are representative Al-Li alloy products replacing existing 2024 products.

In the recent decade, though the weight reduction performance of 3rd generation Al-Li alloys has been surpassed by non-metallic composite materials, this generation of Al-Li alloys remains to be competitive products with its comparable mechanical performances with the composite materials and lower cost. However, the 3rd generation Al-Li alloys have not been widely adopted in CAF fabricated components for its formability difficulty caused by high strength. It has been observed little creep strain can be generated in creep-ageing for high strength Al-Li alloys [15]. Especially for T8 temper condition, which is the most widely used and finish temper for Al-Li alloys, the formability can be limited due to the alloy's higher strength in this temper such as AA2060-T8 and AA2099-T8 [12]. Consequently, further investigation of 3rd generation Al-Li alloy adopting CAF method to fabricate large panel components is urgently needed.

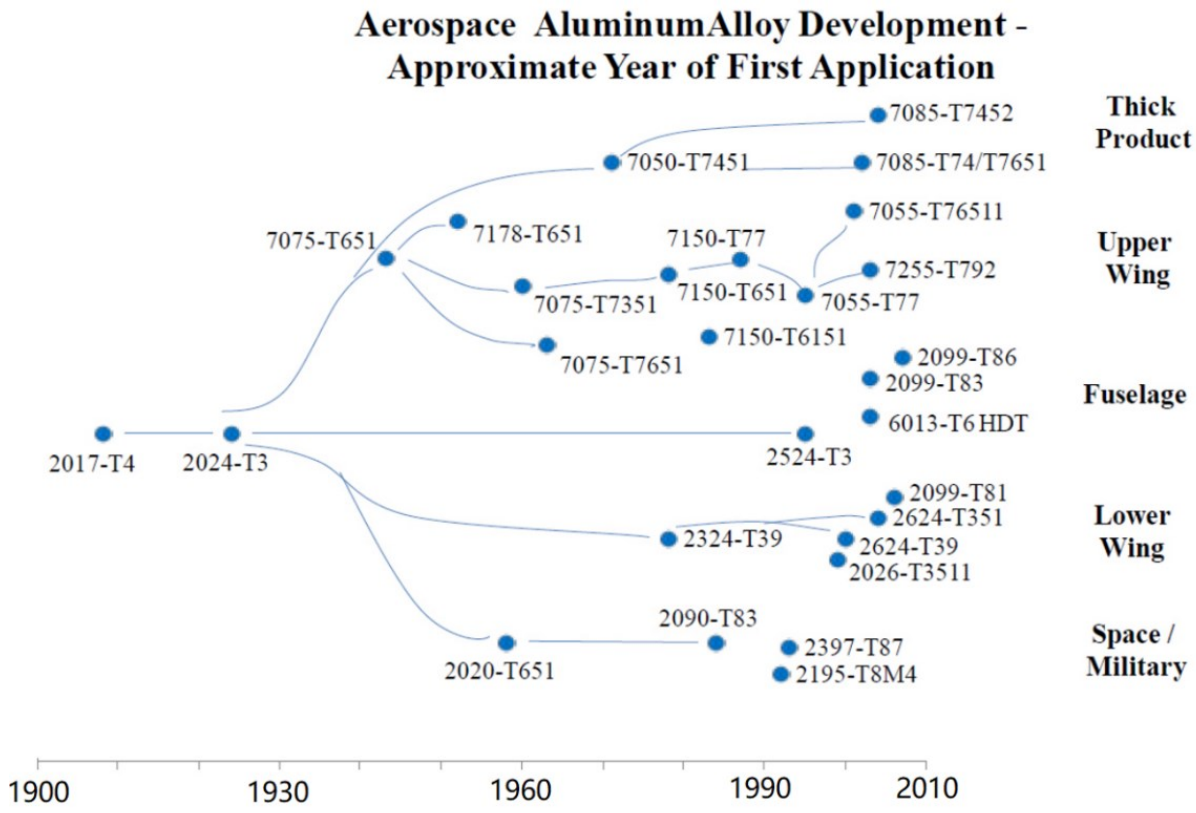


Figure 1-4. Developments of aluminium alloys for aerospace applications over time [12].

1.3 Aim and objectives

Though AA2060 was brought into the market around 2010, few studies have been conducted on

the material behaviours of AA2060 in the application of CAF. Also, the CAF fabrication of Al-Li alloy in T8 temper is still blank and requires further investigation. Hence, to fill this research gap and to develop a feasible method for accurate fabrication of AA2060-T8 panels in different thickness, a systematic research project adopting both experimental and numerical investigation approaches is designed. This project is designed as assembled by four major parts and the scope of work for each part is listed below.

(a) Study of material behaviour in ageing/creep-ageing

- To design appropriate creep-ageing testes for AA2060 in the aspects of temper, temperature, ageing time, for purpose to properly capture the characteristics of the material in CAF.
- To experimentally investigate the creep-ageing and hardening behaviour of AA2060 in CAF.
- To investigate microstructure evolution during creep-ageing.

(b) Material model establishment

- To establish material model which can accurately describe the creep deformation of AA2060 in CAF.
- The primary microstructural evolutions of material and their influences on the macro creep behaviour in CAF will be quantitively reflected in the unified constitutive equations.

(c) CAF process simulation

- The specifically developed material model will be implemented in finite element (FE) software to accurately simulate the material's creeping behaviour in CAF.
- An FE process model will be developed to simulate the multiple stages in CAF including loading, creep-ageing, and unloading stage.

(d) Fabrication of CAF panel

- An FE assisted springback compensation method will be developed to accurately predicted the derived panel shape after springback in the unloading stage.

- To evaluate the validity of the developed simulation and springback compensation method by comparing and analysing prediction results with practical measurements. Optimisation of the fabrication method will be carried out to enhance the efficiency and accuracy of creep age forming of Al-Li alloy panel.

1.4 Thesis structure

The structure of this thesis is demonstrated in Figure 1-5 and is explained below.

- Chapter 1 gives a general introduction to the background of the application and conventionally adopted fabrication methods of large panel components in the aerospace industry, followed by the developments of aluminium alloy over time. The research gap is identified, and the aims and objectives to be achieved are also illustrated. The thesis structure is presented.
- Chapter 2 provides a literature review for previously conducted investigations related to this research, aiming to shed light on further exploration of the application of AA2060-T8 in CAF. The review includes investigations of basic mechanisms of creep and ageing related to aluminium alloy, a general summary of previously proposed mechanism-based constitutive models, and experimental and numerical studies on panels fabrication by CAF.
- Chapter 3 provides detailed information on the designed and conducted experiments on AA2060-T8 to acquire a full image of macro and micro behaviours of material in creep-ageing, including the test equipment and procedures.
- Chapter 4 presents the experimental results including material properties, stress-creep strain evolution under different uniaxial stresses, four-point CAF tests, and CAF adopting the flexible tool. Corresponding discussions regarding to the obtained results are also provided.
- Chapter 5 illustrates the establishment of a mechanism-based constitutive model and modelling results for the uniaxial creep-ageing tests. Also, the nonlinear increase of creep deformation when the applied stress surpassing 400 MPa is adequately reflected in the model.
- Chapter 6 is the presentation of numerical investigations on CAF tests for AA2060 including four-point bending and fabrication with a flexible tool. The proposed constitutive model is

implemented in the simulations and the simulation and experimental results are compared.

- Chapter 7 develops an efficient springback prediction solution and compensation method. The solution predicted results are compared with experimental and numerical ones. The effectiveness of the compensation method is validated through CAF tests with a flexible tool.
- Chapter 8 concludes the main outcomes of this research. Future work which can potentially make breakthroughs on current limitations is briefly discussed.

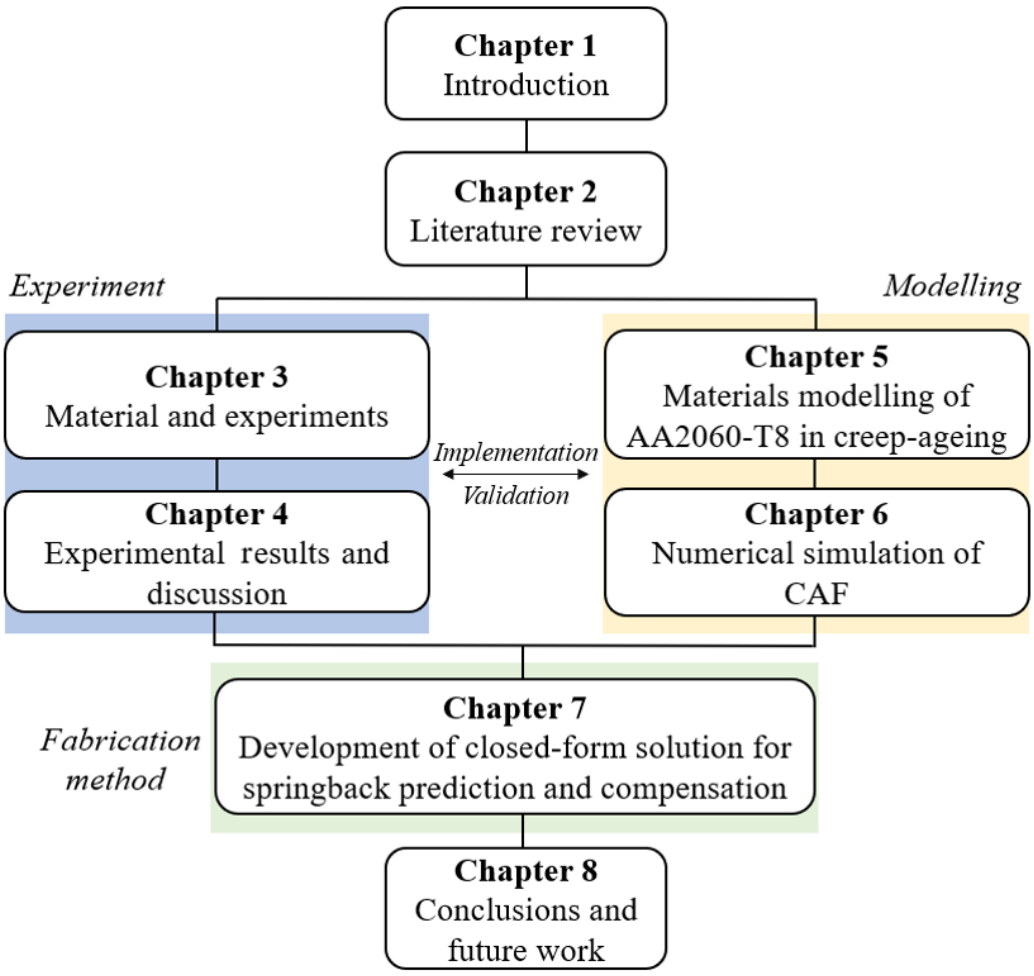


Figure 1-5. Schematic of thesis structure.

Chapter 2

Literature review

2.1 Applications of CAF fabricated components

Based on the characteristics and mechanical performances of the material, CAF fabricated components are suited to be adopted for various applications in the aerospace industry. Additionally, possibilities exist and attempts have been made to broaden the range of applications of CAF fabricated products in aerospace and other industries.

CAF method has proved its adequacy in upper wing panel fabrication with its products successfully applied in different types of aircraft. As a forming method invented initially for military use, CAF fabricated products were known to be put in service on B1-B and Hawk combat aircraft [9]. Later this technology was extended to commercial fields and was quickly accepted due to its advances in forming accuracy. By applying 7xxx series aluminium alloys generally in T6 and T7 tempers, CAF fabricated wing panels are used in a series of Airbus flying aircrafts: A318, A320, A340, and A380 among which the last one utilised the largest CAF fabricated wing panel up to now (Figure 2-1a) [16]. The panel was fabricated in an autoclave of 42 meters long, 6 meters diameter, undergone isothermal ageing at 150 ℃ for nearly 20 hours (Figure 2-1b) [17].

Apart from accomplishments in components fabrication for aircrafts, CAF has also been used to fabricate stiffened panels for launch vehicles. Figure 2-1c demonstrates the CAF fabricated stringer stiffened skin panel for the Saturn V launch vehicle's fuel fuselage [18]. Also, isogrid stiffened panels, which are further optimised based on the stringer stiffened one with superior performance in weight reduction and integral strength, have been explored and proved its feasibility of fabrication through CAF method (Figure 2-1d) [19].

Efforts have also been made to broaden the application of CAF to other structural components for aircraft. Attempts were made on CAF fabrication of integral fuselage panels with friction stir welded

joints and laser beam welded stringers. The joints and stringers were attached on flat panels and were integrally creep-age formed. Satisfying curvature was obtained on the final demonstrator panel (Figure 2-1e) [16]. Furthermore, CAF also has the potentials to be applied in a wider range of industries not limited to aerospace. Advanced aluminium alloys are currently being adopted in state-of-the-art marine and rail vehicles such as high-speed ships and trains [20].Experiments had been conducted on CAF fabrication of complex curved 6xxx alloys panels which can be possibly used as streamlined head panels for the high speed train (Figure 2-1f) [7, 21]. As an alternative panel fabrication method which possesses its unique advantages, there exist possibilities to fabricate these structural components as required through CAF.



(a) A380 panel



(b) CAF autoclave

Figure 2-1. Pictures demonstrating CAF related current and potential applications. (a) Largest CAF fabricated wing panel for A380 [11]. (b) CAF autoclave for fabrication of the A380 wing panel [17]. (c) Stiffened panels built up structural components for launching vehicles [22]. (d) CAF fabricated demonstrator of isogrid panel [19]. (e) CAF fabricated real size integral fuselage panel demonstrator with the length of 3670mm [16]. (f) Aluminium alloy skin panels of high-speed train head with streamline contour [20].



(c) Stiffened panel



(d) CAF isogrid panel



(e) CAF fuselage panel



(f) Skin panels of the train head

Figure 2-1. (*continued*).

2.2 Creep behaviours of aluminium alloy

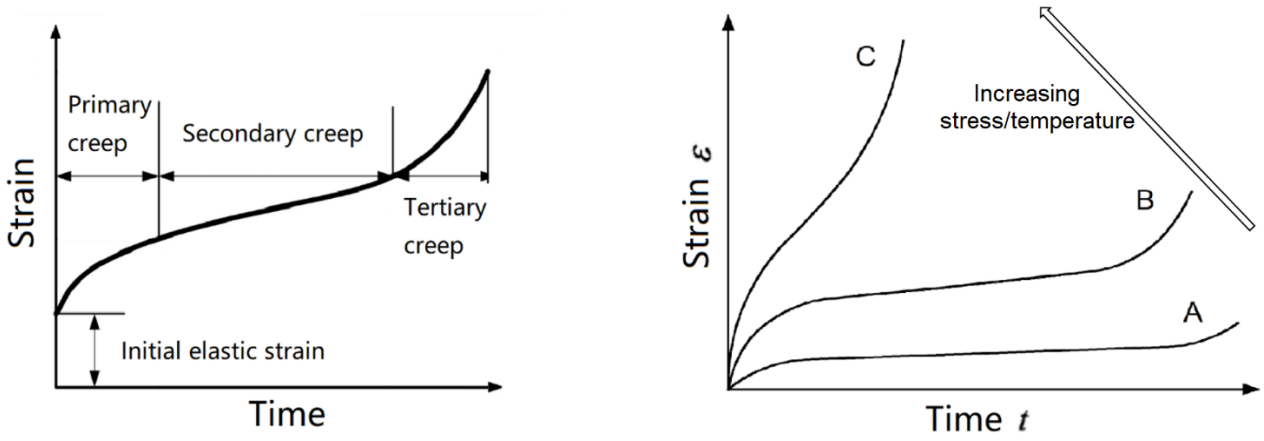
2.2.1 Characteristics of creep of aluminium alloy

Creep is a time-dependent deformation behaviour that solid material is consistently deformed under external stress. The phenomenon of work hardening and dynamic recovery shall happen along with creeping [11]. Creep curve can demonstrate creep strain accumulation with increasing time under constant applied stress and temperature. The typical creep curve for metals can be divided into three stages including primary, secondary, and tertiary stage as shown in Figure 2-2a [23]. In initial stage of primary creep, the strain accumulates rapidly with a high creep rate due to low deformation resistance. This low resistance can be caused by abundant vacancies and moveable dislocations that exist in the initial stage [24, 25]. However, in the latter period of the primary stage, with the increase of creep deformation induced dislocations and dislocation entanglements, whose existence can be hinderance to creep deformation and will strengthen the work hardening effect, the continuously

increasing work hardening effect will correspondingly lead to a decreasing of creep strain rate [26]. In the secondary creep stage, dynamic recovery is enhanced when the dislocation is about to reach saturate state with creep deformation. And gradually an equilibrium state can be achieved between work hardening and dynamic recovery, resulting in a relative constant creep strain rate in this stage [27]. In the last tertiary stage, stress concentration happens with enlarging cavities induced by creep, which can lead to an increase of the strain rate. Finally, creep rupture will happen and finally cause the failure of the creeping specimen [28].

The creep behaviours can be substantially affected by the stress and temperature being adopted [29]. The behaviours can be classified into three types as demonstrated in Figure 2-2b. When processed with low stress/temperature, the creep deformation shall enter a steady state with little creep strain accumulated as curve A in the Figure 2-2b. Also, it can be noticed that the happening of the tertiary stage for curve A can take a relatively long period of time. When applied with higher stress/temperature, the secondary stage of creep deformation can be observed as being reduced to a shorter period as curve B in the figure. If applied with much raised stress/temperature, the lasting period of the secondary creep stage will be greatly shorted and quickly transferred into the tertiary stage with high accumulated creep strain as curve C demonstrated in Figure 2-2b.

CAF takes advantage of the creep strain to deform the material into the required curvature, however, creep damage such as cavity growth and crack propagation induced in the tertiary stage should be avoided. Hence, creep evolution in CAF fabrication is limited in its primary and secondary stages. Also, exploring and adopting proper forming conditions including stress, ageing time and temperature are critical to the quality of the product and the cost efficiency of CAF fabrication.



(a) Creep curves (b) Creep curves under different stress/temperature

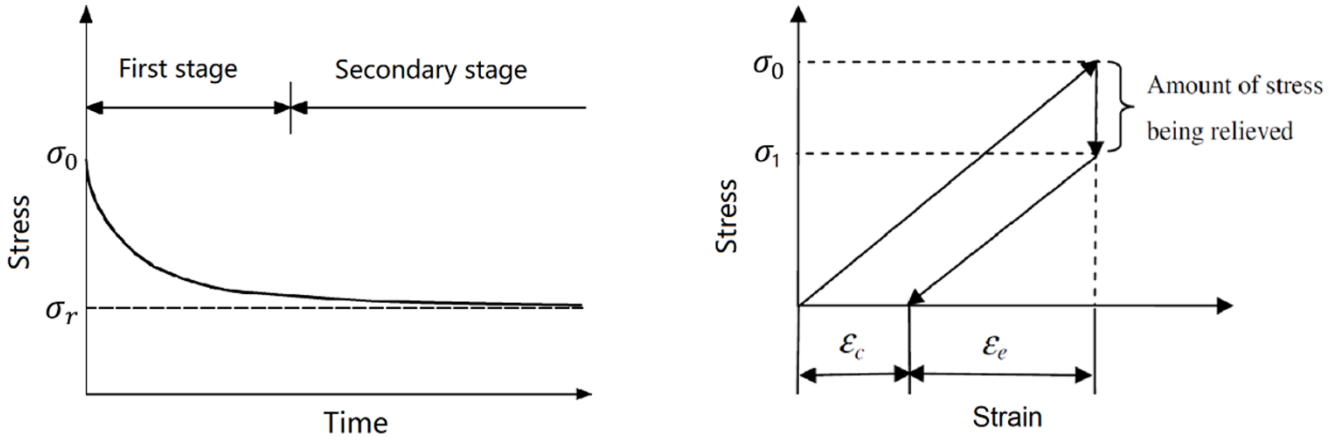
Figure 2-2. Schematic of creep curves and effect of stress/temperature. (a) Creep curves demonstrating three stages in creep deformation [30]. (b) Creep curves under different stress/temperature conditions.

2.2.2 Creep induced stress relaxation

Stress relaxation is induced when an alloy is kept with a constant deformation. Typical stress relaxation under constant deformation and temperature can be divided into two stages as demonstrated in Figure 2-3a. In the first stage, the stress drops at a higher rate due to the rapid growth of creep strain induces by vacancies and moveable dislocations in the alloy. With the increased working effect along with creep strain accumulation, a decreasing creep strain rate is derived which results in the reduction of stress relaxation rate. One of the criteria for reaching the second stage was proposed as when the creep strain rate dropped below $10^{-8}\ \mathrm{s}^{-1}$ in stress relaxation [31]. Without applying constant stress, cavity enlargement and the tertiary stage will not be induced in stress relaxation. Instead, as shown in Figure 2-3a, the stress will gradually decrease and finally approaches a stress level of σ_r defined as the stress relaxation limit for the corresponding deformation and temperature being adopted [32].

In CAF fabrication, stress relaxation can be adopted to generate creep deformation of the forming piece [11]. As demonstrated in Figure 2-3b, when being deformed and holding at the designed contours with elevated temperature, the initial stress σ_0 in the forming piece begins to drop to σ_1 at the end of creep-ageing stage with the accumulation of creep strain ε_c. Also, the remained elastic

strain ε_e will be released in the unloading stage in form of springback. While plastic deformation of the forming piece is caused by the accumulated creep strain ε_c in creep-ageing. To accurately predict the panel's final deformation after unloading, it is of significance to establish reliable relation between accumulated creep strain ε_c in creep-ageing stage and the amount of springback in unloading stage.



(a) Stress evolution curve (b) Stress relaxation in constant deformation

Figure 2-3. Schematic of creep induced stress relaxation. (a) Stress evolution curve along with time in stress relaxation. (b) Stress relaxation in constant deformation [11].

2.3 Ageing behaviours of aluminium alloy

In CAF fabrication, age-hardenable aluminium alloys including 2xxx, 6xxx, and 7xxx series, based on the unique characteristic of each material, have been used to fabricate components for various industries [31, 33, 34]. Ageing behaviours include precipitation of fine particles in the alloy, as well as the subsequently induced age hardening, which can exert critical effects on material's strength evolvements and constitutive relation of stress-creep strain during creep-ageing.

2.3.1 Age-hardenable aluminium alloy

The concept of age-hardenable aluminium alloys co-exists with the other one as strain-hardenable aluminium alloys. When undergoing heat treatment such as solution heat treatment (SHT), quenching, and natural/artificial ageing, phase transformation happens in the age-hardenable alloys from supersaturated solution to Guinier–Preston zones (GP zones), and to precipitates. Accordingly, the strength of the age-hardenable alloys will undergo evolvements associated with two hardening

mechanisms which are induced by phase transformations as precipitation hardening and solid solution hardening [35]. Contrarily, for those strain-hardenable alloys, precipitation will not happen during ageing for the lack of precipitate-forming compositions in the alloys. Hence the strengthening of this group of alloys relies on work hardening induced by dislocation substructures and is limited to the methods of cold working [36]. A general classification of these two groups for aluminium alloys is given in Table 2-1.

It should be noted that the age-hardening mechanisms including precipitation hardening and solid solution hardening which are also part of the hardening mechanisms of creep-ageing. The detailed review of these two shared hardening mechanisms is presented in the following section 2.4.

Table 2-1. Classification of strain-hardenable and age-hardenable aluminium alloys [37].

Strain-hardenable				
Series	1xxx	3xxx	4xxx	5xxx
Major composition	>=99% Al	Al-Mn	Al-Si	Al-Mg
Ultimate strength (MPa)	50-150	100-260	170-390	100-340
Age-hardenable				
Series	2xxx	6xxx	7xxx	
Major composition	Al-Cu/Al-Li	Al-Mg-Si	Al-Zn-Mg	
Ultimate strength (MPa)	300-500	150-310	320-600	

2.3.2 Precipitation of Al-Cu based alloys

2xxx alloys including Al-Li alloys can be defined as Al-Cu system alloys in which Al and Cu altogether can contribute more than 92% of the composition [38]. They are typical age-hardenable alloys in which precipitation is induced when phase stability is affected by external factors such as pressure or temperature change. Ageing is adopted as a conventional way to induce precipitation by soaking SHTed alloys under isothermal or non-isothermal conditions for a certain period. In this

transformation process, finely dispersed precipitates are decomposed from supersaturated solid solution (SSSS) into the alloys. These finely decomposed precipitates have significant effects on properties of the alloys such as yield strength, ultimate tensile strength (UTS), corrosion resistance and fracture toughness [39]. By controlling the decomposition process and the generated precipitates, age-hardenable alloys can be tailored with favoured properties. However, achieving this controlment is complicated when considering the complex coupled effects such as ageing temperature, ageing time, alloy compositions, and treatment tempers. On the other hand, with the continuous developments of 2xxx alloys, the range of the products is expanding by introducing the additional compositions into the alloy. Al-Cu-Mg and Al-Li alloys can be viewed as subsidiary products of Al-Cu alloys: Mg is added in the former to increase the alloy strength through the formation of Al_2CuMg phase and Li is introduced in the latter to achieve further lightweight optimisation [40].

For Al-Cu alloy, the most common observed precipitates are GP zones and θ phase precipitate series including θ'', θ', and θ precipitates. A normal precipitation sequence in Al-Cu based alloy can be summarised as

$$\alpha_0(\text{SSSS}) \rightarrow \alpha_1 + \text{GP zones} \rightarrow \alpha_2 + \theta'' \rightarrow \alpha_3 + \theta' \rightarrow \alpha_4 + \theta \ .$$

where α_0 stands for the SSSS state, α_1 to α_4 are the remaining matrix corresponding to the transformed phases in different stages of precipitation respectively [41] (The notations for the remaining matrix are not shown in the following precipitation sequences for conciseness). GP zones appear as a form of pre-precipitates which are Cu atoms rich disc-shape clusters [42]. Due to the low activation energy barrier to generate, GP zones lie in head positions of precipitation sequence and can be observed in the early stage of ageing. θ phase precipitate series share the same composition as $CuAl_2$ while in different atoms arrangements leading to different activation energy barriers and forming sequence [43].

For θ phase precipitate sequences, θ'' and θ' are called transition phases for their metastable states caused by higher total free energy compared to equilibrium θ phase. θ'' forms as fully coherent plate-like precipitates with $\{001\}$ habit planes in the Al matrix as demonstrated in Figure 2-4. Also, θ' has similar plate-like morphology and possesses the same habit plane and orientation

relationship with the matrix as θ'', which is also illustrated in Figure 2-4 [44]. As the last and most stable form in θ phase precipitate series, θ precipitate requires the highest activation energy to generate that the value was estimated as roughly 3 times to the energy needed to form θ' [45]. Due to the high activation energy, high temperature, and low quantities, θ precipitate has been rarely reported and its effects considered in CAF of Al-Cu based alloys.

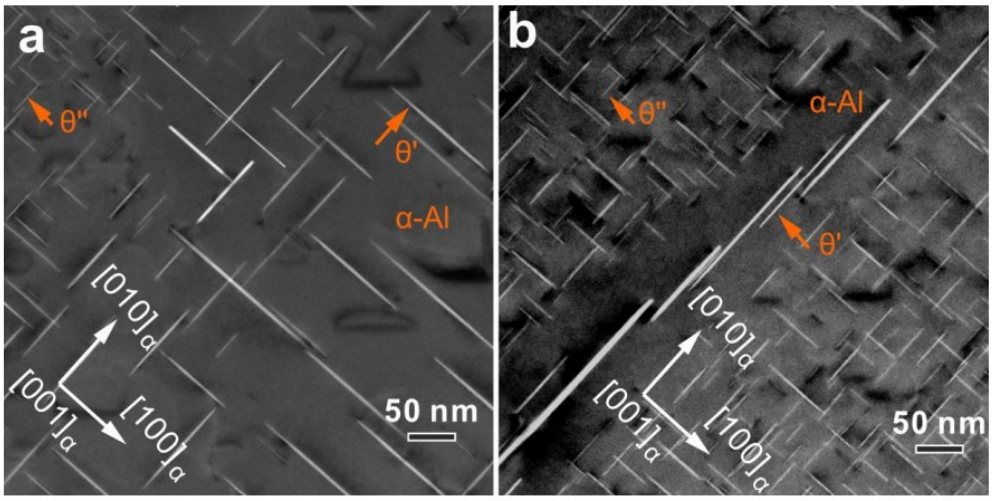


Figure 2-4. HAADF-STEM images demonstrate the morphology and distribution of $\boldsymbol{\theta''}$ and $\boldsymbol{\theta'}$ precipitates. Random distribution and parallel orientation with precipitate's habit plane can be both observed in (a) and (b) [46].

For Al-Cu-Mg alloy, the phase diagram at 200°C is demonstrated in Figure 2-5. Most of the commercially adopted Al-Cu-Mg alloys are designed with compositions which lead to formation of θ and S precipitate series. By adjusting the Cu/Mg ratio, different precipitation sequence can happen as [47, 48]:

$$\text{For } 8 > \text{Cu/Mg} > 4,\ \alpha_0(\text{SSSS}) \rightarrow \text{GP zones} \rightarrow \theta' + \text{S}' \rightarrow \theta + \text{S}\ ,$$

$$\text{For } 4 > \text{Cu/Mg} > 1.5,\ \alpha_0(\text{SSSS}) \rightarrow \text{GP zones} \rightarrow \text{S}'' \rightarrow \text{S}' \rightarrow \text{S}\ .$$

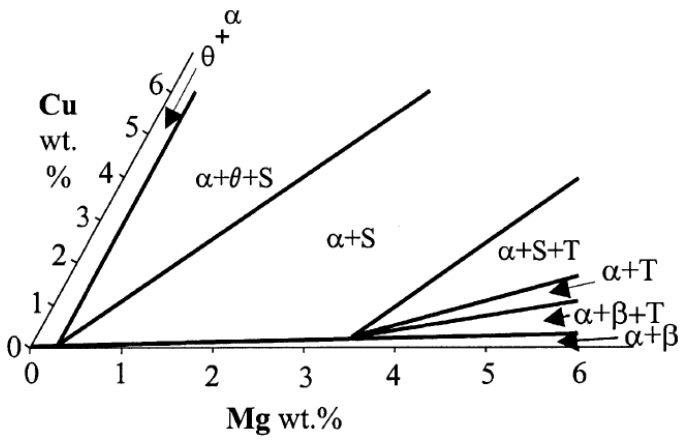


Figure 2-5. Ternary Al–Cu–Mg phase diagram at 200°C ($\boldsymbol{\alpha}$ =Al, $\boldsymbol{\theta}$ =$CuAl_2$, **S** =Al_2CuMg, **T** =Al_6CuMg_4, $\boldsymbol{\beta}$ =$Al_{12}Mg_{17}$) [49].

Similar to the θ precipitation series, S precipitation series is composed of multiple precipitates including S'', S', and S. S'' and S' are transition phases that are metastable and have the tendency to transform following the precipitation sequence as S'' to S' to S for achieving a more stable state when receiving higher activation energy[50].

For Al-Li alloys, Cu/Li ratio can exert solid effects on precipitation presences and sequence in Al-Cu-Li system. Further study has found that the precipitation sequence satisfies the following condition [51]:

$$\text{For Cu/Li} > 4,\ \alpha_0(\text{SSSS}) \rightarrow \text{GP zones} \rightarrow \theta'' \rightarrow \theta',$$

$$\text{For } 2.5 > \text{Cu/Li} > 1,\ \alpha_0(\text{SSSS}) \rightarrow \text{GP zones} + \delta' \rightarrow \theta' + \delta' \rightarrow \delta' + T_1 \rightarrow T_1.$$

δ' and T_1 are precipitates generated with additional compositions in Al-Li alloys. Both precipitates are composed of complicated atomic arrangements; the former contains Al and Li atoms, and the latter contains Al, Li, and Ag atoms.

δ' phase is a metastable spherical precipitate coherent to the Al matrix and is considered one of the main strengthening precipitates for Al-Li alloys [52, 53]. The high extent of coherence with the Al matrix results from low surface free energy at the interface of δ' phase and matrix. This ensures the δ' phase can keep a spherical shape in a wide size range from several nanometres to over a hundred nanometres [54]. In addition, if under continued long time ageing, the δ' phase will be

replaced by stable intermetallic phases such as the δ (AlLi) or T_2 (Al_5CuLi_3 / Al_5CuMg_3) phase [55].

T_1 phase is plate-like precipitate which forms on {111} planes as shown in Figure 2-6a. T_1 is also considered to be one of the main precipitates providing strength contribution to the Al-Cu-Li alloy. The evolution and growth of T_1 during ageing has been further studied recently [34, 56, 57], which assisted better understanding of the hardening effect of T_1 precipitation. It was observed that the thickness of the T_1 phase remained as constant with a single unit cell about 1.3nm during the initial ageing stage at an isothermal temperature of 155°C until being aged to a peak state [57]. Also, the thickness of T_1 was observed to increase gradually until reached the maximum value of four layers about 5nm at 190°C after 90 hours of ageing [56]. A single T_1 precipitate is found to be sheared through dislocation as shown in Figure 2-6b. Also, the diameter of T_1 phase was found to gradually increase with ageing time and temperature and can become shear resistant when growing to a structure with four layers [56, 58].

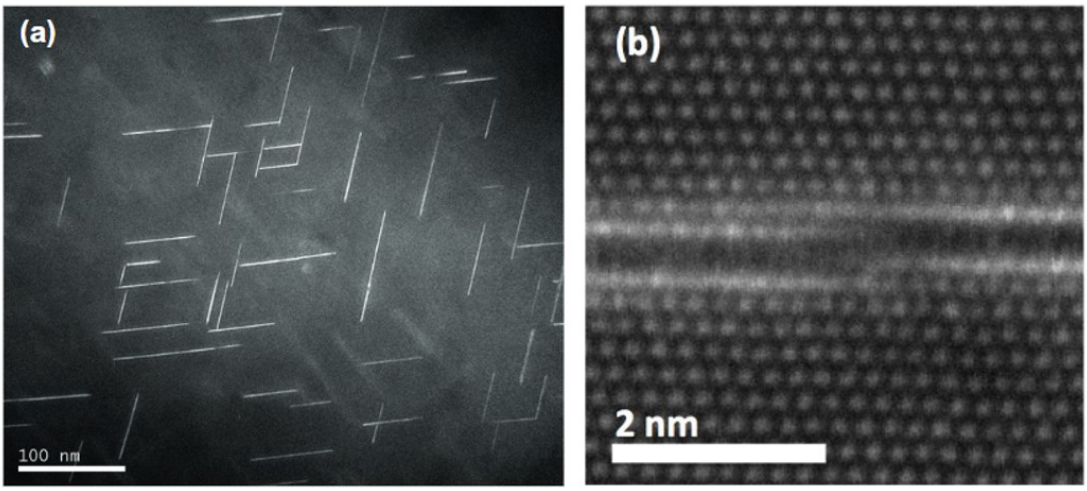


Figure 2-6. TEM images of precipitates: (a) TEM dark field micrograph of T_1 in a <110> zone axis for AA2198 alloy aged 500hr at 155°C [57]. (b) HAADF-STEM image of a sheared T_1 along a <110> zone axis [56].

In a ternary Al-Cu-Li system, the formation and evolution of GP zone, δ' phase, T_1 phase as well as precipitation sequence of other phases are more complex and subjected to additional effects such as alloy's composition, ageing temperature, ageing time and temper condition of the alloy. According to Yoshimura's study [53], δ' phase was found to exist in 550 °C solution heat treated and as-

quenched T4 temper Al-Cu-Li alloy with weight percent of Li of 2.4% but was not observed for the 1.6 wt.% (weight percent) treated with the same condition. The δ' phase was still not detected in the 1.6 wt.% Li alloy after 3 hours ageing at 100 °C. However, when aged at ageing temperature between 180 °C and 200°C, the δ' phase was found to be nucleated and developed on the GP zone by forming a stable interacted structure along with ageing. An arising volume of T_1 phase was also observed in the alloy at the later ageing stage but with much less amount when compared with ageing at T6 temper. In general, more studies are needed to clarify the complex interaction relationships among the phases that appeared in the ternary Al-Cu-Li system during ageing.

2.4 Hardening mechanisms in CAF

Several hardening mechanisms are involved in CAF including precipitation hardening, solid hardening, and dislocation hardening.

The strengthening mechanism of precipitation hardening relies on the formation of fine particles during ageing in CAF. These generated precipitates function as barriers to impede movements of dislocations thus enhance the strength of the material [59]. Two interaction mechanisms are observed when dislocations' propagations and movements are encountered with particles: the precipitates are sheared or bypassed (cross slip mechanism or Orowan loops) by dislocations [60]. It has also been widely observed in numerous investigations that material strength drops with the happening of precipitate coarsening induced by over ageing [35, 61]. This drop in strength is attributed to the decrease of Orowan stress when the gap between precipitates is increased due to precipitate coarsening [62].

θ' precipitate is considered as the primary strengthening phase for Al-Cu based alloys [63]. A significant decrease in material strength has been observed when θ' continues coarsening to a critical aspect ratio and transforms to θ [64]. Also, θ' can be treated as a relatively stable phase in creep-ageing, due to the temperature required for phase transformation from θ' to θ is much higher than the normally adopted creep-ageing temperature for Al-Cu alloys [45, 65].

For Al-Cu-Li alloys, the platelet-shaped T_1 precipitate and the spherical δ' phase are considered as unique strengthening precipitates. As shown in Figure 2-7a to Figure 2-7d, it was found that the T_1

precipitate was shearable by dislocations when structured with a single layer during the states between under-aged to peak-aged, which indicated that the precipitation strengthening mechanism can be dominated by dislocations shearing through the precipitate during these states. However, as demonstrated in Figure 2-7e, along with the proceeding of ageing, the T_1 precipitate was thickened to a four-layer structure and there was no dislocation shearing mechanism observed in over aged state [66]. This indicated that the dislocation bypassing mechanism had dominated with coarsening of the T_1 precipitate in the over-aged state. This was coordinated with the evolution trend of the yield strength which was continually increased as T_1 remained to single layer structure and began to decrease when the thickening of T_1 precipitates was induced [56, 66]. For the interaction mechanism of δ' phase with dislocation, a similar transition of shearing to bypassing along with the coarsening of δ' was also proposed [67].

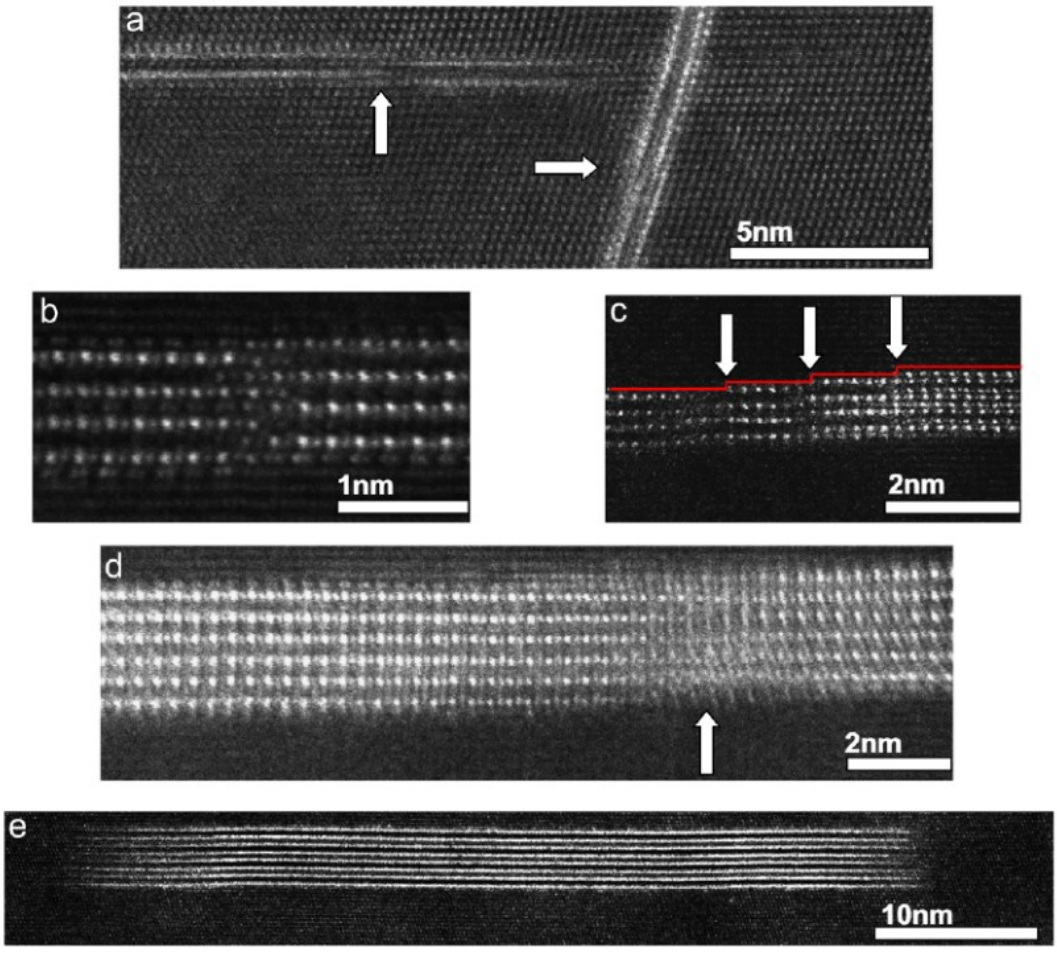
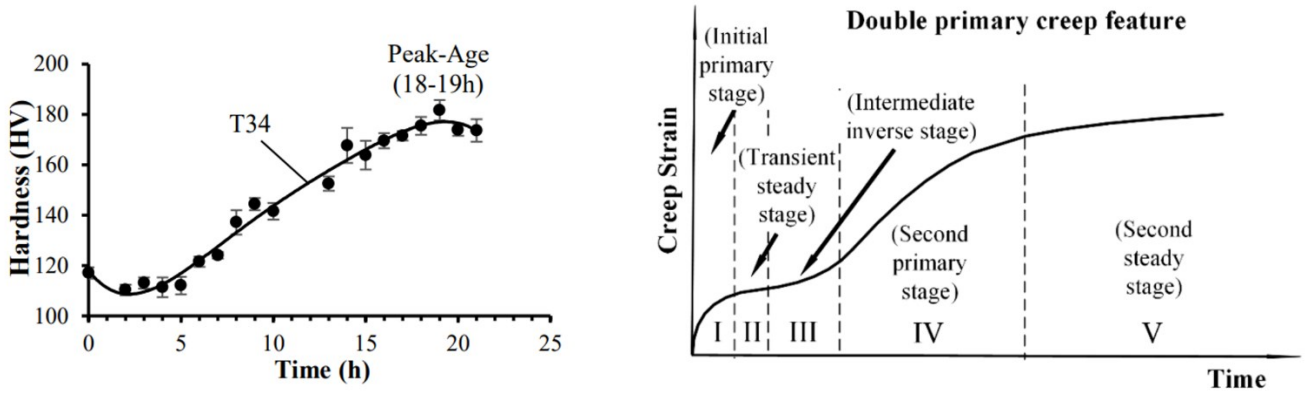


Figure 2-7. HAADF-STEM images of aged AA2198 at 18 h and 70 h. (a)-(d) shows sheared T1

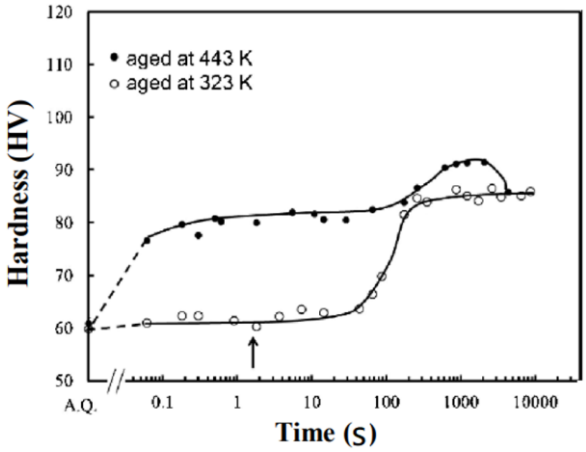
precipitates below three T1 structure layers and (e) shows a shearing resisted four-layer T1 precipitate [66].

Additionally, the material's strength and stress-creep strain constitutive relation are largely affected and evolve with the progress of precipitation in ageing/creep-ageing. As shown in Figure 2-8a and Figure 2-8b, AA2050-T34 demonstrated a strong strength reversion phenomenon during initial 5 hours of ageing and a unique double primary creep feature during creep-ageing [68]. The reverse of strength in ageing and plateau of creep curve in the early stage were attributed to the dissolving of pre-existing precipitates formed during natural ageing [68]. Figure 2-8c demonstrates the phenomenon of double stage hardening for Al-Cu-Mg alloy in ageing treatment, which was caused by the phase transformation from S″ and GP zones to S′ and S accomplished by dissolution of the former group of precipitates [69]. Also, as can be observed in the same figure, different age hardening evolutions were derived when treated at different ageing temperature since ageing temperature affected the precipitation kinetics [70].



(a) Hardness evolution (b) Double primary creep feature

Figure 2-8. The influence of precipitation on material strength and creep deformation. (a) The hardness evolution of AA2050-T34 in ageing [68]. (b) Double primary creep feature of AA2050-T34 in creep-ageing [68]. (c) Hardness evolution of Al-0.97 wt.%Cu-3.08 wt.%Mg alloy in ageing with different temperatures [70].



(c) Hardness evolution in different temperatures

Figure 2-8. (*continued*).

For solid solution hardening, the basic mechanism is that the solute atoms of the alloy are brought into solution by solid solution treatment, which leads to matrix lattice distortion and impending dislocation movements. Consequently, the strength of the alloy is enhanced for the increased difficulty of dislocation motions. Two ways of solute atoms blending into the matrix are observed, called interstitial solid solutions and substitutional solid solutions. Small solute atoms being brought into spaces between matrix atoms are observed in the former while atom replacements are happening in the latter [71].

In dislocation hardening, a phenomenon is observed in creep deformation that the specimen strength increases with creep strain. This deformation induced strengthening is called dislocation hardening [33, 68, 72]. The mechanism of dislocation hardening is controlled by varying of dislocation density caused by plastic/creep deformation[73]. A schematic of the contribution of dislocation hardening to the yield strength is shown in Figure 2-9. As can be observed that the curve for dislocation hardening increases at a fast rate in the early stage of creep-ageing. The rise of dislocation hardening in this period is caused by impediment of dislocation movements due to nucleating of fine precipitates and entanglement of accumulated of dislocations [73]. Later a steady state of dislocation hardening is achieved when reaching an equilibrium state between dislocation hardening and dynamic recovery, which is reflected as the long plateau of the curve along with ageing time.

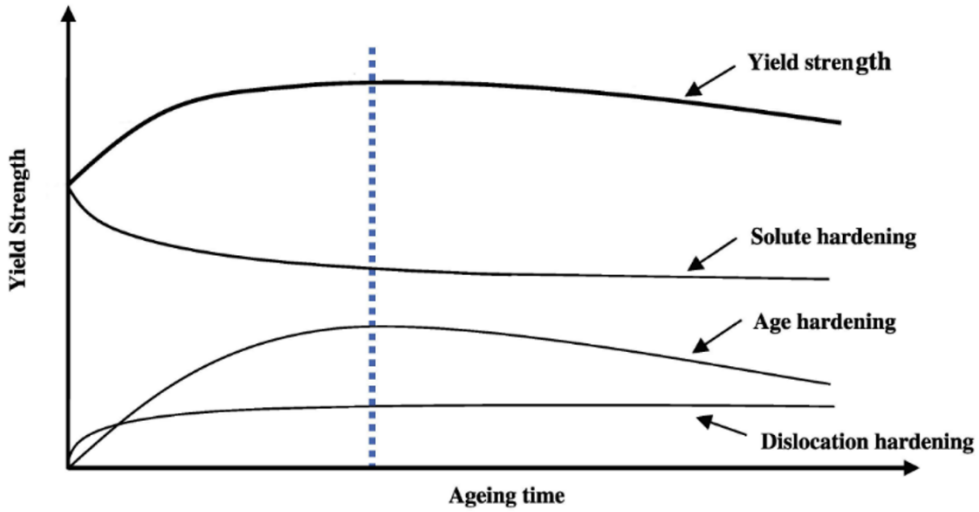


Figure 2-9. Schematic of contributions of solute hardening, age hardening and dislocation hardening to yield strength of AA7055 as a function of creep-ageing time [33].

2.5 CAF of aluminium alloys in different series and treatments

As demonstrated in Figure 1-4, aluminium alloys in 2xxx and 7xxx series have been widely adopted as the material for fabricating different aircraft components, correspondingly extensive efforts have made on investigating the material behaviour of aluminium alloys in these two series in CAF. The creep deformation behaviours of AA2050 and AA7055 had been respectively studied by applying different constant stresses in creep-ageing [33, 74]. On the other hand, the stress relaxation behaviour of AA2219 and AA7050 aluminium alloys were investigated by applying different extents of constant strain on the material in the creep-ageing tests [75, 76]. However, the initial conditions of theses investigated alloys were undergone SHT (solution heat treatment) or in T3 temper, the creep deformation behaviour of aluminium alloys at T8 temper has seldom been focused even it is the most adopted final temper for the Al-Li alloy sheets and plates [12]. Though Rong et al. [21] had investigated the stress relaxation behaviour of AA6082 with initial T6 temper in creep-ageing, the research gap of the material behaviour of aluminium alloys at T8 temper especially for the Al-Li alloys in creep-ageing, is urgently required to be filled.

Apart from the investigations being conducted on studying the creep deformation of aluminium alloy in different series, the effects of different treatments and routines adopted prior to or in creep-ageing also have drawn much attention in the recent years. The main purpose of these investigations

is to find a proper way to increase the creep deformation in CAF to achieve fabrication components with larger curvatures and better cost-efficiency, especially for adopting the recently introduced high strength aluminium alloys in creep-ageing. It has been reported that low creep strain was generated in creep-ageing tests of some 2xxx series aluminium alloys including Al-Li alloys [15]. Pre-stretching was found to be an optional treatment to improve the creep behaviour of the material in CAF, an increased creep strain was achieved for 2xxx aluminium alloys undergoing solution heat treatment (SHT) and subsequent pre-deformation, when compared with the non-pre-deformed ones in creep-ageing [77–79]. On the other hand, Yang et al. [75] investigated the stress relaxation behaviour of AA2219 under high stresses up to 210 MPa which well surpassed its yield strength of 145 MPa. Stress relaxation behaviours in both elastic and plastic regions covering different initial strain levels ranging from 0.2% up to 2% were also investigated for AA6082 [21]. Both studies manifested the happening of nonlinear change of relaxed stress when the applied stress and initial strain surpassed a certain value. Additionally, the effects of adopting treatments of multi-stage temperatures and electric pulse in on the stress relaxation of the material in creep-ageing had been respectively investigated by Zheng et al. [76] and Zhan et al. [80]. However, few study has focused on improving the creep behaviour of the 3rd generation high strength Al-Li alloys in creep-ageing, particularly on overcoming the strong creep resistance in the case of constant loading. Hence, challenges still exist in applying these advanced Al-Li alloys in CAF, and methods to improve the creep formability of these high strength alloys are urgently needed.

2.6 Unified mechanism-based materials modelling for creep age forming

It is of significance to establish proper constitutive models to predict creep behaviour of materials during CAF process. By implementing the model in numerical simulation for springback compensation and surface die design, reduction of tooling cost and enhancement of forming efficiency can be achieved. In the early stage of studies, mathematically based material models were proposed to describe macro creep deformation, without linking microstructural evolution in CAF [81–83]. With further understanding of the effects of microstructural evolutions on macro creep deformation behaviour, unified mechanism-based constitutive models were proposed, which revealed microstructural evolution features and their effects on creep deformation and hardening during CAF.

Materials modelling for aluminium alloys in CAF are reviewed in this section.

2.6.1 Development of constitutive models for CAF

In 1991, Sallah et al. [81] proposed a constitutive equation by adopting Maxwell model to predict material's viscoelastic behaviour in CAF and was given in the form of

$$\dot{\sigma} + F(\sigma, \varepsilon) = E\dot{\varepsilon} \tag{2-1}$$

where σ, ε, E stands for the stress, creep strain and Young's modulus of the material respectively. $F(\sigma, \varepsilon) = \sigma/\tau(\varepsilon)$ is the function to express stress relaxation in corresponding stress levels, where τ is a parameter dependent on the strain ε. Later simplified power-law, exponential-law, sinh-law constitutive equations were widely adopted to describe creep behaviour in primary and secondary stages [82–86]. The forms of these equations are listed in Table 2-2.

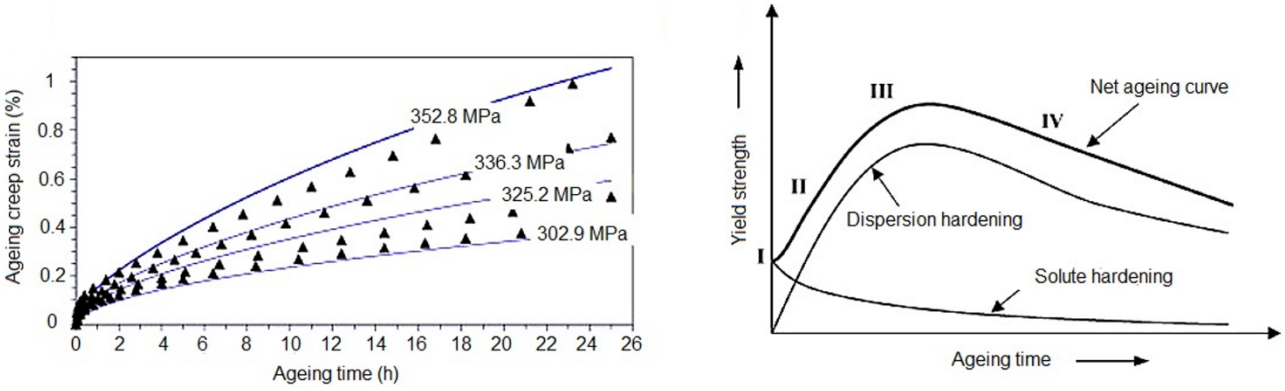
Table 2-2. Constitutive equations in different forms

Power-law equation	**Exponential-law equation**	**Sinh-law equation**
$\dot{\varepsilon} = A_1\sigma^n$	$\dot{\varepsilon} = A_2 \exp\left(\frac{\sigma^n}{B_1}\right)$	$\dot{\varepsilon} = A_3 \sinh\left(\frac{\sigma^n}{B_2}\right)$

In 2004, Ho et al. [87] proposed a mechanism-based constitutive model which focused on predicting the creep deformation and age hardening behaviour of AA7010-T3 during CAF as shown in Table 2-3. The model can well predict the creep strain under different stress levels, as illustrated in Figure 2-10a. The model may be divided into three sub-models. In the microstructure variables sub-model, the precipitate radius *r* is expressed in a rate form to reflect its growth during CAF. In the strength evolution sub-model, yield strength (σ_y) is composed of precipitation hardening (σ_A) and solid solution hardening (σ_{ss}) of the material, as shown schematically in Figure 2-10b, which are related to the precipitate radius *r*. A sinh law equation is adopted in the creep strain-stress relationship sub model. The variable *H* is introduced to represent the effect of dislocation hardening which is not directly related to the microstructure sub-model.

Table 2-3. Unified mechanism-based constitutive model proposed by Ho et al. [87].

Microstructural variables	Strength evolution model	Creep strain-stress relationship
$\dot{r} = C_0 \dot{\varepsilon}_c^{0.2} (Q - r)^{1/3}$	$\sigma_A = C_A r^{m_0}$ $\sigma_{SS} = C_{SS}(1 + r)^{-m_1}$ $\sigma_y = \sigma_{SS} + \sigma_p$	$\dot{\varepsilon}_c = A\sinh\left\{B(\sigma - \sigma_A)(1 - H)\left(\frac{C_{SS}}{\sigma_{SS}}\right)^n\right\}$ $\dot{H} = \frac{h}{\sigma^{0.1}}\left(1 - \frac{H}{H^*}\right)\dot{\varepsilon}_c$



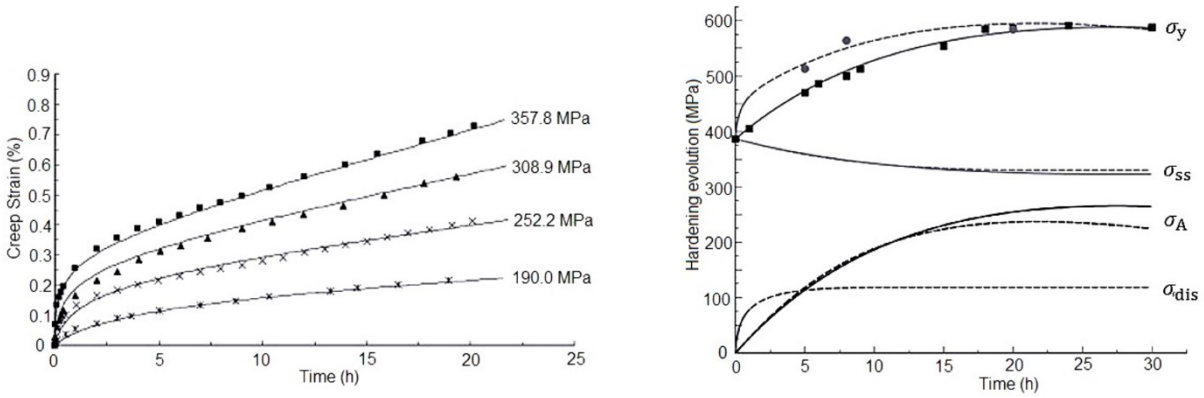
(a) Creep strains from modelling and experiment (b) Schematic of yield strength evolution

Figure 2-10. Evolution of creep strain and strength during CAF of AA7010-T3: (a) Creep strains from modelling (lines) and experiment (symbols) ; (b) Schematic of yield strength evolution and contributors [87].

With further understanding of microstructural evolution during CAF, more microstructural variables are incorporated into material models. In 2010, Zhan et al. [33] proposed a constitutive model for CAF of AA7055 which can also be separated into three sub-models as shown in Table 2-4. In this model, dislocation density ρ is modelled, considering its accumulation due to creep and reduction due to recovery. Its contribution to strength σ_{dis} is incorporated into the strength sub-model, and its effect on creep strain is also considered. Figure 2-11 shows a comparison of modelled results with experimental results for the evolution of creep strain and yield strength, showing good agreement.

Table 2-4. Unified mechanism-based constitutive model proposed by Zhan et al [33].

Microstructural variables	Strength evolution model	Creep strain-stress relationship
$\dot{\bar{r}} = C_r(Q - \bar{r})^{m_3}(1 + \gamma_0 \bar{\rho}^{m_4})$ $\dot{\bar{\rho}} = A_3(1 - \bar{\rho})\lvert\dot{\varepsilon}_{cr}\rvert - C_p \bar{\rho}^{m_5}$	$\dot{\sigma}_A = C_A \dot{\bar{r}}^{m_1}(1 - \bar{r})$ $\dot{\sigma}_{ss} = C_{ss} \dot{\bar{r}}^{m_2}(\bar{r} - 1)$ $\dot{\sigma}_{dis} = A_2 \cdot n \cdot \bar{\rho}^{n-1} \dot{\bar{\rho}}$ $\sigma_y = \sigma_{ss} + \sqrt{\sigma_A^2 + \sigma_{dis}^2}$	$\dot{\varepsilon}_{cr} = A_1 \sinh\{B_1[\lvert\sigma\rvert(1 - \bar{\rho}) - k_0 \sigma_y]\} \text{sign}\{\sigma\}$



(a) Creep strains from modelling and experiment (b) Predicted evolution of yield strength

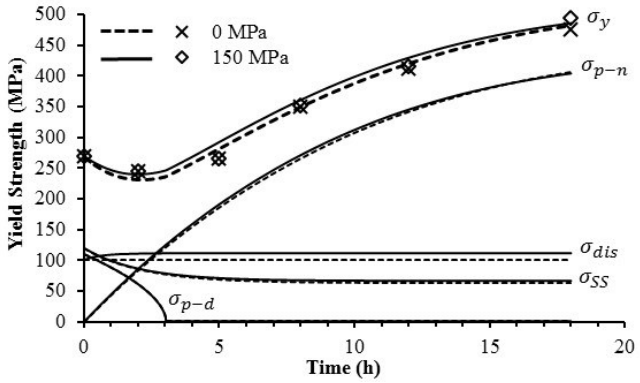
Figure 2-11. Evolution of creep strain and strength during CAF of AA7055. (a) Creep strain curves from experiments (symbols) and modelling (lines). (b) Predicted evolution of yield strength and its components under 0 MPa (solid lines) and 250 MPa (dash lines), and corresponding experimental data (symbols) [33].

More recently, Li et al. [74] investigated the creep-ageing behaviour of Al-Cu-Li alloy AA2050 and revealed the characteristics of asymmetric creep behaviour under tension and compression, double primary creep feature, and initial reversion in age hardening. They proposed an advanced constitutive model to describe the creep-ageing behaviour with the above characteristics, as shown in Table 2-5 [74]. This model has disassociated creep strain rate at ageing temperature with room temperature yield strength, both of which are related to microstructural variables.

Table 2-5. Unified mechanism based constitutive model proposed by Li et al [13].

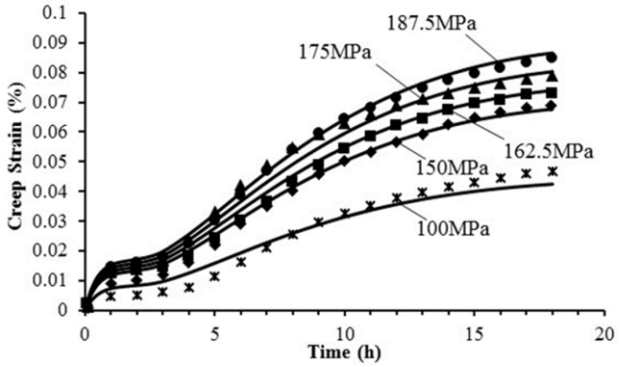
Microstructural variables	**Strength evolution model**
$\dot{\bar{\rho}} = A_1(1-\bar{\rho})\lvert\dot{\varepsilon}_{cr}\rvert^{m_1} - C_p\bar{\rho}^{m_2}$ $\dot{\bar{r}}_n = C_r(Q-\bar{r}_n)^{m_3}(1+\gamma_0\bar{\rho}^{m_4})$ $\dot{\bar{r}}_d = -\frac{C_{r1}}{\bar{r}_d}$ $\dot{\bar{c}} = -A_2(\bar{c}-\bar{c}_a)(1+\gamma_0\bar{\rho}^{m_4})$	$\dot{\sigma}_{p-n} = C_a\dot{\bar{r}}_n^{m5}\left(1-\bar{r}_n^{m_6}\right)$ $\dot{\sigma}_{p-d} = C_{a1}\bar{r}_d^{m}\dot{\bar{r}}_d$ $\dot{\sigma}_{ss} = -C_{SS}\lvert\dot{\bar{c}}\rvert^{m_8}(\bar{c}-\bar{c}_a)$ $\dot{\sigma}_{dis} = A_3 n\bar{\rho}^{n-1}\dot{\bar{\rho}}$ $\sigma_y = \sigma_{ss} + \sqrt{\sigma_{dis}^2 + \left(\sigma_{p-d}^2 + \sigma_{p-n}^2\right)}$
Creep strain-stress relationship	
$\dot{\varepsilon}_{cr} = A_4\sinh\left\{B_1\left[\left(\lvert\sigma\rvert - \sigma_{th_0}\right)(1-H)\right]\right\}\text{sign}\,(\sigma)$ $H = k'_{1_1}\bar{\rho} + k'_2\bar{c} + k'_3\left(\bar{r}_n + \beta^{1/2}\bar{r}_d\right)$	

In the microstructure variables sub-model, two types of precipitates were considered, new precipitates (r_n) and pre-existing (or dissolving) precipitates (r_d). The latter dissolves at the initial stage, leading to the reversion in age hardening as shown in Figure 2-12a. Other microstructural variables include dislocation density (ρ) and solute concentration (c) in the normalised forms which evolve with ageing progress.

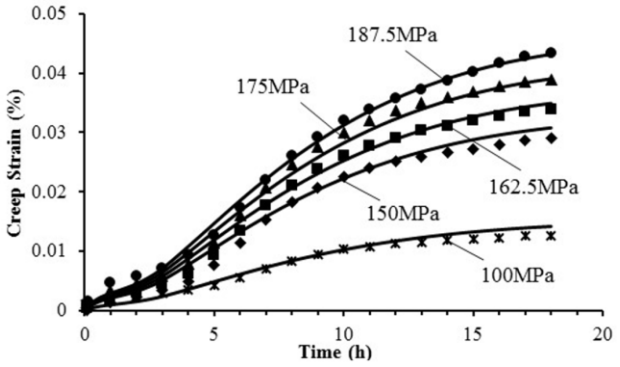


(a) Predicted evolution of yield strength

Figure 2-12. Prediction of yield strength and creep strain. (a) Reversed hardening due to precipitates dissolving [88]. Comparison of experimental (symbols) and modelled (lines) creep strain curves for AA2050 under (b) tension and (c) compression during creep-ageing [74]



(b) Creep strain curves under tension



(c) Creep strain curves under compression

Figure 2-12. (*continued*)

This model is characterised by adequate prediction of asymmetric creep behaviour under tension and compression and the double primary creep feature exhibited in AA2050. A sinh law equation is used for the strain rate-stress relationship. By introducing the variable H in the equation, the asymmetric creep behaviour is well captured after calibrating constants k_1', k_2', and k_3' with experimental data, as shown in Figure 2-12b and 2-12c. The modelled results agree well with the experimental data and have the double primary creep feature. This model is versatile and is adoptable to natural ageing and artificial ageing as well as CAF of other aluminium alloys [88].

2.6.2 Development of the sub models

2.6.2.1 Microstructure variables

Studies have shown that dislocations influence the growth and density increase of precipitates [89–91]. For heterogenous nucleation, dislocations provide crystallographic defects which lower the total free energy required for the nucleation of precipitates.

Kocks-Mecking-Estrin (KME) [92, 93] equation is widely adopted in characterising the relationship between the evolution of statistically stored dislocation density ρ_s (i.e. excluding geometric necessary dislocation density induced by Orowan loops) and plastic strain ε_p. This equation is given as

$$\frac{\partial \rho_s}{\partial \dot{\varepsilon}_p} = M(k_1\sqrt{\rho_s} - k_2\rho_s) \tag{2-2}$$

where M is the Taylor factor, k_1 is the constant related to the rate of dislocation storage, and k_2 is the constant associated with dynamic recovery.

Several other equations were proposed based on the modification of KME model such as [94]

$$\dot{\rho} = K_1\sqrt{\rho}\dot{\varepsilon}_{cr} - K_2\rho(\dot{\varepsilon}_{cr})^N \tag{2-3}$$

and [33, 74]

$$\dot{\bar{\rho}} = A_1(1-\bar{\rho})|\dot{\varepsilon}_{cr}|^{m_1} - C_p\bar{\rho}^{m_2} \tag{2-4}$$

where $\bar{\rho}$ is the normalised dislocation density, $\dot{\varepsilon}_{cr}$ is the strain rate in creep aging, and the additional term $-C_P\bar{\rho}^{m_2}$ stands for the effect of dislocation recovery.

A cubic coarsening law to approximate the evolution kinetics was proposed by Ashby [95] based on the assumption that the precipitate growth in respect of ageing time is a single peak curve:

$$r(t_a)^3 - {r_0}^3 = \frac{c_1 t}{T}\exp\left(-\frac{Q_a}{RT}\right) \tag{2-5}$$

where $r(t_a)$ is the average precipitates radius at ageing time t_a, r_0 refers to the radius at the beginning time $t_a = 0$. Q_a is the activation energy and c_1 is the material constant depending on the matrix composition.

Based on the above equation, a normalised precipitate radius $\bar{r} = r_n / r_c$ was introduced [33, 74]. r_n is the average precipitate radius at current ageing time, r_c is the critical radius at peak-ageing state. With corresponding mathematical transformation, the general modified equation can be derived as

$$\dot{\bar{r}} = C_r(Q - \bar{r})^{m_3}(1 + \gamma_0\bar{\rho}^{m_4}) \tag{2-6}$$

where Q is the factor representing the saturation state of precipitate growth; C_r, γ_0, m_3 and m_4 are material constants. The term $(1 + \gamma_0\bar{\rho}^{m_4})$ represents the effect of dislocation density.

Two parameters are required to quantify the morphology of the precipitates. For rod/needle shaped

precipitate, an aspect ratio q is defined with length l and section diameter d as $q = l / d$ [96]. Similarly, Ma et al. [97] adopted *d* and *t* as two morphology parameters to describe the diameter and thickness of plate shape precipitates respectively.

Precipitate volume fraction has effects on precipitation hardening and solid solution hardening in ageing. Some models treat this effect as a function of precipitate radius and therefore do not express it explicitly [74]. Others introduce explicit equations for precipitate volume fraction [96, 97].

As a basic form to express volume fraction evolution, Kolmogorov-Johnson-Mehl-Avrami (JMAK) equation has been adopted as a continuous process to fit the evolution of precipitate volume fraction with experimental data [98]. The form of the JMAK equation is given as

$$f_v = 1 - exp\,(-Kt^n) \tag{2-7}$$

where f_v is the relative transformed precipitate volume fraction, *t* is the ageing time, *K* and *n* are constants.

2.6.2.2 Strength evolution model

Shercliff and Ashby [99] proposed a precipitation hardening model, considering the interactions between dislocations and precipitates:

$$\sigma_A = c_3 f^m r^n;\ \sigma_B = c_4 \frac{f^{1/2}}{r} \tag{2-8}$$

where σ_A stands for the strengthening effect caused by dislocation interaction with weak precipitate and σ_B is for the strong precipitate. The equations show that the strengthening effect will increase with volume fraction f, while the effect of precipitate radius depends on shearing and bypassing interaction mechanisms. A harmonic equation in the form of $\sigma_p = ({\sigma_A}^{-1} + {\sigma_B}^{-1})^{-1}$ can be adopted to combine the two interaction effects, as shown by [74].

In solid solution hardening, the strength of the material is enhanced by the obstructing of dislocation motion by solute atoms [100]. The yield strength contribution from dislocation glide resistance caused by solutes at normalised concentration $\bar{c}$ can be expressed as [99]:

$$\sigma_{ss} = \alpha \bar{c}^{2/3} \tag{2-9}$$

where α is a material constant related to precipitate size and modulus of the solute.

By substituting $\bar{c}$ with the relationship with relative volume fraction f_v proposed by Shercliff and Ashby [99] , a general form can be derived as:

$$\sigma_{ss} = C_{ss}(1 - f_v)^{2/3} \tag{2-10}$$

where C_{ss} is material constant. This form of equation was widely adopted in investigations of the strength contribution of solid solution hardening [78, 91, 94, 101] and was proved to be an adequate approximation.

The dislocation hardening is generally modelled as a function of the dislocation density ρ [97, 102]:

$$\sigma_{dis} = M\alpha\mu b\rho^{1/2} \tag{2-11}$$

A simplified general version is given as in Eq. (2-12), where n is a constant:

$$\sigma_{dis} = A_3\bar{\rho}^n \tag{2-12}$$

All the above strength components, i.e., $\sigma_p, \sigma_{ss}, \sigma_{dis}$, contribute to the yield strength of the material. Their contributions, however, may be represented in different ways. Some researchers use a linear summation model for the overall macroscopic yield strength σ_y as follows [33, 72, 78, 103, 104]:

$$\sigma_y = \sigma_i + \sigma_{ss} + \sigma_p + \sigma_{dis} \tag{2-13}$$

However, the linear summation equation can lead to double counting of precipitation hardening and dislocation hardening [104, 105]. Hence, the addition law strength model is used by some other researchers with variable n varying between 1 and 2 [33, 74, 94]:

$$\sigma_y = \sigma_i + \sigma_{ss} + ({\sigma_p}^n + {\sigma_{dis}}^n)^{1/n} \tag{2-14}$$

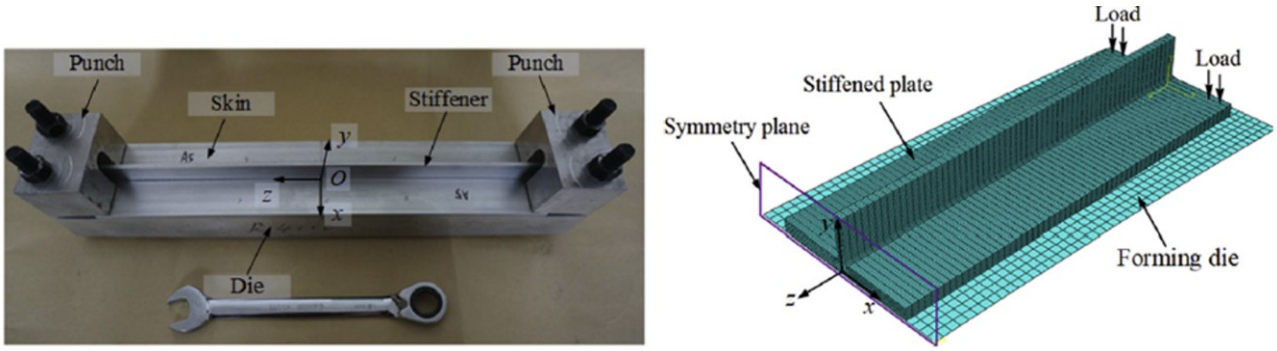
2.7 CAF fabrication and springback

2.7.1 CAF fabrications of single and double curvature structures

Single curved panels and stiffened panels are common CAF fabricated components. Also, this structure was commonly adopted as a preliminary experimental structure model to study mechanisms of stress relaxation and springback. Two kinds of the forming tools are widely adopted in fabricating single curved structures as respectively shown in Figure 2-13. The first one is the end clamp/punch device in which the forming panel is deformed with the displacements of the die (Figure 2-13a) or the punches (Figure 2-13b). The second one is the four-point bending device in which the panel is supported by two supporting heads at each end and is loaded by two loading heads in the middle (Figure 2-13c). These two devices will be fixed after the deforming panel is fully loaded to allow stress relaxation being induced in the material in CAF.

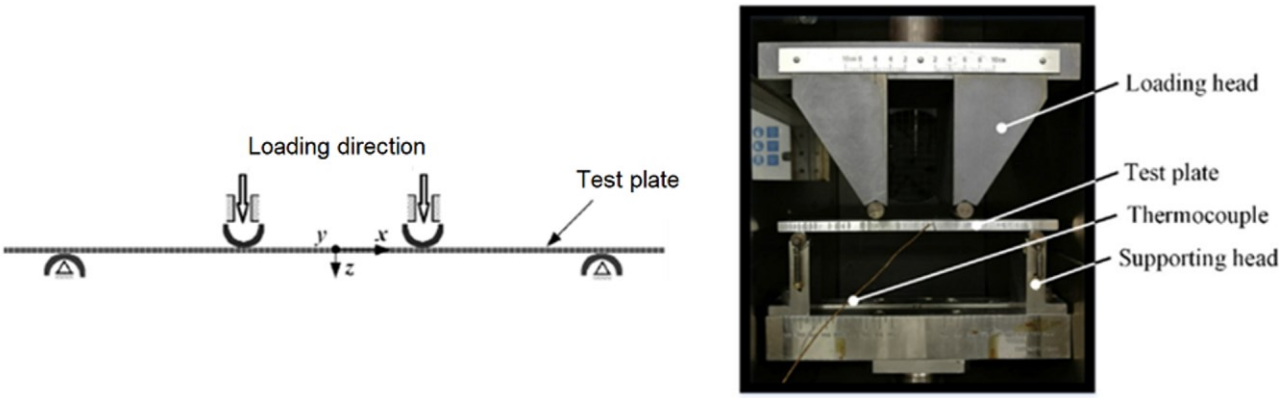


(a) End clamp device [19]



(b) End punch device and the numerical simulation model [106]

Figure 2-13. Schematic and picture illustrations of CAF devices.



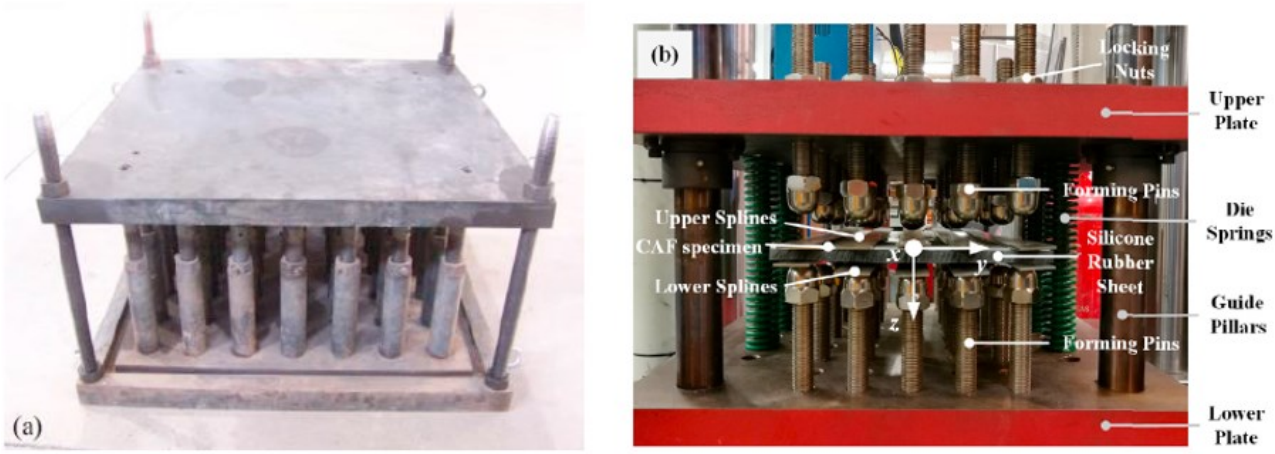
(c) Four-point bending device [107]

Figure 2-13. (*continued*).

Both devices have proven its efficiency in the investigations of CAF fabrication of single curvature structure. AA7055 panel with a half dimension of 185 mm×80 mm×12 mm fabricated by an end clamp device as demonstrate in Figure 2-13a in CAF was investigated in [19]. The CAF was set to be processed at 120°C for 20 hours. In addition, the CAF panel and the end clap device model was established in ABAQUS with the developed material constitutive model implemented through the CREEP subroutine. Significant stress relaxation was found in the creep-ageing stage, which reduced the equivalent stress by approximately 50%. Higher stress distribution areas were found to be distributed in the middle of the panel and near the clamp than the rest of the areas. By adopting an end punch device as shown in Figure 2-13b, a single curved AA7B04-T651 stiffened panel in CAF was experimentally and numerically studied [106]. Different stiffener heights ranging from 10 mm to 30 mm were selected for CAF tests of forming different single curved panels. Tests were conducted at 120°C for 20 h. The numerical simulation was conducted in ABAQUS by implementing the self-defined material model into CREEP subroutine. The simulation model is shown in Figure 2-13b. Good convergences were achieved between experimental and simulation results, which were in 6.7% and 3.3% error ranges in aspects of springback and yield strength respectively. Also, it has been found that due to the discrepant creep strains developed in different parts of the component, higher residual stress existed in the stiffener than in the plate. Figure 2-13c shows the CAF adopting the four-point bending to fabricate AA2050-T34 single curvature sheets [108]. The rectangular sheets with a dimension of 220 mmx20 mm and thicknesses of 8 mm and 10 mm were conducted in CAF at 155°C

for 18 h. The FE simulations were completed with PAM-STAMP by implementing an asymmetric material model into the software. At the end of ageing stage, tension induced creep strain at the bottom surface was found to be more than twice the compression induced creep strain at the top surface with values of 0.090% and 0.044% respectively.

With the development of the fabrication tool and the rising requirements of the fabricated components with more complexed contour, the multipoint flexible tool, as one of the state-of-the-art forming tools, is characterised by its flexibility in setting required loading shape and has been adopted to not only CAF but also other sheet forming processes [109–111]. As shown in Figure 2-14, the flexible tool is composed of the major parts including forming pins, upper and lower plates. By adjusting the positions of the forming pins, the forming sheet can be deformed to the designed shape through exerting downward displacement of the upper plate. Similar to the single curvature CAF fabrication devices, the flexible die will be fixed after the sheet is fully deformed to induce stress relaxation in creep-ageing.

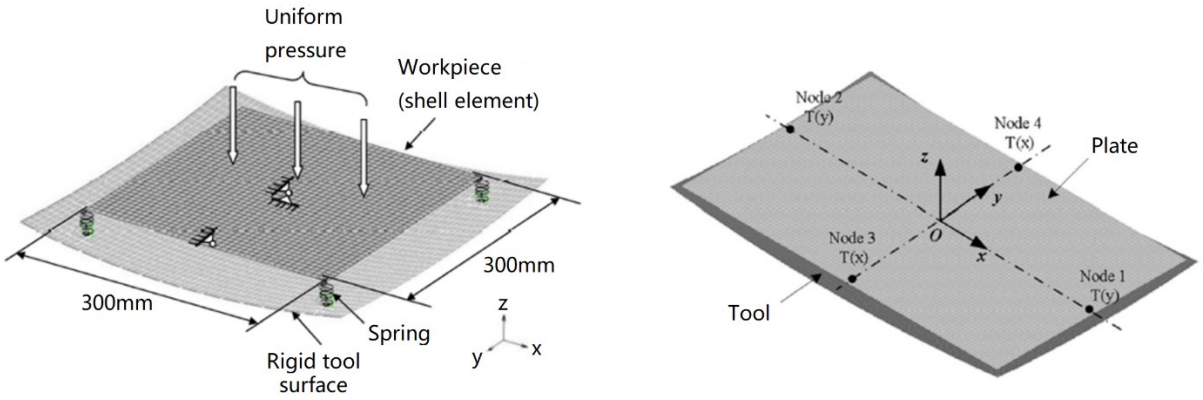


(a) Fabrication tool adopted by Lyu et al. (b) Fabrication tool adopted by Li et al.

Figure 2-14. Multipoint flexible forming tools for CAF. (a) Tool used for fabrication of AA7050 saddle shaped sheet [112]. (b) Tool used for fabrication of AA2050 sheet [113].

In the investigation of CAF of double curvature sheet, numerical simulations were conducted priorly to verify the fabrication feasibility. Zhan et al. [33] established a double curved numerical model in MSC.MARC and implemented the defined material model for AA7055 through user defined

subroutine. This model was able to predict stress relaxation, creep strain evolution, precipitation growth as well as springback amount for the double curved sheets in CAF. Li et al. [108] also managed to simulate the material evolvements of AA2050 CAF double curved sheets in the above aspects by applying PAM-STAMP. Besides, the asymmetric creep behaviour of AA2050 under tension and compression was able to be simulated in the model. The schematic of these two FE models is shown below in Figure 2-15.



(a) AA7055 double curved sheet model [33] (b) AA2050 double curved sheet model [108]

Figure 2-15. Schematic of two CAF FE numerical models.

Latterly by adopting the flexible tool as shown in Figure 2-14a, Lyu et al. [112] managed to fabricate a CAF double curvature AA7050 sheet with dimensions of 600x600x6 mm with curvature radius of 1333 and 4000mm respectively along the length and width directions of the sheet. Li et al. [113] also conducted an investigation of CAF fabrication of double curvature AA2050 sheets with different thicknesses of 3 and 6 mm by adopting the flexible tool demonstrated in Figure 2-14b. In addition, numerical simulation models were established in the above two studies. For the double curved CAF AA7050 sheet, the simulation results of Lyu et al. [112] verified the positive relationship among stress states level, creep strain rate, and stress relaxation rate. Li et al. [113] found that stress concentration was induced in the area surrounding the forming pin, which can be reduced by increasing the number of the pin. Both studies achieved good convergence between experimental and simulation results, with a maximum prediction error of 0.9 mm in Lyu et al. [112] and 3 mm in Li et al. [113], which validified the feasibility of CAF prediction and accurate fabrication control of double curved sheets by numerical simulation.

2.7.2 Springback investigation in CAF

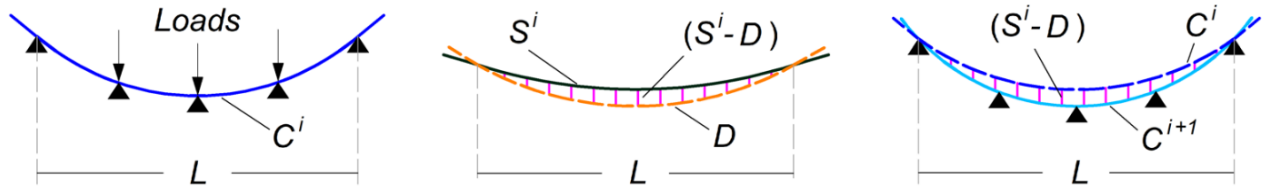
Springback happens in the unloading stage of metal forming as a result of recovery of elastic strain induced in loading stage, which has long been a focus in the whole metal forming field due to its substantial association with forming accuracy and fabrication efficiency. In the past decades, as reviewed by Wagoner et al. [114], analytical solutions and methods utilising finite element (FE) analysis were proposed to predict springback regarding to different metal forming conditions such as pure bending [115], bending combined with tension [116, 117], and draw bending [118, 119]. Additionally, in recent years, investigation of springback has extended to the non-linear plastic bending behaviour with large deformation [120], bending of curved beam and tube [121, 122], and multiple reciprocating bending [123]. In the area of CAF, early investigation of springback analysis was conducted based on Euler–Bernoulli beam theory for predicting the formed sheet shape in single-curvature case [81]. Latterly by independently considering relations of moment and bending curvature derived from the beam theory along length and width directions, prediction of springback for double-curvature bending was fulfilled [124]. With the development of constitutive model for creep-ageing, by adopting the mechanism-based model to reflect stress-creep strain relationship in CAF, Jeunechamps et al. [125] further proposed an analytical springback prediction method which can be applied to double-curvature bending case of CAF sheet. Li et al. [126] further extended the application of springback prediction surpassing elastic region, by utilising the beam theory and FE analysis.

In practical fabrication, to deform sheets to the target shape/curvature, the idea of springback control by compensating tool shape to achieve the target shape/curvature has been widely adopted. Displacement adjustment (DA) method, initially proposed by Gan et al. [127], is a direct geometric iterative control method by continually adjusting tool shape to let shape/curvature of the formed sheet gradually approaching the target value. The iterative algorithm of DA method can be expressed as

$$C^{i+1} = C^i - (S^i - D) \tag{2-15}$$

where C^i and S^i are the tool shape and the deformed shape after springback in i^{th} iteration as shown in Figure 2-16a. D is the target shape to be formed as illustrated in Figure 2-16b. Hence the term $(S^i - D)$ can be viewed as the geometric error between the deformed and target shape in i^{th} iteration as shown in Figure 2-16b. C^{i+1} is the tool shape taken in the $(i+1)^{th}$ fabrication

iteration, as demonstrated in Figure 2-16c, which is directly obtained by compensating the tool shape C^i in previous i^{th} iteration with the geometric error $(S^i - D)$. Based on the proposed DA method and utilising FE simulation, satisfactory convergence was achieved between the shape of the sheet and its target surface formed by compensated flexible dies [110]. In the study, FE simulations were used to replace experimental iterations in DA method. By considering compensation direction, Yang and Ruan [128] improved the prediction accuracy of DA method for the case of stamping of high strength steel, in which large displacement and rotation can happen during springback. In their study, errors between experimental and FE simulation results were observed after completion of one iteration. When the tool shape C and deformed sheet shape S were obtained from FE results to replace experimental ones, the validity of the DA method becomes highly dependent on the accuracy of simulated springback prediction results [114]. Hence the simulation error can become an issue for adopting FE analysis as an alternative tool, especially for fabrication of components requiring high precision. On the other hand, when the values of C and S are determined from experimental results without proper analytical method, it can be highly time-consuming and costly on approaching the target value by iterations. It is of significance to find the balance between prediction accuracy of springback and cost of practical experiments to ensure the validity and effectiveness of the DA method.



(a) Loaded to tool shape C^i (b) Geometric error $(S^i - D)$ (c) Loaded to tool shape C^{i+1}

Figure 2-16. Schematic of DA method for springback compensation.

With the continued advancements in new generation aluminium alloys possessing superior mechanical properties, these high strength aluminium alloys have been widely adopted in practical fabrication recently [12]. Among these high strength alloys, the latest 3rd generation Al-Li alloy has drawn much attention. However, with the prominent strength promotion for these Al-Li alloys, the creep resistance is enhanced simultaneously which in turn reduces the creep deformation in CAF:

limited creep strain was observed in creep-ageing for this alloy [129]. Consequently, plastic strain can be needed and be introduced through large deformation in loading stage as supplement for CAF of the material. Hence, due to the required high stress in creep-ageing for the Al-Li alloy and large deformation in loading stage, the applicability of the beam theory for springback prediction may be limited. When large deformation is exerted which induces plastic region in outer bending layers of the forming sheet, the Euler–Bernoulli beam theory, established within elastic region with assumption of small deflection, becomes inappropriate to describe deflection and induced stress: the relation of bending strain ε and curvature k can lose its geometry validity in the case of large deformation. Hence a new analytical method to properly reflect the stress states of material in large deformation for CAF with high strength Al-Li alloys is urgently required, based on which the prediction accuracy of springback and the validity of corresponding developed compensation method can be ensured.

2.8 Summary

Creep age forming is a panel forming method that takes advantage of both creep and ageing behaviour of aluminium alloys. Since its invention in the 1980s, this method has been widely adopted not only to the fabrication of aircraft components but also has been broadened to the applications of forming stiffened panels for launch vehicles. Additionally, studies have been conducted to verify the feasibility of applying CAF in the fabrication of components with more complex contours such as head panels for high-speed trains.

The creep behaviour of aluminium alloy, with the induced microstructure evolution and reflected macro deformation at different stages in creep, has been reviewed. On the other hand, the ageing induced precipitates for the Al-Li alloys, such as θ phase precipitate series and T_1 precipitate, have been reviewed. Age hardening mechanisms in creep-ageing, including precipitation hardening, solid solution hardening, and dislocation hardening have been discussed. Developments of the constitutive models for CAF, from the previous mathematical-based models to the current developed mechanism-based ones which reasonably link the intrinsic microstructure evolution with macro creep deformation in creep-ageing, have been reviewed. Moreover, the state of art CAF fabrication with the corresponding tools and numerical simulation techniques, in aspects of experiments and simulations of single and double curvature CAF components, and springback investigation in CAF have been

reviewed.

Though extensive efforts have been made to a wide range of investigations including material behaviour, constitutive modelling, and fabrication techniques for CAF, which solidly improved the application of this method in different scenarios, the application of high strength Al-Li alloys in CAF has seldom been studied and remained blank. As the most adopted finish temper for the Al-Li alloys, the material behaviour with T8 temper during creep-ageing still requires further investigations to fill the knowledge gap. In addition, with the remarkable promotion of strength and creep resistance of this new generation of Al-Li alloys, new challenges have been raised in fulfilling the fabrication requirements of large-scale panels with higher curvatures. A method to induce increased creep strain for the high strength Al-Li alloys in CAF to obtain larger deformed deflection, as well as the corresponding constitutive modelling and implementation is urgently needed. Simultaneously, as a larger loading displacement is required to obtain higher stress and creep strain for the alloy in CAF, the traditional beam theory with the assumption of small deflection can lose its geometry validity and prediction accuracy in the case of adopting high strength Al-Li alloys. As a result, an effective springback prediction and compensation method for the high strength aluminium alloy adopted in CAF should be proposed.

Chapter 3

Experimental programme and techniques

3.1 Introduction

This chapter provides a detailed description of the experimental programme and techniques used in this study for the investigation of AA2060 in CAF. In section 3.2, the basic information including composition and heat treatment history of the as-received AA2060 is provided. An overview of all the experiments performed with test programme in this study has been given. The adopted specimens and equipment, as well as the test setup and procedures for the conducted experiments, are introduced in detail in Sections 3.3, 3.4, and 3.5.

3.2 Material and experimental overview

3.2.1 Material

The material adopted in this research is AA2060-T8. The basic composition of the material is listed in Table 3-1.

Table 3-1. Chemical composition of investigated AA2060.

Element	**Li**	**Cu**	**Mg**	**Zn**	**Ag**	**Mn**
wt.%	0.6-0.9	3.4-4.5	0.6-1.1	0.3-0.5	0.05-0.5	0.1-0.5
Element	**Fe**	**Si**	**Ti**	**Zr**	**Al**	
wt.%	Min-0.07	Min-0.07	Min-0.1	0.05-0.15	Remainder	

The material was provided by Shanghai Aircraft Manufacturing Company (COMAC) with a T8 initial temper. According to the information provided by the supplier, the as-received material had undergone solution heat treatment (SHT), quenching, cold working, and then artificial ageing at 143 °C for 30 h. Based on the provided information, 143 °C was determined to be the ageing temperature in the research program.

3.2.2 Overall experimental plan for investigation of AA2060 in CAF

The objective of this research program is to investigate the application of 3rd generation Al-Li alloy AA2060 in CAF for a single curvature panel. To fulfil the aim, a series of experiments were designed and conducted sequentially to investigate the material property, micro and macro creep-ageing behaviours, as well as CAF fabrication adopting AA2060. The overall experimental plan with the object and data usage for each test group is demonstrated in Table 3-2.

Table 3-2. General experiment plan.

Experiment	Aim	Data usage
Room and elevated temperature tensile test	To obtain material tensile properties at room and elevated temperature.	Used as material property values (yield strength, Young's modulus, etc.).
Hardness tests	To obtain information of the strength evolution of the material in ageing.	To help determine the duration of creep-ageing stage.
Uniaxial creep-ageing with subsequent tensile test	To investigate the relation of stress-creep strain, and material strength evolution under different applied stress in creep-ageing.	Used for the constitutive model establishment.
Microstructural investigation	To investigate precipitation and dislocation evolution of material in creep-ageing under different stresses.	Used for constitutive model establishment.
Four-point bending CAF tests	To investigate CAF in four-point bending tests. To verify the accuracy of numerical simulation with the adopted established constitutive model.	Used for developing springback prediction method of CAF fabrication and verification of numerical simulation analysis.
Fabrication of CAF panel with multipoint tool	To investigate CAF panel fabrication with a multipoint forming tool.	Used for development of workflow of CAF fabricated panel with target curvature.

3.2.3 Test programme

3.2.3.1 Material property tests

A series of material property tests including tensile tests at room temperature and elevated temperature, as well as hardness tests for material with different ageing time were conducted to investigate basic properties of the material involved with CAF.

Table 3-3 shows the information of test programme for material property tests. Strain-stress relations of the material at room temperature (RT) and elevated temperature of 143 °C were investigated from corresponding tensile tests. Both tests were conducted with a strain rate of 0.001 s^{-1}. Hardness evolution of the material with ageing time was investigated with tests of the as-received material and the specimens after ageing of 3, 6, 10, 15, 20, 25, and 30 h at 143°C respectively.

Table 3-3. Material property test programme.

Material property test	Heat treatment condition
RT tensile test	As-received
Tensile test at 143 °C	As-received
Hardness test	As-received and after ageing of 3, 6, 10, 15, 20, 25, 30 h at 143°C

3.2.3.2 Uniaxial creep-ageing test and subsequent tensile test

The creep-ageing experiments conducted in this research included uniaxial creep-ageing tests and subsequent tensile tests at room temperature (RT). The test programme of uniaxial creep-ageing tests and subsequent tensile tests are demonstrated in Table 3-4.

Table 3-4. Uniaxial creep-ageing and subsequent RT tensile test programme.

Test	Stress (MPa)	Ageing time (h)
Uniaxial creep-ageing test and subsequent RT tensile test	300, 400, 430	3, 6, 15
Uniaxial creep-ageing test only	300, 360, 400, 415, 422.5, 430	20

3.2.3.3 Microstructural investigation

Transmission electron microscopy (TEM) observation and X-ray diffraction (XRD) test were conducted to investigate precipitation and dislocation evolution of material with different stress and creep-ageing time respectively. Table 3-5 is the test programme demonstrating treatment conditions

of the specimen for conducted TEM an XRD tests respectively.

Table 3-5. Samples selected for TEM and XRD tests.

Test	Treatment condition
TEM	As-received: creep-aged for 0 h 300 MPa: creep aged for 6, 15 h 400 MPa: creep-aged for 3, 6, 10, 15 h 430 MPa: creep aged for 6, 15 h
XRD	As-received: creep-aged for 0 h 300 MPa: creep-aged for 6, 15 h 400 MPa: creep aged for 6, 15 h 430 MPa: creep aged for 6, 15 h

3.2.3.4 Four-point bending CAF test

The overall four-point bending CAF test was divided into two groups: with the same maximum surface stress in elastic region and with a target curvature radius of 2000 mm. The first group is to verify the accuracy of the established constitutive model and develop simulation technology. The second is to develop and verify the proposed method of CAF fabrication with target curvature. For each group, tests were conducted with three thicknesses (2 , 4, and 6 mm).

Based on the dimension of the test specimen, a four-point bending model was designed as shown in Figure 3-1. L is the distance between lower supporting cylinders. a is the distance between the centre of support and loading cylinders. F denotes the load applied on each loading cylinder.

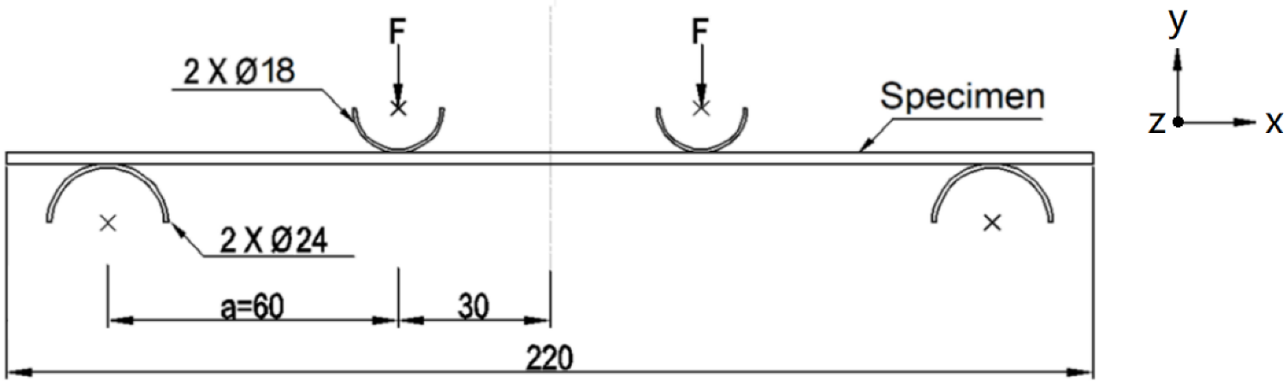


Figure 3-1. Schematic of designed four-point bending test (dimension in mm).

Derived from the Euler–Bernoulli beam theory, the equation to analyse the deflection of the model is

$$d_{ll} = \frac{Fa}{6EI}(L^2 - 4a^2) \tag{3-1}$$

d_{ll} is the displacement at the loading point. E and I are respectively Young's modulus and moment inertia of the specimen for the z axis. With $L = 3a$ and $I = bt^3 / 12$, the equation can be further written as

$$d_{ll} = \frac{10Fa^3}{Ebt^3} \tag{3-2}$$

b is the width and t is the thickness of the specimen. The stress at the surface layer of the specimen σ_{surf} gives

$$\sigma_{surf} = \frac{2FL}{bt^2} \tag{3-3}$$

With above equations (Eq. (3-1) to Eq. (3-3)), the experiment plan for four-point bending CAF within the elastic region was designed and shown in Table 3-6. For CAF with four-point bending within elastic region, appropriate stress under which adequate creep strain can be generated should be employed to investigate its effects on the forming. Based on the uniaxial creep-ageing tests results, 430 MPa is chosen as the investigation stress.

Table 3-6. Experiment plan for four-point bending CAF with the same maximum surface stress within the elastic region

Thickness (mm)	**Loading displacement d_{ll} (mm)**	**Loading force F (N)**	**Maximum stress σ_{surf} (MPa)**
2	18.7	78.2	430
4	9.2	319.3	430
6	5.9	788.3	430

For the experiment of four-point bending CAF with a target curvature radius of 2000 mm, the experiment was designed based on numerical simulation results which will be further discussed in the following section. With given curvature radius, the geometry relation between target deflection d_{tf} and curvature radius R_c is demonstrated in Figure 3-2.

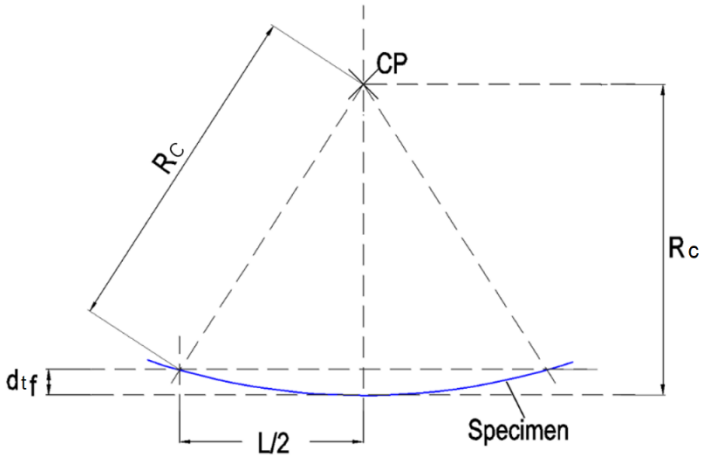


Figure 3-2. Schematic of geometry relation between target curvature radius R_c and deflection after springback d_{tf} (CP stands for centre point of the curvature and L is the distance between supporting points).

As demonstrated in Figure 3-2, the geometry relation between d_{tf} and curvature radius R_c can be expressed as

$$d_{tf} = R_c - \sqrt{(R_c)^2 - (L/2)^2} \tag{3-4}$$

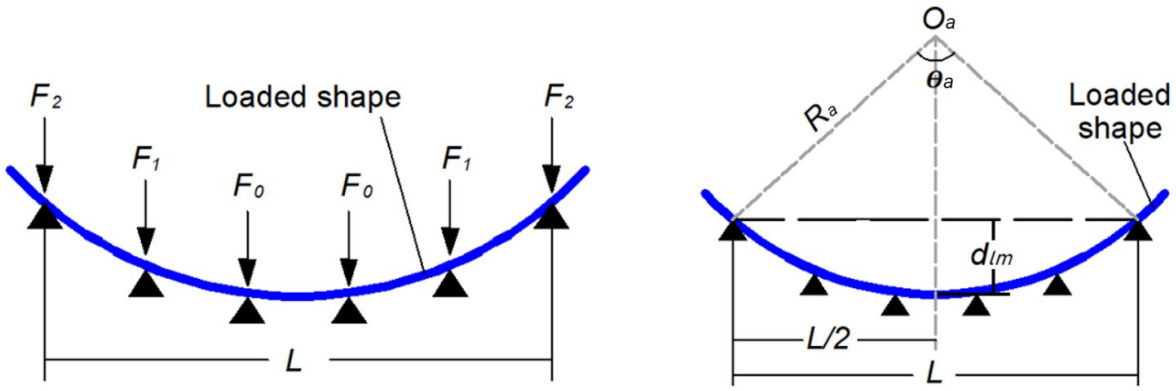
Based on Eq. (3-4), with a given curvature radius R_c of 2000 mm and L of 180 mm, the target deflection of specimen d_{tf} derives a value of 2.03 mm. The plan is presented in Table 3-7.

Table 3-7. Experimental plan for four-point bending CAF with the same target curvature.

Thickness (mm)	Target deflection (mm)	Loading displacement d_{ll} (mm)
2	2.03	20.2
4	2.03	10.8
6	2.03	7.3

3.2.3.5 Fabrication of CAF panel with a flexible tool

The experiments conducted to investigate panel fabrication with the multipoint flexible tool were aimed at fabricating single curvature panels with target curvature. The schematic and geometry relation of adopting a flexible tool to fabricate single curvature panel in CAF is demonstrated in Figure 3-3. As demonstrated in the figure, the specimen is loaded to a designed shape with the flexible tool (Figure 3-3a). For the loaded shape (Figure 3-3b), d_{lm} is the deflection under loading at the midpoint of the specimen, O_a and R_a are respectively the centre point and radius of the loaded curvature, and θ_a is the centre angle for the loaded curvature.



(a) Fabrication adopting the flexible tool (b) Geometry relation

Figure 3-3. Schematic of adopting multipoint flexible tool and geometry relation.

For CAF fabrication with target curvature, by utilising the developed springback prediction method which will be detailed in Chapter 7, the conducted experimental conditions are presented in Table 3-8. The target curvature radius is 2000 mm.

Table 3-8. Experiments for multipoint tool CAF fabrication with target curvature.

Thickness (mm)	**Loading deflection d_{lm} (mm)**	**Target curvature radius (mm)**
2	72.6	2000
4	41.5	2000

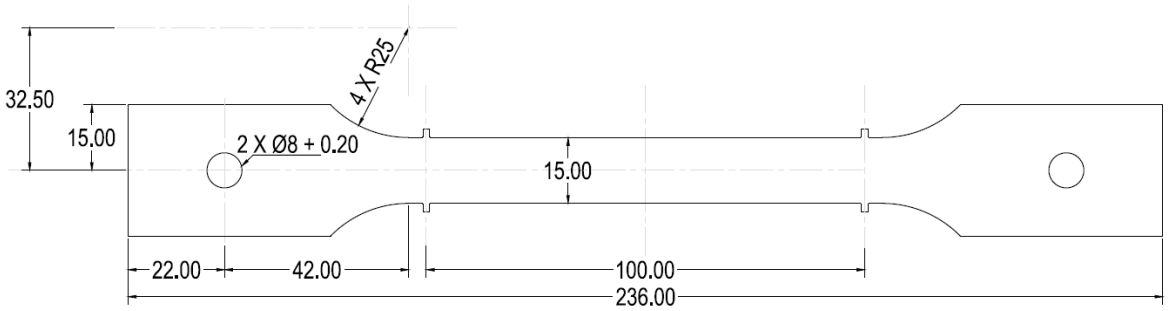
3.3 Mechanical tests

In this section, uniaxial tensile tests in room and elevated temperature, as well as the hardness tests were conducted to obtain an overall information of the material property in CAF and the tests are introduced accordingly.

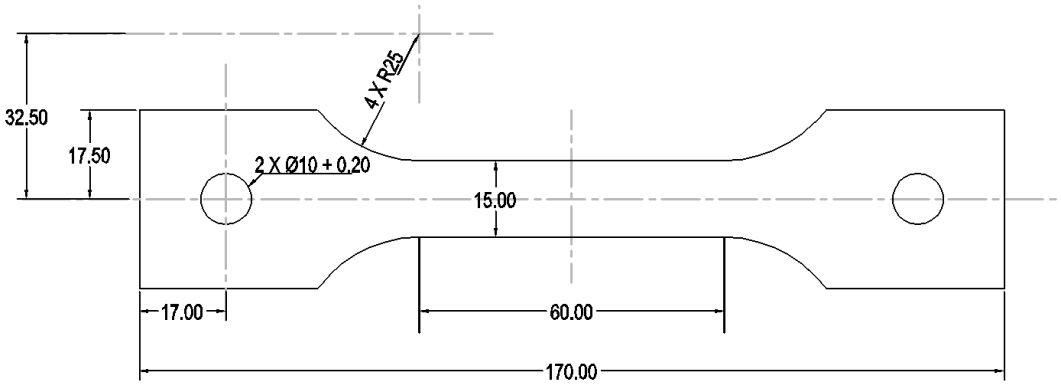
3.3.1 Tensile tests

3.3.1.1 Test specimen

For both RT and elevated temperature tensile tests, the test specimens were cut from the as-received 250 mm x 35 mm sheets with 2 mm thickness along the rolling direction. The shape and dimensions of the specimens for the RT and elevated temperature tests are shown in Figure 3-4 (a) and (b) respectively.



(a) Room temperature



(b) Elevated temperature

Figure 3-4. Specimen geometry for room temperature (a) and elevated temperature (b) tensile test (dimension: mm).

3.3.1.2 Equipment and test setup

For RT tensile test, a Sinotest DNS tensile test machine was used to conduct room temperature tensile tests. A MCT CY series extensometer with 50 mm gauge length was used to measure the strain of the specimen during the test. The detailed setup for the test is demonstrated in Figure 3-5. The test specimen was fixed with hydraulic clamps assembled on the upper and lower grips, and the extensometer was attached to the middle of the test specimen. The test was conducted at a strain rate of 0.001 s^{-1}.

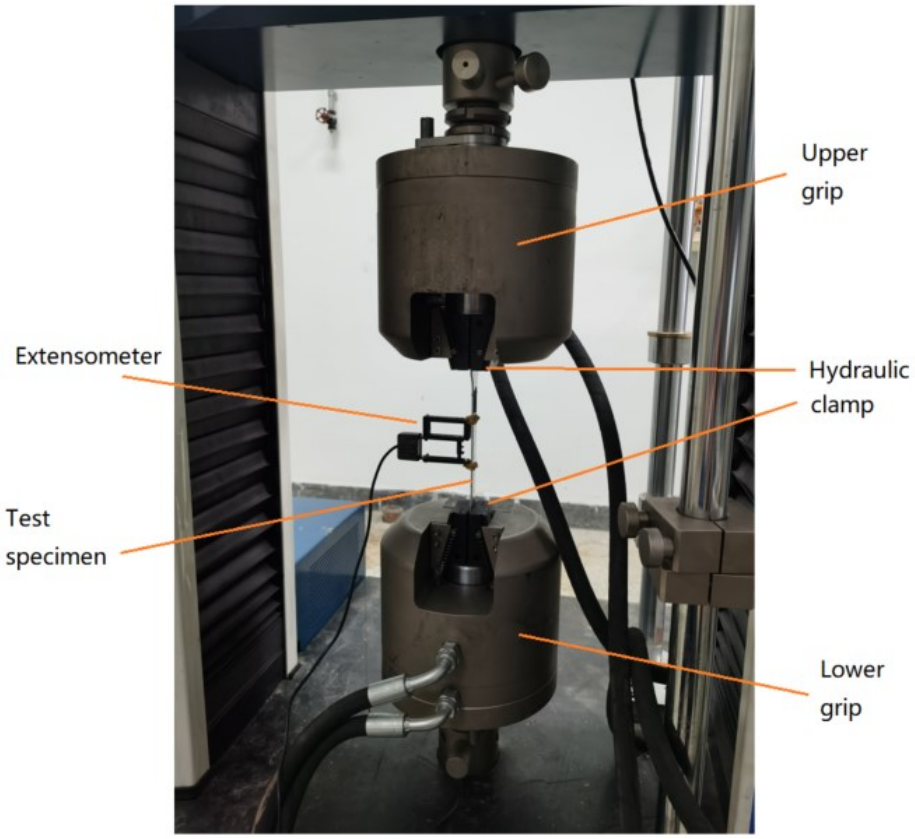


Figure 3-5. Equipment setup for room temperature tensile test.

For elevated temperature tensile test, a Sinotest DNS tensile test machine with a supporting furnace was adopted. An Epsilon 3549 high-temperature extensometer with 25 mm gauge length was used to measure the strain. The extensometer and furnace were linked via data receiver and temperature monitor respectively to the computer. The setup of the elevated temperature tensile test is presented in Figure 3-6. As demonstrated in the figure, the extensometer and rail were lifted by a lift arm and positioned at the same height with the middle of specimen. The enlarged figure in Figure 3-6 demonstrates the extensometer was installed on a supporting rail which can let the extensometer slide along. A thermocouple was attached to the middle of the specimen. The elevated tensile test was performed at 143 °C $\pm$ 3 °C with a strain rate of 0.001 s^{-1}. The subsequent tensile test of the specimen after creep-ageing is conducted with the same equipment and procedure.

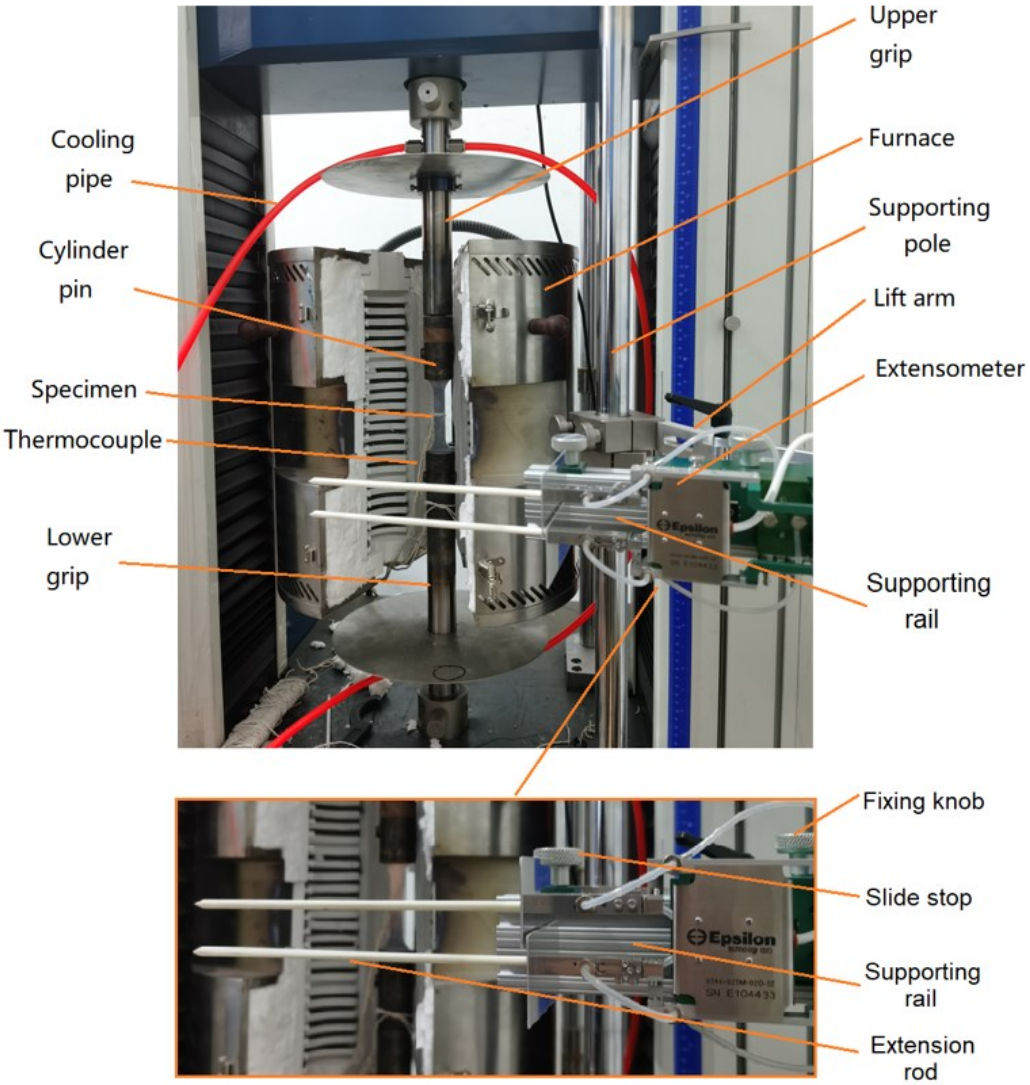


Figure 3-6. Setup for elevated temperature tensile test.

3.3.1.3 Test procedure

For RT tensile test, the test was conducted following the procedure:

(a1) Before clamping, adjust the specimen with length direction centre line parallel with the centre line of the grips. Then clamp and fix the specimen with the hydraulic clamp demonstrated in Figure 3-5. Attach the extensometer to the middle area of the specimen.

(b1) Apply load with a strain rate of 0.001 s^{-1}.

(c1) The test ends when the specimen is fractured.

For the elevated temperature tensile test, the test was conducted following the below procedure:

(a2) Fix specimen with the upper and lower grips via cylinder pins.

(b2) Position the extensometer and let the extension rods contact the middle of the specimen. Exert appropriate contact force by repositioning the extensometer along the supporting rail and fix the position with the fixing knob (Figure 3-6).

(c2) Close the furnace and heat up to 143 °C within 20 minutes, and soak at 143 °C for 10 minutes

(d2) After soaking, apply the load at an extension rate of 0.001 s^{-1}.

(e2) The test ends when the specimen is fractured.

3.3.2 Hardness test for ageing specimens

3.3.2.1 Test specimen

The as-received 2 mm-thick sheets were cut into square specimens with a dimension of 20 mm x 20 mm for heat treatment and subsequent hardness test.

3.3.3.2 Equipment and test setup

An HVS-1000 digital hardness test machine shown in Figure 3-7 was used. The machine was connected to a computer installed with the test machine manufacturer developed software that can display the transmitted view from the microscope of the machine and calculate the hardness accordingly. Vickers hardness method was adopted to calculate the hardness of the material (hardness unit in HV). The tests were performed with an indention load of 2.94 N and a dwell time of 15 s.

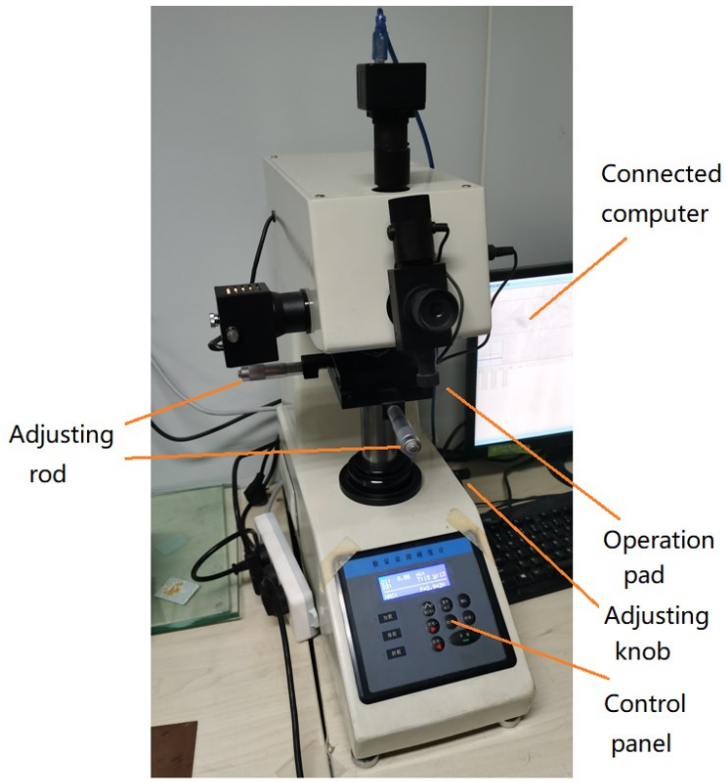


Figure 3-7. Hardness test equipment.

3.3.3.3 Test procedure

The test was conducted following the below sequences:

(a) Put the specimen on the operation pad and adjust it being in the view range of the microscope.

(b) Adjust the distance between microscope and specimen to acquire a clear vision of the specimen surface with the adjusting knob.

(c) Start the test with an indention press of 2.94 N and dwelling time of 15 s.

(d) Area of the pressed square dent is calculated by the software by manually marking the dent boundaries. The hardness can be automatically calculated by software with equation $HV = 0.18\,F/S$. HV is material hardness (HV), F is the applied indention force (N), S is the dent area (mm^2).

3.4 Uniaxial creep-ageing test

In this section, the creep deformation behaviour of the material in CAF was investigated by

conducting uniaxial creep-ageing tests under different stresses and the detailed information of the test is introduced.

3.4.1 Test specimen

Specimens for uniaxial creep-ageing test were cut from 2 mm thick as-received sheets along the rolling direction, and the dimension are the same as the RT one shown in Figure 3-4 (a) .

3.4.2 Equipment and test setup

The creep-ageing tests were conducted by a Sinotest RDL tensile test machine with a Sinotest RH elevated temperature chamber. The accuracy and stability of the chamber were verified with thermocouples attached to different areas in the chamber prior to the creep-ageing tests. The test setup was demonstrated in Figure 3-8. As shown in the enlarged picture of Figure 3-8, the specimen was assembled on the machine through pin cylinders inserted through the preserved holes of the grips and specimen on both the upper and lower sides. Four extension brackets were used to transfer the creep deformation. The upper ends of the four brackets were respectively attached to the four ridges of the specimen and were fixed with upper and lower embracing rings. The lower ends of the brackets were attached to the grip with slide rollers to allow the brackets to slide along the grip to transfer the creep deformation. Four springs were used to fasten the brackets and lower grip to let the sliding only along the axial direction of the grip. A pair of HEIDENHAIN SPECTO series incremental length gauges with a measuring accuracy of $\pm 1\ \mu m$ were installed on the end of extension brackets to capture the transferred creep deformation. The gauges were connected with the controller to send real-time measured length increments to be displayed and recorded in the computer.

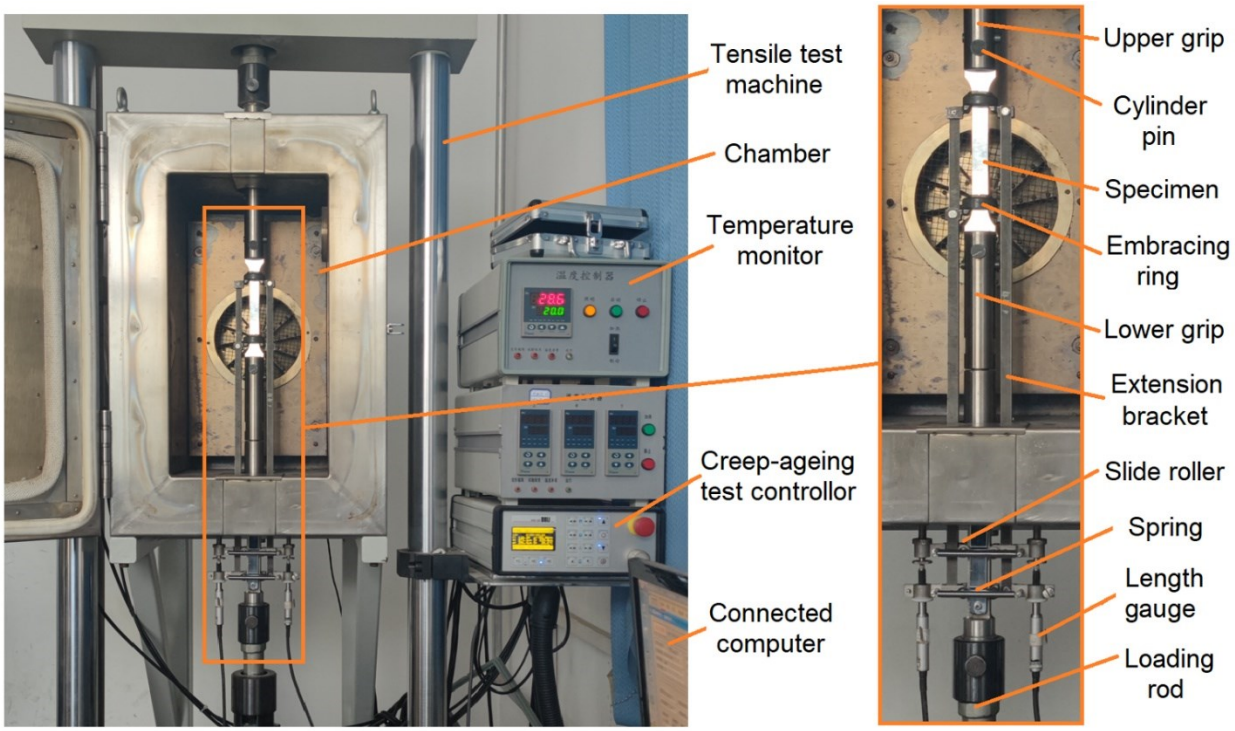


Figure 3-8. Equipment and setup for uniaxial creep-ageing test.

3.4.3 Experiment procedure

The creep-ageing tests were conducted with below procedures:

(a) Connect the test specimen to the upper and lower grips by inserting cylinder pins through the preserved holes.

(b) Attach the upper ends of extension brackets on the specimen. Install the incremental length gauges on the lower ends of the extension brackets.

(e) Close the chamber and start to heat up to 143 °C $\pm$ 3 °C followed with 15 minutes soaking.

(f) After soaking, load the specimen with a rate of 1 kN/min to pre-determined stress and keep at this stress for creep-ageing with pre-determined ageing time.

(g) When reaching the designed creep-ageing time, unload the specimen and open the chamber for cooling down.

Generalised uniaxial creep-ageing test stages and heating curve in creep-ageing test are demonstrated in Figure 3-9.

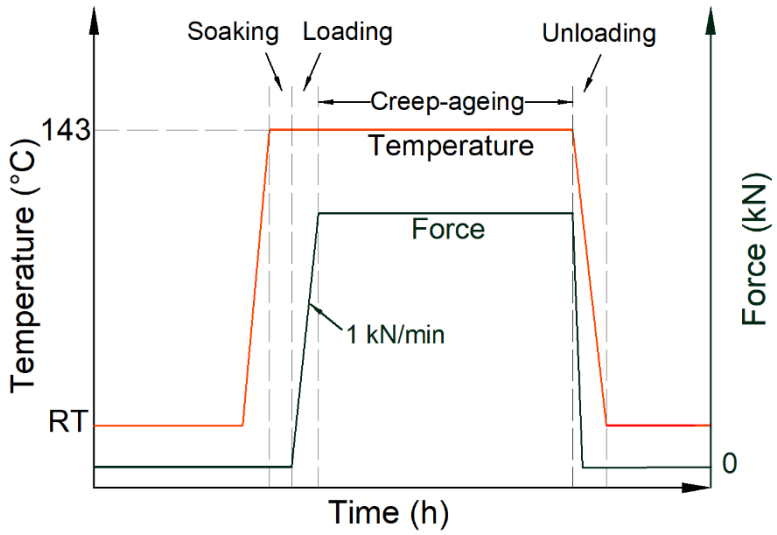


Figure 3-9. Schematic of uniaxial creep-ageing test stages and heating curve.

3.5 Microstructural investigation

In this section, the microstructural evolution of the material in creep-ageing in aspects of dislocation and precipitation were respectively investigated by conducting TEM and XRD tests and the test details are presented.

3.5.1 Test specimen

Transmission electron microscopy (TEM) observations of selected samples were carried out to analyse the evolution of precipitates during CAF under different stresses and ageing times. TEM samples with dimensions of 15 x 10 x 0.5 mm were cut from the middle of the creep-aged specimens. The treatment condition for the selected samples were shown in Table 3-5. The cut samples were then grounded to a foil with a thickness of around 80 μm and punched into discs of 3 mm diameter. The discs were electropolished using a mixed solution of nitric acid and methanol with a volume ratio of 1:3. The electropolishing was conducted at a temperature in the range of -35 °C to -25 °C with a voltage of 15 V.

X-ray diffraction (XRD) tests were conducted to investigate the evolution of dislocation density during creep-ageing under different stresses. Rectangular XRD specimens with dimensions of 15 x 20 x 0.8 mm were cut from the middle of the specimens with the creep-ageing conditions illustrated in Table 3-5 and then grounded to 0.5 mm thickness.

3.5.2 Equipment and test setup

For TEM observation, a TECNAI G220 TEM machine with an acceleration voltage of 200 kV was used (Figure 3-10a). XRD tests were conducted on a Rigaku Smartlab equipped with a 9 kW Cu Kα (λ = 0.154 nm) rotating anode operating at 40 kV and 150 mA. The scanning angle range was from 35° to 85° with a step size of 0.01° (Figure 3-10b).



(a) TECNAI G220 TEM (b) Rigaku Smartlab XRD machine

Figure 3-10. The equipment adopted for microstructural analysis in this research.

3.5.3 Test procedure

For TEM observation, the general procedure was followed as:

(a) Place the specimen properly on a holder in a cylinder pipe pulled out from the machine. Then re-inserted the cylinder pipe with a specimen in the machine.

(b) Start vacuuming the machine to be prepared for observation.

(c) After completion of the vacuum work, adjust the observation direction of the machine parallel with <110> direction and start microstructural observation and image recording.

For XRD test, the general procedure was followed as:

(a) Place the prepared specimen on the operation pad underneath the rotation anode.

(b) Close the machine doors and charge it up to be prepared for testing.

(c) Once the required voltage is reached in preparation, the anode starts to rotate and scan.

(d) When scanning is completed, open the machine door to take out the specimen.

3.6 Four-point bending CAF test

This section introduces details of the conducted four point bending CAF tests.

3.6.1 Test specimen preparation

The as-received 220 mm x 20 mm sheets with the rolling direction parallel to length (220 mm) direction and thickness of 2 mm, 4 mm, and 6 mm were used as test specimens. For the convenience of following description, a local coordinate established for the specimen is demonstrated in Figure 3-11, with x axis located on centre line along length direction, y axis along the thickness direction, and z axis along the width direction.

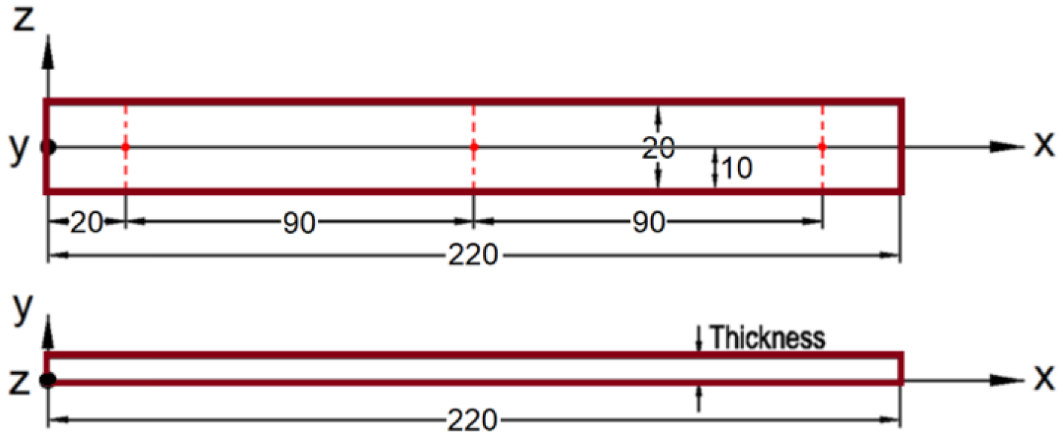


Figure 3-11. Schematic of CAF specimen and the assigned local coordinate (dimension in mm).

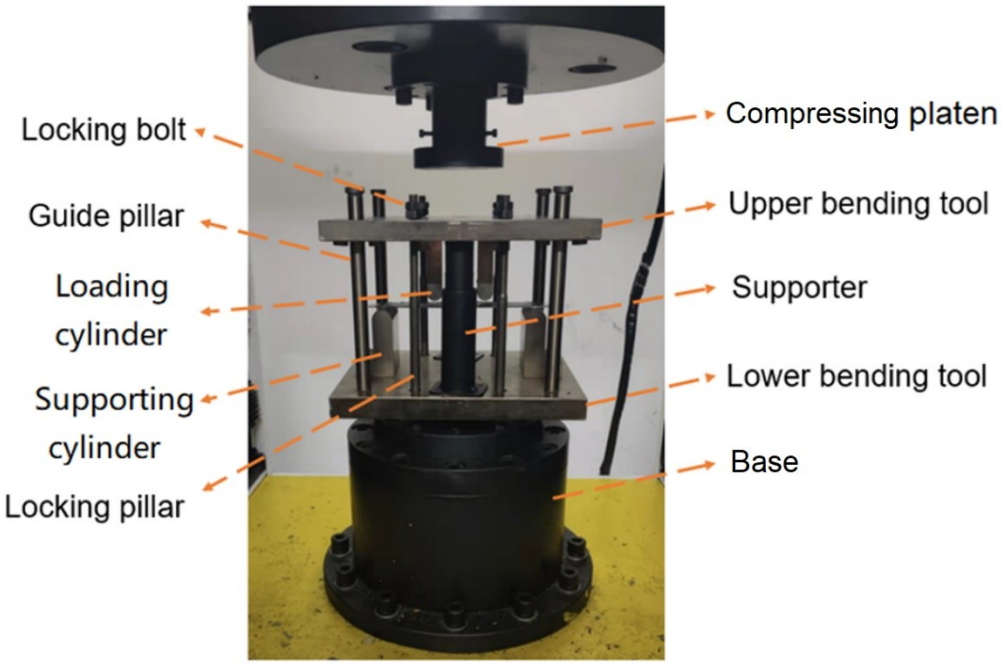
3.6.2 Equipment and test setup

A four-point bending tool was manufactured based on the dimension of the proposed four-point bending model in Figure 3-1. The bending tool was composed of upper and lower bending tools which had loading cylinders and supporting cylinders fixed respectively as demonstrated in Figure 3-12a.

Four locking pillars were inserted through the preserved holes of the upper and lower bending tool. The upper bending tool was lifted by two additional supporters prior to the start of experiment.

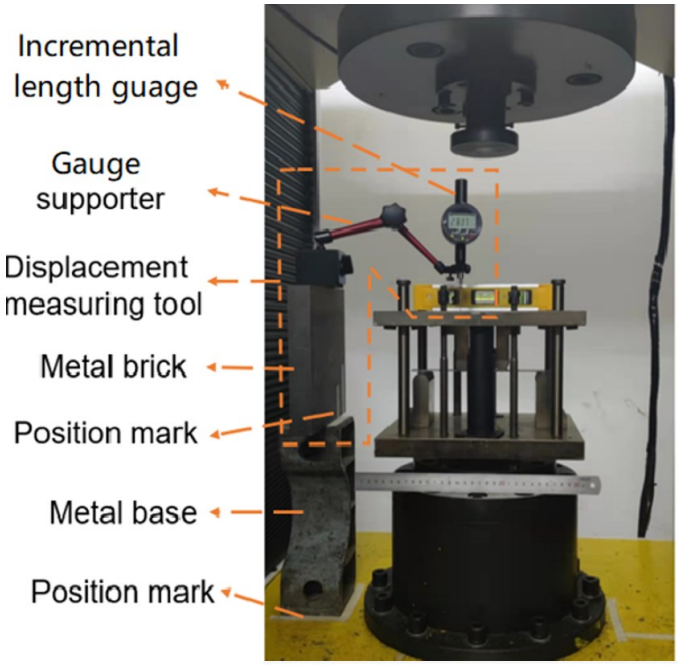
A DOCER machine was adopted in the experiment to apply downward displacement as shown in Figure 3-12a. The bending tool was placed on the base with both centres aligned. The machine was connected with supporting computer and manufacture developed operation software to achieve load or displacement control.

A displacement measuring tool composed of length incremental gauge, gauge supporter, and metal brick was used as demonstrated in Figure 3-12b. The maximum length that incremental gauge could measure was up to 30 mm with an accuracy of 0.01 mm and the incremental gauge was clamped and supported by the gauge supporter. The gauge supporter was fixed on the metal block with its magnetic base which can provide 200 N attachment force.



(a) Bending tool

Figure 3-12. Equipment and setup for the four-point bending CAF experiment.



(b) Experiment setup

Figure 3-12. (*continued*).

3.6.3 Experiment procedure

The four-point bending CAF experiment was conducted following the below sequences:

(a) Measure the initial deflection as demonstrated in Figure 3-13. Measurements are taken on three marked positions as the red dots demonstrated in Figure 3-11. The red lines and dots in Figure 3-11 are the supporting and centre positions at 20, 110, and 200 mm along length direction (x axis) of the specimen. Set the gauge to zero in the first measurement point at 20 mm as d_i = 0. Note the readings of the second point (110 mm) and third point (200 mm) as d_i' and d_i'' (i stands for the i^{th} round of measurement). The deflection at centre position (110 mm) can be derived as

$$d_{ave} = \frac{1}{3}\sum_{i=1}^{3}(d_i' - d_i''/2) \tag{3-5}$$

(b) Place the specimen on the supporting cylinder with the supporting marks (20 mm and 200 mm) aligned with the cylinders. Lower the upper bending tool till the loading cylinder attaches the specimen (Figure 3-12b). Record the height by positioning the measuring tool to align with position marks on both sides of the bending tool (Figure 3-12b). Note the measured initial heights were as h_j $(j = 1, 2, 3, 4)$. j stands for the j^{th}measurement point.

(c) Lower the compressing platen into contact with the upper bending tool (Figure 3-14a). Then remove the supporters and continue to lower the platen with a displacement of d_l at the rate of 0.1 mm/s.

(d) When the downward displacement d_l is completed. Lock the tool with the locking bolts. Measure the compressed height following the same procedure as (b). Note the measured compressed heights as h_j' $(j = 1, 2, 3, 4)$. The loading displacement d_{ll} was derived as

$$d_l = \frac{1}{4}\sum_{i=\mathrm{j}}^{4}(h_j - h_j') \tag{3-6}$$

Minor adjustments can be made by fastening or loosening the locking bolts to make d_l fall in the range of $d_{ll} \pm 0.1$ mm.

(e) Attach a pair of thermocouple wires on the specimen and move the fixed bending tool into the preheated furnace at 120 °C $\pm$ 3 °C (Figure 3-14d). Then heats up the furnace to 143 °C $\pm$ 3 °C for 30 minutes and soak for 15 minutes to start creep-ageing.

(f) When reaching the designed creep-ageing time, open the furnace and cool down in air to room temperature. Then take the tool out of the furnace and loosen the locking bolts. Remeasure the specimen for deformed deflection following the same procedure of (a).

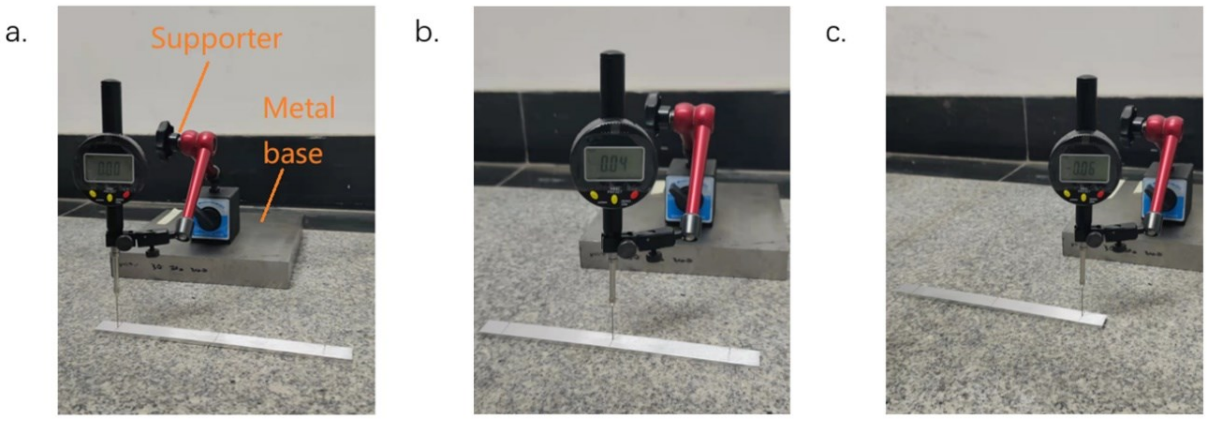


Figure 3-13. Measurement of deflections on the (a) first, (b) second, and (c) third mark.

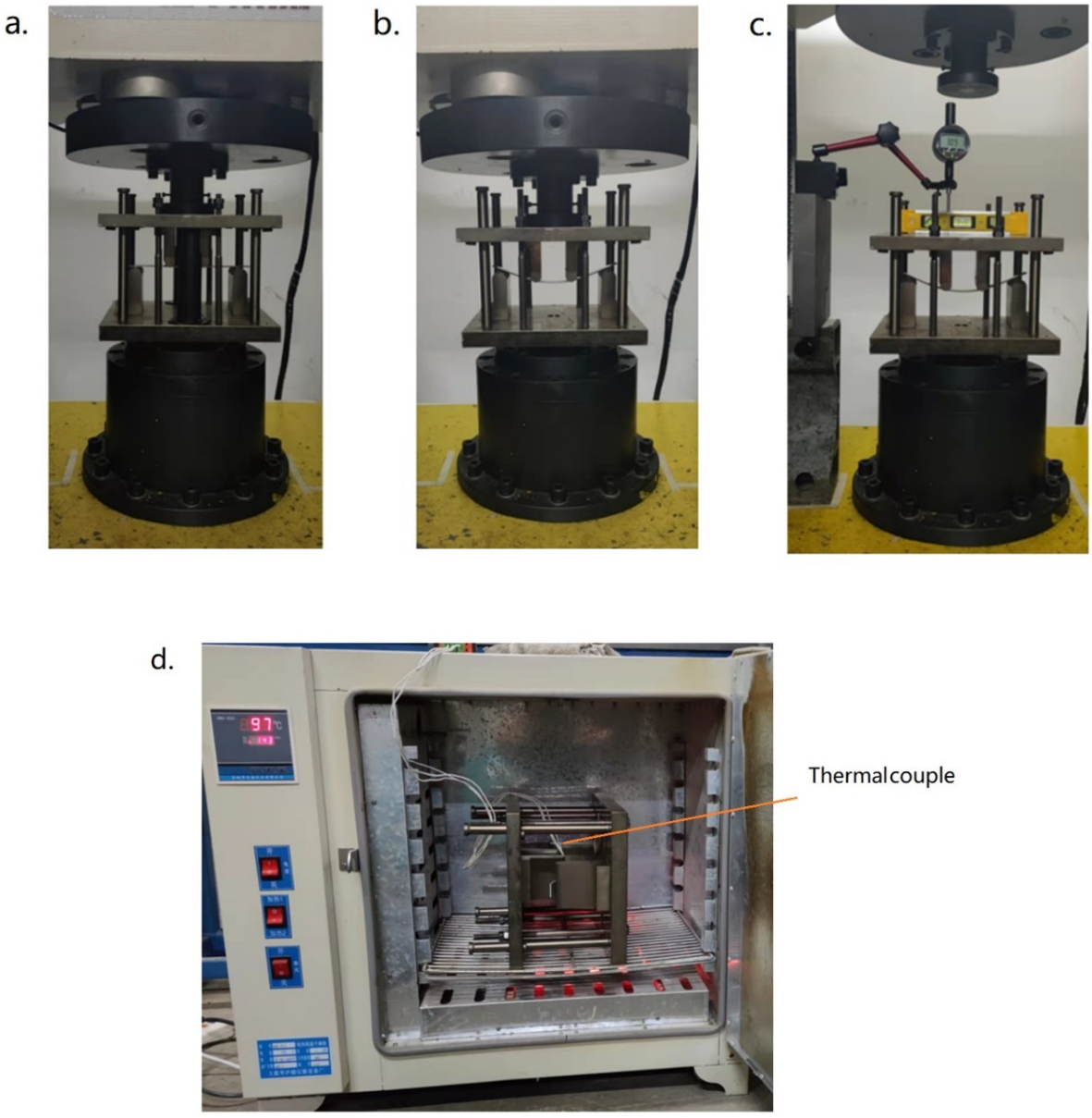


Figure 3-14. Experimental procedure for four-point bending CAF tests: (a) Initial state; (b) material is loaded and the tool was locked with locking bolts; (c) measurements of compressed height. (d) move the tool into the furnace for creep-ageing.

3.7 Fabrication of CAF panel with a flexible tool

In this section, the conducted test of CAF fabrication adopting a flexible tool is introduced.

3.7.1 Test specimen

The test specimens were cut from the 2 and 4 mm thick as-received sheets with dimensions of 335

mm x 165 mm for the 2 mm thickness and 320 x 165 for the 4 mm, the rolling direction is parallel to the length direction. For the convenience of following description, a local coordinate for the specimen was established and demonstrated in Figure 3-15. The x axis of the coordinate locates on the centre line of specimen along the length direction, z axis along the width direction, and y axis along the thickness direction.

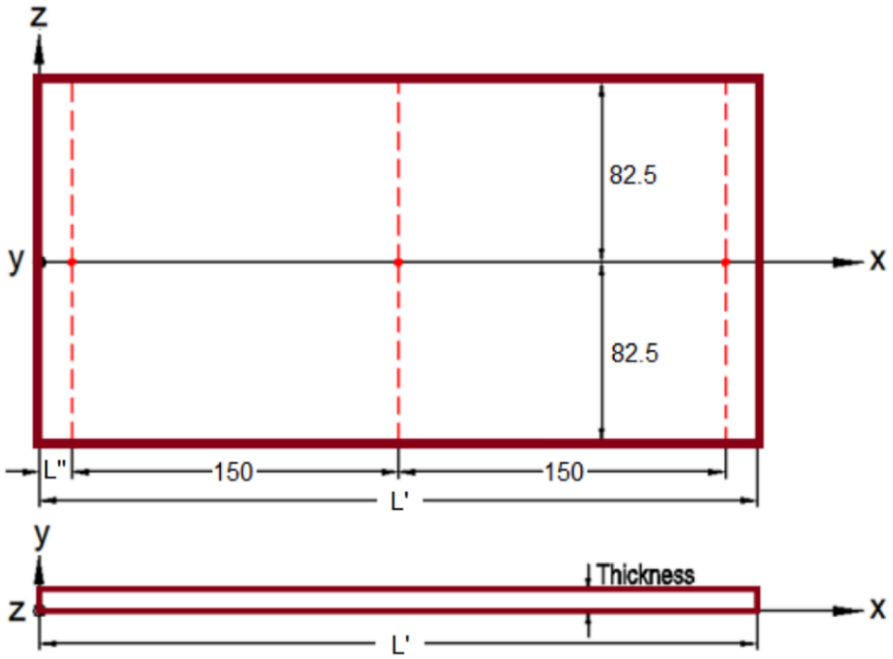
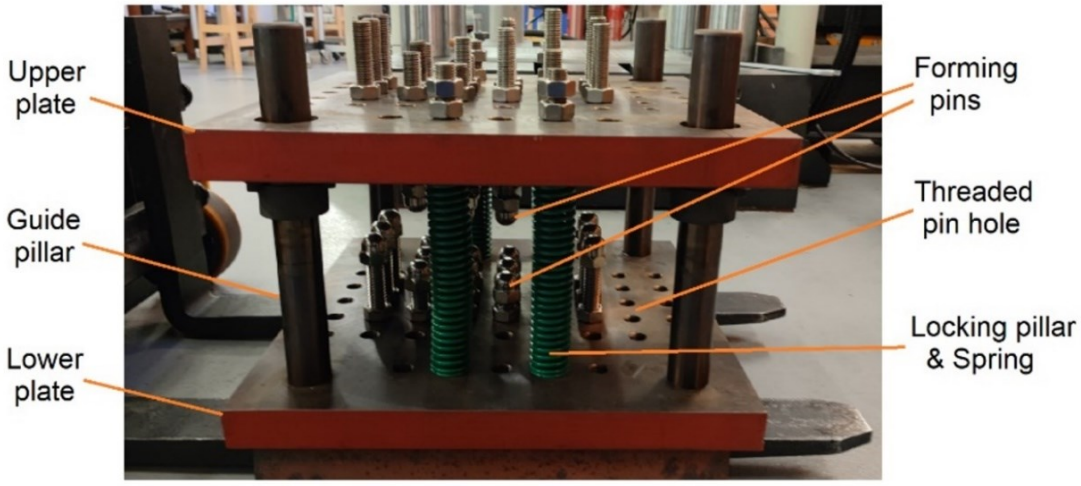


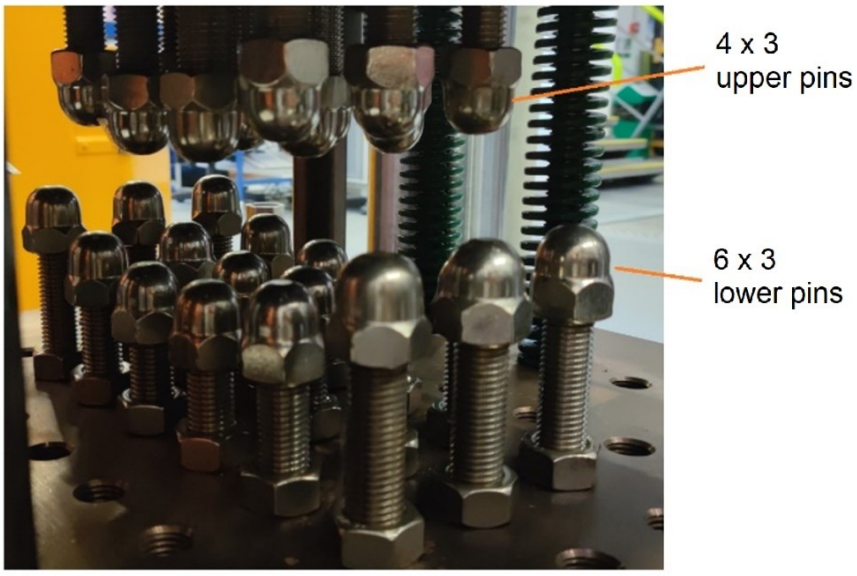
Figure 3-15. Schematic of specimen dimension and assigned local coordinates (dimension in mm). L'=335 and L''=17.5 for the 2 mm, L'=320 and L''=10 for the 4 mm.

3.7.2 Equipment and setup

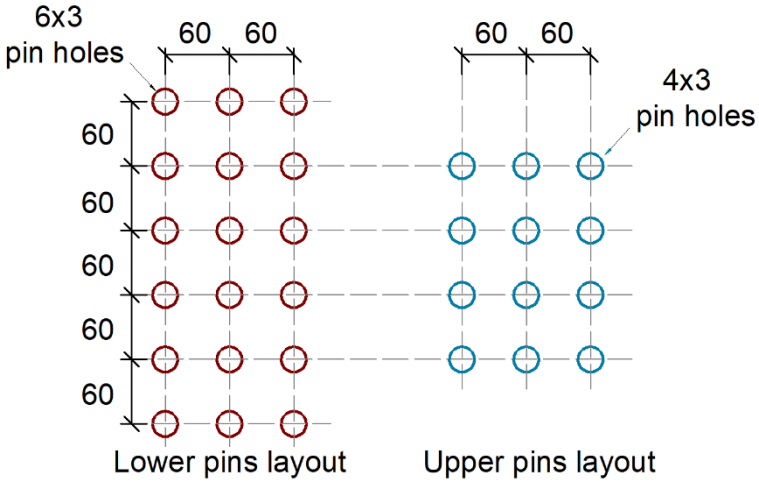
A multipoint forming tool designed and manufactured by Lam [130] was adopted in this research. As demonstrated in Figure 3-16a, the major components of the tool are upper and lower plates, locking pillars surrounded by supporting springs, guide pillars, and multiple forming pins. Threaded holes M24 in a matrix of 9 x 5 were drilled in the same position of upper and lower plates. The centre distance for two adjacent holes in each row and column is 60 mm. Pins were assembled on the upper and lower plates through threaded holes, by adjusting the position and height of which the specimen can be compressed to the designed shape in forming process. For CAF test in this test, as demonstrated in Figure 3-16b and Figure 3-16c, a 4 x 3 layout for upper pins and 6 x 3 for lower pins were used.



(a) Multipoint tool setup



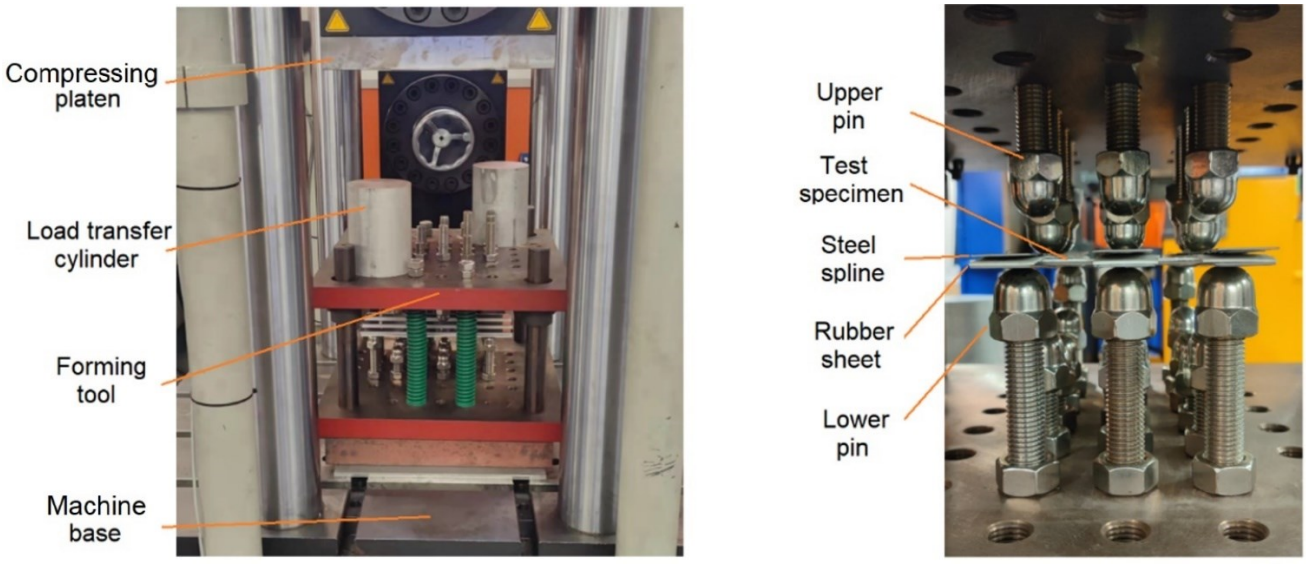
(b) Upper and lower pins



(c) Pins layout

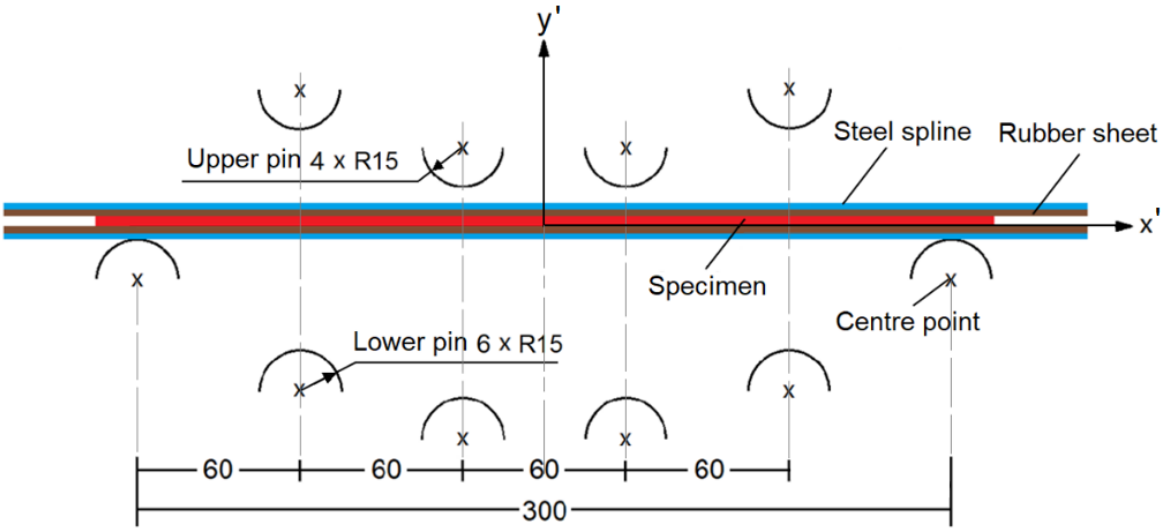
Figure 3-16. Demonstration of multipoint tool and pins layout for CAF fabrication.

A 250-tonne Instron machine was used to apply downward displacement for the forming tool in the experiment. Load or displacement control of the machine can be achieved by manufacturer developed software installed in the connected computer. Figure 3-17 demonstrates the equipment and setup for the experiment. The general test setup is shown in Figure 3-17a. As demonstrated in the figure, the multipoint forming tool was placed on the central area of the base. Two metal cylinder blocks were placed diagonally to transfer the downward force/displacement to the forming tool. The compression rate for this test was set to be 6 mm/min. Figure 3-17b further illustrated the setup for specimen placed on the tool. As shown in Figure 3-17b, the specimen was placed on the tool supported by three rows of lower pins. Additionally, to achieve more evenly distributed pressure applied on the specimen, for each row of pins, two steel splines with a dimension of 400 mm x 30 mm and 1.2 mm thickness were placed on the top and bottom of the specimen aligned with the pin row. Rubber sheets with thickness of 1.5 mm were used to between the upper/lower splines and the specimen to eliminate/minimise any damage to the specimen. An AEROTHERM large furnace was adopted for the creep-ageing tests.



(a) Multipoint tool loaded in the Instron machine (b) Setup of loaded specimen

Figure 3-17. Test setup for multipoint tool CAF fabrication and setup of specimen with the tool. (a) Setup for loading and unloading of the tool. (b) Setup for the specimen with a multipoint tool. (c) Schematic of general setup in the $x' - y'$ section of the specimen (dimension in mm).



(c) Schematic of general setup in $x' - y'$ section

Figure 3-17. (*Continued*).

3.7.3 Experiment procedure

The experiment procedure for multipoint CAF fabrication was conducted following the below sequences:

(a) Adjust the pin heights to obtain the designed tool surface. The pin heights were manually adjusted with a right-angle tool and height measuring tool (Figure 3-18a). The upper ruler of the right-angle tool can slide perpendicularly to measure the height. The magnetic base of the right-angle tool helps the tool to attach to the lower and upper plates of the multipoint forming tool. To adjust the pin to the designed position, firstly, the height measuring tool was descended to touch the lower plate and set the gauge to zero (Figure 3-18a). Then lift the measuring tool to the designed height (the thickness of the upper ruler of the right-angle tool is considered) and adjust the upper ruler to the derived height and fix at this position (Figure 3-18b). Lastly, adjust the height of the pin with the fixed right-angle tool (Figure 3-18c).

(b) Measure the initial deflection of the specimen with three marked positions demonstrated as red dots in Figure 3-15 at L'', L''+150, and L''+300 mm along the length (x axis) direction following the same procedure as in section 3.6.4 (a). The red line marks are respectively the supporting positions (17.5 mm and 317.5 mm for 2 mm; 10 mm and 310 mm for 4 mm) and centre position of specimen

in $x - y$ section.

(c) Move the multipoint tool with the specimen to Instron loading machine. The setup of the forming tool with Instron machine, and the specimen with forming tool is demonstrated in Figure 3-17. Lower the compressing platen to contact the diagonally placed load transfer metal cylinders (Figure 3-19a).

(c) When the platen touches the metal cylinders, the platen begins to compress at a rate of 6 mm/min. When the specimen is fully deformed to reach the lower pins, the downward movement of platen is immediately stopped and kept at the position (Figure 3-19b). Then fix the tool with the locking bolts (Figure 3-19c).

(d) Lift the compressing platen and move the tool out of the Instron machine. Attach the thermocouples on the specimen and move the tool into the furnace (Figure 3-19c and Figure 3-19d).

(e) Heat up the furnace to 143 °C and soak for 15 minutes as the start of creep-ageing. When the 5 h creep-ageing is completed, open the furnace for cooling down in air.

(f) Bring the cooled down tool back to the Instron machine repeating the same procedure of (c) letting the compressing platen attach the cylinders for unloading. After loosening the locking bolts, lift the compressing platen and take out the deformed specimen. Deformed deflection measurements with the same procedure in (a) was conducted.

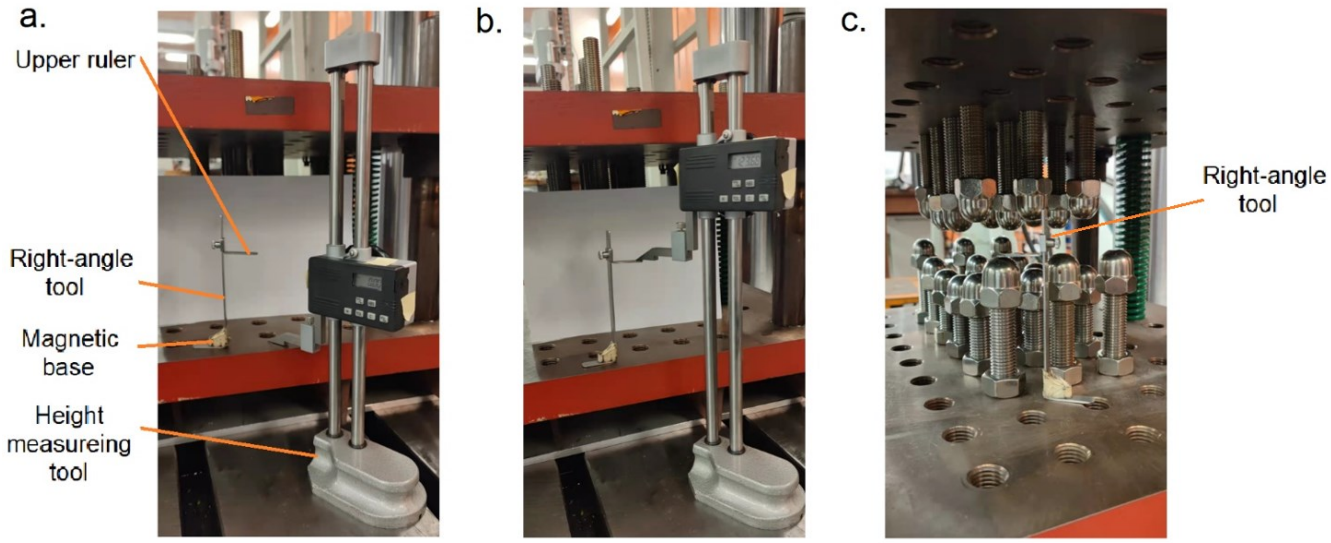


Figure 3-18. Adjustment of pin heights to derive designed tool surface.

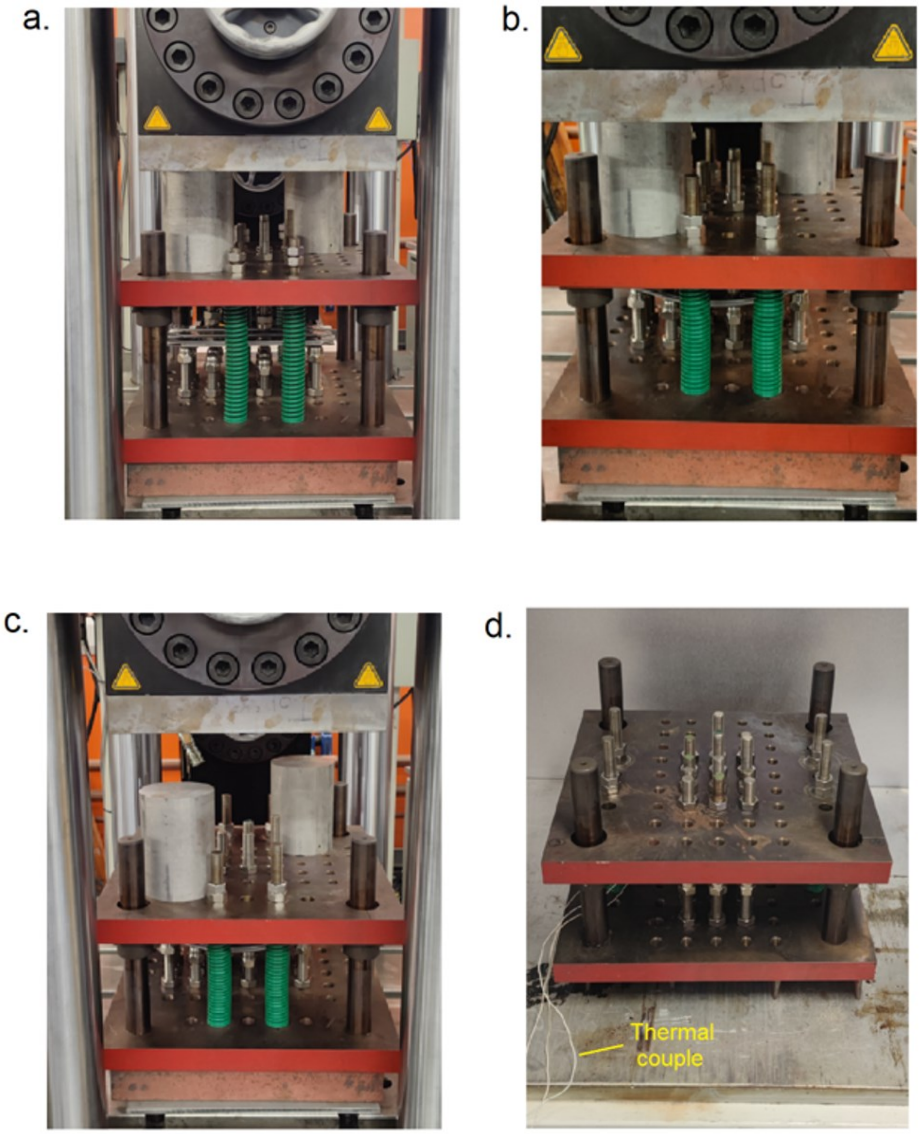


Figure 3-19. General experiment procedure of CAF fabrication with a multipoint tool. (a) The compressing platen was lowered down to touch the metal cylinders. (b) The specimen was deformed to the designed curvature. (c) The tool was locked when deforming was completed. (d) The tool was moved to the furnace to start creep-ageing.

3.8 Summary

In this chapter, the general experiment plan to fully investigate AA2060-T8 in CAF is presented. For each specific experiment, the detailed information including the test programme, specimen preparation, equipment and tool setup, as well as the test procedure is illustrated.

Chapter 4

Experimental results and discussion

4.1 Introduction

This chapter presents the experiment results of corresponding tests described in Chapter 3. A summary of the results is demonstrated in Table 4-1 which includes information on the results for each experiment. Additionally, discussions regarding the obtained results are given accordingly.

Table 4-1. Summary of experiment results presented in each section.

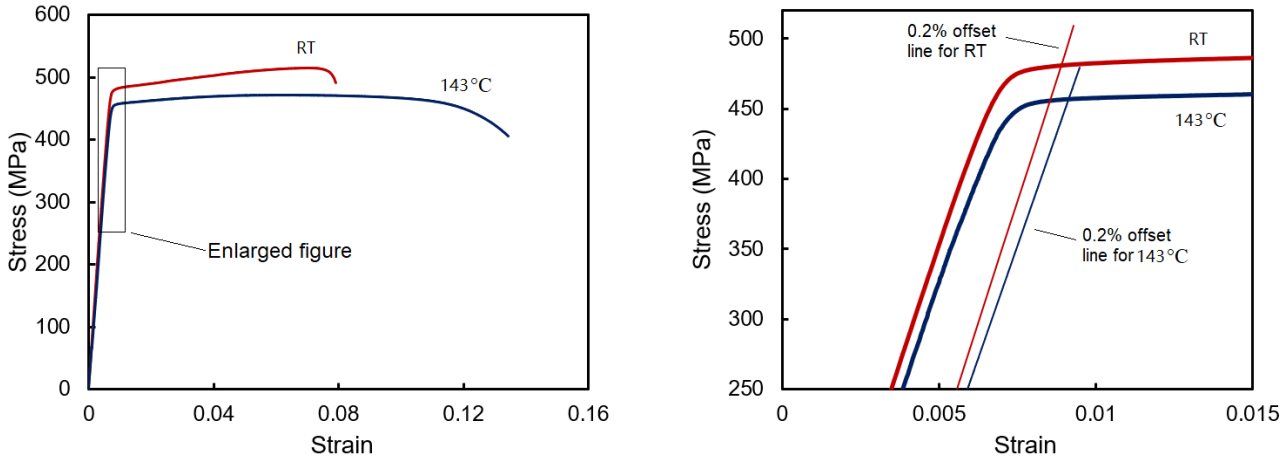
Results	Section	Contents
Mechanical properties of AA2060-T8	4.2	1. Tensile test results 2. Age hardening results
Uniaxial creep-ageing and subsequent tensile test results	4.3	1. Stress-creep strain results 2. Strength evolution results
Microstructural investigation results	4.4	1. TEM observation results 2. XRD test results
Four-point bending CAF test results	4.5	Deflection results
Multipoint CAF fabrication results	4.6	Deflection results

4.2 Mechanical properties of AA2060-T8

4.2.1 Tensile test results

Through conducting room temperature and elevated temperature tensile tests, the tensile

mechanical property of AA2060-T8 was investigated. The obtained stress-strain curves for both conditions are demonstrated in Figure 4-1. The total stress-strain curves for room temperature and elevated temperature are presented in Figure 4-1a. The yield strength of AA2060-T8 at room and elevated temperature is determined with a 0.2% strain offset as shown in the enlarged Figure 4-1b. With the obtained curves, the material properties of AA2060-T8 determined in this research are given in Table 4-2.



(a) Stress-strain curves (b) Enlarged figure with 0.2% offset line

Figure 4-1. Stress-strain curves at room temperature (RT) and elevated temperature of 143 °C. (a) is the stress-strain curves of both conditions and (b) is the enlarged figure with a 0.2% offset line to determine the yield strength.

Table 4-2. Material properties for AA2060-T8.

Condition	Yield strength (MPa)	Young's modulus (MPa)
RT	480	69800
143 °C	456	62600

4.2.2 Age hardening test results

Figure 4-2 demonstrates the hardness evolution of AA2060-T8 with different ageing time at 143 °C. The result for each condition was obtained from 5 repeating measurements. As can be noticed in the figure, for AA2060 with T8 temper, limited hardness increasing within 10 HV was observed which

reached a peak plateau around 167 HV after 15 h.

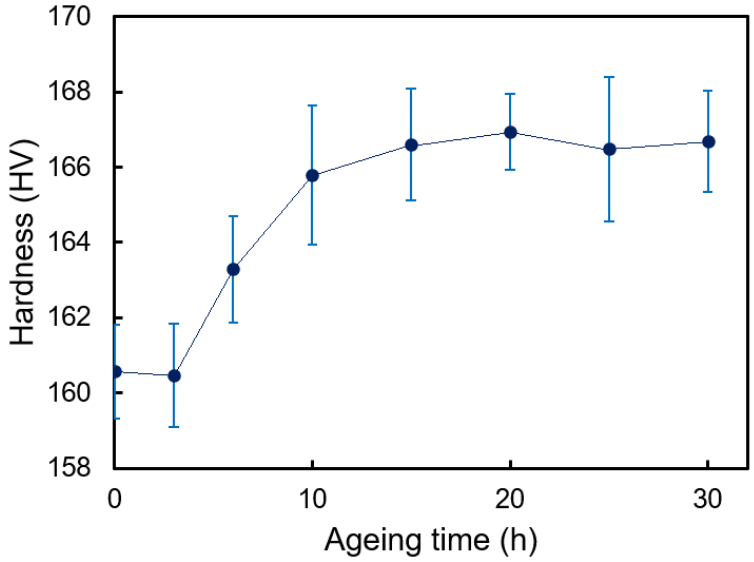


Figure 4-2. Hardness evolution of AA2060-T8 at 143 °C

4.2.3 Discussion of test results

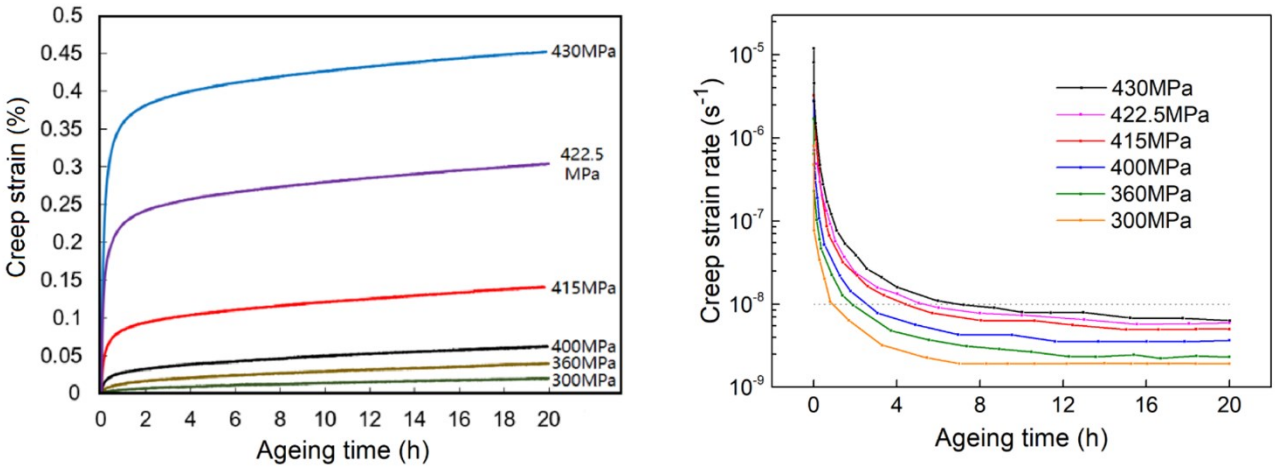
For creep-ageing test, the adopted stress should be below the yield strength of the material to avoid entering the tertiary stage during creep-ageing and inducing creep damage of the material. On the other hand, too low stress being adopted can lead to little creep deformation which will decrease the cost-efficiency of CAF. Based on the tensile test results curve at 143 °C, a little divergence from linear stress-strain relation was identified in Figure 4-1b when the applied stress surpassed about 400 MPa, hence a stress range from 300 to 430 MPa was selected. Additionally, no obvious hardness loss caused by over ageing was observed in 30 h ageing at 143 °C as shown in Figure 4-2. With the obtained results of the hardness evolution, the uniaxial creep-ageing time was designed to be with maximum duration of 20 h. Considering the creep deformation characteristic that most of creep strain is generated in the primary stage, 6 h of creep-ageing was determined for the four-point bending CAF tests and fabrication of CAF panel with the flexible multipoint tool for cost-efficiency in practical fabrication.

4.3 Uniaxial creep-ageing and subsequent tensile tests

4.3.1 Creep-ageing test results

The creep-ageing test results under different stresses are summarised and demonstrated in Figure 4-3. Figure 4-3a presents the stress-creep strain evolutions under different stresses and the creep strain curves under all stresses demonstrated a classical two-stage behaviour (primary and secondary creep stages) in creep-ageing for 20 h at 143 °C. Figure 4-3b is the evolution of creep strain rate under different stresses. A dramatic decrease in strain rate occurred at the beginning of the tests under all stresses. A higher creep strain rate was obtained with the increase of the applied stress. As shown in Figure 4-3b, it can be seen that with increased applied stress, a longer time was needed to enter the steady state which was defined with a creep strain rate below 1 x 10^{-8} s^{-1} in this research[131].

The steady state creep strain rate is plotted with symbols against the applied stress in Figure 4-4, showing that the creep strain rate increased with higher applied stress and the rate of increase became much higher when the stress was above 400 MPa. In the figure, *n* is the stress exponent which will be further discussed in section 4.3.3.



(a) Stress-creep strain curves (b) Evolution of strain rate under different stresses

Figure 4-3. Results of uniaxial creep-ageing test. The dotted line in (b) indicates a strain rate of 1.0 x 10^{-8} s^{-1} which is treated as the upper limit of steady state defined in this research.

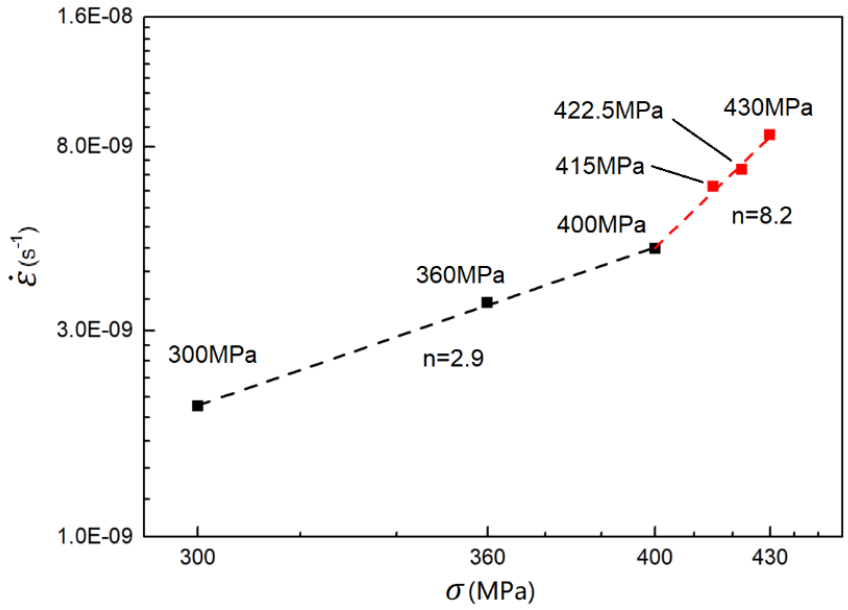
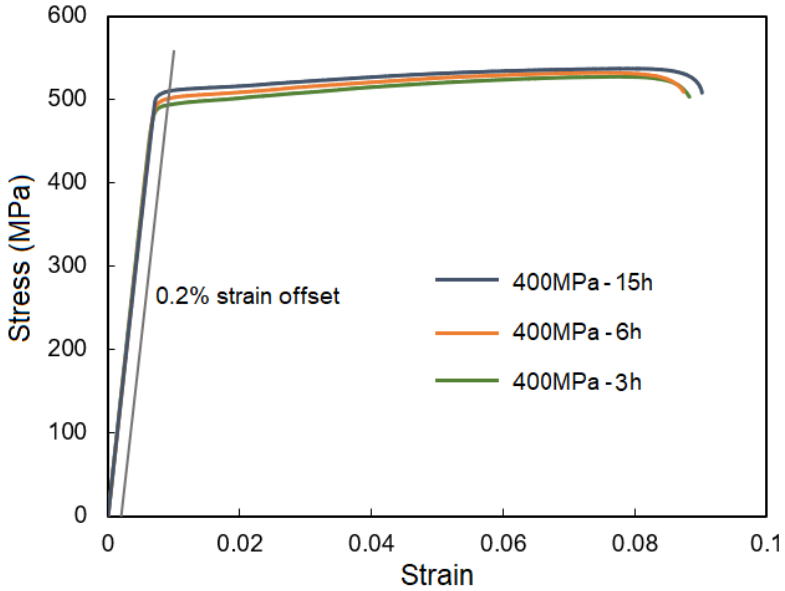


Figure 4-4. Logarithm plot of steady state creep strain rate versus nominal stress.

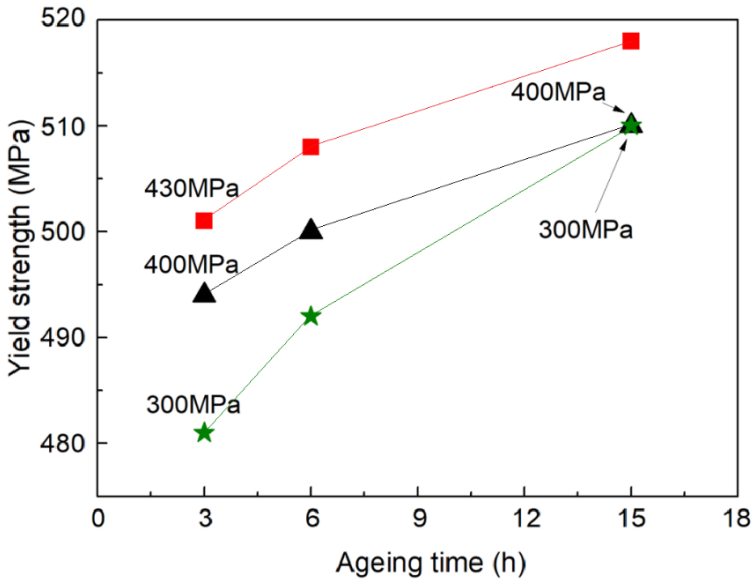
4.3.2 Subsequent tensile test results

Figure 4-5 demonstrates the subsequent tensile test curves for 400 MPa and the strength evolution of AA2060-T8 in creep-ageing under different stress. As can be seen in the figure, the material strength was enhanced with creep-ageing up to 15 h. And the strength increased most when creep-aged under 430 MPa.



(a) Subsequent tensile test curves for 400 MPa

Figure 4-5. Subsequent tensile test curves for 400 MPa (a) and strength evolution of AA2060-T8 in creep-ageing under different stress (b).



(b) Strength evolution

Figure 4-5. (*continued*).

4.3.3 Discussion of test results

4.3.3.1 Creep-ageing strain and hardening behaviour

As demonstrated in Figure 4-3a, it can be observed that creep deformation increased with increasing applied stress. However, comparing with the creep strain accumulated at 20 h under different stresses show that the creep strain increase was not linear with the increase of applied stress. When the applied stress increased from 300 to 400 MPa, the accumulated creep strain at 20 h increased from 0.02% to 0.06%, while the creep strain increased from 0.06% to 0.45% when the applied stress increased from 400 to 430 MPa. The strain increased at higher rate in the stress level from 400 to 430 MPa than from 300 to 400 MPa. Furthermore, for the strain evolution under 400 and 430 MPa in the 20 h creep-ageing, most of the difference in the accumulated strain was derived in the primary stage, where the material showed much higher strain under 430 MPa because the applied stress was close to the yield strength, inducing high creep deformation.

creep strain rate in steady state stage can be appropriately described in the widely adopted Dorn equation [132]:

$$\dot{\varepsilon} = A\sigma^{n}\exp\left(-\frac{Q_a}{RT}\right) \tag{4-1}$$

where A is a material constant, Q_a is the activation energy, R is the gas constant, T is the absolute temperature, and n is the stress exponent. When the temperature is a constant value, which is 143 °C in this study, the equation can be simplified and transformed to a logarithm form as:

$$\ln(\dot{\varepsilon}) = \ln(A') + n\ln(\sigma) \tag{4-2}$$

where A' is the product of A times the exponential part. Hence the exponent n can be obtained by linearly fitting experimental data of steady state creep strain rate and corresponding applied stress using logarithm plot. The fitting result is shown in Figure 4-4 with the dashed lines.

As shown in Figure 4-4, the creep strain rate and stress in logarithmic form have a bilinear relationship with the crossover point around 400 MPa: the results for 300, 360, and 400 MPa fell in a linear line with the slope n = 2.9; while the data points for 400, 415, 422.5 and 430 MPa formed another line with n = 8.2. The stress exponent has been widely used to indicate the dominant creep deformation mechanism: For n with value smaller than 3, the dominant creep mechanism is lattice diffusion / diffusional creep; when the n value is larger than 3, dislocation creep mechanism become dominant in creep deformation [132, 133]. According to the results in Figure 4-4, the selected stresses can thus be classified into two groups based on the dominated creep deformation mechanism: stresses of 300, 360, and 400 MPa are classified as a lower-level stress group in which diffusional creep mechanism dominates; 415, 422.5 and 430 MPa can be classified as a higher-level stress group that dislocation creep mechanism dominates during creep-ageing.

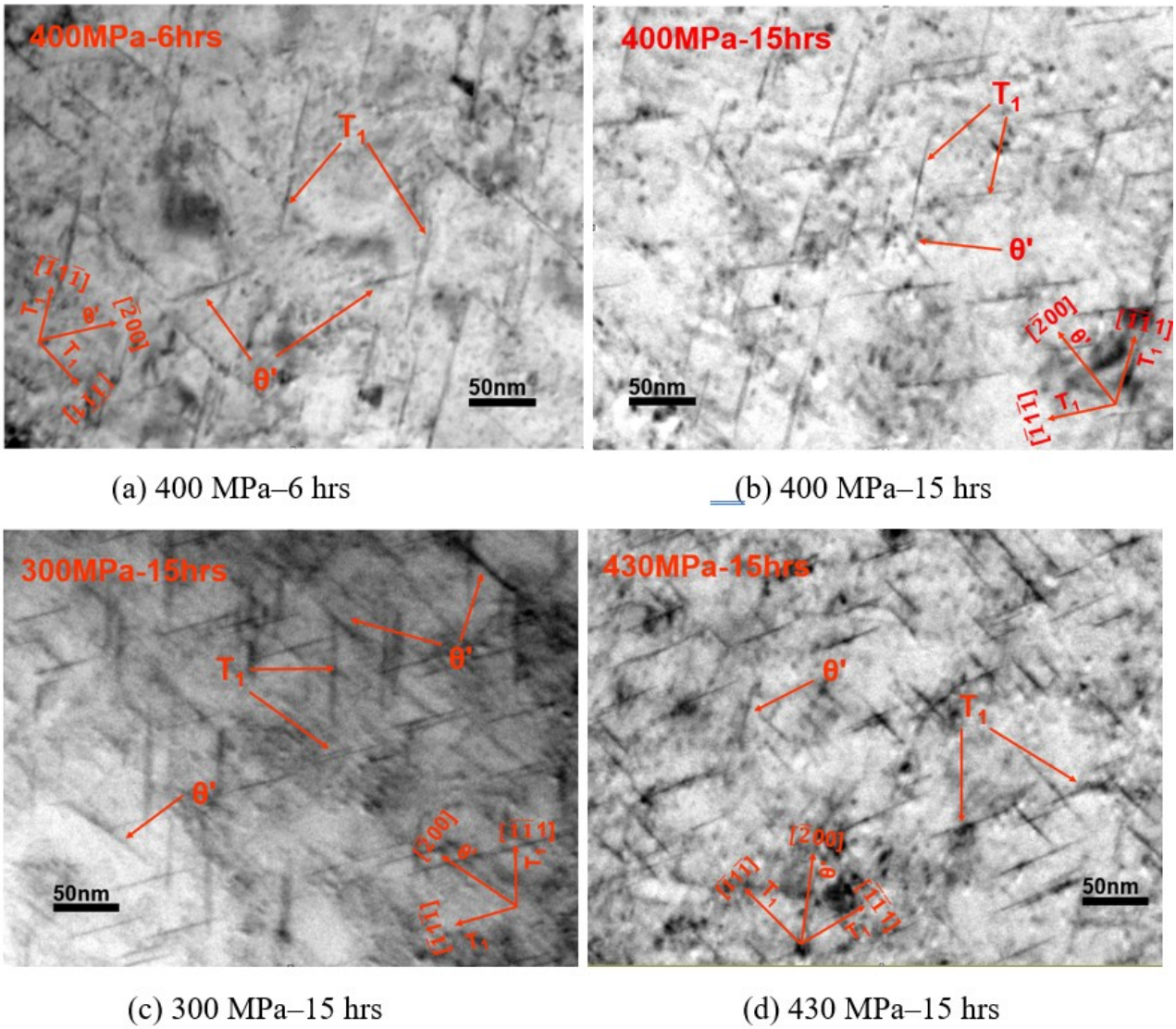
From the tensile tests results demonstrated in Figure 4-5, the increasing trend of yielding strength with creep-ageing up to 15 h can be identified in the applied stresses of 300, 400, and 430 MPa. This raising trend indicates the peak ageing state for the material is not yet reached when creep-aged to 15 h under the collective hardening effects of precipitation, dislocation, and solid solution. Further discussion on the microstructural evolution during creep-ageing is given in next section.

4.4 Microstructural investigation results

4.4.1 TEM observation results

Figure 4-6 demonstrates selected TEM bright field images along $[011]_{Al}$ zone axis under different

stress and ageing time. As can be observed from Figure 4-6, T_1 and θ′ precipitates can be observed and differentiated with their specific orientations as indicated in the figure. According to Figure 4-6, the dominant precipitates were T_1 during the creep-ageing process, and θ' was found to be sparsely distributed in the material, compared to the quantity of T_1 precipitates.



(a) 400 MPa–6 hrs (b) 400 MPa–15 hrs

(c) 300 MPa–15 hrs (d) 430 MPa–15 hrs

Figure 4-6. TEM bright field images along $[011]_{Al}$ zone axis under different stress and ageing time.

The ratios of relative frequency between T_1 and θ' precipitates under different stress during creep-ageing are presented in Figure 4-7. As demonstrated in the figure, the relative frequency of T_1 to θ′ increased with ageing time. Additionally, a higher relative frequency ratio of T_1 to θ′ was observed when creep-aged under higher stress. The frequency ratio of T1 to θ′ increased from 75% to 25% in

the as-received state to 84% to 16%, 93% to 7%, and 97% to 3% under 300, 400 and 430 MPa respectively after creep-ageing for 15 h.

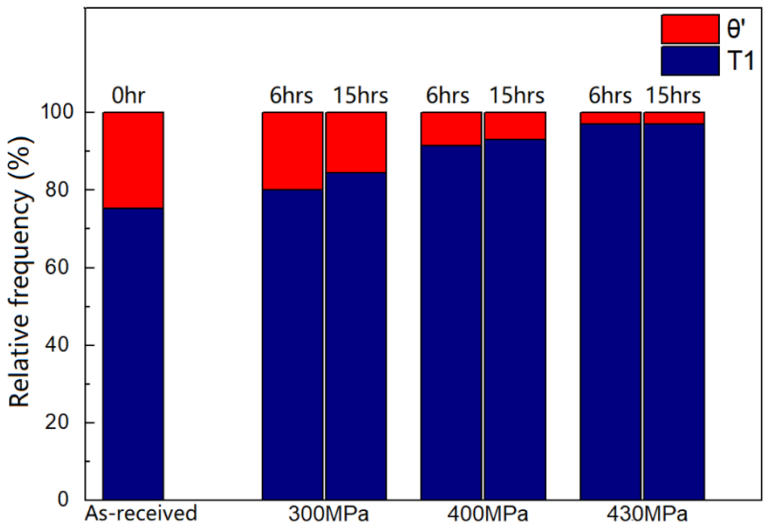


Figure 4-7. Statistical results of evolution of relative frequency of T_1 and θ' during creep-ageing.

Due to the dominance of T_1 precipitates during creep-ageing of AA2060-T8, this precipitate is considered as a representative one to investigate the precipitation phenomenon for AA2060-T8 in creep-ageing. For each sample, more than 120 precipitates were measured to acquire relatively reliable statistical information on precipitate diameter as demonstrated in Figure 4-8. The average size evolution of T_1 precipitate creep-aged under 300, 400, and 430 MPa is shown in the figure. A similar trend for size evolution of precipitate was found under 400 and 430 MPa, which increased at the initial 6 h and reached a stable state afterwards. When creep-aged under 300 MPa, a continuously rising trend in diameter was observed during the whole creep-ageing process up to 15 h. In addition, the average precipitate size under these three stresses all fell into a narrow range from 50.8 nm to 52.4 nm after creep-ageing for 15 h.

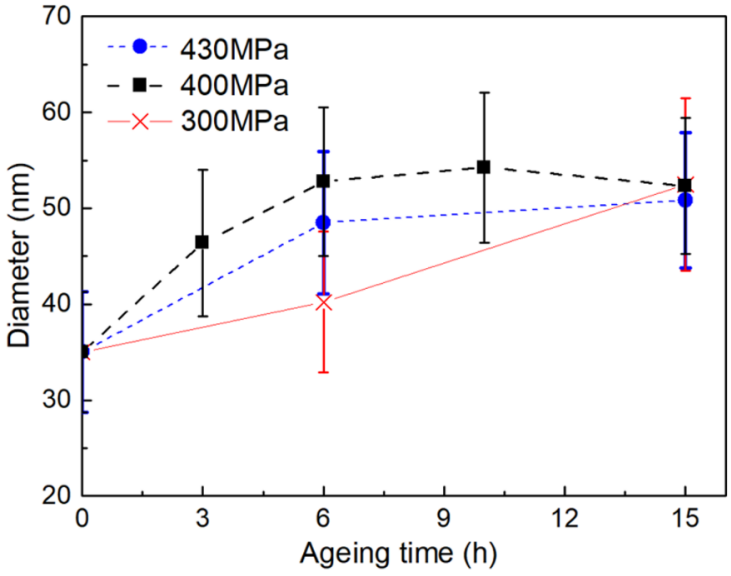


Figure 4-8. T_1 precipitate size evolution under different stress.

4.4.2 XRD test results

The full width at half maximum (FWHM) of the obtained XRD line profiles was measured and used in the modified Williamson-Hall method to determine the dislocation density [129]. For each condition, the average density was obtained from 3 repeated test results. The results of dislocation density evolution with creep-ageing time under the stresses of 300, 400 and 430 MPa are presented in Figure 4-9. A general rising trend of dislocation density with creep-ageing time under each stress can be clearly identified from the results. The fast increase in dislocation density in the first period is due to the plastic strain induced in the primary creep stage. On the other hand, with the increase of dislocation density, static and dynamic recovery becomes more important which can reduce the dislocation density. As a result, as shown in Figure 4-9, the dislocation density increases faster within first 6 h and tends to reach a saturated state with stable level with a longer creep-ageing time.

Additionally, with the increase of applied stress in creep-ageing, a nonlinear increase in dislocation density was observed when the applied stress increased from 300 MPa to 430 MPa. The rate of dislocation density variation with stress, which is defined as the ratio of the dislocation density increase to the increase of stress, was 2.2 x 10^{11} m^{-2} MPa^{-1} when the stress increased from 300 to 400 MPa and increased to 4.7 x 10^{11} m^{-2} MPa^{-1} for 400 to 430 MPa. It demonstrates the nonlinear increase of dislocation density with increasing applied stress, i.e., more dislocations will be induced for the

same stress increase above 400 MPa than below 400 MPa.

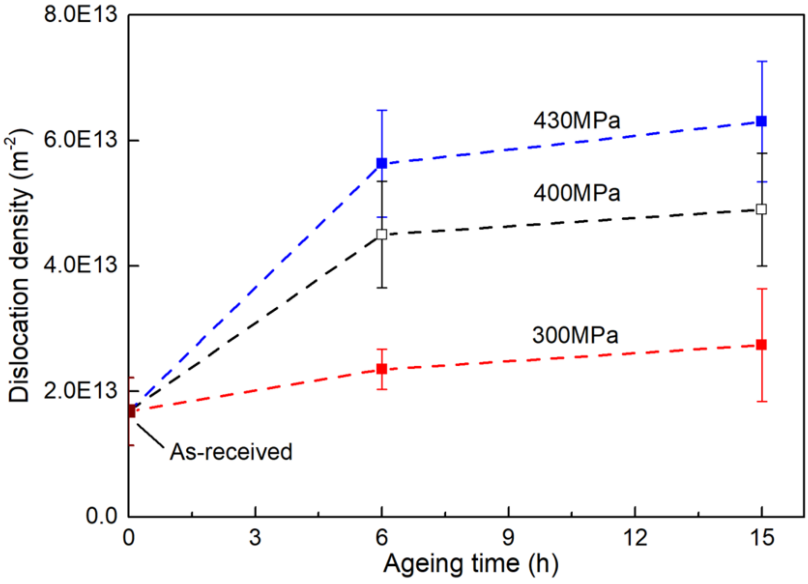


Figure 4-9. Evolution of dislocation density with ageing time under different stresses.

4.4.3 Discussion of test results

4.4.3.1 Effect of creep-ageing on precipitation competition of T_1 and θ'

Figure 4-7 demonstrates the dominance of T_1 in relative frequency between T_1 and θ' from 0 up to 15 h in creep-ageing under different stress levels. There is a competition between T_1 and θ' in precipitation during creep-ageing and the fraction of T_1 was higher at all applied stresses. This competition phenomenon for the evolution of $T_1(Al_2CuLi)$ and θ'(Al_2Cu) during ageing can be caused by the limited Cu atoms available in the matrix [134, 135]. The enhancement of precipitation kinetics of T_1 precipitates under the effect of increasing heterogenous nucleation sites in the matrix induced by pre-stretching or creep-ageing has been widely observed [56, 102]. The high ratio of relative frequency of T_1 to θ' precipitates can be attributed to the lower energy required for T_1 precipitates to nucleate and grow in dislocation generated heterogenous defects, which leads to the dominance of T_1 precipitates in this precipitation competition [134, 136].

Additionally, the effect from the applied stress on the relative frequency of T_1 to θ' in creep-ageing can be observed from Figure 4-7: the frequency of T_1 to θ' increased with higher applied stress. This can be attributed to the fact that more dislocations are generated under higher stress during creep-

ageing, as shown in Figure 4-9, which means that increased nucleation sites are induced for T_1 precipitates. Hence the nucleation and growth of T_1 precipitate are accelerated under higher applied stress, which in turn will restrict the evolution of θ' precipitates and finally leads to the increased ratio of T_1 to θ' with higher applied stress in creep-ageing.

4.4.3.2 The correlation of stress, dislocation density, and precipitation evolution in creep-ageing

As shown in Figure 4-8, the precipitate size under 400 and 430 MPa increases when creep-aged in the first 6 h and enters a stable state with minor size changes afterwards. Furthermore, after 15 h creep-ageing, the average precipitate sizes are almost the same for the three stresses of 300, 400 and 430 MPa. This observation is different from some studies of 2xxx series Al alloys treated with SHT or in T3 state, for which the average precipitate size decreases with increasing pre-stretching or higher applied stress in subsequent ageing/creep-ageing treatment [102, 136–138]. The decrease of precipitate size with increased pre-stretch and applied stress was attributed to the higher dislocation density induced at greater strain, which can lead to more defects acting as heterogeneous nucleation sites in the matrix [102, 134, 137]. With increased nucleation sites and more nuclei, the size to which a precipitate can grow is limited because of enhanced competition for solute atoms with surrounding sites, leading to a reduction in precipitate size [56, 102].

It has been reported that the average diameter values of T_1 in AA2050 increase fast in the first 18 h and then remain at a comparatively stable level for a long ageing time [34, 139, 140], indicating a size limit. In this study, the slight change in precipitate size for the ageing time above 6 h under 400 and 430 MPa can be attributed to the increased competition for solute atoms in the surrounding diffusion field when reaching the size limit. The minor effect of applied higher stress on precipitate size reduction in this research can be attributed to the fact that, for Al-Li alloy in T8 state, precipitate nucleation process is no longer at its peak stage when compared with conditions of SHT and T3. As a result, the effects of dislocation induced nucleation and growth on precipitate size evolution is reduced to a large extent after reaching stable state. On the other hand, the observed results show that they have reached the size limit.

4.5 Four-point bending CAF test results

4.5.1 Results of four-point bending CAF test with same maximum surface stress

Results of the four-point bending CAF test with the same maximum surface stress of 430 MPa within the elastic region are demonstrated in Table 4-3. In the table d_{id}, d_{ll}, d_f are respectively the initial deflection, displacement at the loading point, and final deformed deflection of the specimen at centre position. For d_{id} and d_f, the measurement procedure was the same as that introduced in previous sections 3.6.4 (a) and (f). The measurement procedure for d_{ll} was illustrated in the same section 3.6.4 (d). The springback percentage S_p is calculated following the equation below

$$S_p = 1 - (d_f - d_{id}) / d_{ll} \tag{4-3}$$

With the above equation, the experimental springback results are also demonstrated in Table 4-3. It can be noticed in the table that the thickness of the specimen exerted solid influence on the required loading displacement to reach the same maximum surface stress. The loading displacement of the 2 mm thickness was respectively about 2 and 3 times of the displacements of the 4 and 6 mm specimens. However, the final deformed deflections of all three thicknesses fell in similar range with the lowest value of 0.99 mm and the heights of 1.41 mm. As a result, the highest springback percentage derived is for the 2 mm thickness and decreases with increasing plate thickness.

Table 4-3. Four-point bending CAF test results and corresponding springback with the same maximum surface stress of 430 MPa.

Thickness (mm)	**Initial deflection d_{id} (mm)**	**Loading displacement d_{ll} (mm)**	**Deflection after springback d_f (mm)**	**Springback percentage S_p (%)**
2	0.02	18.7	1.41	92
4	0.04	9.2	0.99	89
6	0.33	5.9	1.04	88

4.5.2 Results of four-point bending CAF test with target curvature

The target curvature is set to be 2000 mm^{-1} for the four-point bending CAF tests. Also, as introduced above in section 3.3.3.3, with the determined target curvature, the target deformed deflection is calculated as 2.03 mm as illustrated in Figure 3-2 and Eq. (3-4).

Results of the four-point bending CAF test with the same target curvature and different thicknesses are presented in Table 4-4. The springback percentage for this test group is also calculated following the same Eq. (4-3) and is given in Table 4-4. As the final deformed deflection results shown in the table, satisfying test results were obtained with the maximum error of 0.1 mm for the 2 mm thickness. The deformed specimens are demonstrated in Figure 4-10.

Table 4-4. Results of target curvature CAF four-point bending test and corresponding springback.

Thickness (mm)	**Initial deflection d_{id} (mm)**	**Loading displacement d_{ll} (mm)**	**Deflection after springback d_f (mm)**	**Springback percentage S_p (%)**
2	0.03	20.2	1.92	90
4	0.07	10.8	1.97	82
6	0.38	7.3	2.01	78

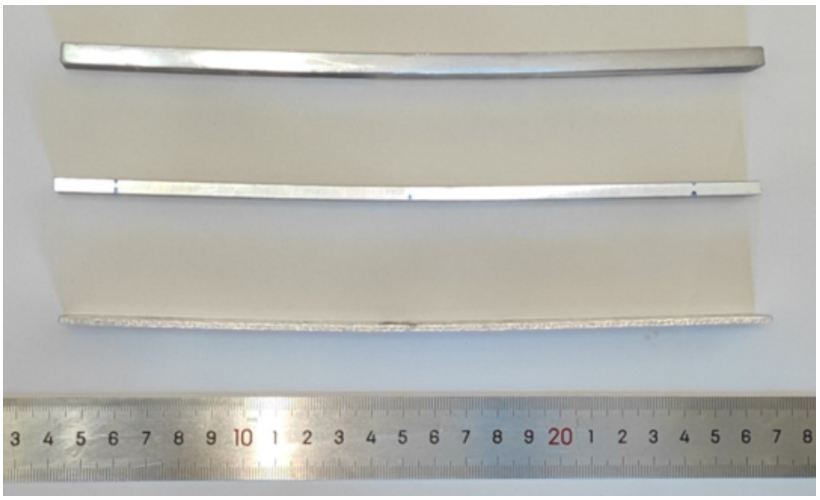


Figure 4-10. Photo of the deformed specimens with target curvature in the four-point bending CAF

tests.

4.5.3 Discussion of test results

Large springback of the forming specimens were derived for both test conditions, with the lowest springback of 78% and the highest of 92% in the conducted tests, reflecting the formability difficulty of applying AA2060-T8 in CAF. For the four-point bending tests with target curvature, the tests results of all the thicknesses were in good convergences with the target deflection value of 2.03 mm. For the four-point bending CAF test with the same maximum stress of 430 MPa within the elastic region, with the measured deflection of the deformed specimen, the corresponding curvature radius is calculated as 2873, 4091, 4939 mm for 2, 4, and 6 mm specimens respectively, indicating relatively small curvatures were generated in CAF tests within elastic region. Hence, due to characteristics of high strength and strong creep resistance of AA2060-T8, CAF formability difficulty of the material exists when CAF fabrication is limited in the elastic region. Hence plastic strain needs to be introduced in loading stage to assist CAF fabrication of AA2060-T8 with large curvature.

Figure 4-11 demonstrates the comparison of springback of four-point bending CAF with the same maximum stress and target curvature. As can be noticed, in both test conditions, springback was reduced with an increase of specimen thickness which can be caused by the larger loading displacement required by the specimen with less thickness. Also, for specimens with the same thickness, less springback occurred when applied with larger loading displacement: the springback derived in tests with target curvature was lower than the tests within the elastic region, as the loading displacement of the former was larger than the latter.

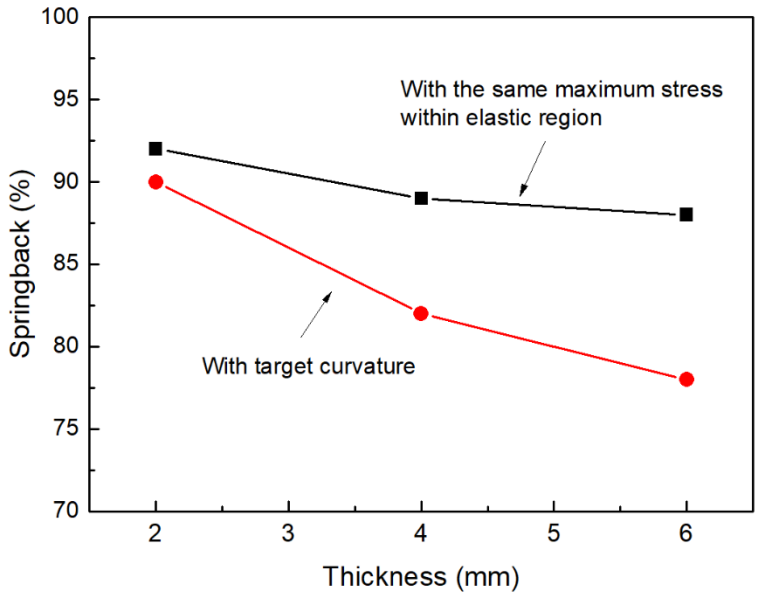


Figure 4-11. Comparison of springback of four-point bending CAF with the same maximum surface stress and with target curvature.

4.6 Multipoint CAF fabrication results

The test results of fabricating 2000 mm^{-1} target curvature sheets of 2 and 4 mm are demonstrated in Table 4-5. By applying an efficient closed-form solution for springback compensation in elastic-plastic creep age forming, a final formed curvature radius of 2195.5 and 2133.3 mm are respectively obtained for the 2 and 4 mm thickness. Both results are within 10% error of the target curvature radius of 2000 mm, indicating that the developed method is adequate to fabricate sheets with target curvature through CAF adopting a flexible tool. Further information and discussion regarding to the developed closed-form solution for springback prediction and compensation in elastic-plastic creep age forming will be presented and discussed in Chapter 7.

Table 4-5. Test results for 2 and 4 mm thickness specimen.

Thickness (mm)	**Initial deflection (mm)**	**Loading displacement d_{lm} (mm)**	**Deflection after springback d_f (mm)**	**Formed curvature radius (mm)**
2	0.17	72.6	5.13	2195.5
4	0.28	41.5	5.28	2133.3

4.7 Summary

The experimental results are presented in this chapter. With the obtained results of tensile tests at room and elevated temperature, an appropriate stress range from 300 to 430 MPa for creep-ageing of the material is determined. Based on the hardness evolution result, appropriate creep-ageing time for different tests is determined considering the reasonability and cost-efficiency. A nonlinear increase of the creep deformation when the applied stress surpasses 400 MPa is identified: when the applied stress increased from 300 to 400 MPa, the accumulated creep strain at 20 h increased from 0.02% to 0.06%, while the creep strain increased from 0.06% to 0.45% when the applied stress increased from 400 to 430 MPa. Based on the obtained results of TEM observations and XRD tests, the microstructural evolution of the material and the correlation of stress, dislocation density, and precipitation evolution in creep-ageing is further revealed and discussed. The results of CAF tests adopting the four-point bending tool and the flexible tool are respectively demonstrated in sections 4.5 and 4.6. It is observed that for specimens of the same thickness, less springback occurred when applied with larger loading displacement/stress.

Chapter 5

Materials modelling of AA2060-T8 in creep-ageing

5.1 Introduction

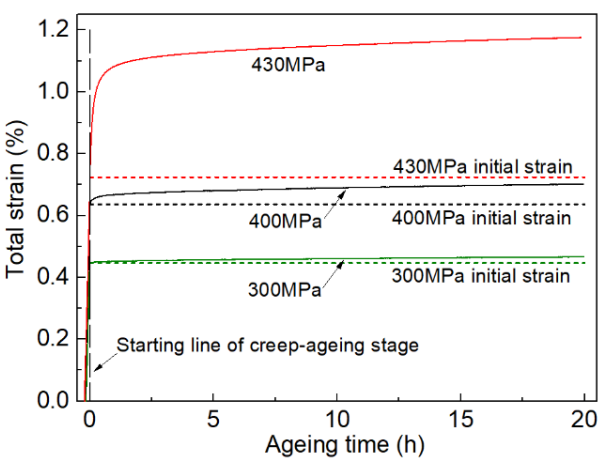
In this chapter, a unified constitutive model is established for predicting the stress-creep strain evolution of AA2060-T8 in creep-ageing. A broader scope of the material behaviour for the adopted Al-Li alloy in creep age forming is provided in this study, including the loading and creep-ageing stages with different applied stresses ranging from 300 to 430 MPa. The link between the pre-introduced dislocations and the subsequent creep behaviour of the material is investigated and reflected in the proposed constitutive model.

5.2 Effects of applied stress on creep deformation

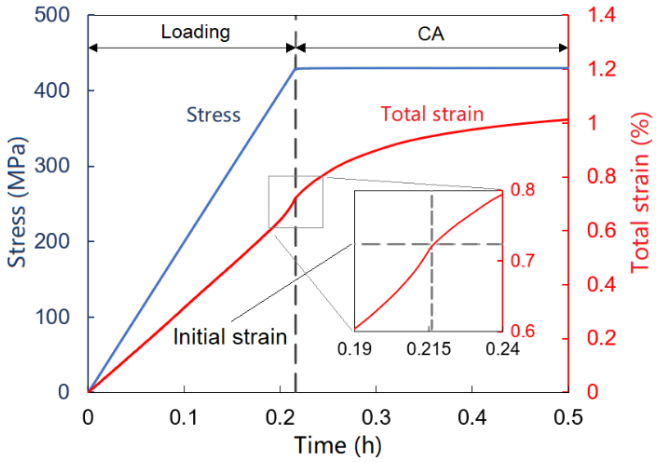
The total strain evolutions under 300, 400, and 430 MPa and the levels of corresponding strain accumulated in the loading and the following creep-ageing stages is demonstrated in Figure 5-1a. It can be noticed that when applied with higher stress, higher initial strain was also obtained at beginning of creep-ageing stage. In addition, the creep strain of 430 MPa was much higher than 300 and 400 MPa as shown in Figure 5-1a. Figure 5-1b demonstrates the determination of the loading and creep-ageing stages in the uniaxial tests, as well as the stress and total strain evolutions in the first 0.5 h including the loading and initial creep-ageing stages under 430 MPa. The creep-ageing stage is deemed to begin at the time when the applied stress reaches its designed value which are kept constant afterwards. The strain at this point is denoted as initial strain and the strain accumulated in the creep-ageing stage is denoted as creep strain. It is noticed that the total strain does not increase linearly with stress at the later stage of loading to 430 MPa (see the inset in Figure 5-1b). This is because that 430 MPa is above the proportionality limit and approaching the 0.2% offset yield strength of 456 MPa.

To further illustrate the nonlinear creep deformation with increasing applied stress, creep strain ε_{cr} in respect of applied stress at the 20 h creep-ageing is plotted in Figure 5-1c. A bilinear increase trend can be observed to intersect around 400 MPa in the relationship of applied stress and ε_{cr} in semi-

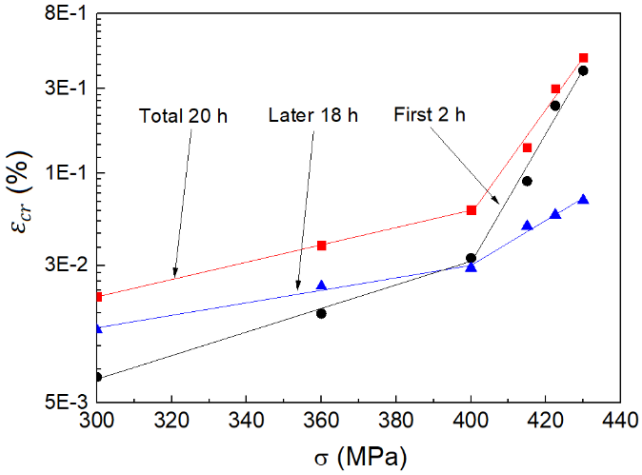
logarithm form. As demonstrated in Figure 5-1a and Figure 5-1c, the creep strain evolution differs significantly in the first 2 h of creep-ageing in the primary stage, which can be attributed as the major cause resulting in the difference in the accumulated creep strain with increasing applied stress. Figure 5-1c also illustrates the comparison of the creep strain accumulated under different stresses in the first 2 h and later 18 h. A similar bilinear increase trend can be recognised in the first 2 h and later 18 h, which also intersects at the applied stress of 400 MPa. It can be observed in Figure 5-1c, that the contribution of the creep strain in the first 2 h exceeds the later 18 h and becomes the major accumulated creep strain for the total 20 h when the applied stress surpasses 400 MPa. When combining of the observation in Figure 5-1a that different initial strains are accumulated at the end of loading stage with different applied stress, it can be noticed that the strain accumulated in the loading stage can exert effects on the creep deformation in the subsequent creep-ageing stage, to which more attention should be paid. Figure 5-1d shows the stress-total strain curves during the loading and creep-ageing stages for 415 and 430 MPa. From the curves in Figure 5-1d, when the applied stress surpasses the value around 400 MPa in the loading stage, the stress-strain evolution begins to slightly diverge from the linear relationship shown as the dotted red line in the inset. σ_{end} in Figure 5-1d is the stress at the end of the linear elastic stress-strain relation. The breakdown of the linear stress-strain relationship indicates that plastic strain was generated in the loading stage. A modelled stress-strain curve (red dashed line) for the loading stage to 430 MPa is also plotted in Figure 5-1d, which will be discussed in Section 5.3.



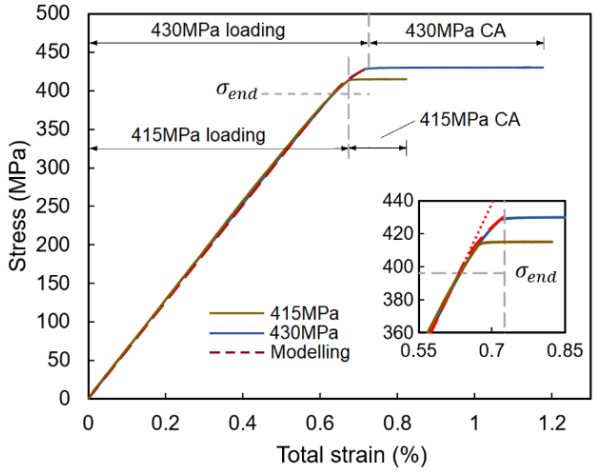
(a) Total strain curves



(b) Stress and strain curves under 430 MPa



(c) Accumulated creep strain



(d) Stress – total strain curves

Figure 5-1. Material deformation behaviour in the loading and creep-ageing stages (CA is the abbreviation for creep-ageing in the figures). (a) demonstrates the total strain curves for 300, 400 and 430 MPa. The determination of the initial strain is demonstrated in (b). (c) shows the accumulated creep strain for the first 2 h, later 18 h and total 20 h under different stresses and (d) is the stress – total strain curves for the loading and creep-ageing stages under 415 and 430 MPa showing the deviation from linear stress-strain relation above σ_{end}. The dotted line in the inset in (d) is the extrapolation of linear stress-strain relation.

5.3 Constitutive model development

In this section, by combining a work hardening model in the loading stage, a mechanism-based constitutive model is developed to describe the increased creep deformation behaviour observed in

creep-ageing with a unified structure. The proposed model consists of four groups of constitutive equations:

(1) Work hardening model proposed to obtain initial plastic strain and corresponding dislocation density at the end of the loading stage (beginning of creep-ageing stage) to determine the threshold stress for creep.

(2) Microstructural constitutive equations to describe precipitate growth and dislocation density evolution during creep-ageing.

(3) Strengthening equations to express material hardening induced by microstructural evolutions (precipitates and dislocations).

(4) Macro stress-creep strain relationship expressed with a sinh-law function which can reflect the effects of internal microstructural variables on macro creep deformation behaviour.

5.3.1 Threshold stress determination

5.3.1.1 Initial threshold stress

Threshold stress σ_{th} is the critical value under which creep cannot be induced [21, 75]. The presence of the threshold stress has long been identified in creep of different alloys [141–143]. It has been established that threshold stress is the resistance stress generated when overcoming second phase obstacles in deformation-induced dislocation movements (dislocation climb/glide) [142]. When threshold stress is considered, creep deformation behaviour is no longer considered to be only affected by the total stress σ, instead the stress $(\sigma - \sigma_{\mathrm{th}})$ should be adopted. As a result, the steady state creep rate $\dot{\varepsilon}$ can be written as [143]:

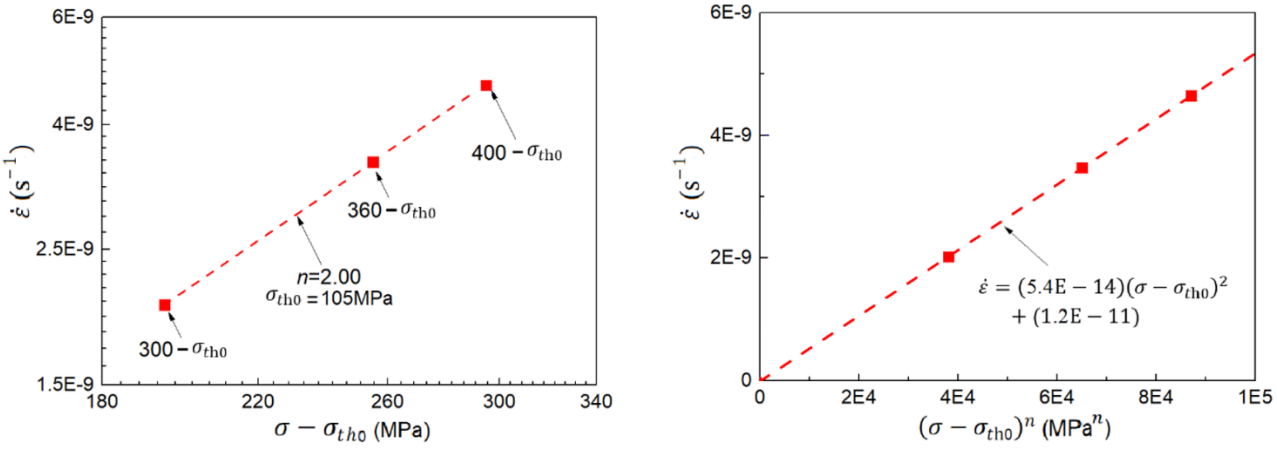
$$\dot{\varepsilon} = A(\sigma - \sigma_{\mathrm{th}})^n \exp\left(\frac{-Q_a}{RT}\right) \tag{5-1}$$

where A is a temperature dependent material constant related to the shear modulus; n is the stress exponent as an index indicating the dominant creep mechanism; Q_a is the activation energy. R is the gas constant; T is the absolute temperature in Kelvin degree.

To determine initial threshold stress σ_{th0} with the fit value of n for the as-received materials, a linear extrapolation method to estimate the initial threshold stress with constant temperature is employed by adopting the logarithm form of Eq. (5-1), i.e. $\ln(\dot{\varepsilon}) = n\ln(\sigma - \sigma_{\mathrm{th}}) +$

ln $(A\exp(-Q_a/RT))$. The lower stress group including 300, 360 and 400 MPa under which linear elastic stress-strain relation is maintained in the loading stage was selected for the initial estimation. If σ_{th} was not considered in Eq. (5-1), n values of 2.9 was obtained with the average creep strain rate in the steady state ($\dot{\varepsilon}$ drops below 1.0×10^{-8} s^{-1}) of the selected stress range, indicating that the diffusion creep mechanism, i.e. with n ranges from 1 to 3 [133], was dominant when creep-aged within lower stress group.

The procedure of the method can be generalised as follows: (i) Given a trial value of σ_{th0} (the initial trial values of σ_{th0} were zero with n of 2.9), a fitting line $\ln(\dot{\varepsilon}) = a_1\ln(\sigma - \sigma_{th0}) + b_1$ can be obtained. Figure 5-2a demonstrates such fitting lines with trial σ_{th0} values of 105 MPa. According to the logarithm form of Eq. (5-1), n is equivalent to a_1. (ii) With the acquired value of n $(= a_1)$, another fitting line as $\dot{\varepsilon} = a_2(\sigma - \sigma_{th0})^n + b_2$ can be obtained, as shown in Figure 5-2b. The derived fitting equation becomes $\dot{\varepsilon} = b_2$ when $\sigma = \sigma_{th0}$. If the criterion $|b_2| \leq \dot{\varepsilon}_{300}/100$ is satisfied ($\dot{\varepsilon}_{300}$ is the steady state creep strain rate at 300 MPa), b_2 can be considered as a negligible creep strain rate $\dot{\varepsilon}$ achieved with $(\sigma - \sigma_{th0})$, and σ_{th0} can be deemed as the suitable initial threshold stress under which creep is not induced. If not, the above steps (i) and (ii) are repeated for different σ_{th0} values.



(a) Logarithmic plot of $\dot{\varepsilon}$ with $(\sigma - \sigma_{th0})$ (b) Plot of $\dot{\varepsilon}$ with $(\sigma - \sigma_{th0})^n$

Figure 5-2. Determination of initial threshold stress with plots of $\dot{\varepsilon}$ against respectively $(\sigma - \sigma_{th0})$ and $(\sigma - \sigma_{th0})^n$. (a) shows the fitting lines with the initial threshold stress of 105 MPa; (b) demonstrates that the second term in the well fitted creep strain rate equation is negligible.

5.3.1.2 Effect of pre-existing dislocation

The breakdown of the linear stress-strain relationship and the introduction of plastic strain in the loading stage, as noticed in Figure 5-1b and Figure 5-1d, can induce the nonlinear increase of creep deformation at the primary creep-ageing stage with the applied stress levels. A similar phenomenon was found in stress relaxation; When the initial loading was in the plastic region, a nonlinear increase of relaxed stress was identified [21, 75, 142]. The promotion of creep deformation and reduction of creep resistance with the plastic strain-introduced dislocations have been reported in many studies [21, 75, 77]. There are mainly two reasons for this effect: First, with increasing mobile dislocations introduced in the matrix, the duration of the primary stage in creep-ageing is extended which can lead to an evident rise of the accumulated total creep strain; Second, when adopting high stress, plastic strain and corresponding dislocations can be induced in the alloy matrix. Dislocation glide then becomes the dominating mechanism, causing a significant reduction of creep resistance/threshold stress with an estimated 10 times lower dragging force in dislocation movement compared with dislocation climb [144]. When considering the lowered creep resistance caused by the induced dislocation at higher stress, different forms of exponential decay functions were proposed to express the dramatic drop of threshold stress with increasing dislocation density [75, 142]. A term $n_1 \bar{\rho}_0{}^{m_1}$ was introduced to account for the reduction of threshold stress due to the existence of plastic strain-induced initial dislocation density $\bar{\rho}_0$ [75]. Thus, the threshold stress in creep-ageing can be expressed in the form of a ramp function equation (RFE) as:

$$\sigma_{th} = < \sigma_{th_0} - n_1 \bar{\rho}_0{}^{m_0} > \tag{5-2}$$

where $< \mathrm{X} >$ is Macaulay brackets, indicating a ramp function in which negative values return 0; σ_{th_0} is the intrinsic threshold stress of the as-received material under which creep cannot be induced; n_1 and m_0 are material constants. $\bar{\rho}_0$ is the normalised dislocation density generated in the loading stage and is defined as $\bar{\rho}_0 = (\rho_0 - \rho_i)/(\rho_m - \rho_i)$, ρ_i is the initial dislocation density at the as-received state, ρ_m is the dislocation density at the saturated state. Based on the definition, $\bar{\rho}_0$ value can range from 0 to 1.

When adopting Eq. (5-2) to describe the threshold stress σ_{th}, σ_{th} decreases at an increasing rate with the increase of $\bar{\rho}_0$, as demonstrated with the dotted curve in Figure 5-3. Consequently, threshold

stress has a sudden turn when it drops to zero without smooth transition, which can cause an abrupt change in predicted creep strain. Hence, to eliminate this issue, a modified equation is given in the form of reversed exponential equation (REE) as:

$$\sigma_{th} = \sigma_{th_0}/(1 + \exp(n_{1a}\bar{\rho}_0{}^{m_{1a}} - B)) \tag{5-3}$$

where n_{1a}, m_{1a}, B are material constants. Figure 5-3 shows the schematic relation of σ_{th} and $\bar{\rho}_0$ for both functions. For REE, a smooth transition is introduced as σ_{th} approaches 0. Hence, REE is adopted as the threshold stress equation in the following sections.

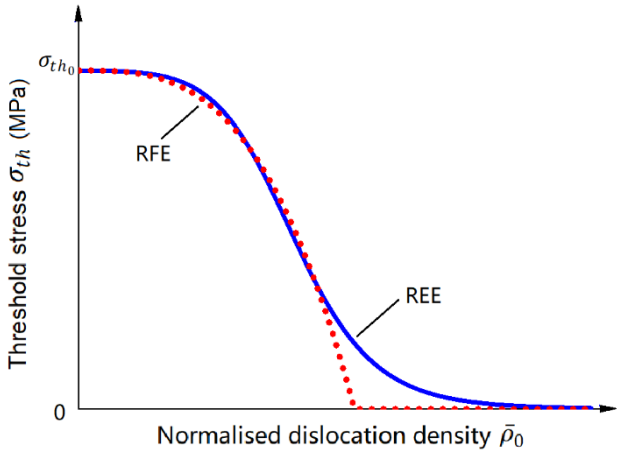


Figure 5-3. Schematic of threshold stress σ_{th} variation with normalised dislocation density $\bar{\rho}_0$ for the ramp function equation (RFE, Eq. (5-2)) and the reversed exponential equation (REE, Eq. (5-3)), showing the sudden turn for the former and smooth transition for the latter when σ_{th} approaches zero.

5.3.1.3 Loading stage dislocation density determination with work hardening model

To calculate the threshold stress with proposed Eq. (5-3), the plastic strain ε_p and resultant dislocation density ρ_0 in the loading stage need be determined. The inducement of a non-linear stress-strain relationship is an indication of introducing plastic strain through work hardening. A form of Nadai model able to express stress-strain response in both elastic and work hardening regions was adopted to obtain the total strain induced in the loading stage as [145]:

$$\varepsilon = \begin{cases} \sigma/E & \sigma \leq \sigma_{end} \\ \sigma/E + K(\sigma - \sigma_{end})^{n'} & \sigma > \sigma_{end} \end{cases} \tag{5-4}$$

where K and n' are material constants. When the applied stress σ surpasses σ_{end}, the plastic strain can be calculated by deducting the linear elastic strain as:

$$\varepsilon_p = \begin{cases} 0 & \sigma \le \sigma_{end} \\ \frac{\sigma-\sigma_{end}}{E} + K(\sigma-\sigma_{end})^{n'} & \sigma > \sigma_{end} \end{cases} \quad (5\text{-}5)$$

With derived plastic strain in the loading stage, the dislocation density can be obtained through a widely adopted rate form dislocation density constitutive equation as [146]:

$$\dot{\bar{\rho}}_0 = A_1(1-\bar{\rho}_0)\left|\dot{\varepsilon_p}\right|^{m_1} - C_p{\bar{\rho}_0}^{m_2} \quad (5\text{-}6)$$

where $\dot{\varepsilon_p}$ is the plastic strain rate which can be derived through the differentiation of Eq. (5-5) with regard to time; A_1, m_1, C_p and m_2 are material constants. The dynamic term $A_1(1-\bar{\rho}_0)\left|\dot{\varepsilon_p}\right|^{m_1}$ in Eq. (5-6) is the dislocation density variation due to creep deformation and dynamic recovery, ${C_p\bar{\rho}_0}^{m_2}$ is the static term accounted for the recovery of the dislocation at elevated temperature.

5.3.2 Microstructural constitutive equations

Creep can be viewed as time dependent plastic deformation, hence Eq. (5-6) is also applicable to express the evolution of creep strain-induced dislocation density in creep-ageing by substituting plastic strain ε_p with creep strain ε_{cr} as:

$$\dot{\bar{\rho}} = A_1(1-\bar{\rho})|\dot{\varepsilon_{cr}}|^{m_1} - C_p\bar{\rho}^{m_2} \quad (5\text{-}7)$$

where $\bar{\rho}$ is the normalised dislocation density with the same form of Eq. (5-2) as $\bar{\rho} = (\rho - \rho_i)/(\rho_m - \rho_i)$ and has a value range from 0 to 1. It should be noted that due to the pre-existing dislocation density $\bar{\rho}_0$ at the end of the loading stage, the value of dislocation density at the beginning of creep-ageing is $\bar{\rho} = \bar{\rho}_0$. Additionally, since the loading and creep-ageing stages are continuous and conducted at the same temperature, it is reasonable to adopt the same material constants A_1, m_1, C_p, and m_2 in Eq. (5-6) for Eq. (5-7).

A normalised precipitate size $\bar{r}$ is adopted to describe precipitate growth in creep-ageing, defined as:

$$\bar{r} = \frac{r}{r_0} \quad (5\text{-}8)$$

where r stands for the average precipitate radius and r_0 is the radius at the as-received T8 state. Thus, the initial value of the normalised precipitate size is 1. The as-received precipitate size r_0 is adopted to facilitate linking the simulation results with experimental data. For precipitate growth, a widely adopted growth rate equation is used [33]:

$$\dot{\bar{r}} = C_r(Q - \bar{r})^{m_3}(1 + \gamma_0\bar{\rho}^{m_4}) \tag{5-9}$$

where Q represents the upper limit of precipitate growth during creep-ageing stage, at which a stable state is reached with the growth rate dropping to zero. C_r, m_3, γ_0, and m_4 are material constants. The observed strong stress-dependent characteristic of precipitate growth is accomplished by introducing the term $(1 + \gamma_0\bar{\rho}^{m_4})$, expressing the acceleration of precipitation kinetics with higher dislocation density. The extent of the positive effect on precipitate growth caused by stress-induced dislocation density can be controlled through this term.

5.3.3 Strengthening constitutive equations

The phenomenon of dislocation hardening behaviour in creep-ageing is well recognised [33, 76]. The hardening behaviour is closely related to the dislocation density evolution induced by creep deformation. Additionally, in this study, the strength contribution of dislocation density generated in the loading stage is also considered by assuming $\bar{\rho} = \bar{\rho}_0$ at the beginning of creep-ageing stage. A well-established dislocation hardening (σ_{dis}) equation is adopted [33, 74]:

$$\dot{\sigma}_{dis} = A_2 n_d \bar{\rho}^{n_d - 1}\dot{\bar{\rho}} \tag{5-10}$$

where A_2 and n_d are material constants.

Precipitates are obstacles to dislocation movements during creep/plastic deformation. When a dislocation encounters precipitates during moving, two interaction mechanisms can happen based on the precipitate size: dislocation can shear through small precipitates or bypass large precipitate in the form of Orowan loop [99]. Hence precipitation hardening can be viewed as composed of two types of strengthening contributions, i.e. shearing strength σ_A, and bypassing strength σ_B, which have been given respectively as [147]

$$\begin{aligned} \sigma_A &= c_1 f^{m_a} r^{n_a} \\ \sigma_B &= c_2 f^{m_b}/r^{n_b} \end{aligned} \tag{5-11}$$

where f is the volume fraction of precipitates; c_1 and c_2 are material constants; m_a, n_a, m_b, and n_b are coefficients determining strength contributions from volume fraction and precipitate size. An approximation of cubic exponential relationship between normalised volume fraction $\bar{f}$ and precipitate size r was proposed by Reti and Flemings [148], and is adopted here:

$$\bar{f} = \frac{f}{f_s} = \frac{f}{f_0}\frac{f_0}{f_s} = \left(\frac{r}{r_0}\right)^3 \bar{f}_0 = \bar{r}^3 \bar{f}_0 \tag{5-12}$$

where f_s is the equilibrium volume fraction at ageing temperature, f_0 is the initial volume fraction at beginning of creep-ageing stage, $\bar{f}_0$ is the corresponding normalised volume fraction defined as $\bar{f}_0 = f_0/f_s$. By substituting Eq. (5-12) into Eq. (5-11) and utilising the derivation process used in a previous research [74], equation for precipitate hardening in normalised form can be written as:

$$\begin{aligned} \sigma_A &= {c_1}'\bar{r}^{m_{na}} \\ \sigma_B &= {c_2}'/\bar{r}^{m_{nb}} \end{aligned} \tag{5-13}$$

where ${c_1}'$, ${c_2}'$, m_{na},and m_{nb} are material constants. From Eq. (5-13), it can be derived that when dislocation-precipitate interaction is dominated by shearing mechanism (σ_A), the precipitate hardening increases with precipitate growth. On the other hand, when the dominating mechanism changes to bypassing (σ_B), precipitate hardening decreases with the growth of precipitate. A harmonic function to combine the hardening effects generated by the two interaction mechanisms was proposed in [99] as:

$$\sigma_{ppt} = ({\sigma_A}^{-1} + {\sigma_B}^{-1})^{-1} \tag{5-14}$$

where σ_{ppt} is the overall precipitation hardening combining strength contribution of shearing (σ_A) and bypassing (σ_B) mechanisms. When $\sigma_A = \sigma_B$, the change of interaction mechanisms from shear to bypassing happens, indicating the start of over-aged state.

The overall yield strength evolution can be considered as composed of hardening effects caused by different mechanisms, such as dislocation and precipitation hardening. An addition law is adopted to express the evolution of yield strength σ_y as:

$$\sigma_y = \sigma_i + ({\sigma_{ppt}}^{n_y} + {\sigma_{dis}}^{n_y})^{1/n_y} \tag{5-15}$$

where σ_i is the intrinsic strength including solid solution hardening of the alloy, n_y is an exponent constant to control the relative strength contribution of precipitation and dislocation hardening, which was determined in the range of 1 to 2 as suggested by [94].

5.3.4 Stress-creep strain relationship

The classical sinh-law equation is adopted to link the creep strain rate $\dot{\varepsilon_{cr}}$ with the applied stress in creep-ageing stage. To account for the decrease of creep strain rate caused by material hardening

induced by microstructural evolution during creep-ageing, a creep variable H is introduced, representing the effects of normalised dislocation density $\bar{\rho}$ and precipitate size $\bar{r}$ [74]. In this study, considering the effect of threshold stress, the group of constitutive equations to express stress-creep strain relationship is given as:

$$\begin{cases} \dot{\varepsilon}_{cr} = A_3 \sinh(B_1(\sigma - \sigma_{th})(1-H)^{n_2}) \\ H = k_1'(\bar{\rho} - \bar{\rho}_0) + k_2'\bar{r} \end{cases} \tag{5-16}$$

where A_3 and B_1 are material constants. n_2 is an exponent constant controlling the effect of creep variable *H*.

By combining the proposed equations above, a unified constitutive model is presented in Table 5-1. Through the work hardening sub-model, the plastic strain and plastic strain-induced dislocation density in the loading stage can be determined, with which the threshold stress at the beginning of creep-ageing stage is obtained. With the expression of microstructure variables in creep-ageing, the creep deformation behaviour and material strength evolution can be modelled with the proposed corresponding constitutive equations.

Table 5-1. Unified constitutive model including work hardening

Work hardening sub-model	**Microstructure variables**
$\varepsilon_p = (\sigma - \sigma_{end})/E + K(\sigma - \sigma_{end})^{n'}$ $\dot{\bar{\rho}}_0 = A_1(1-\bar{\rho}_0)\lvert\dot{\varepsilon}_p\rvert^{m_1} - C_p{\bar{\rho}_0}^{m_2}$ $\sigma_{th} = \sigma_{th_0}/(1+\exp(n_{1a}{\bar{\rho}_0}^{m_{1a}} - B))$	$\dot{\bar{\rho}} = A_1(1-\bar{\rho})\lvert\dot{\varepsilon_{cr}}\rvert^{m_1} - C_p\bar{\rho}^{m_2}$ $\dot{\bar{r}} = C_r(Q-\bar{r})^{m_3}(1+\gamma_0\bar{\rho}^{m_4})$
Stress-creep strain relationship	**Strengthening equations**
$\dot{\varepsilon}_{cr} = A_3 \sinh(B_1(\sigma - \sigma_{th})(1-H)^{n_2})$ $H = k_1'(\bar{\rho} - \bar{\rho}_0) + k_2'\bar{r}$	$\dot{\sigma}_{dis} = A_2 n_d \bar{\rho}^{n_d - 1}\dot{\bar{\rho}}$ $\sigma_{ppt} = ({\sigma_A}^{-1} + {\sigma_B}^{-1})^{-1}$ $\sigma_y = \sigma_i + ({\sigma_{ppt}}^{n_y} + {\sigma_{dis}}^{n_y})^{1/n_y}$
Parameters in work hardening sub-model	
ε_p: plastic strain induced in loading stage	σ_{end}: stress at the end of linear stress-strain relation
$\bar{\rho}_0$: normalised dislocation density in loading	σ_{th}: threshold stress
σ_{th_0}: initial threshold stress	$\Delta\bar{\rho}_0$: accumulated dislocation density in loading
$E,\ K,\ n',\ A_1,\ m_1,\ C_p, m_2, n_{1a}, m_{1a}, B$ are material constants	
Parameters for microstructure variable	
$\bar{\rho}$: normalised dislocation density in creep-ageing	ε_{cr}: creep strain

$\bar{r}$: normalised precipitate size	$A_1, m_1, C_p, m_2, C_r, Q, m_3, \gamma_0, m_4$ are material constants
Parameters in stress-creep strain relationship	
H: creep variable	$A_3, B_1, n_2, n_3, k_1', k_2'$ are material constants
Parameters in strengthening equations	
σ_{dis}: dislocation hardening	σ_{ppt}: precipitation hardening
σ_A: strengthening by dislocation cutting through precipitate	σ_B: strengthening by dislocation bypassing precipitate
σ_i: material intrinsic strength	A_2, n_d, n_y are material constants

5.4 Model calibration, results and discussion

5.4.1 Determination of initial values and material constants

Since the constitutive equations are ordinary differential equations (ODE) requiring initial values to solve, adopting reasonable initial values for internal variables in the constitutive model is significant for its establishment. These values include initial strength hardening contribution of dislocation density σ_{dis0}, precipitation hardening σ_{ppt0}, and intrinsic strength σ_i. To determine the initial values of these strength components, a SHT and pre-stretching method was adopted as demonstrated in Figure 5-4. σ_i is defined to be equal to SHTed yield strength σ_{y1}. σ_{dis0} can be approximated as the difference between the SHTed yield strength σ_{y1} and the 3% pre-stretched yield strength σ_{y2}, as shown in the figure. σ_{ppt0} can be calculated through Eq. (5-15). The remaining variables can be determined directly from experimental data or assigned with initial values as defined. The initial values for the material in this study are listed in Table 5-2.

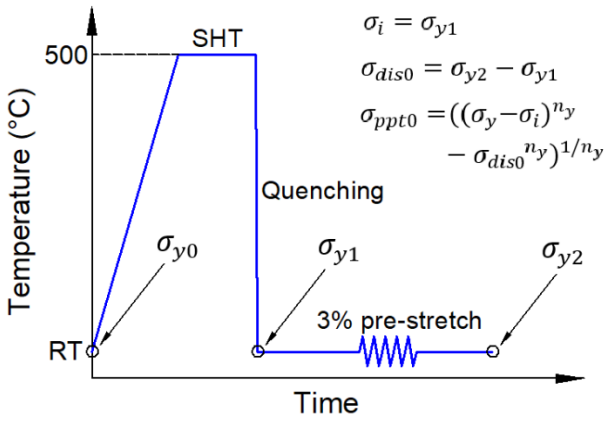


Figure 5-4. Schematic of the thermal history and the determination method for initial values of strength components. RT stands for room temperature.

Table 5-2. Determined initial values for the constitutive model.

$\bar{\rho}_0$	ε_p	$\bar{r}$	σ_{end} (MPa)	σ_{th0} (MPa)
0	0	1	396	105
σ_i (MPa)	σ_{dis0} (MPa)	σ_{ppt0} (MPa)		
299	56	140.2		

The proposed constitutive model is composed of groups of non-linear ODEs that cannot be solved analytically. In this study, the forward Euler method was adopted to solve the equations:

$$s_{n+1} = s_n + \dot{s}_n \, \Delta t \tag{5-17}$$

where s_{n+1} and s_n are values of internal variable s at time step n+1 and n respectively; $\dot{s}_n$ is the evolution rate at time step n; Δt is the time increment. With the derivation of approximate solutions of internal variables, the least square method is adopted to determine the material constants that allow the model to be best fitted with experimental data, i.e. with the minimum value of an objective function. The objective function is written as

$$f(x) = \sum_{i=1}^{L2} \sum_{j=1}^{L3} \left(y_{ij}^m - y_{ij}^e\right)^2 \tag{5-18}$$

where $x = (x_1, x_2, x_3, \ldots, x_{L1})$ is the material parameters with a total number of $L1$ to be determined in the model. $L2$ is the number of series classified by different applied stresses, $L3$ is the number of data points in each series. y_{ij}^m and y_{ij}^e stand for the i-th stress series and j-th data point of the model-

derived value and experimental value respectively. The determined material constants are listed in Table 5-3. In this study, the experimental data of 422.5 MPa was used for verification only and not used in the determination of material constants.

Table 5-3. Determined material constants for the proposed constitutive model.

A_1 (h^{-1})	A_2 (MPa)	A_3 (h^{-1})	B	B_1 (MPa^{-1})	c_1'	c_2'
26	14	8.43E-8	10.5	3.6E-2	225	365
C_p	C_r (h^{-1})	E (MPa)	K (MPa^{-1})	k_1'	k_2'	m_1
6.5E-3	8E-2	6.26E4	9.36E-8	0.5	5.2E-2	5.42E-1
m_{1a}	m_2	m_3	m_4	m_{na}	m_{nb}	n'
0.52	0.75	1.05	1.5	0.83	0.03	2.35
n_{1a}	n_2	n_d	n_y	Q	γ_0	
50	1.28	4.2	1.16	1.52	8	

5.4.2 Stress-creep strain relationship

Figure 5-5 compares the modelled creep strain curves with the experimental data under different stresses. The modelled creep strain curves fit very well with the data. The distinct 6 times increase of creep strain when the applied stress increases from 400 to 430 MPa has been adequately reflected in the model. This nonlinear increase in creep strain can be attributed to the higher initial plastic strain and dislocation density being generated in the loading stage with higher stress, causing a dramatic decrease of the threshold stress within the applied stress ranging from 400 to 430 MPa. The 422.5 MPa result was not used for determining material constants, and the good agreement with the model prediction verifies the adequacy of the proposed model.

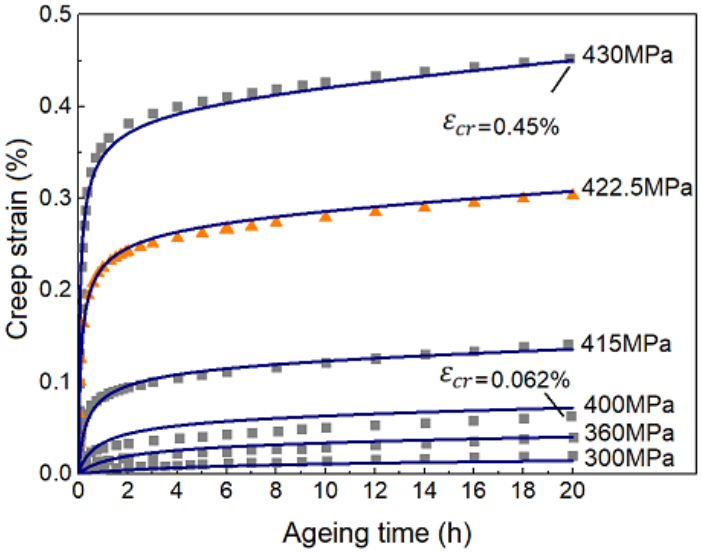
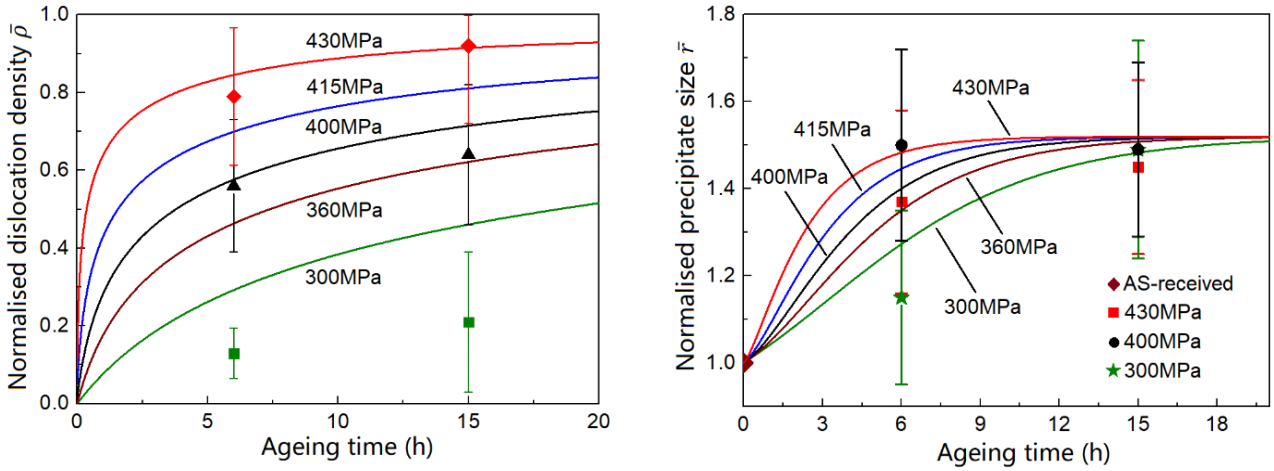


Figure 5-5. Comparison of modelled (lines) and experimental (symbols) creep strain evolutions of the as-received materials under indicated stress levels. The triangle symbols are data used for verification.

5.4.3 Microstructural evolution

Figure 5-6 shows the comparison of fitting results with normalised experiment data for dislocation density and precipitate size during creep-ageing for CA. As shown in Figure 5-6a, the dislocation density evolution under different stresses is reflected by the model (a ρ_m value of 6.8 x 10^{13} m^{-2} was determined by fitting with the experimental data and simulation results using $\bar{\rho} = (\rho - \rho_i)/(\rho_m - \rho_i)$). It can be noticed that under all stresses, the dislocation density increases at a higher rate in the initial hours in which fast creep strain increase is obtained and then increases at gradually reduced rates afterwards. Additionally, discrepancies are observed with the dislocation density under 300 MPa. This can be caused by the term $(1 - \bar{\rho})$ adopted in Eq. (5-7), which may overestimate the dislocation increase rate when the value of $\bar{\rho}$ is low. Figure 5-6b shows the precipitate size evolution under different stresses, which generally increases quickly and then comes to a plateau. Dislocation-enhanced precipitate growth can be observed from the modelling curves that the size growth rate of 430 and 400 MPa is higher than the 300 MPa. Similarly, a higher precipitate size is observed in the simulation results with lower stress of 300 MPa at 6 h which can be attributed to the overestimation of dislocation density $\bar{\rho}$ with lower stress. There are also differences between the model and experimental results for the precipitate size under 400 and 430 MPa. However, the predicted curves

of precipitate size evolution with the three selected stresses fall into the error range of corresponding experiment data, indicating the model's ability to reflect the stress dependency effect on microstructure evolutions in creep-ageing.

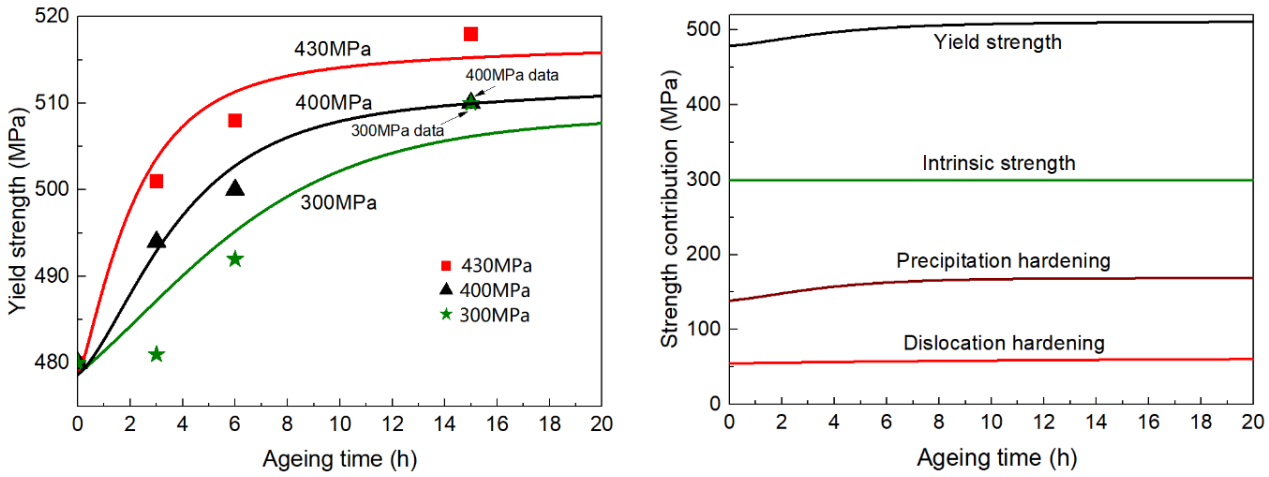


(a) Dislocation density evolution (b) Precipitate size evolution

Figure 5-6. Comparison of modelled (lines) and experimental (symbols) evolutions of the normalised dislocation density and normalised precipitate size with ageing time in material under the indicated applied stress levels.

5.4.4 Strength evolution

Figure 5-7 presents the evolution of yield strength and strength contribution of corresponding hardening mechanisms during creep-ageing for CA. The yield strength evolution in creep-ageing under 300, 400 and 430 MPa are demonstrated in Figure 5-7a. A rising trend can be seen under all stresses during creep-ageing. It can be observed that higher material strength is obtained with higher applied stress in creep-ageing due to the effects of precipitation and dislocation hardening. Figure 5-7b schematically illustrates the strength contribution by different hardening effects under 400 MPa, including intrinsic strength, precipitation hardening, and dislocation hardening. It should be noted that solid solution hardening is included in the intrinsic strength which is not expected to change significantly as the as-received material was in T8 temper.



(a) Yield strength evolution (b) Strength contribution under 400 MPa

Figure 5-7. Evolution of the yield strength and strength contributions with ageing time for the material. The experimental results are marked with symbols and modelling with lines.

5.5 Summary

A unified mechanism-based constitutive model adequate to reflect the stress-creep strain relation has been established in this section. By combining work hardening equations, the wide range of creep deformation of T8 tempered Al-Li alloy from 0.02% to 0.45% with corresponding applied stresses ranging from 300 to 430 MPa can be described by the model. Consistent results have been achieved between experimental and modelling results for macro creep-ageing behaviour and microstructural evolutions in aspects of dislocation and precipitation of material in loading and creep-ageing stages.

Chapter 6

Numerical simulation of CAF

6.1 Introduction

This chapter presents the techniques and settings adopted in numerical simulations of CAF as well as corresponding simulation results. Section 6.2 illustrates the implementation and verification of the material model in numerical simulation. Section 6.3 presents the complete simulation workflow and model setup for simulations of four-point bending CAF and CAF with a multipoint flexible tool. Section 6.4 illustrates the obtained simulation results.

6.2 Implementation and verification of the proposed constitutive model in FE

6.2.1 Constitutive model extends to multiaxial condition

The proposed material model is derived from uniaxial creep-ageing tests under different applied stress. To utilise the model in multiaxial CAF cases like four-point bending and flexible tool bending, the model is required to be extended to multiaxial conditions, which is qualified to describe stress-creep strain relation in multiple directions. The extension can be followed by a previous proposed energy dissipation rate potential method [149]. By ignoring the creep variable H standing for the microstructural hardening effects of dislocation and precipitation, the creep strain rate expressed in Eq. (5-16) reduces to the form of $\dot{\varepsilon}_{cr} = A\sinh(B\sigma_e)$. Based on the derived simplified form of the creep strain rate equation, an energy dissipation rate potential Ψ can be proposed as [149]

$$\Psi = (A'/B')\cosh(B'\sigma_e) \tag{6-1}$$

where $\sigma_{\mathrm{e}} = \left(3S_{ij}S_{ij}/2\right)^{1/2}$ is the Mises effective stress in which S_{ij} denotes the deviatoric stress as $S_{ij} = \sigma_{ij} - \delta_{ij}\sigma_{kk}/3$. Assuming the associated flow rule, the multiaxial creep strain rate can be derived as

$$\dot{\varepsilon}_{ij}^{cr} = \left(\partial\Psi/\,\partial S_{ij}\right) = 3S_{ij}/(2\sigma_{\mathrm{e}})A'\sinh\left(B'\sigma_{\mathrm{e}}\right) \tag{6-2}$$

where $\dot{\varepsilon}_{ij}^{cr}$ denotes the creep strain rate components. When introducing back of the previously ignored creep variable *H*, the creep strain rate is derived as

$$\dot{\varepsilon}_{ij}^{cr} = 3S_{ij}/(2\sigma_{\mathrm{e}})A_3\sinh\left(B_1\sigma_{eff}(1-H)^{n_2}\right) \tag{6-3}$$

In creep-ageing stage, the remaining elastic strain ε_{ij}^{e} can be expressed as $\varepsilon_{ij}^{e} = \varepsilon_{ij}^{t} - \varepsilon_{ij}^{cr}$, where ε_{ij}^{t} is the total strain components and ε_{ij}^{cr} is the creep strain components. Hence the elastic strain rate and stress evolution rate in creep-ageing stage can be respectively expressed in Eq. (6-4) and Eq. (6-5) as

$$\dot{\varepsilon}_{ij}^{e} = \dot{\varepsilon}_{ij}^{t} - \dot{\varepsilon}_{ij}^{cr} \tag{6-4}$$

$$\dot{\sigma}_{ij} = 2G\dot{\varepsilon}_{ij}^{e} + \lambda\dot{\varepsilon}_{kk}^{e} \tag{6-5}$$

where $\dot{\varepsilon}_{ij}^{e}$, $\dot{\varepsilon}_{ij}^{t}$, and $\dot{\varepsilon}_{ij}^{cr}$ are respectively the components of elastic strain, total strain, and creep strain in rate form. $\dot{\sigma}_{ij}$ is the rate of Cauchy stress. G and λ are the Lame elasticity constants expressed as $G = E/[2(1+v)]$ and $\lambda = Ev/[(1+v)(1-2v)]$, where E and v are Young's modulus and Poisson's ratio of the material.

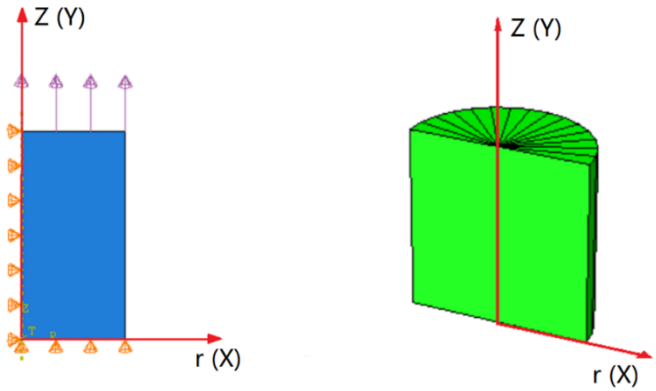
6.2.2 Constitutive model implementation and verification

In this study, ABAQUS is chosen to be the tool not only for its popularity in numerical simulation for both academic and industrial fields, but also for the extensive freedom provided by the software for users to implement self-defined constitutive models through various inset subroutines.

To allow the numerical simulation to be conducted with a user-defined constitutive model, ABAQUS provides various user subroutines as independent modules to allow users to implement self-developed material models into the software. For creep-ageing simulation, three subroutines can be utilised to carry the user-defined constitutive relation of material including CREEP, UMAT, and VUMAT. CREEP is a subroutine specifically designed to implement user-defined creep behaviour of

material into the software. In CREEP subroutine, only user-defined uniaxial creep-ageing stress-creep strain relation is required to be provided and the software will automatically calculate the corresponding strain and stress components in multiaxial condition. UMAT and VUMAT are subroutines which can carry a wider range of constitutive equations not only restricted to creep. When adopting UMAT or VUMAT as the subroutine, all the constitutive relations involved in the simulation process need to be provided, e.g., in a complete creep-age forming process, the stress-elastic/plastic strain relations in the loading and unloading stage, as well as the relation of stress-creep strain in creep-ageing stage are required to be defined in the subroutine. UMAT adopted the algorithm of implicit integration and for VUMAT is explicit integration. For implicit integration, in order to ensure achieving convergence within reasonable iterations, a proper Jacobian matrix J must be provided at the end of each iteration. The Jacobian matrix J is defined as $J = \partial\Delta\sigma / \partial\Delta\varepsilon$, where $\partial\Delta\sigma$ and $\partial\Delta\varepsilon$ are respectively the patrial derivatives of Cauchy stress increment and the strain increment. With a given displacement/load increment, convergence between the Jacobian matrix derived and simulated values need to be checked at each integration iteration. For explicit integration, no convergence check is required and hence the Jacobian matrix is not necessary to be provided.

In this study, to verify the validity of the implemented constitutive model proposed in chapter 5 in ABAQUS, VUMAT is selected as the subroutine to carry the model in simulation. An axisymmetric one element model (CAX4R) with dimension of 10 mm x 5 mm is established in ABAQUS. As demonstrated in Figure 6-1, the model was pinned along the bottom (X axis) along Z direction and axial axis (Z axis) along X direction. The model is subjected to uniaxial stress on the top surface to simulate creep strain evolution of the condition in uniaxial creep-ageing test.



(a) Established element model (b) 180 degrees sweep view

Figure 6-1. Axisymmetric one element model established in ABAQUS under uniaxial stress.

Simulations for uniaxial creep-ageing for 6 h with the same range of stresses adopted in previous tests including 300, 360, 400, 415, 422.5, and 430 MPa were conducted. The simulation results were compared with MATLAB derived stress-creep strain results and demonstrated in Figure 6-2. As can be observed in the figure, good convergences between ABAQUS and MATLAB derived results were achieved under different stresses, indicating the constitutive model was effectively implemented and correctly functioned in the FE simulations.

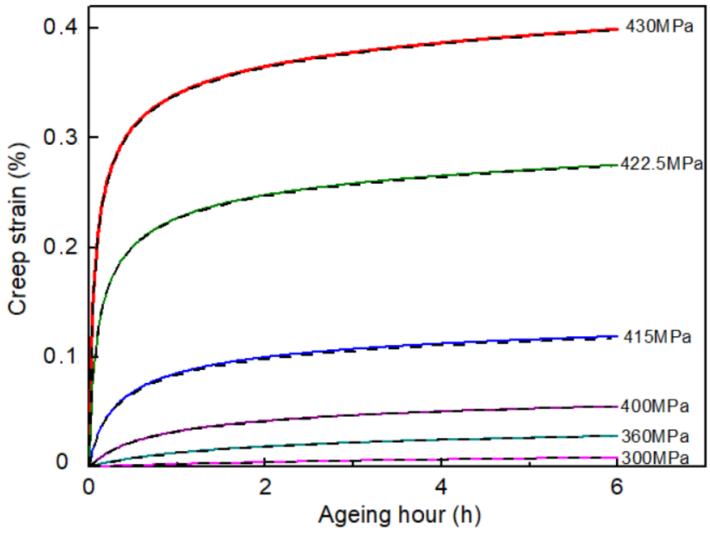


Figure 6-2. ABAQUS simulation results (solid lines) of implemented stress-creep strain constitutive relation for 6 h creep-ageing under different stresses and comparison with MATLAB derived results (dashed lines).

6.3 Process modelling technique

6.3.1 Numerical simulation workflow

A complete creep-age forming simulation includes three stages as loading, creep-ageing, and unloading stage. Considering the characteristics of the stages in CAF and provided subroutines in ABAQUS, different subroutines can be adopted to optimise the simulation of CAF. In this study, two different simulation workflow were adopted to respectively simulate the four-point bending tests and CAF fabrication with the flexible tool. The CREEP subroutine was used for the former and a combination of VUMAT and UMAT subroutine was developed for the latter in this research.

For the workflow of simulation with CREEP subroutine, it can be summarised as:

(a) CAF model is established in ABAQUS CAE interface with proper settings including component dimensions and assembly, material properties input, boundary and loading conditions determination, and simulation step setup.

(b) The established constitutive model is implemented in CREEP subroutine to be called in the creep-ageing stage.

(c) The loading, creep-ageing, and unloading stages are all simulated with ABAQUS implicit algorithm following continuous simulation steps.

The general numerical simulation workflow can be derived as follows and demonstrated in Figure 6-3 as:

(a) CAF model is established in ABAQUS CAE interface with settings the same as (a) in previous CREEP subroutine properly setup.

(b) The loading and creep-ageing stages are simulated in ABAQUS explicit solver with VUMAT.

(c) When VUMAT simulation of the two stages is completed, the results derived at the last simulation step including deforming shape and stress states are transferred to UMAT through ‘IMPORT’ command in ABAQUS as the initial states for UMAT simulation.

(d) Unloading stage is simulated in UMAT subroutine with an implicit solver to obtain the springback

result.

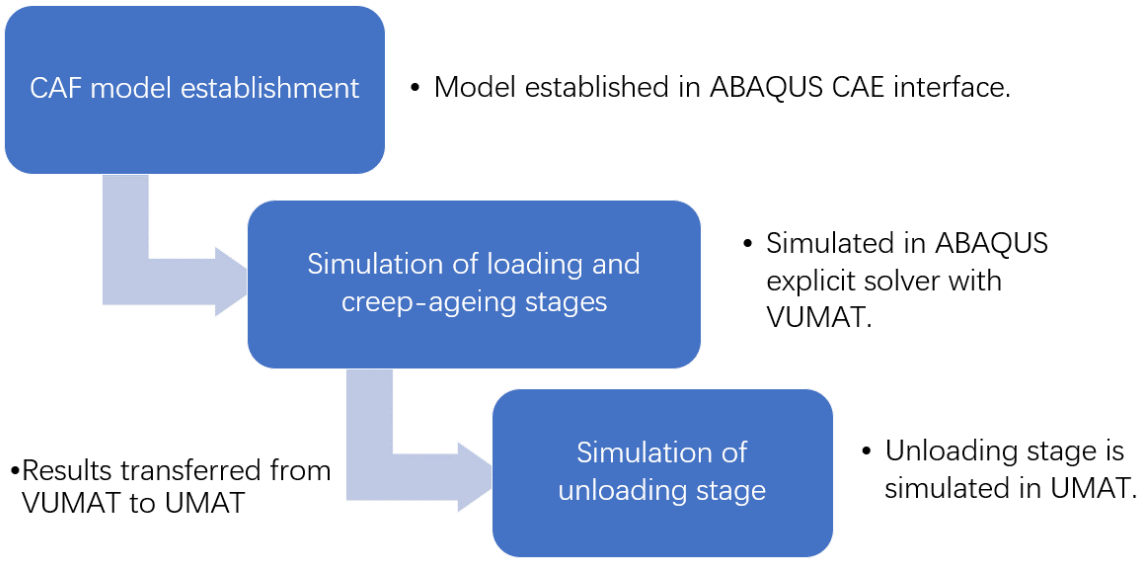


Figure 6-3. Schematic of CAF numerical simulation workflow adopting VUMAT and UMAT subroutine.

6.3.1.1 Simulation with CREEP subroutine

The CREEP subroutine is specially invented to describe the creep behaviour of the material in ABAQUS, which is straightforward that only the equivalent/uniaxial creep strain increment at the end of each integration step is required to be given and the program will automatically calculate the strain increment components in the multiaxial state. The calculation flow chart is illustrated in Figure 6-4, where t_0 and t_1 are respectively the total accumulated time at the beginning and end of the current integration step, Δt is the time length of the integration step. $\dot{\varepsilon}_{cr}$ is the uniaxial creep strain rate in this integration step which can be calculated by applying the constitutive model proposed in Chapter 5, $\Delta\varepsilon_{cr}$ is the uniaxial creep strain increment which is required to be provided to the main solver through this subroutine and can be expressed as $\Delta\varepsilon_{cr} = \dot{\varepsilon}_{cr}\Delta t$.

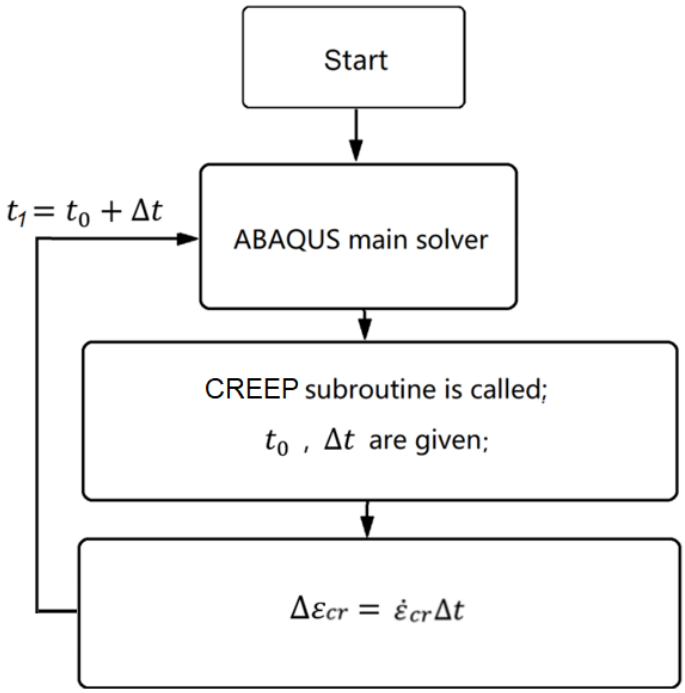


Figure 6-4. Schematic of calculation flow of CREEP subroutine.

6.3.1.2 Simulation with VUMAT subroutine

For simulation with VUMAT subroutine of loading and creep-ageing stages, various constitutive relations are involved.

In the loading stage, the material is initially deformed within the elastic state, in which the linear stress-strain relation is expressed as

$$\Delta\sigma_{ij} = C_{ijkl}\Delta\varepsilon_{kl}^{e} \tag{6-6}$$

where C_{ijkl} is elasticity tensor, $\Delta\varepsilon_{kl}^{e}$ and $\Delta\sigma_{ij}$ are respectively the elastic strain and stress increment components. Eq. (6-6) can be rewritten in the commonly adopted matrix form as

$$\begin{bmatrix}\Delta\sigma_{11}\\ \Delta\sigma_{22}\\ \Delta\sigma_{33}\\ \Delta\sigma_{23}\\ \Delta\sigma_{13}\\ \Delta\sigma_{12}\end{bmatrix} = \begin{bmatrix}\lambda+2G & \lambda & \lambda & 0 & 0 & 0\\ & \lambda+2G & \lambda & 0 & 0 & 0\\ & & \lambda+2G & 0 & 0 & 0\\ & & & G & 0 & 0\\ & symm & & & G & 0\\ & & & & & G\end{bmatrix}\begin{bmatrix}\Delta\varepsilon_{11}\\ \Delta\varepsilon_{22}\\ \Delta\varepsilon_{33}\\ 2\Delta\varepsilon_{23}\\ 2\Delta\varepsilon_{13}\\ 2\Delta\varepsilon_{12}\end{bmatrix} \tag{6-7}$$

where G and λ are the Lame constants. With the derived stress increment $\Delta\sigma_{ij}$, the stress state at the current integration step can be calculated as

$$\sigma_{ij} = \sigma_{ij0} + \Delta\sigma_{ij} = \sigma_{ij0} + C_{ijkl}\Delta\varepsilon_{kl}^{e} \tag{6-8}$$

where σ_{ij0} and σ_{ij} are respectively the stress state components at the beginning of the integration step and the components updated with the stress increment $\Delta\sigma_{ij}$. With increase of the deformation in the loading stage, when the Mises effective stress σ_{e} ($\sigma_{\mathrm{e}} = \left(3S_{ij}S_{ij}/2\right)^{1/2}$, where $S_{ij} = \sigma_{ij} - \delta_{ij}\sigma_{kk}/3$ is the deviatoric stress of the ij component) surpassed the material yield strength σ_{yield}, the material is considered as entering the plastic loading state. The incremental strain-stress constitutive relation of plastic loading state is written as

$$\begin{cases} \Delta\varepsilon_{kl}^{e} = \Delta\varepsilon_{kl}^{t} - \Delta\varepsilon_{kl}^{p} = \Delta\varepsilon_{kl}^{t} - \Delta\varepsilon^{p}\dfrac{3s_{ij}}{2\sigma_{e}} \\ \sigma_{ij} = \sigma_{ij0} + C_{ijkl}\Delta\varepsilon_{kl}^{e} \end{cases} \tag{6-9}$$

where $\Delta\varepsilon_{kl}^{t}$ and $\Delta\varepsilon_{kl}^{p}$ are the incremental components of total strain and plastic strain. Assuming normality and associated flow rule, the relation of $\Delta\varepsilon_{kl}^{p} = \Delta\varepsilon^{p}\frac{3S_{ij}}{2\sigma_{e}}$ can be derived, where $\Delta\varepsilon^{p}$ is effective plastic strain increment. The effective plastic strain increment $\Delta\varepsilon^{p}$ can be calculated by adopting Newton-Raphson method with the objective function written as

$$\begin{cases} RS^{i} = \sigma_{\mathrm{e}} - 3G\,\Delta\varepsilon_{p}^{i} \; - \sigma_{yield}^{i-1} \\ \Delta\varepsilon_{p}^{i+1} = \Delta\varepsilon_{p}^{i} + RS^{i}/(3G + H_{1}) \\ \varepsilon_{p}^{i} = \varepsilon_{p}^{i-1} + \Delta\varepsilon_{p}^{i} \end{cases} \tag{6-10}$$

where RS^{i} is the value of the objective function in the i^{th} Newton-Raphson iteration, G is the Lame elasticity constant, $\Delta\varepsilon_{p}^{i}$ is the trial value of effective plastic strain increment of i^{th} iteration, ε_{p}^{i-1} and ε_{p}^{i} are respectively the plastic strain accumulated in previous $(i-1)^{th}$ iteration and the strain updated in the i^{th} iteration, σ_{yield}^{i-1} is the yield stress at the yield surface of previous $(i-1)^{th}$ iteration which can be determined from the uniaxial tensile stress-strain relation with the determined ε_{p}^{i-1} in previous iteration. H_{1} is the derivative of σ_{yield}^{i-1} which is given in the form as $H_{1} = \Delta\sigma_{yield}^{i-1}/\Delta\varepsilon_{p}^{i-1}$. It should be noticed that for the first iteration, ε_{p}^{1} is calculated following $\varepsilon_{p}^{1} = \varepsilon_{p}^{0} + \Delta\varepsilon_{p}^{1}$ where ε_{p}^{0} equals zero. When the value of RS^{i} is smaller than 1 x 10^{-4} MPa, a proper $\Delta\varepsilon_{p}$ close enough to its true value is considered to be derived after i^{th} iterations.

When the loading stage is completed, the implemented creep function will be called to calculate creep strain and the corresponding stress state in the following creep-ageing stage. By adopting Eq. (6-4) and Eq.(6-5), the stress components in creep-ageing stage can be expressed as

$$\Delta\varepsilon_{ij}^{e} = \Delta\varepsilon_{kl}^{t} - \Delta\varepsilon_{kl}^{p} - \dot{\varepsilon}_{ij}^{cr}\Delta t \tag{6-11}$$

$$\sigma_{ij}' = \sigma_{ij0}' + C_{ijkl}\Delta\varepsilon_{kl}^{e} \tag{6-12}$$

where Δt is the time length of the integration step, σ_{ij0}' is the stress state at the beginning of the integration step in creep-ageing stage, σ_{ij}' is the updated stress components with evolution of creep strain increment $\dot{\varepsilon}_{ij}^{cr}\Delta t$. Also, since the forming sheet is kept at a constant shape in creep-ageing stage, the strain increment components $\Delta\varepsilon_{kl}^{t}$ and $\Delta\varepsilon_{kl}^{p}$ can be defined as zero. Hence Eq. (6-11) can be further expressed as $\Delta\varepsilon_{ij}^{e} = -\dot{\varepsilon}_{ij}^{cr}\Delta t$.

At the end of each integration step, the total accumulated time for simulation is updated as

$$t_1 = t_0 + \Delta t \tag{6-13}$$

where t_1 and t_0 are the total accumulated time at the end and beginning of the current integration step respectively.

The general calculation flow adopting VUMAT subroutine is generalised in Figure 6-5.

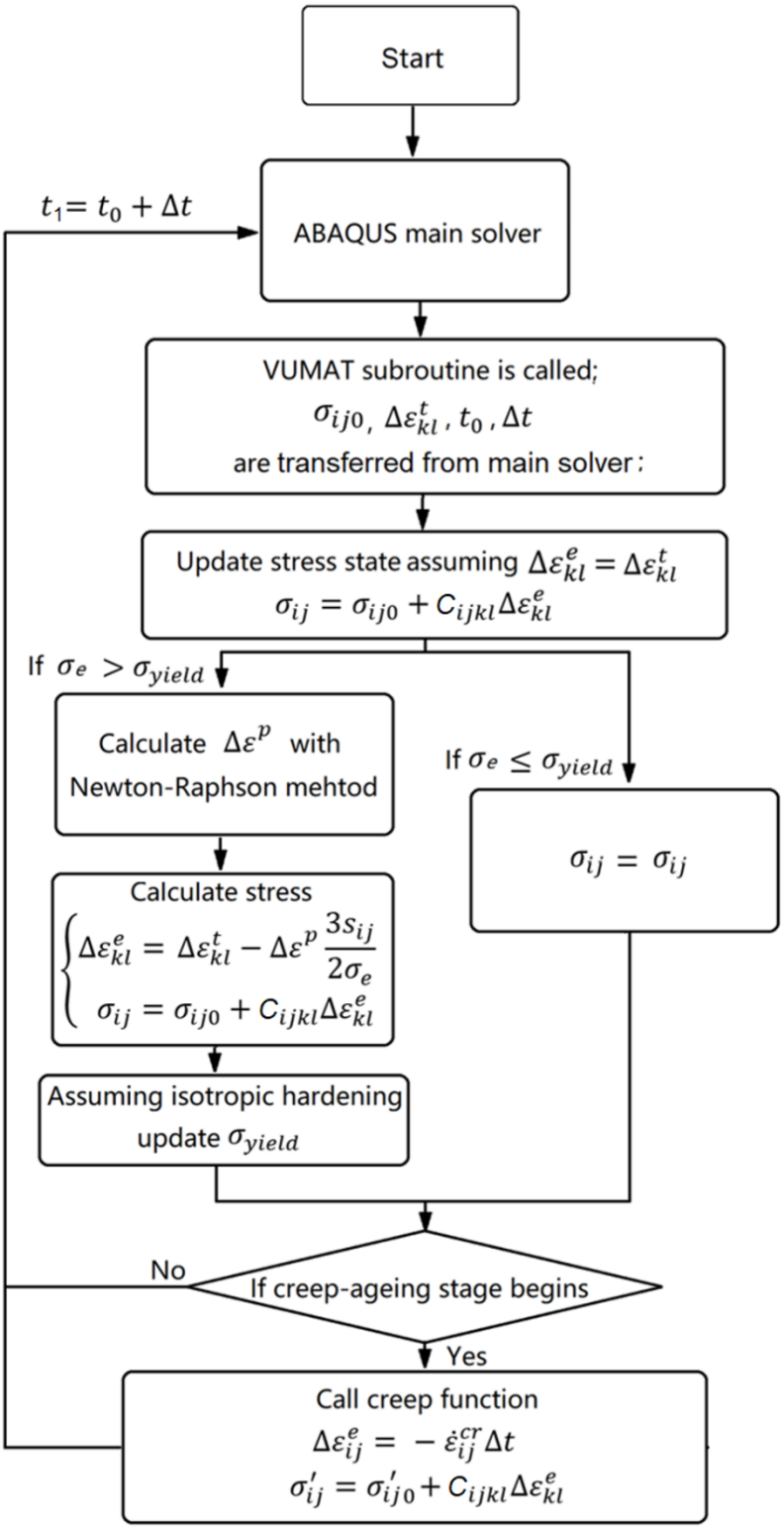


Figure 6-5. Schematic of calculation flow for VUMAT subroutine.

6.3.1.3 Simulation with UMAT subroutine

For the unloading stage in CAF, the happening of springback is driven by recovering of remaining elastic strain in the forming piece after creep-ageing. Hence the springback behaviour in unloading stage can be considered as elastic deformation for stress relaxation and the stress-strain relation in this process can be adequately expressed with the linear elastic constitutive equation as

$$\Delta\sigma_{ij} = C_{ijkl}\Delta\varepsilon_{kl}^{t} = C_{ijkl}\Delta\varepsilon_{kl}^{e} \tag{6-14}$$

It should be noted that in the unloading stage, $\Delta\varepsilon_{kl}^{t}$ is equivalent to $\Delta\varepsilon_{kl}^{e}$ with a relation of $\Delta\varepsilon_{kl}^{t} = \Delta\varepsilon_{kl}^{e}$. When adopting UMAT and the implicit solver in simulation, a Jacobian matrix $J = \partial\Delta\sigma/\partial\Delta\varepsilon$ is required to be defined to help converge. Based on Eq. (6-14), with the linear elastic stress-strain relation, C_{ijkl} can be adopted as a proper Jacobian matrix in the simulation of the unloading stage with UMAT subroutine.

Figure 6-6 illustrates the general calculation flow by adopting UMAT subroutine to simulate the unloading process. σ_{ij0} and t_0 are respectively the stress state components and total accumulated time at the end of previous integration step.

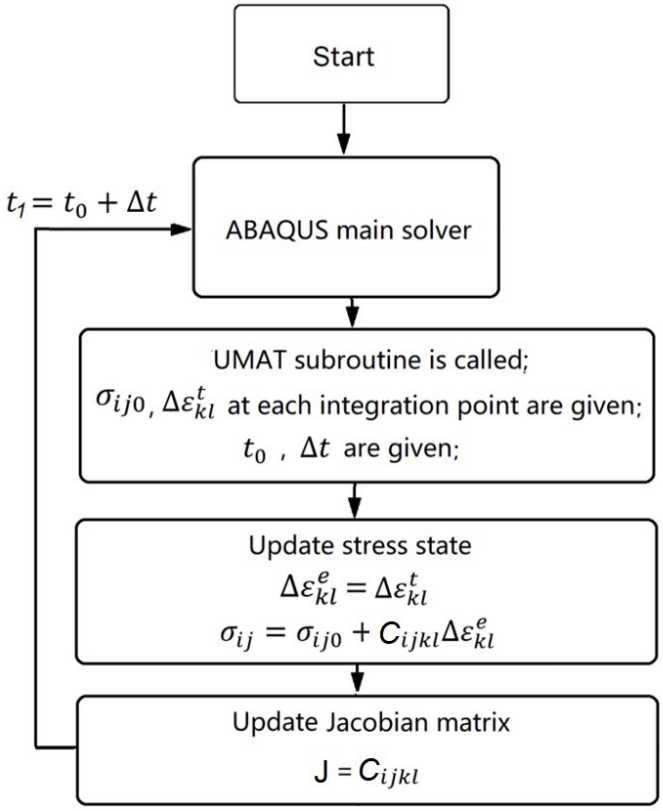


Figure 6-6. Schematic of calculation flow adopting UMAT subroutine to simulate unloading stage.

6.3.2 Simulation models setup

6.3.2.1 FE model setup of four-point bending CAF

Finite element (FE) models were established to simulate four-point bending CAF tests as described in section 3.6. The model was established in three-dimensional space based on the setup and dimensions in Figure 3-1. The schematic and dimension of the model is demonstrated in Figure 6-7. In the figure, RP stands for the reference point of the cylinder.

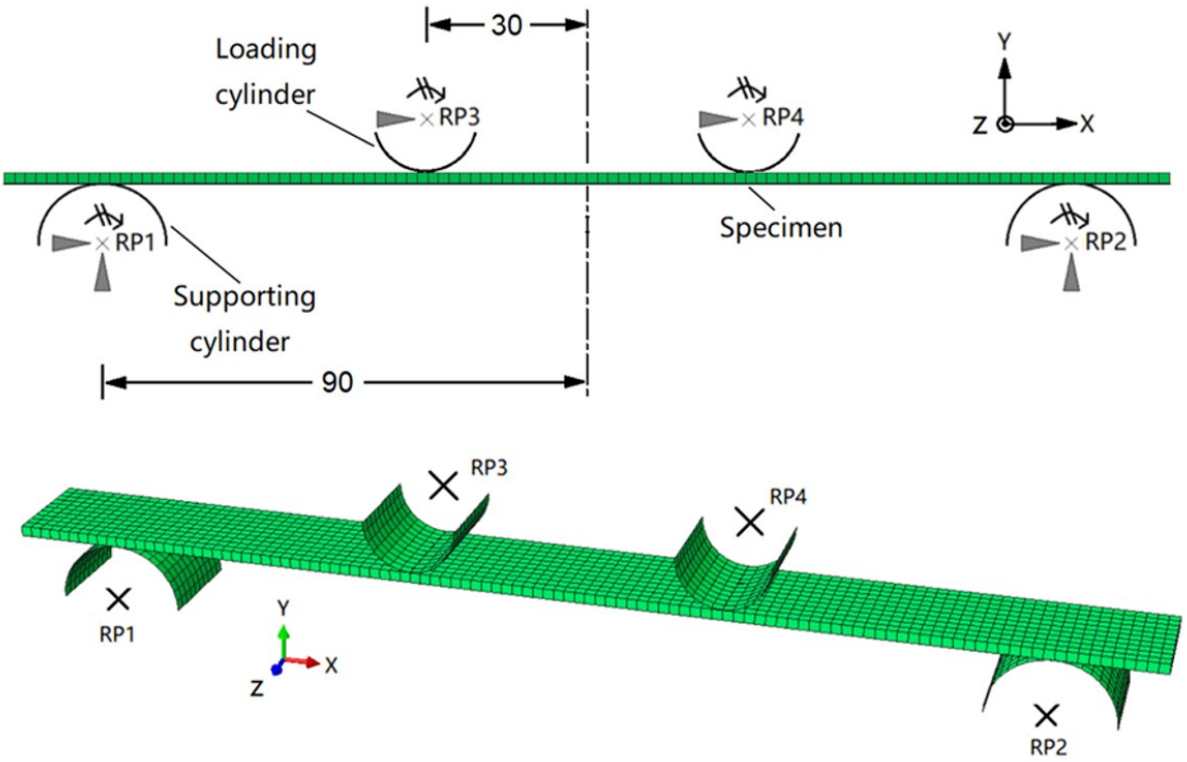


Figure 6-7. Schematic of established FE model for single curvature four-point bending CAF test, dimension in mm.

As demonstrated in Figure 6-7, the model was assembled with three components including specimen, loading and supporting cylinders. The upper and lower cylinders were simplified to be half with dimensions demonstrated in Table 6-1. The part dimensions of the model are summarised in Table 6-1.

Table 6-1. Summary of dimensions of FE Model parts.

Thickness (mm)	Specimen dimension (mm)	Loading Cylinder (mm)	Supporting Cylinder (mm)
2	220 x 2	Ø 18	Ø 24
4	220 x 4	Ø 18	Ø 24
6	220 x 6	Ø 18	Ø 24

Tensile properties of the material are adopted from experimental results in Table 4-2. The stress-strain curve at 143 °C as represented in Figure 4-1 was implemented in the Material Property to reflect the plastic behaviour of the specimen. Loading and supporting cylinders were considered rigid without definition. The generalised information for material properties is listed in Table 6-2.

Table 6-2. Information of the material properties.

Parts	Young's modulus (MPa)	Poisson's ratio	Plastic behaviour
Forming specimen	69800	0.3	Defined in 'Material Property'
Loading and supporting cylinders	N/A	N/A	N/A

As shown in the enlarged figure in Figure 6-7, the specimen was composed of S4R shell element with mesh size of 2 x 2 mm and 11 integration points through the thickness direction. The loading and supporting cylinders were rigid bodies composed of discrete rigid elements. The detailed information for the element and mesh is listed in Table 6-3.

Table 6-3. FE model element information.

Thickness (mm)	Specimen element type	Element dimension (mm)	Cylinder element type	Cylinder element dimension (mm)
2	S4R	2x2	Discrete rigid	2
4	S4R	2x2	Discrete rigid	2
6	S4R	2x2	Discrete rigid	2

As can be observed in Figure 6-7, for the loading cylinders, freedom for all directions apart from displacement along Y (U_Y) axis were fixed, allowing the loading cylinders only move parallelly along Y axis. The supporting cylinders were completely fixed in all directions. Surface contact was setup between the cylinders and specimen. The contact was modelled with penalty tangential behaviour with a friction coefficient of 0.25. The summarised information of boundary conditions and contact behaviour is listed in Table 6-4.

Table 6-4. Summary of setup of boundary conditions and surface contact.

Part	Boundary conditions	Surface contact	Friction coefficient
Loading cylinder	All fixed apart from U_Y	Cylinder-specimen	0.25
Supporting cylinder	All fixed	Cylinder-specimen	0.25
Specimen	None	Cylinder-specimen	0.25

The numerical simulation of CAF with four-point bending is composed of three stages, i.e. loading stage, creep-ageing stage, and unloading stage:

(a) Loading stage: The specimen is loaded through downward displacements exerted by loading

cylinders. Loading stage ends when the designed loading displacement is achieved and the duration of this stage is set to be 1 s.

(b) Creep-ageing stage: The specimen is kept at the designed loading displacement to allow accumulation of creep deformation. The duration of this stage is set as 5 h.

(c) Unloading stage: The specimen is unloaded to obtain the final deformed shape after springback. The duration of this stage is 1 s.

6.3.2.2 FE model setup of multipoint bending CAF

The schematic of the FE simulation model for CAF of a single curvature panel with multipoint flexible tool simulation is demonstrated in Figure 6-8. A two-dimensional FE model in the XY plane with a unit depth of 1 mm along the Z axis was established. The model is composed of three parts including the loading and supporting pins, splines, and specimen. The dimension of the model is consistent with the flexible tool introduced in Figure 3-17c. Compared to the experiment setup illustrated in Figure 3-17, for simplification of this FE model, the pins were considered as half cylinders with the same diameter of the pins. The dimensions of the parts adopted in the model are summarised in Table 6-5.

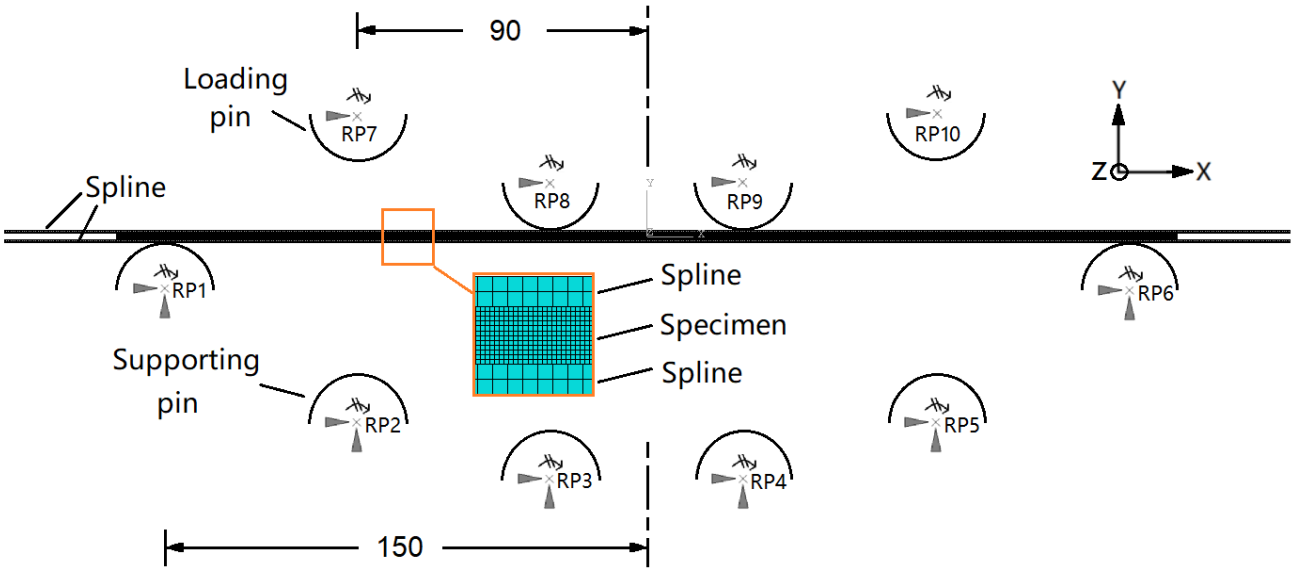


Figure 6-8. Schematic of simulation model for flexible tool CAF of single curvature panel, dimension in mm. RP stands for the reference and centre point of the pin.

Table 6-5. Summary of parts dimension.

Thickness (mm)	Specimen dimension (mm)	Spline dimension (mm)	Pin dimension (mm)
2	335 x 2	400 x 1	Ø 30
4	320 x 4	400 x 1	Ø 30

The same specimen material properties for CAF of four-point bending was adopted in this model as demonstrated in Table 6-6. Considering the steel splines only functioned as load/displacement transfer tools in the model, they were assumed to be purely linear elastic with Young's modulus of 206000 MPa for steel with Poisson's ratio of 0.3. The pins were assumed to be rigid with no physical material properties. Table 6-6 gives the generalised information of material property of the parts created in this model.

Table 6-6. Information of material property.

Parts	Young's modulus (MPa)	Poisson's ratio	Plastic behaviour
Specimen	69800	0.3	Defined in VUMAT
Steel splines	206000	0.3	Nonapplicable
Loading and supporting pins	N/A	Nonapplicable	Nonapplicable

As shown in the enlarged figure in Figure 6-8, both the specimen and splines were composed of four-node plane strain elements with reduced integration (CPE4R). The pins were composed of rigid shell elements. The generalised information of element type and dimensions for the created parts were demonstrated in Table 6-7.

Table 6-7. FE model element information.

Measured thickness (mm)	Specimen/spline element type	Specimen element (mm)	Spline element (mm)	Cylinder element type	Cylinder element (mm)
2	CPE4R	0.2x0.2	0.5x0.5	Discrete rigid	0.5
4	CPE4R	0.4x0.4	0.5x0.5	Discrete rigid	0.5

As demonstrated in Figure 6-8, for supporting pins, the same boundary conditions as those for four-point bending were applied on the reference points which were completely fixed with displacements in directions along the X and Y axis and rotation around the Z axis (U_x=0; U_y=0; R_z=0). For loading pins, the same boundary conditions (U_x=0; R_z=0) were applied to allow the loading pins can only

move parallel along the Y axis. Surface contact was respectively setup between pins and splines, and between splines and specimen. The contact was modelled with penalty tangential behaviour with a friction coefficient of 0.25. Summarised information of boundary conditions and contact behaviour is listed in Table 6-8.

Table 6-8. Summary of setup of boundary conditions and surface contact.

Part	Boundary conditions	Surface contact	Friction coefficient
Loading pins	U_x=0; R_z=0	Pins-splines	0.25
Supporting pins	U_x=0; U_y=0; R_z=0	Pins-splines	0.25
Splines	None	Pins-splines/ Splines-specimen	0.25
Specimen	None	Splines-Specimen	0.25

The numerical simulation of CAF with a multipoint flexible tool is also composed of three stages, i.e., loading stage, creep-ageing stage, and unloading stage:

(a) Loading stage: The specimen is loaded through downward displacements exerted by loading pins. The loading stage ends when the designed loading displacement is achieved and the duration of this stage is set as 1 s.

(b) Creep-ageing stage: The specimen is kept at the designed loading displacement to allow accumulation of creep deformation. The duration of this stage is set as 5 h.

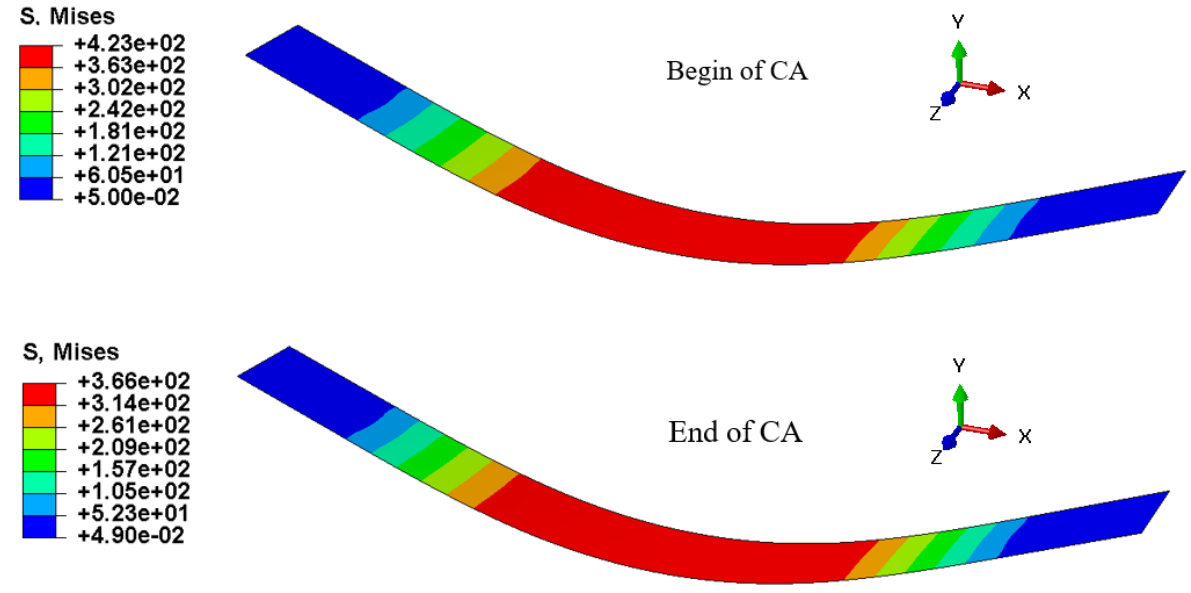
(c) Unloading stage: The specimen is unloaded to obtain the final deformed shape after springback. The duration of this stage is set as 1 s.

6.4 Simulation results

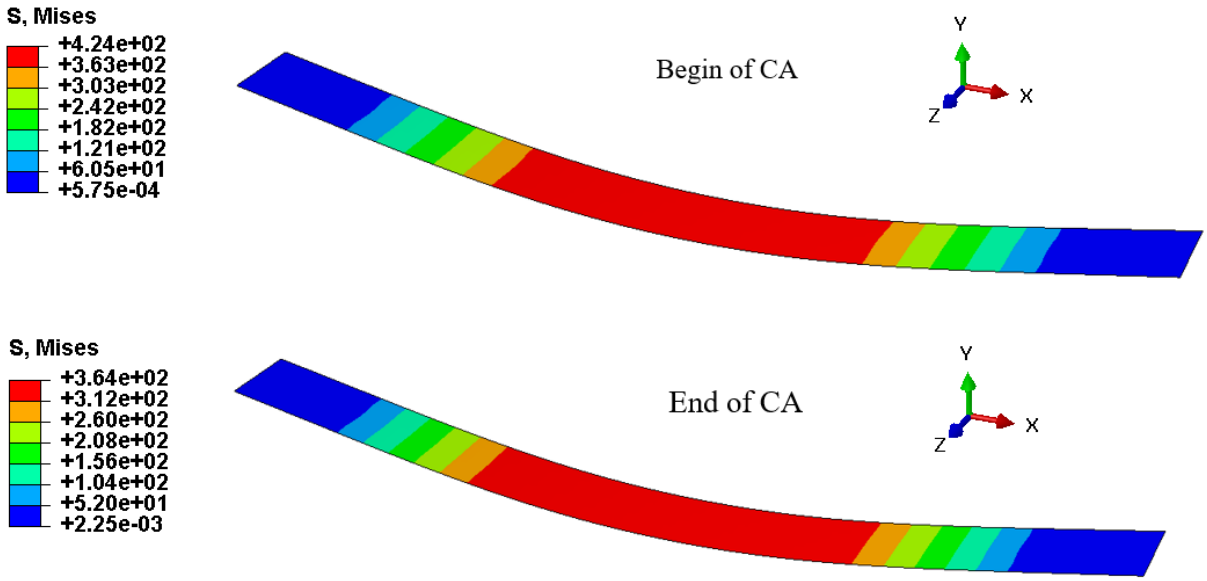
6.4.1 Simulation results of four-point bending CAF tests with the same maximum surface stress within elastic region

Numerical simulations were conducted based on the information in Table 3-6, the thicknesses of 2, 4, and 6 mm models were established as described in previous section 6.3.2.1. The simulation results of the stress relaxation and creep strain evolution from the beginning to the end of creep-ageing (CA) stage are respectively shown in Figure 6-9 and Figure 6-10.The deformed deflection results are demonstrated in Figure 6-11. The stress/creep strain in the surface layer are exhibited in

the results.

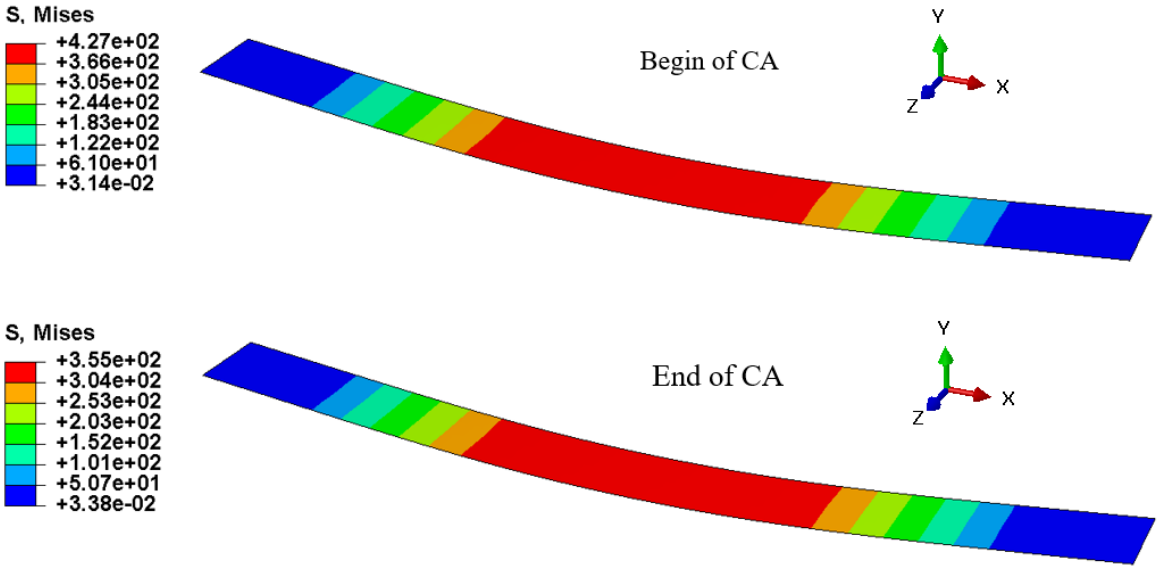


(a) 2 mm



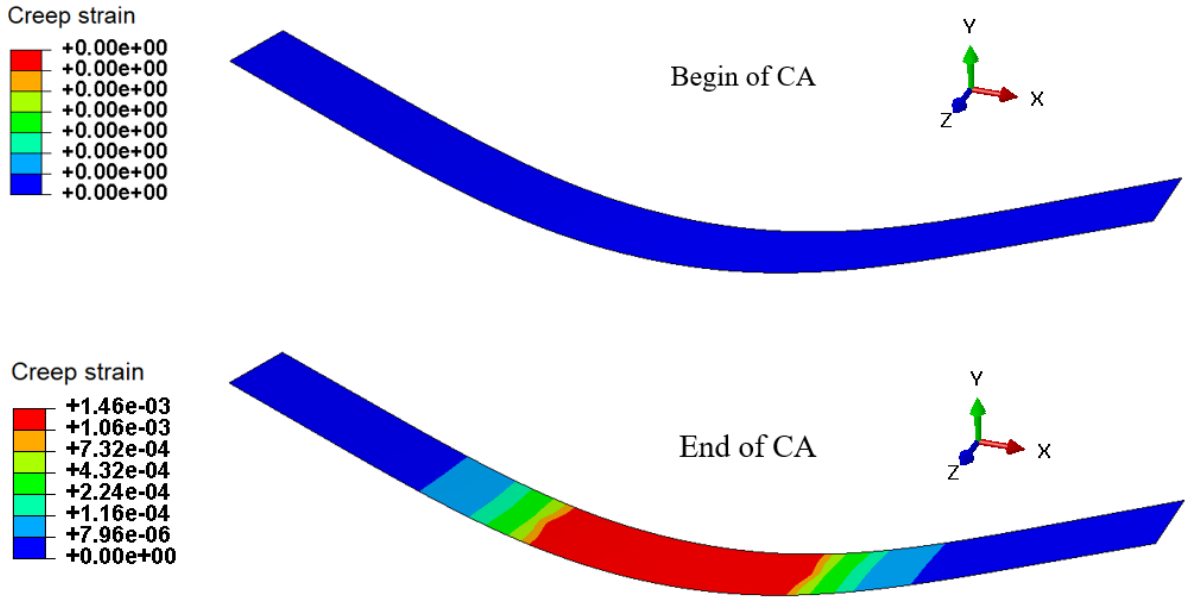
(b) 4 mm

Figure 6-9. Simulation results of stress relaxation with the same maximum surface stress within elastic region (unit: MPa).



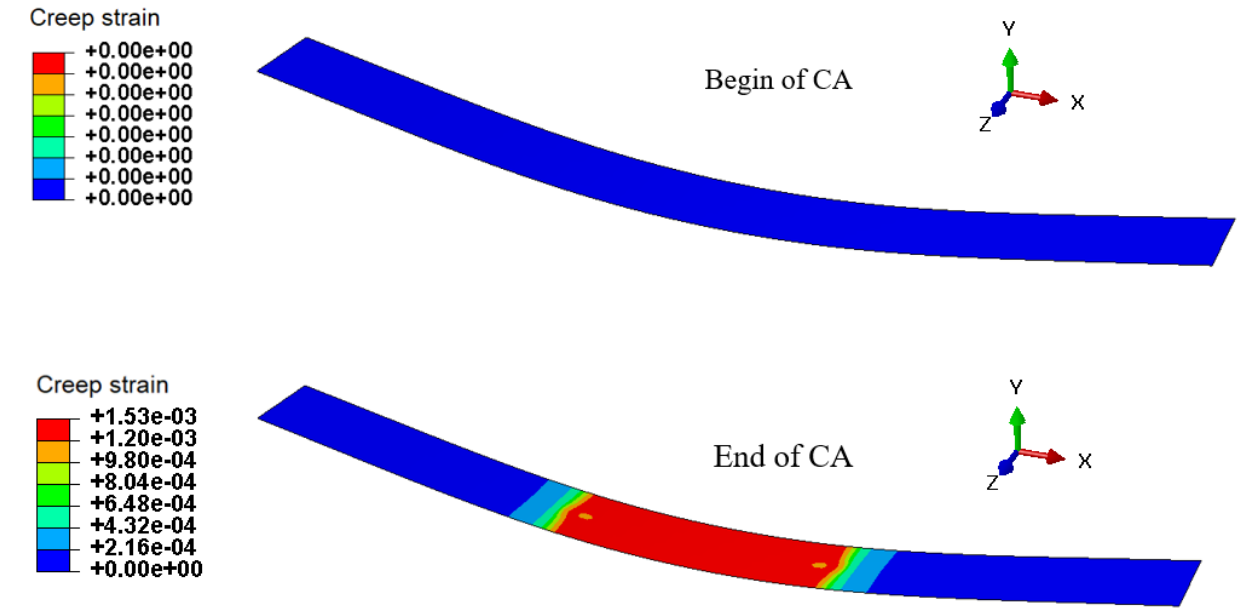
(c) 6 mm

Figure 6-9. (*continued*).

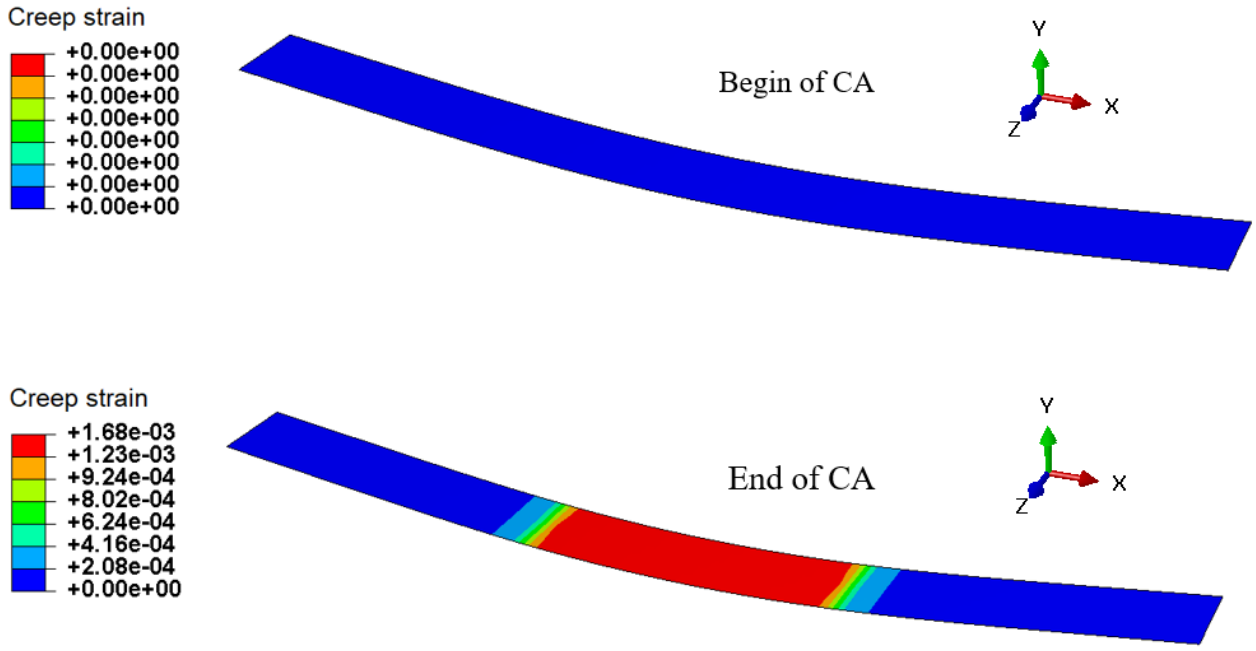


(a) 2 mm

Figure 6-10. Simulation results of creep strain evolution with the same maximum surface stress within elastic region.

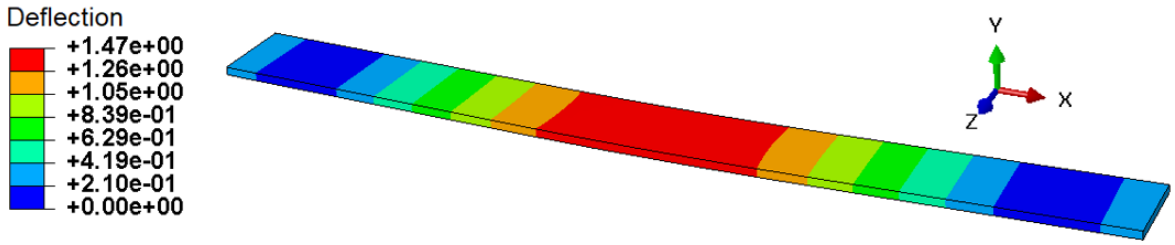


(b) 4 mm

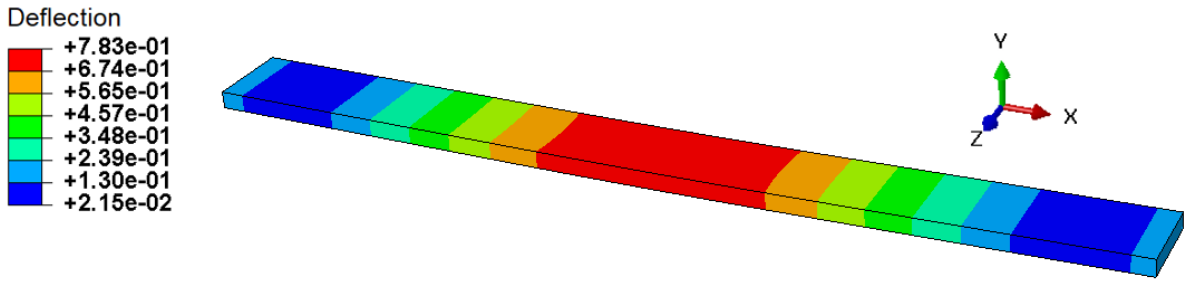


(c) 6 mm

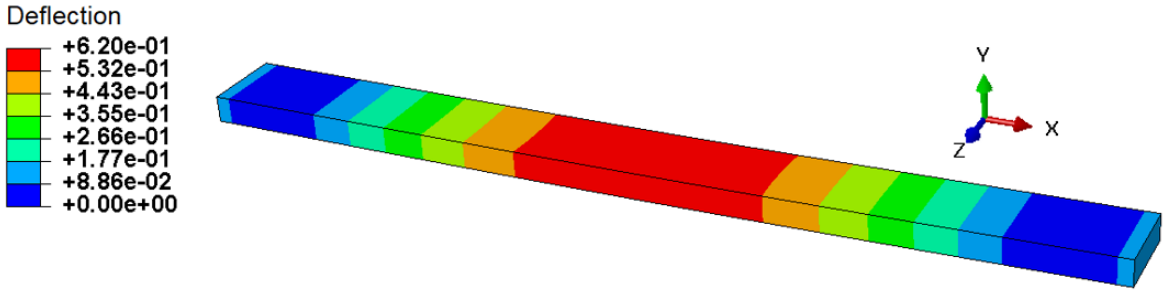
Figure 6-10. (*continued*).



(a) 2 mm



(b) 4 mm



(c) 6 mm

Figure 6-11. Deformed deflection simulation results of four-point bending CAF (unit: mm).

As the simulation results shown in Figure 6-9 and Figure 6-10, the induced stress and creep strain were mostly generated between the two loading cylinders. Similar stress values ranging from 423 to 427 MPa were obtained when the loading is completed for the three thicknesses as the numerical simulation predicted stress results shown in Figure 6-9. After 5 h creep-ageing, the stresses dropped to the values in the range from 366 to 355 MPa. Similar values of accumulated creep strain were induced in creep-ageing in the range from 1.46% to 1.68% can be observed in Figure 6-10. It can also be noticed that with the higher stress induced at the end of loading stage, a higher value of the reduced

stress due to relaxation and the creep strain were obtained in the subsequent 5h creep-ageing stage.

With the obtained simulation results of final deflection for the three thicknesses presented in Figure 6-11, the springback percentage can be calculated following the Eq. (4-3) (the initial deflection d_{id} was not considered in the numerical simulation with the value of zero). As the results demonstrate in in Figure 6-12, when comparing with the experimental results of the springback percentage, satisfying convergence is achieved with a maximum error of 0.03 in for the 6 mm specimen.

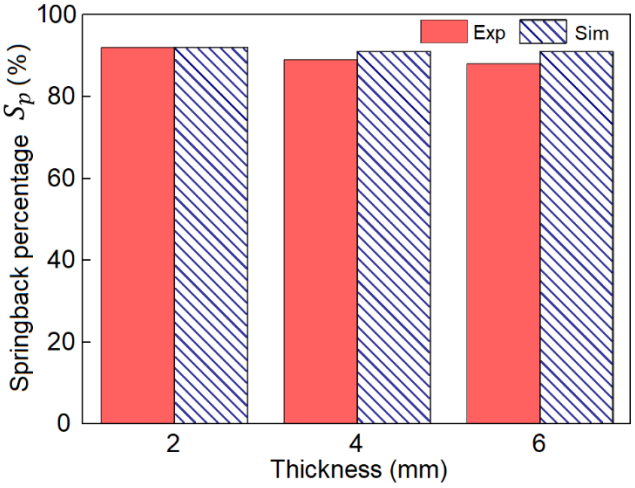
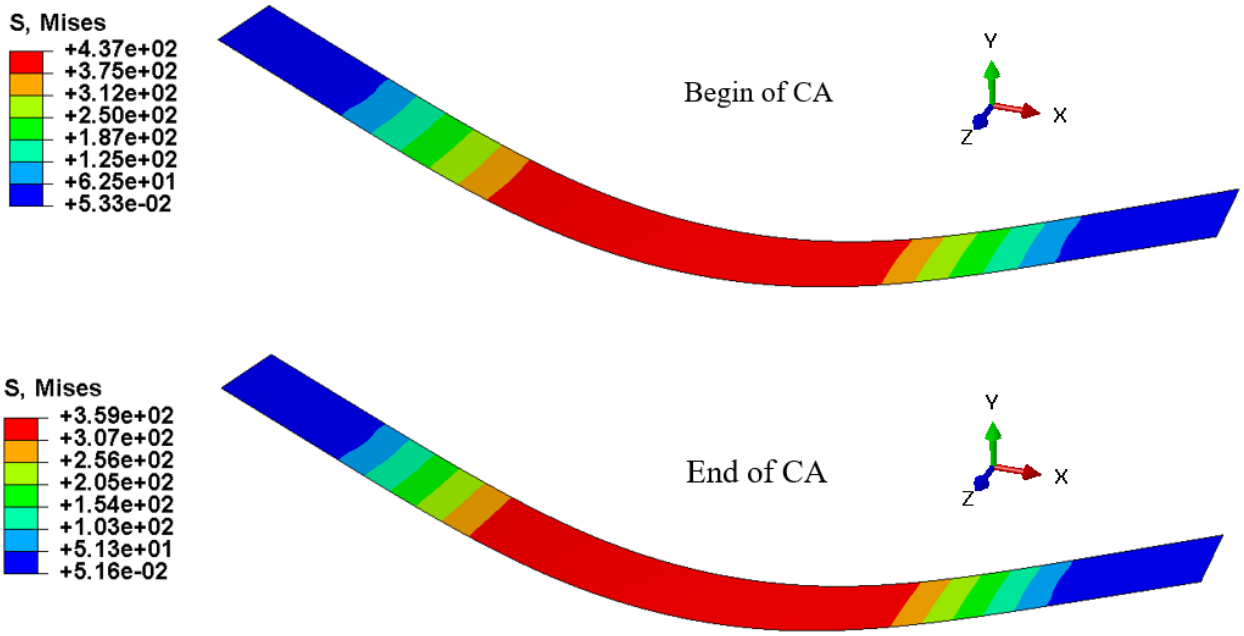


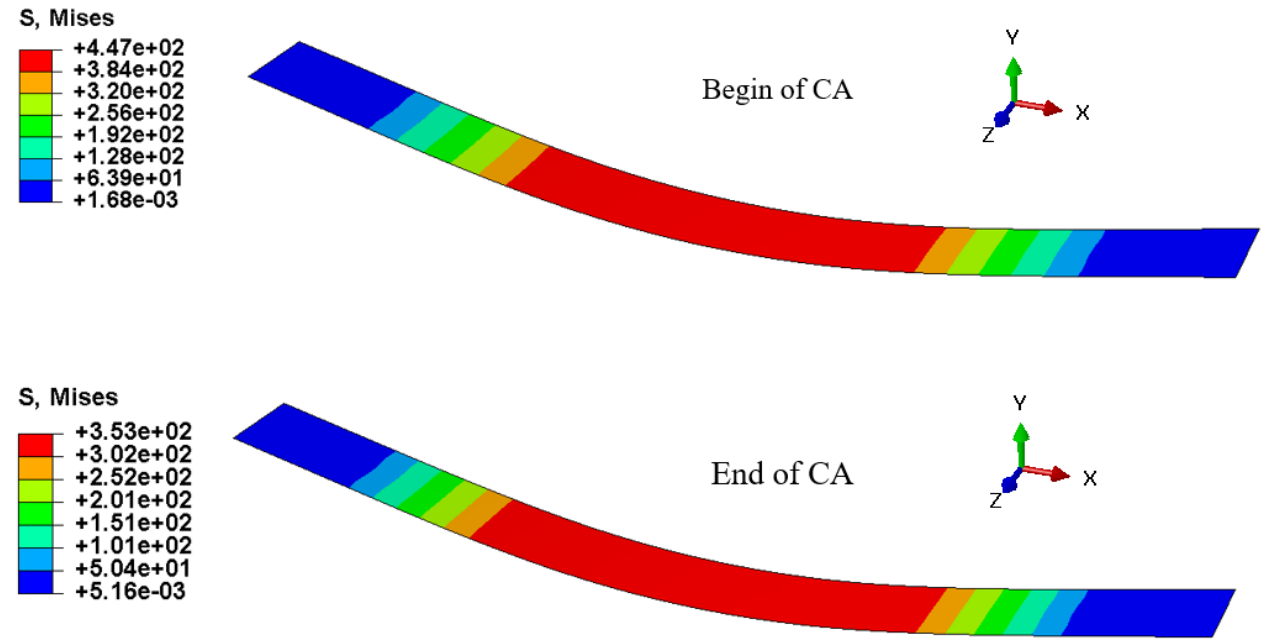
Figure 6-12. Comparison of the springback results of experiment and simulation (Exp stands for experiment and Sim stands for simulation).

6.4.2 Simulation results of four-point bending CAF tests with target curvature

The simulation results of the stress relaxation and creep strain evolution from the beginning to the end of creep-ageing stage are respectively shown in Figure 6-13 and Figure 6-14. The deformed deflection results are demonstrated in Figure 6-15. Similar to the results demonstrated in section 6.4.1, the surface stress/creep strain are presented in the results.

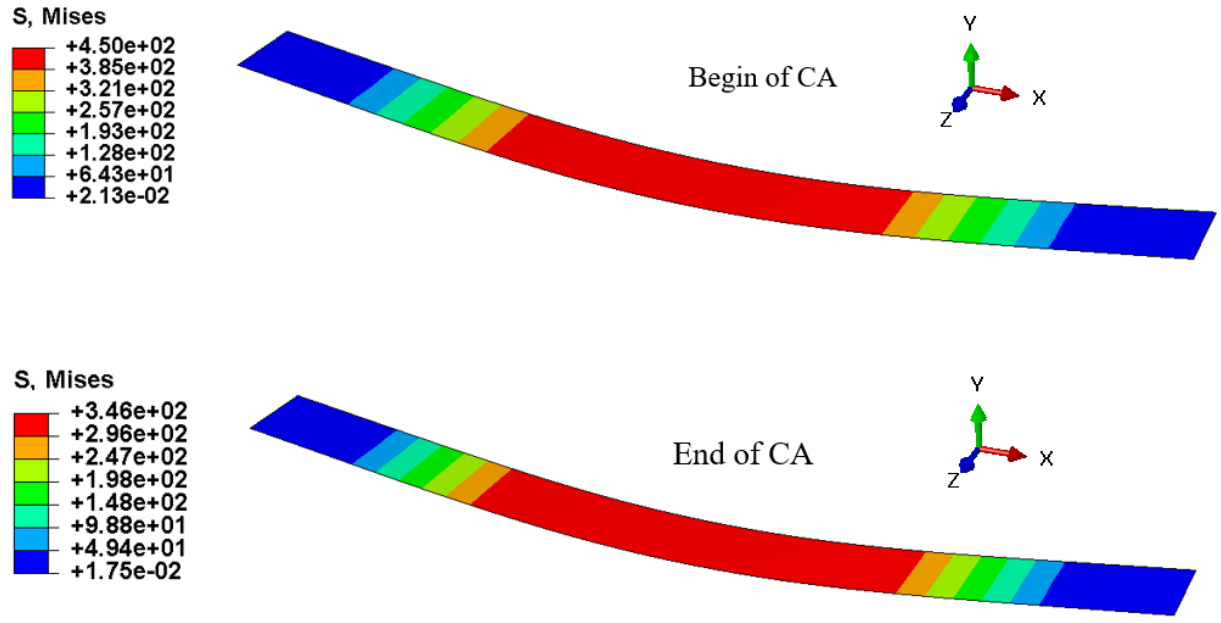


(a) 2 mm



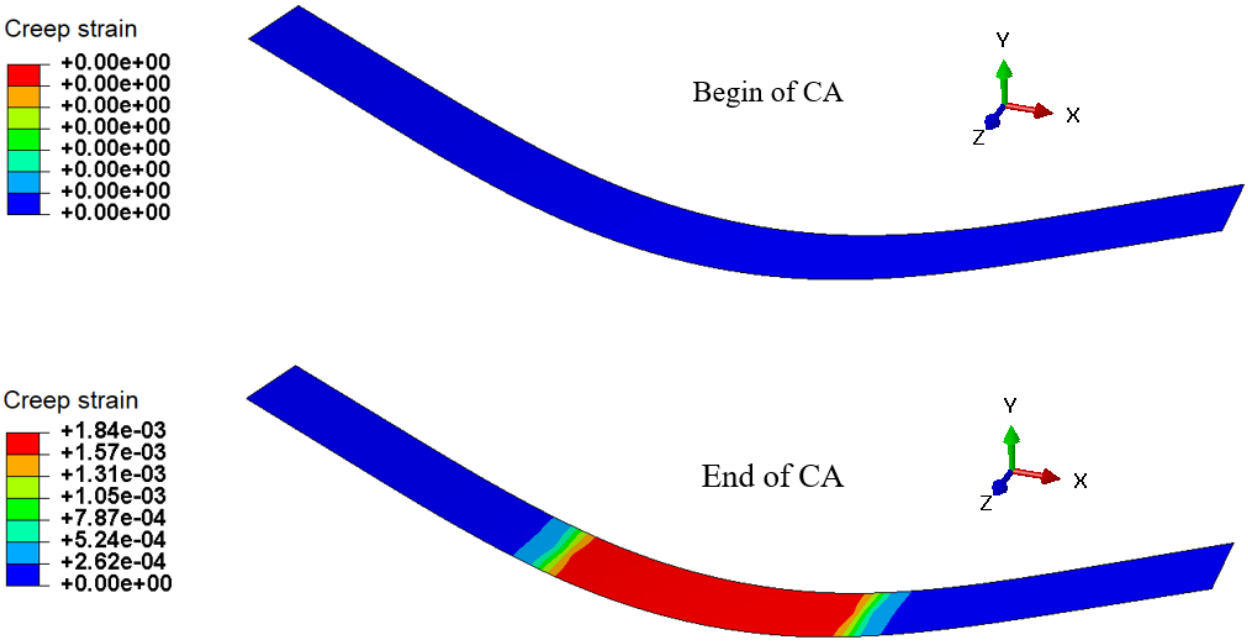
(b) 4mm

Figure 6-13. Simulation results of stress relaxation with target curvature (unit: MPa).



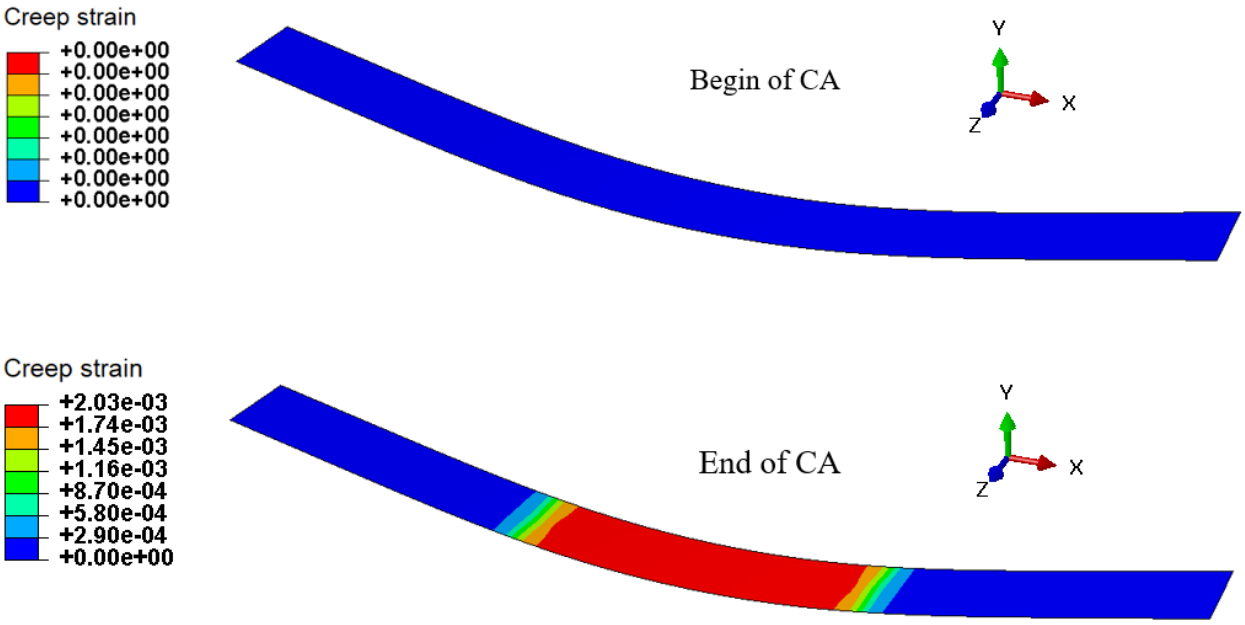
(c) 6 mm

Figure 6-13. (*continued*).

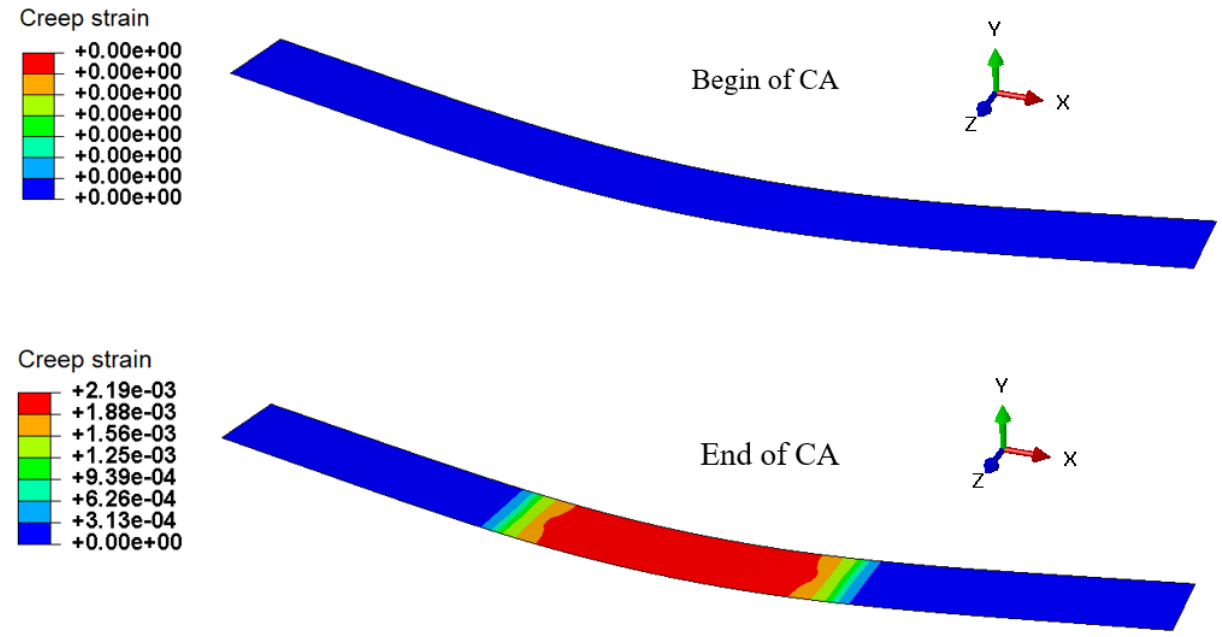


(a) 2 mm

Figure 6-14. Simulation results of creep strain evolution with target curvature.

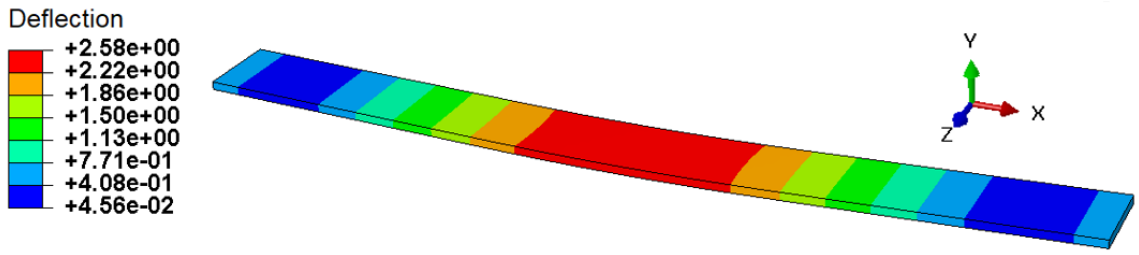


(b) 4 mm

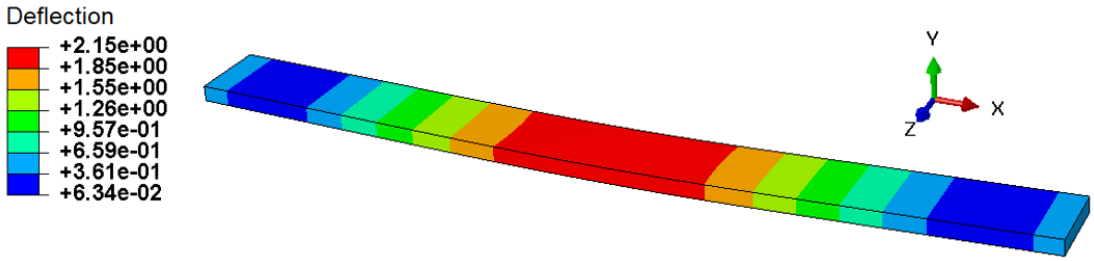


(c) 6 mm

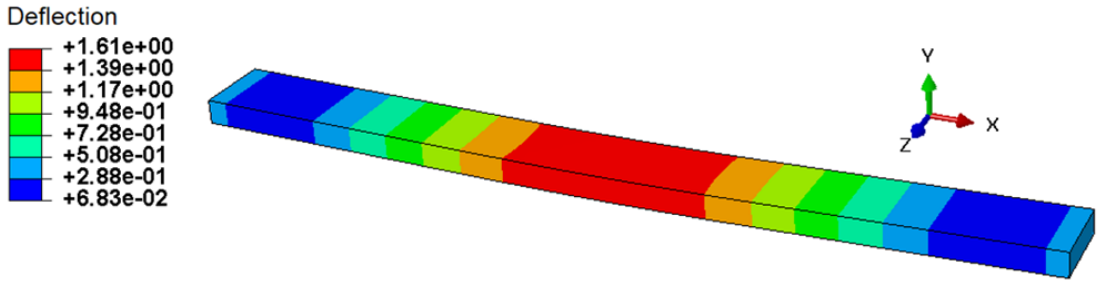
Figure 6-14. (*continued*).



(a) 2 mm



(b) 4 mm



(c) 6 mm

Figure 6-15. Deformed deflection results of four-point bending CAF with target curvature (Unit: mm).

As shown in Figure 6-13, the predicted stresses at the end of loading fell into the range from 437 to 450 MPa, with the corresponding relaxed stress obtained in the range from 346 to 359 MPa. Similar to the trend observe in previous section 6.4.1, with a higher stress induced at the end of loading stage, an increased amount of reduced stress and creep strain were resulted in the subsequent creep-ageing. In addition, it can be noticed that with the increasing of loading displacement, the values of the stress induced at the end of loading stage, as well as the creep strain obtained at the end of creep-ageing stage were increased when compared with the results of the same thicknesses shown in Figure 6-9 and Figure 6-10 in previous section.

The comparison of springback percentage between experiment and simulation result is demonstrated

in Figure 6-16. As manifested in the figure, satisfying convergence between the results of experiment and simulation were obtained with a maximum error of 0.03 for the thickness of 2 mm.

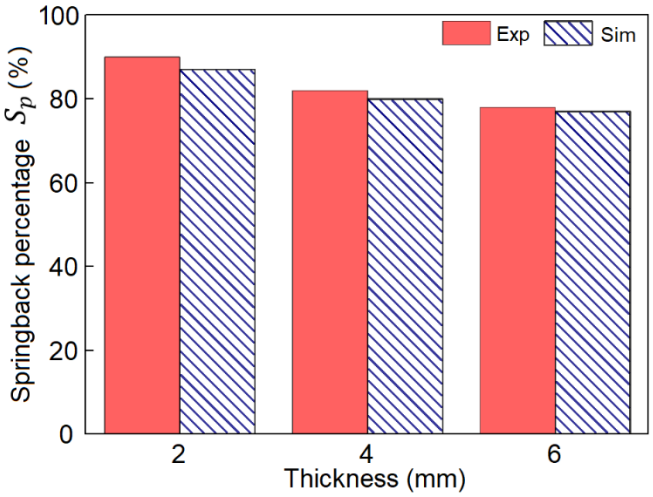
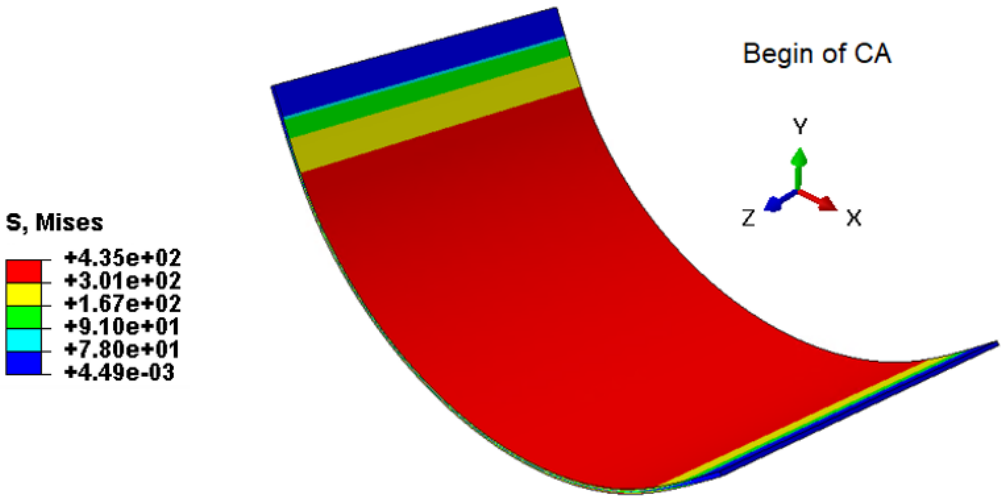


Figure 6-16. Comparison of the springback results of experiment and simulation.

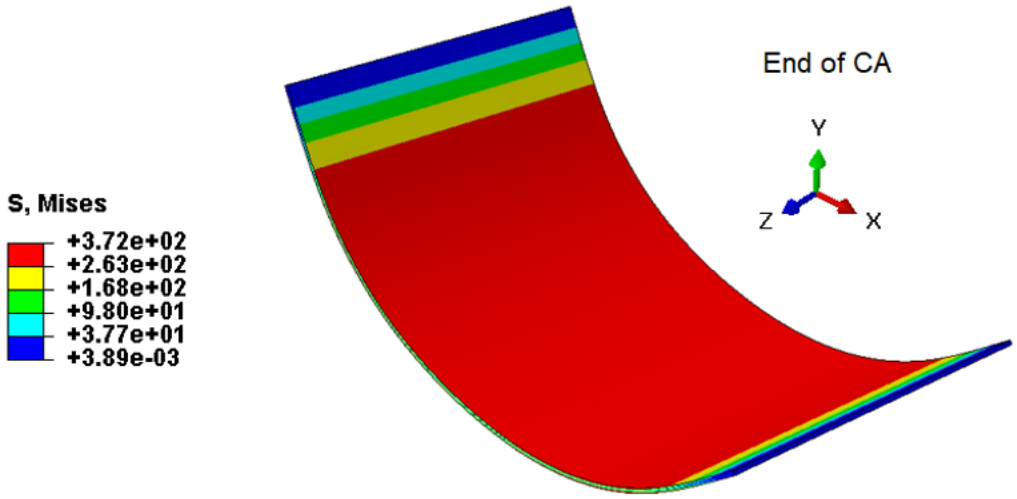
6.4.3 Simulation results of CAF adopting the multipoint flexible tool

The numerical simulation results of stress relaxation for CAF adopting the multipoint flexible tool is demonstrated in Figure 6-17. The deformed deflection results are shown in Figure 6-18.

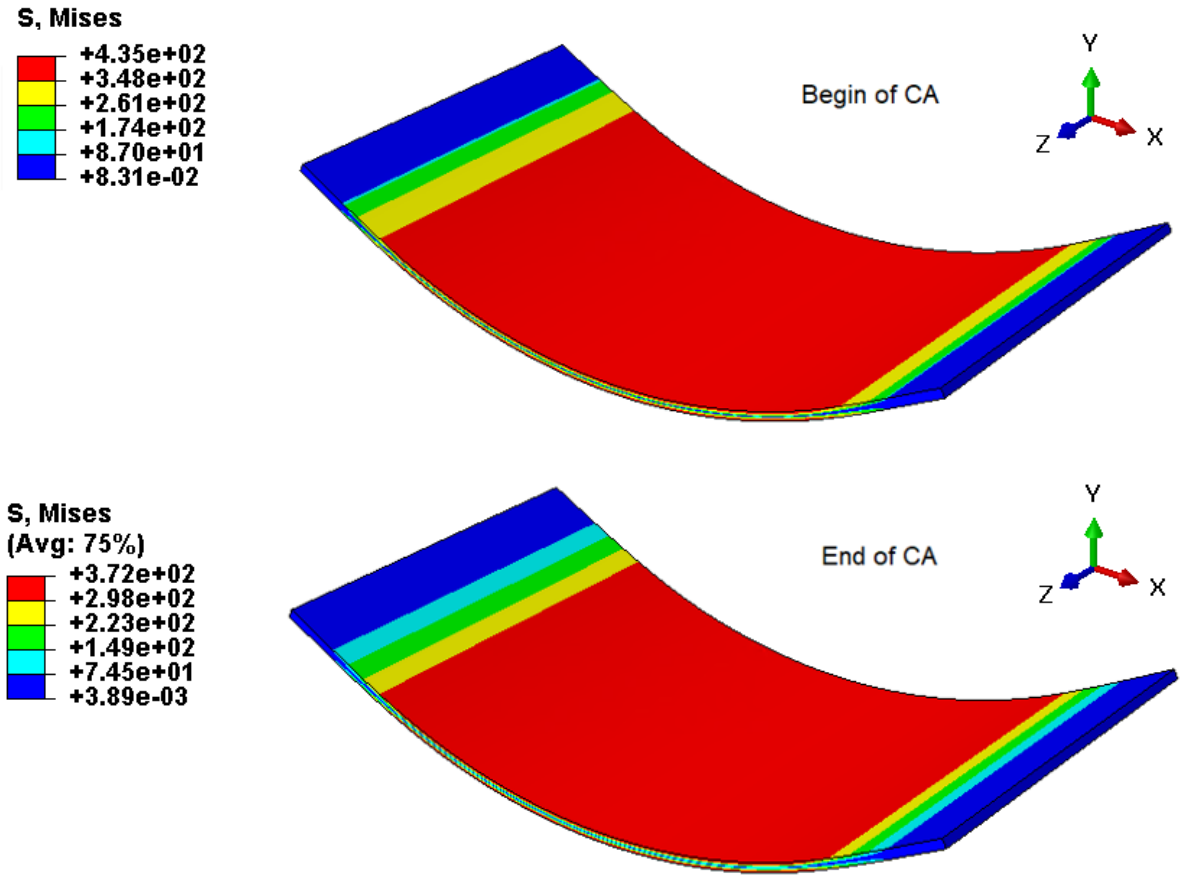


(a) 2 mm

Figure 6-17. Simulation results of stress relaxation from the beginning to the end of creep-ageing (unit: MPa).

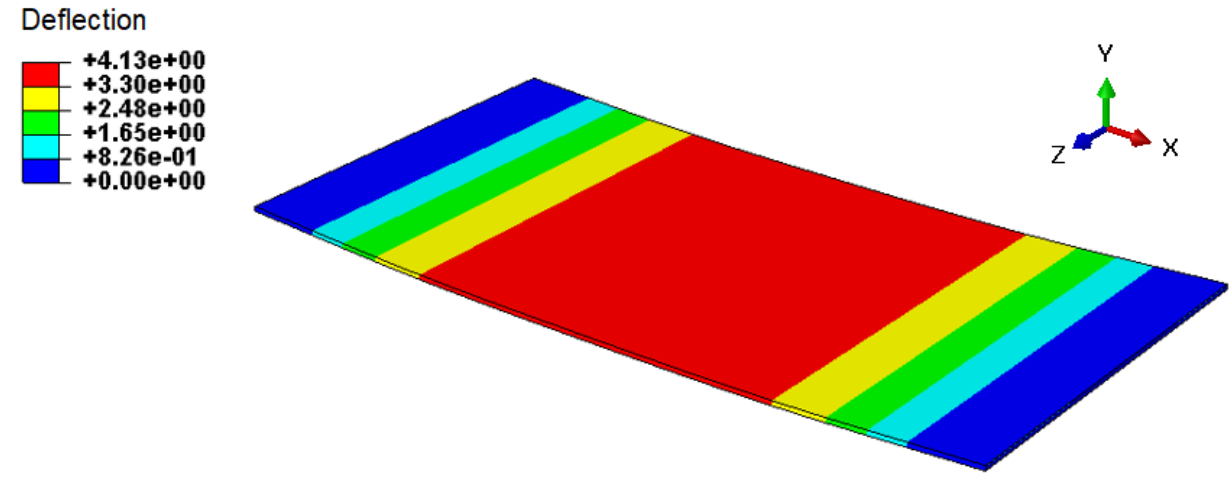


(a) 2 mm

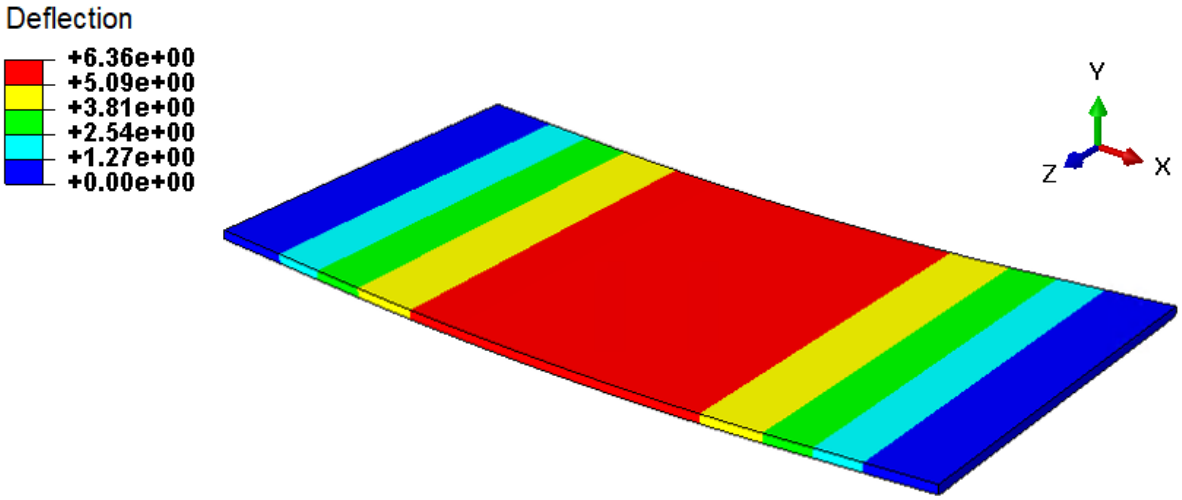


(c) 4 mm

Figure 6-17. (*continued*).



(a) 2 mm



(b) 4 mm

Figure 6-18. Simulation results of deformed deflection (unit: mm).

As the deformed deflection results demonstrated in Figure 6-18, for numerical simulation of CAF fabrication of sheets with target curvature adopting the flexible tool, prediction error exists with the maximum value of 1.5 mm for the sheet of 2 mm thickness when compared with the target deflection of 5.63 mm. Hence an appropriate compensation method to optimise the existing prediction error is required and will be further discussed in next chapter.

6.5 Summary

In this section, the method to extend the established uniaxial creep-ageing constitutive model to

multiaxial condition is introduced. The established model has been implemented in the VUMAT subroutine of ABAQUS and the simulation results for the strain evolution of uniaxial creep-ageing under different stresses has been verified with the results obtained from MATLAB.

The numerical simulation workflow to simulate different stages in CAF including the loading, creep-ageing, and unloading is demonstrated. Detailed information of the simulation model is also provided. With the simulation results of the deformed deflection for four-point bending CAF tests, the springback percentage has been calculated and compared with the experimental derived percentage with satisfying results: a maximum error springback percentage of 0.03 was obtained for both the four-point bending within elastic range and with target curvature. However, for numerical simulation of CAF sheets fabrication with target curvature adopting the flexible tool, prediction error exists with a maximum value of 1.5 mm when compared with the target deflection of 5.63 mm. Hence a proper method to compensate this observed prediction error is required and will be proposed and discussed in next chapter.

Chapter 7

A closed-form solution for springback prediction and compensation

7.1 Introduction

Due to the required high stress in creep-ageing for the Al-Li alloy and large deformation in loading stage, the applicability of the beam theory for springback prediction may be limited. When large deformation is exerted which induces plastic region in outer bending layers of the forming sheet, the Euler–Bernoulli beam theory, established within elastic region with assumption of small deflection, becomes inappropriate to describe deflection and induced stress: the relation of bending strain ε and curvature k can lose its geometry validity in the case of large deformation. Hence a new analytical method to properly reflect the stress states of material in large deformation for CAF with high strength Al-Li alloys is urgently required, based on which the prediction accuracy of springback and the validity of corresponding developed compensation method can be ensured.

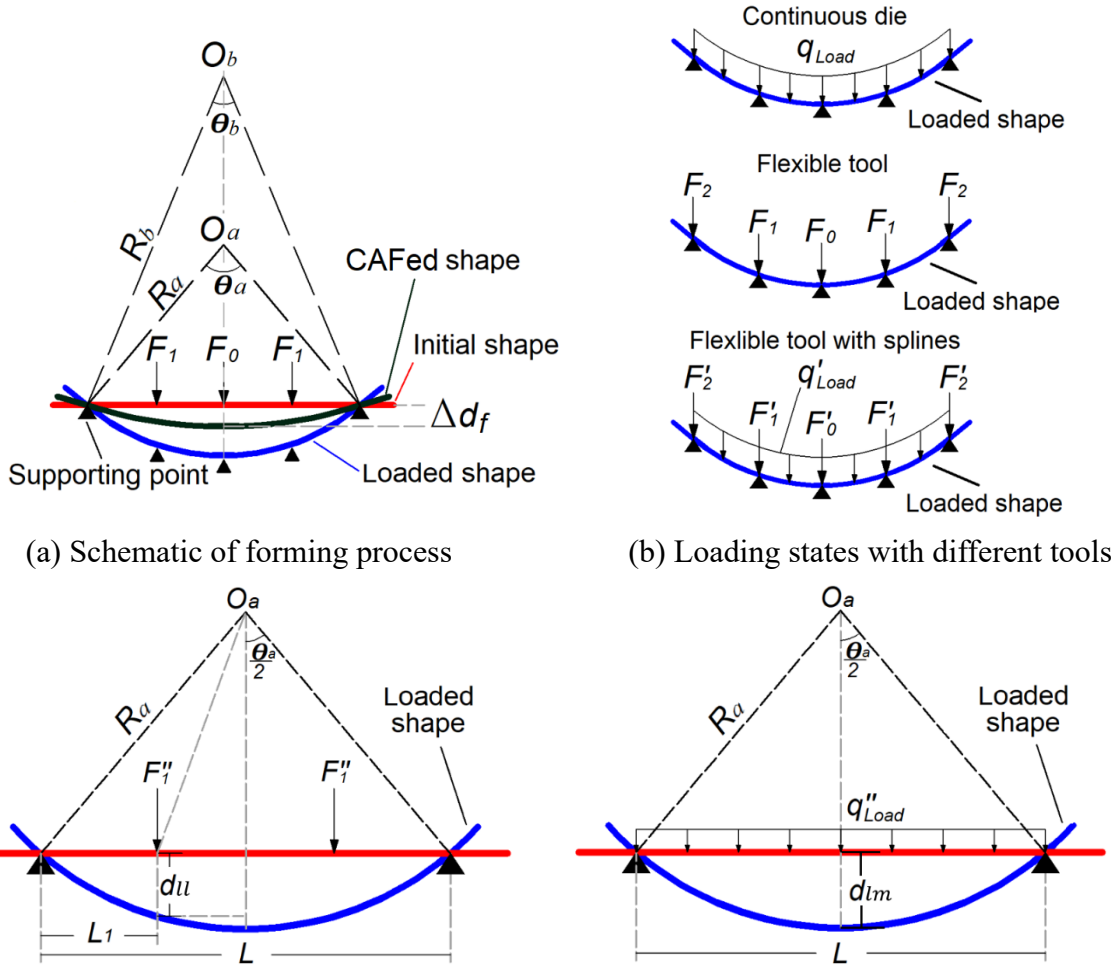
A closed-form prediction solution covering constitutive relations from elastic to plastic in CAF is developed in this section by combining the beam theory and Winkler's theory. The solution is verified with the four-point bending CAF test results. To improve the efficiency in experimental iterations and solve the accuracy issue raised by prediction error from FE analysis, an efficient springback compensation method, based on the developed springback prediction solution, is proposed by introducing an adjustment factor for CAF with the complex flexible tool. The effectiveness and adaptivity of the proposed method are verified through CAF of target single-curvature sheets by using the flexible tool and the same Al-Li alloy with different thicknesses.

7.2 Closed-form solution of CAF springback prediction

7.2.1 Geometric relation in CAF of single curvature sheet

In practical CAF fabrication, metal sheets are formed in forming tools with designed curvature, which can be continuous upper and lower dies, lower supporting dies/ribs in vacuum autoclave, or flexible tool with multiple loading and supporting points. Figure 7-1a schematically shows the sheet

shape at various CAF stages. (i) Initially, the sheet is placed and supported on the forming tool, shown as the red initial shape. (ii) Then the downward loads/displacement (F_0, F_1, etc) are applied and the sheet is deformed to the designed loaded shape in blue. O_a is the centre point of the loaded shape with curvature radius R_a, and θ_a is the centre angle for the loaded curvature between the two supporting points on the edges. (iii) After deforming to the loaded shape, the sheet is kept in this shape and creep-aged at elevated temperature for designed ageing time. (iv) Finally, the sheet is unloaded after completion of creep-ageing and the final CAFed sheet is obtained after springback. As shown in Figure 7-1a, the CAFed sheet has a curvature radius of R_b with O_b as the centre point and θ_b as the centre angle for the final CAFed shape. Δd_f is the deflection at midpoint of the final CAFed sheet from its initial undeformed state.



(a) Schematic of forming process

(b) Loading states with different tools

(c) Four-point bending loading model

(d) Uniform stress loading model

Figure 7-1. Schematic of forming in CAF fabrication and two proposed loading models.

Figure 7-1b illustrates schematically the loading states with different forming tools. For loading with continuous die or autoclave vacuum, the load is applied in the form of pressure, and can be treated as a line load q_{Load} when considering unit width. When adopting multipoint flexible tool, the sheet is deformed with multiple point loads F_x. When deforming with a flexible tool, elastic pads/splines are normally added between loading points and forming sheet to achieve more uniformly distributed stress and smoother forming curvature, thus minimising surface damages [110, 126, 150]. Therefore, as shown in Figure 7-1b, the loading state for flexible tool with splines can be treated as combination of point loads F_x' and line load q_{Load}'. Furthermore, when CAF fabrication is conducted in complex forming tool, the loaded structure is in hyperstatic state which significantly raises the difficulty of stress analysis for the deforming sheet. To simplify the analysis procedure, as demonstrated in Figure 7-1c and 1d, fundamental loading models, i.e. four-point bending with two supporting and loading points and uniformly distributed stress bending, are adopted for the deforming process of the sheet. To approach the stress state of the sheet in complex forming tools, the sheet is deformed to the same shape using the loading models shown in Figure 7-1c and 1d. Because the loaded shapes in Figure 7-1c and 1d are the same as in Figure 7-1a, the same centre point O_a and curvature radius R_a are used for the two loading models. In Figure 7-1c, L is the distance between the two supporting points. L_1 is the distance between the supporting point and the loading point with exerted loads of F_1''. d_{ll} is the loading displacement of the loading points to reach designed loaded shape. In Figure 7-1d, q_{load}'' is the line load and d_{lm} is the displacement of the midpoint. The geometrical relation between loading point displacement d_{ll} and R_a can be obtained as

$$R_a{}^2 = (L/2 - L_1)^2 + \left(\sqrt{R_a{}^2 - (L/2)^2} + d_{ll}\right)^2 \tag{7-1}$$

for centre point displacement d_{lm} and R_a, the geometric relation can be expressed as

$$R_a = \sqrt{R_a{}^2 - (L/2)^2} + d_{lm} \tag{7-2}$$

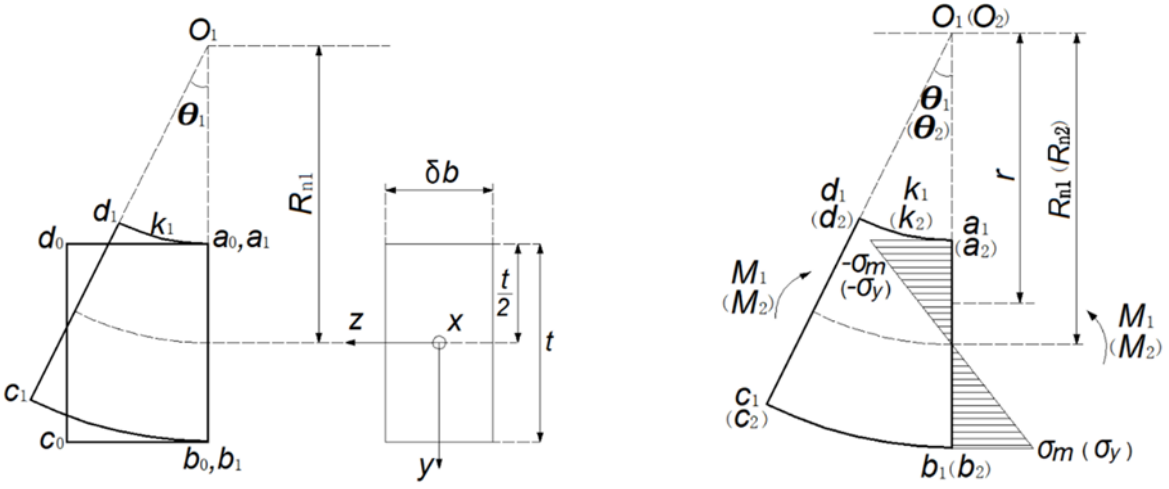
and the relation between θ_a and R_a can be derived as

$$\theta_a = 2\arctan\left((L/2)/\sqrt{R_a{}^2 - (L/2)^2}\right) \tag{7-3}$$

hence, R_a and θ_a can both be determined with displacement d_{ll} or d_{lm}.

7.2.2 Strain and stress determination in loading stage

In loading stage, depending on the displacement exerted to achieve the target shape, the process can range from elastic to plastic loading. By dividing the initial undeformed sheet into equivalent m segments, Figure 7-2a shows one of the sheet elements, defined as $a_0b_0c_0d_0$. Within elastic range, the sheet element $a_0b_0c_0d_0$ is deformed to the shape $a_1b_1c_1d_1$. k_1 is defined as the deflection curvature and O_1 is the centre point of k_1. A polar coordinate system (r, θ) with the origin at the centre point O_1 is used to express the location of the sheet layers along thickness direction. As shown in Figure 7-2a, θ_1 is the centre angle of $a_1b_1c_1d_1$. R_{n1} is the distance of the neutral plane to the centre point O_1 in elastic state, which can also be defined as the curvature radius in this state. Additionally, a local Cartesian coordinate system (x, y, z) is established to depict the plane perpendicular to the neutral plane of the sheet, in which y- and z-axis form the plane perpendicular to the deflection curvature and the neutral plane, and x axis locates at centroid of yz plane and is parallel to the neutral plane, as shown in the right half of Fig. 3(a). Based on the assumption of Euler–Bernoulli beam theory, the neutral axis and neutral plane pass the centroid of yz plane as the mid layer of the sheet and no strain is generated at neutral plane. δb is the unit width of the sheet segment and is defined as 1 mm in this study. t is the sheet thickness.



(a) Elastic deforming (b) Stress distribution

Figure 7-2. Schematic of deforming process when loaded in elastic range and stress distribution through thickness. The labels in bracket in (b) are for the condition at the end of loading in elastic range.

When loading begins as exerting downward displacements on the sheet, elastic strain and stress are generated along x-axis direction of yz plane. The relation of deflection and induced moment depends on different loading model. For four-point loading model demonstrated in Figure 7-1c, by utilising the Euler-Bernoulli beam theory, the relation between the loading point displacement d_{ll} and the generated moment M_1 in yz plane (Figure 7-2b) in elastic range can be expressed as [107]

$$d_{ll} = \frac{M_1}{6EI}(3L_1L - 4{L_1}^2) \tag{7-4}$$

where E is the Young's modulus and I is the moment inertia of yz plane for z-axis. For uniform stress loading case demonstrated in Figure 7-1d, the relation between the midpoint loading displacement d_{lm} and the moment M_1 in elastic range is derived as [151]:

$$d_{lm} = \frac{40M_1L^2}{384EI} \tag{7-5}$$

Within linear elastic state, the stress distribution along x direction in yz plane is shown in Figure 7-2b. In the figure, r is the distance of a random layer to the centre point O_1, $-\sigma_m$ and σ_m are respectively the maximum compressive and tensile stresses achieved at the top and bottom surface of the sheet. The stress distribution can be expressed as

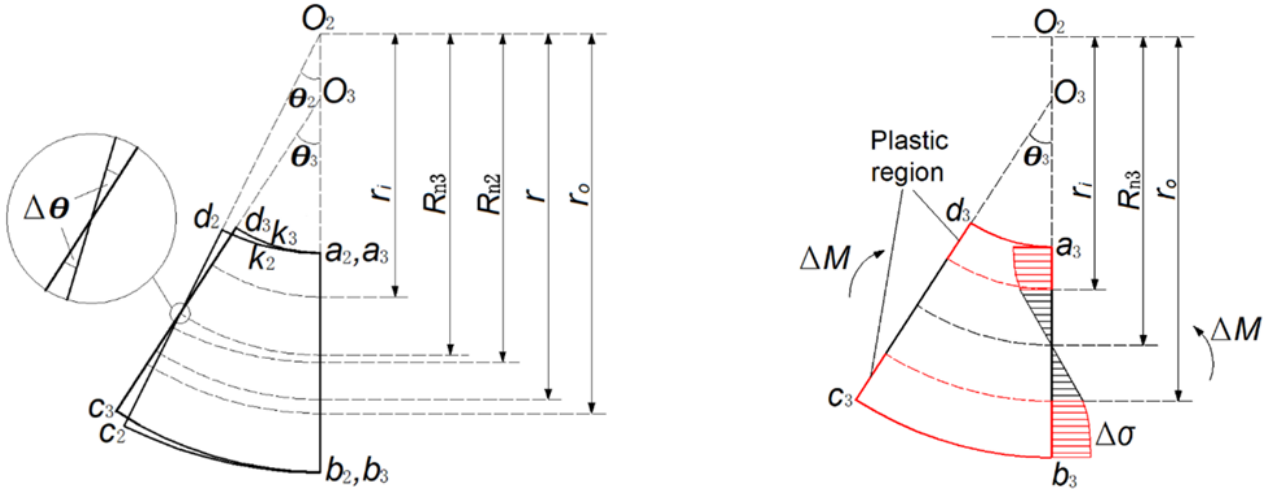
$$\sigma = \frac{M_1}{I}(r - R_{n1}), \qquad R_{n1} - \frac{t}{2} \le r \le R_{n1} + \frac{t}{2} \tag{7-6}$$

as demonstrated in Figure 7-2b, when loaded in elastic range, the stress follows linear distribution along thickness (y direction).

With continued increasing of deflection, the strain and stress in x direction increases. When the absolute value of $-\sigma_m$ and σ_m reaches the yield stress σ_y, the current stress state is defined as end of elastic loading state. As illustrated in Figure 7-2b, the deformed sheet segment, curvature, centre point, centre angle, and moment at the end of elastic loading state are respectively defined as $a_2b_2c_2d_2$, k_2, O_2, θ_2 and M_2, and the distance of neutral plane to the centre point O_2 at the end of the state is defined as R_{n2}.

Further increase in deflection will lead to the stress surpassing the elastic region, i.e. reaching plastic region. Figure 7-3 shows the case after entering the plastic loading state. In the plastic loading state, the elastically loaded shape of sheet element $a_2b_2c_2d_2$ further deforms to $a_3b_3c_3d_3$, with deflection curvature increasing from k_2 to k_3 as shown in Figure 7-3a. Simultaneously, the centre angle increases from θ_2 to θ_3, and the centre point and neutral plane respectively change from

position O_2 to O_3 and R_{n2} to R_{n3} (R_{n3} is the distance of neutral plane to the centre point O_2 in plastic loading). In this situation, the linear elastic stress-strain relation is broken down in the outer bending layers, and plastic strain is generated in the plastic regions near the top and bottom surfaces of the sheet as shown in the red regions in Figure 7-3b. The location of the transition boundary from elastic to plastic region near the top surface is defined using r_i as the distance to the centre point O_2; while r_o is used to mark the distance to the centre point for the position of transition boundary near the bottom. The layers above r_i and underneath r_o are the plastic regions. With the increase of deflection, the upper elastic-plastic boundary will move downwards, and the lower boundary will move upwards, i.e. r_i increases and r_o decreases. $\Delta\sigma$ and ΔM in Figure 7-3b are respectively the increment of stress and corresponding moment in deformation from $a_2b_2c_2d_2$ to $a_3b_3c_3d_3$.



(a) Schematic of deforming process (b) Stress distribution

Figure 7-3. Schematic of deforming process from elastic to plastic loading state in CAF and stress distribution through the thickness of the sheet.

By applying the Winkler's theory, the strain generated at layer at position r when the element deforms from $a_2b_2c_2d_2$ to $a_3b_3c_3d_3$ can be expressed as

$$\Delta\varepsilon = \frac{\Delta\theta(r - R_{n3})}{r\theta_2} \tag{7-7}$$

where $\Delta\varepsilon$ is the strain accumulated at layer of position r in the transformation process from $a_2b_2c_2d_2$ to $a_3b_3c_3d_3$, and $\Delta\theta$ is the change of centre angle as $\Delta\theta = \theta_3 - \theta_2$, as illustrated in Figure 7-3a. From Eq. (7-7), zero strain increment was derived in the layer of neutral plane R_{n3}. When layer r locates underneath R_{n3}, i.e. $r > R_{n3}$, positive strain is generated and the layer in that

position is in tension state. In contrast, when located above the neutral plane ($r < R_{n3}$), negative strain is induced as in compression state. When r is equivalent to r_i or r_o, the layer is at the transition boundary from elastic region to plastic region. According to the definition, the strain at elastic-plastic boundary at r_i and r_0 equals to

$$\varepsilon_y = \begin{cases} -\dfrac{\sigma_y}{E}, & r = r_i \\ \dfrac{\sigma_y}{E}, & r = r_0 \end{cases} \tag{7-8}$$

where ε_y is the strain at yield stress σ_y at transition boundary r_i and r_0. Additionally, under the assumption that transverse shear strain is neglected in Winkler's theory, ε_y can be derived as comprised of two parts as

$$\varepsilon_y = \varepsilon_2' + \Delta\varepsilon' \tag{7-9}$$

where ε_2' is the strain generated at the same layer at r_i or r_0 when the sheet is loaded to the end of elastic loading state. $\Delta\varepsilon'$ is the accumulated strain at r_i or r_0 during deformation from the end of loading in elastic range $a_2b_2c_2d_2$ to $a_3b_3c_3d_3$ in plastic loading state. By utilising the linear stress-strain relation shown in Figure 7-2b and applying Eq. (7-8) and Eq. (7-9), ε_y can be further expressed as

$$\begin{cases} \varepsilon_2' = \varepsilon_y\left(\dfrac{r - R_{n2}}{t/2}\right) \\ \Delta\varepsilon' = \dfrac{\Delta\theta(r - R_{n3})}{r\theta_2}, & r = r_i \text{ or } r = r_0 \\ \varepsilon_y = \varepsilon_2' + \Delta\varepsilon' \end{cases} \tag{7-10}$$

Due to the linear relation for strain and stress within elastic region, Eq. (7-10) can be further extended to describe the elastic strain ε_e and stress σ_e at random position r within elastic region ($r_i \leq r \leq r_0$) when deforms to $a_3b_3c_3d_3$ as

$$\begin{cases} \varepsilon_2'' = \varepsilon_y\left(\dfrac{r - R_{n2}}{t/2}\right) \\ \Delta\varepsilon'' = \dfrac{\Delta\theta(r - R_{n3})}{r\theta_2}, & r_i \leq r \leq r_0 \\ \varepsilon_e = \varepsilon_2'' + \Delta\varepsilon'' \\ \sigma_e = E\varepsilon_e \end{cases} \tag{7-11}$$

where ε_2'' is the strain generated at position r in elastic region ($r_i \leq r \leq r_0$) when deforms to $a_2b_2c_2d_2$ as the end of loading in elastic range. $\Delta\varepsilon''$ is the accumulated strain at r in plastic

loading state from $a_2b_2c_2d_2$ to $a_3b_3c_3d_3$. ε_e and σ_e are respectively the strain and stress at position r in linear elastic region of $a_3b_3c_3d_3$.

As shown in Figure 7-3b, plastic strain is induced in the layers located above r_i and below r_0. To reflect the relation between plastic strain and flow stress beyond linear elastic relation in the plastic region, the classical power law function was used to express work hardening behaviour of the material as

$$\sigma_p = \sigma_y + h\varepsilon_p^{n^*} \tag{7-12}$$

where σ_p is defined as the flow stress in the plastic region. σ_y is the yield stress of material and ε_p is the plastic strain. h and n^* are material constants. By fitting with the obtained stress-strain curve at 143 °C as shown in Figure 4-1, h and n^* are determined with the values of 91 and 0.53. By combining Eq. (7-11) and Eq. (7-12), the flow stress at specific layer r in plastic region can be expressed as

$$\sigma_p = \sigma_y + h\left(\frac{\Delta\theta(r - R_{n3})}{r\theta_2}\right)^{n^*}, \quad r < r_i \; or \; r > r_0 \tag{7-13}$$

In the yz plane of the sheet, the force equilibrium function can be derived as

$$\int \sigma \, dA = 0 \tag{7-14}$$

where A is the area of the yz plane of the sheet. With further transformation of $dA = \delta b dy = dy = d(r - R_{n2}) = dr$, the equation can be written as

$$\int_{R_{n2}-t/2}^{R_{n2}+t/2} \sigma dr = \int_{r_i}^{r_0} \sigma_e dr + \int_{r_i}^{R_{n2}-t/2} \sigma_p dr + \int_{r_0}^{R_{n2}+t/2} \sigma_p dr = 0 \tag{7-15}$$

By inserting Eq. (7-11) and Eq. (7-13) into Eq. (7-15) , Eq. (7-15) can be expressed in a function which R_{n3} is the only parameter as

$$f(R_{n3}) = 0 \tag{7-16}$$

The bisection method is applied as an iterative algorithm tool to approach the value of R_{n3}. The process of utilising bisection method to obtain the value of R_{n3} is manifested in Figure 7-4. Considering the possible extent of deflection increase from $a_2b_2c_2d_2$ to $a_3b_3c_3d_3$ in CAF and corresponding potential neutral plane variation range in plastic loading state, in the first iteration, the initial values of ${R_{n3a}}^i$ and ${R_{n3b}}^i$, as the upper and lower limits of R_{n3} for bisection method, are

given with values as $R_{n3a}{}^{1} = R_{n2} + t/5$ and $R_{n3b}{}^{1} = R_{n2} - t/5$. Tol_2 is defined as the error tolerance comparing with obtained results of $f(R_{n3})$, which is set to be the value of 5E-4 in this study.

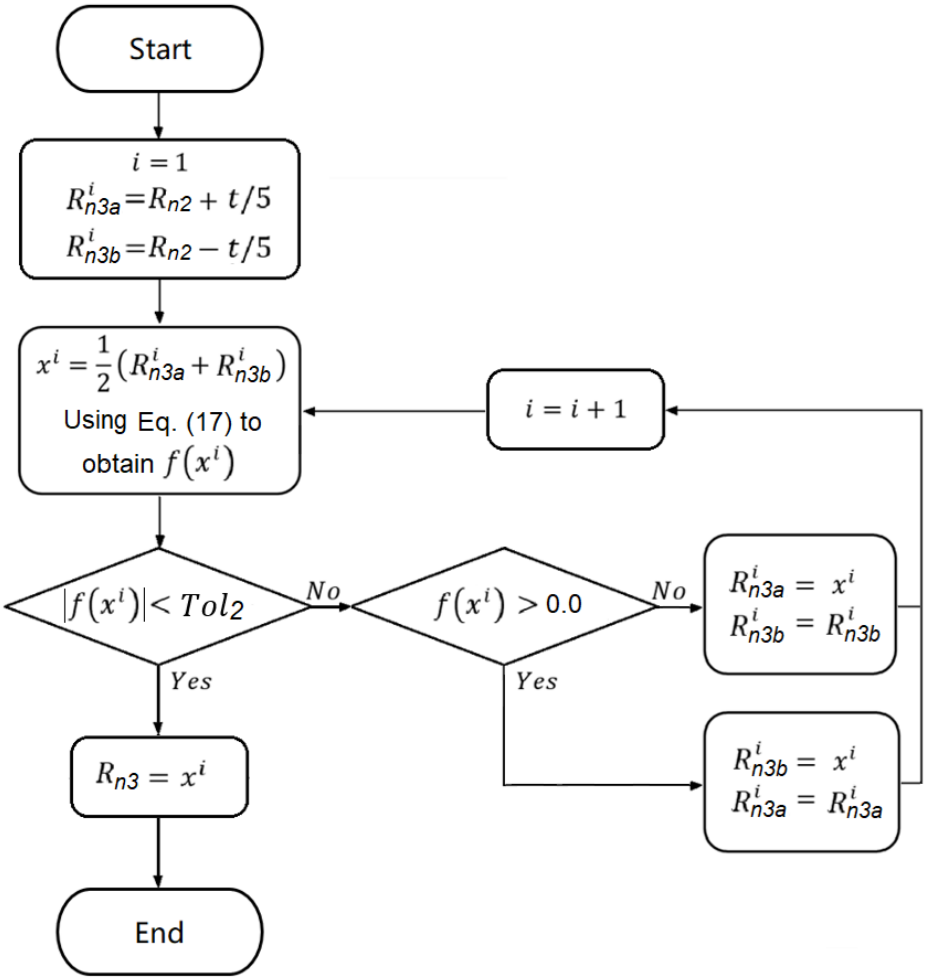


Figure 7-4. Flow chart of bisection method.

With the determination of R_{n3}, by adopting Eq. (7-11) and Eq. (7-13), the strain and stress in both elastic and plastic regions can be determined. Hence the moment in yz plane around z axis for $a_3b_3c_3d_3$ defined as M_3 can be derived as

$$M_3 = M_2 + \Delta M = \int \sigma(r - R_{n2})\, dA \tag{7-17}$$

where M_2 is the moment at $a_2b_2c_2d_2$ and ΔM is the moment increased during the deformation from $a_2b_2c_2d_2$ to $a_3b_3c_3d_3$ as respectively shown in Figure 7-2b and Figure 7-3b.

7.2.3 Springback prediction after creep-ageing

In creep-ageing stage, stress relaxation will be induced due to accumulation of the creep strain. For layer at location r in the deformed element with loading in elastic range $a_1b_1c_1d_1$ or loading in plastic range $a_3b_3c_3d_3$, the stress variation in creep-ageing stage in respect of ageing time t_a can be expressed as

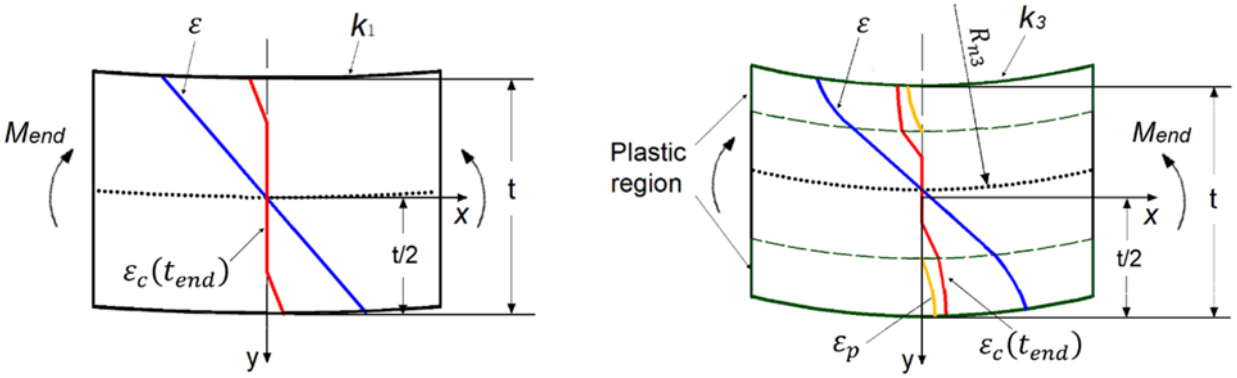
$$\sigma(t_a) = \sigma - \sigma_r(t_a) = \sigma - E\varepsilon_c(t_a) \tag{7-18}$$

where $\sigma(t_a)$ is the stress at ageing time t_a of the layer, σ is the stress generated at the end of loading stage. $\sigma_r(t_a)$ is the extent of stress relaxation at ageing time t_a due to generation of creep strain, which can be calculated as $\sigma_r(t_a) = E\varepsilon_c(t_a)$ where $\varepsilon_c(t_a)$ is the creep strain accumulated at layer r at ageing time t_a. It is also known that the evolution of creep strain is determined by the stress in creep-ageing, by applying proper constitutive model reflecting the relation of stress and creep strain, $\varepsilon_c(t_a)$ can be obtained as:

$$\varepsilon_c(t_a) = f_c\big(\sigma(t_a)\big) \tag{7-19}$$

f_c denotes the constitutive model being proposed in Chapter 5. The creep strain accumulated after completion of creep-ageing at time of t_{end} is denoted as $\varepsilon_c(t_{end})$.

In unloading stage, with the upward movement of the loading points and decrease of d_l and d_{lm}, driven by the recovery of remaining elastic strain after creep-ageing, springback of the deformed sheet is induced. The springback of the sheet will stop when recovery of elastic strain is completed. Hence, the strain and stress in springback follows linear elastic relationship and the unloading process can be viewed as a reversed process of elastic loading. The strain distribution along the thickness of the sheet at the end of creep-ageing in elastic/plastic loading state is demonstrated in Figure 7-5.



(a) Loading in elastic range (b) Loading in plastic range

Figure 7-5. Schematic of strain ($\boldsymbol{x}$ direction) distribution along thickness of the sheet ($\boldsymbol{y}$ direction) after completion of creep-ageing. $\boldsymbol{\varepsilon}$ is the bending strain along *x* direction. The dotted lines stand for neutral plane of the sheet.

As shown in Figure 7-5, after completion of creep-ageing, the remaining elastic strain $\varepsilon_e(d)$ at specific layer d of the sheet, along with the induced moment M_{end} for yz plane around z axis as the recovery moment at the end of creep-ageing/start of unloading stage, can be expressed as

$$\begin{cases} \varepsilon_e(d) = \varepsilon(d) - \varepsilon_p(d) - \varepsilon_c(t_{end}) \\ M_{end} = \int E\varepsilon_e(d) y_d \, dA \end{cases} \tag{7-20}$$

where $\varepsilon(d)$, $\varepsilon_p(d)$, $\varepsilon_c(t_{end})$ are respectively the circumferential strain, plastic strain, and creep strain at layer d of the sheet, y_d is the distance of the layer to the neutral plane. For four-point bending cases, by applying Eq. (7-4), the recovered deflection at loading point (d_{rl}) during springback can be obtained as $d_{rl} = \frac{M_{end}}{6EI}(3L_1L - 4{L_1}^2)$. For uniform stress bending cases, by applying Eq. (7-5), the recovered deflection at midpoint of the sheet (d_{rm}) can be derived as $d_{rm} = \frac{40M_{end}L^2}{384EI}$. By utilising Eq. (7-1) and Eq. (7-2) respectively for four-point bending and uniform stress bending cases, the curvature $1/R_b$, as the final curvature of CAFed sheet can be derived as ${R_b}^2 = (L/2 - L_1)^2 + \left(\sqrt{{R_b}^2 - (L/2)^2} + (d_{ll} - d_{rl})\right)^2$ for the former case and $R_b = \sqrt{{R_b}^2 - (L/2)^2} + (d_{lm} - d_{rm})$ for the latter. By applying geometric transformation derived in Eq. (7-2), the final deflection of the sheet at the midpoint can be expressed as

$$\Delta d_f = R_b - \sqrt{{R_b}^2 - (L/2)^2} \tag{7-21}$$

7.3 Springback compensation method based on closed-form solution

The above closed-form solution of springback prediction for CAF is based on two simplified loading models, i.e. four-point bending and uniform stress bending. In practical CAF fabrication, however, specialised forming tool may be used, in which a higher complexity of loading state for the forming sheet is involved. Multipoint flexible tool, as one of the state-of-the-art forming tools, is characterised by its flexibility in setting required loading shape and has been adopted to not only CAF

but also other sheet forming processes [109–111]. When deforming with flexible tool, depending on the designed loaded shape, the loading process can span from linear elastic to nonlinear plastic loading. For loading in elastic range with a multipoint flexible tool, the loading state is varying with the increase of loading displacement, which can be difficult to analytically derive the relation between loading deflection and stress states of the forming sheet. Furthermore, the derived solution will lose its validity once the locations of loading points are modified. By applying the simplified uniform stress bending model and Eq. (7-5), when the sheet is deformed in elastic range with flexible tool, an equation with higher convenience and robustness to express the relation between loading displacement d'_{lm} and induced moment M_1 is proposed as

$$d'_{lm} = \alpha' \frac{40 M_1 L^2}{384 EI} \tag{7-22}$$

where d'_{lm} is the displacement at midpoint of the sheet adopting flexible tool, α' is the adjustment factor to approach real relation between generated moment M_1 and d'_{lm} within elastic range. When d'_{lm} continues to increase and reach the end of elastic loading state, Eq. (7-22) can be further written as $d'_{lm} = \alpha' \, 40 M_2 L^2 / 384 EI$, where M_2 is the moment induced at the end of elastic loading state as illustrated in Figure 7-2b.

When the stress surpasses elastic region during loading, as shown in Eq. (7-7), the strain increment $\Delta\varepsilon$ in plastic loading state is derived based on geometrical change with the increase in deflection from the end of elastic loading. Consequently, the proposed solution for stress analysis and springback prediction in plastic loading state (from Eq. (7-7) to Eq. (7-21)) remains its validity in the case of multipoint flexible forming tool. Hence, by replacing Eq. (7-5) with Eq. (7-22), a modified closed-form springback prediction solution (Eq. (7-6) to Eq. (7-22)) is obtained for multipoint flexible tool. As can be noticed, the accuracy of this modified springback prediction solution for CAF with flexible tool is highly depending on the determination of adjustment factor α'. This adjustment factor not only helps to approach true relation of deflection and the generated moment within elastic range, but also defines the transformation boundary from elastic to plastic loading. The solution-based springback compensation method, aiming at forming sheet with target curvature by approaching appropriate adjustment factor α' through iterations, can be generalised as following:

(1) With a determined target curvature as $1/R_c$ and adjustment factor α'_i, the loaded shape with

curvature as $1/R_a^i$ for i^{th} iteration CAF can be derived based on the modified closed-form springback prediction solution (Eq. (7-6) to Eq. (7-22)). For the first iteration, the initial adjustment factor α_i' is set to be 1.

(2) The i^{th} iteration CAF is conducted with flexible forming tool which is adjusted to the derived loaded curvature $1/R_a^i$. After completion of CAF, curvature of the CAFed sheet in that iteration is obtained and denoted as $1/R_b^i$. R_b^i is then compared with the target curvature radius R_c. Δe is the shape error at midpoint between the CAFed and target shape and can be obtained by using Eq. (7-21) as $\Delta e = \left(R_c - \sqrt{{R_c}^2 - (L/2)^2}\right) - \left(R_b^i - \sqrt{{R_b^i}^2 - (L/2)^2}\right)$.

(3) If the absolute value of shape error $|\Delta e|$ exceeds the tolerance range Tol_1, with the obtained CAFed curvature $1/R_b^i$ in i^{th} iteration, the adjustment factor α_{i+1}' for next $(i+1)^{th}$ iteration is updated based on the modified closed-form springback prediction solution (Eq. (7-6) to Eq. (7-22)). With the updated adjustment factor, the next iteration is started from step (1).

A flowchart of the proposed closed-form solution-based springback compensation method is demonstrated in Figure 7-6, where i stands for the i^{th} iteration with the method, function g stands for the modified springback prediction solution (Eq. (7-6) to Eq. (7-22)).

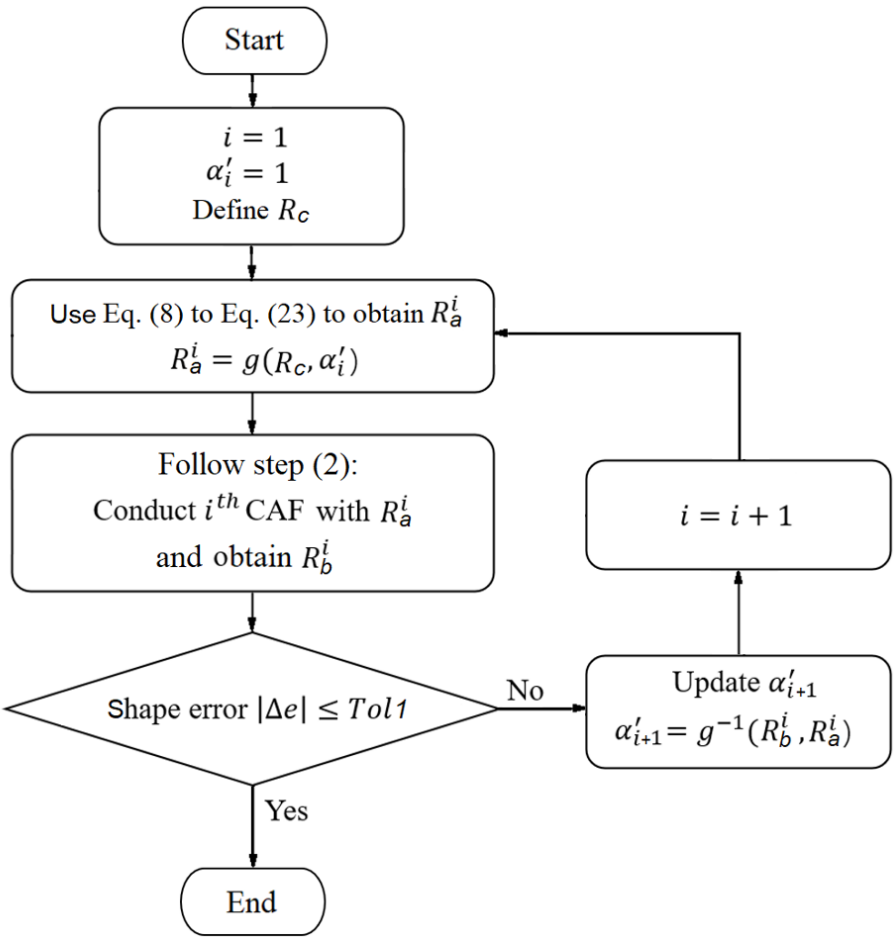


Figure 7-6. Flowchart of closed-form solution-based springback compensation method.

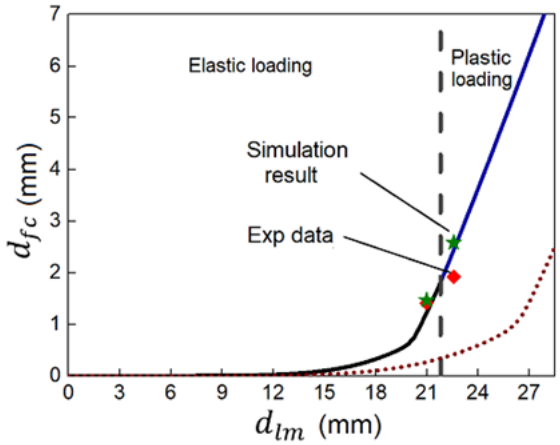
7.4 Prediction solution and compensation method verification

7.4.1 Solution verification with four-point bending CAF experiment results

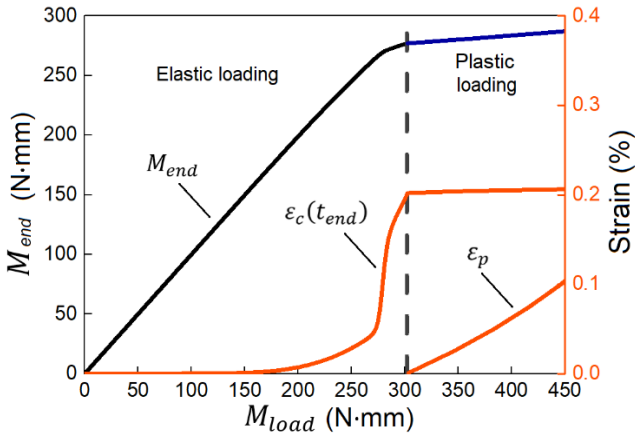
Figure 7-7 shows the springback results for all thicknesses, including the prediction curves of the midpoint loading deflection d_{lm} with the final deflection Δd_f at the same midpoint of the CAFed specimen, and the moment release curves in creep-ageing for the moment at the end of creep-ageing stage M_{end} as a function of the moment at the end of loading stage M_{load}. The evolutions of maximum absolute values of creep strain $\varepsilon_c(t_{end})$ and plastic strain ε_p at the end of creep-ageing, which were obtained at upper surface layer of the sheet, are also demonstrated with the increase of M_{load} in the figure. These results (solid lines) were obtained using the closed-form solution proposed in this study. For comparison, the dotted lines are the prediction results derived from the traditional beam theory with assumption of small deflection as [126]

$$\begin{cases} \varepsilon(d) = k_b y_d, & -t/2 \le y_d \le t/2 \\ \sigma(d) = E\varepsilon(d), & -\sigma_y/(Ek_b) \le y_d \le \sigma_y/(Ek_b) \\ \sigma(d) = \sigma_y + h(\varepsilon(d) + \sigma_y/E)^n, & \sigma_y/(Ek_b) \le y_d \le t/2 \\ \sigma(d) = \sigma_y + h(\varepsilon(d) - \sigma_y/E)^n, & -t/2 \le y_d \le -\sigma_y/(Ek_b) \end{cases} \quad (7\text{-}23)$$

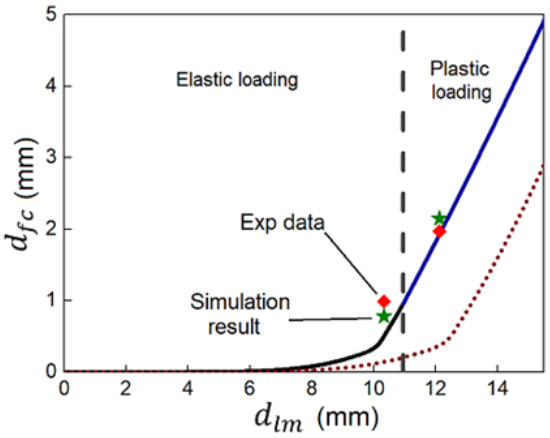
where k_b is the loaded curvature as $1/R_b$, $\sigma(d)$ is the corresponding induced stress at layer d. The experimental data and numerical simulation results are also presented using diamond and star shape symbols respectively.



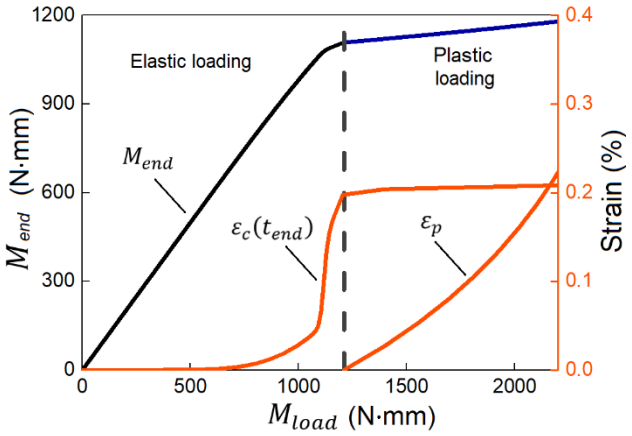
(a) Deflection prediction for 2 mm



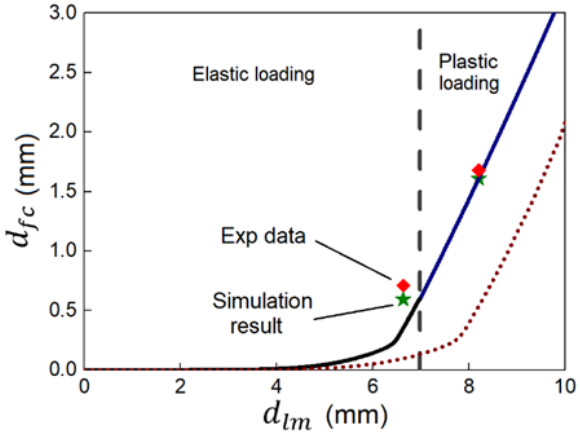
(b) Moment release and strain evolution for 2 mm



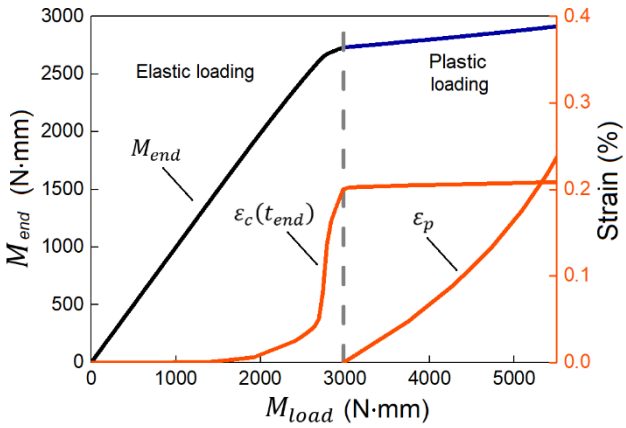
(c) Deflection prediction for 4 mm



(d) Moment release and strain evolution for 4 mm



(e) Deflection prediction for 6 mm



(f) Moment release and strain evolution for 6 mm

Figure 7-7. Creep age forming behaviour for 2, 4 and 6 mm sheets, showing the predicted, FE simulated and experimental final deflection Δd_f vs loading displacement d_{lm}; the moment M_{end}, strain ε_c and plastic strain ε_p at the end of creep-ageing as a function of loading moment M_{load}.

As demonstrated in Figure 7-7, for all thicknesses, satisfactory agreement was achieved among results of the solution-based prediction, four-point bending CAF experiments, and numerical simulation, indicating validity of the proposed closed-form solution. The predicted springback results by the current solution method have a maximum difference of 0.49 mm from the experiments and 0.27 mm from the FE simulations; while the beam theory-based results have much larger deviation from other methods in large loading deflection, with a maximum prediction error of 1.6 mm for the 4 mm thickness sheet.

In addition, based on the obtained prediction curves, different evolution trend can be observed in elastic and plastic loading conditions for all thicknesses as shown in Figure 7-7. In elastic range, the CAFed deflection Δd_f and moment release $(M_{load} - M_{end})$ gradually increased at the beginning and surged with higher rate when approaching the plastic loading. In plastic loading, a high increase rate of Δd_f and $(M_{load} - M_{end})$ were obtained for all thicknesses. On the other hand, as demonstrated in Figure 7-7b, d, and f, the final creep strain surged when approaching plastic loading state and maintained at a level slightly above 0.2% with minor increase in plastic loading; while the plastic strain during loading increased sharply with increasing moment. The observed surge for deflection Δd_f, moment release $(M_{load} - M_{end})$, and maximum creep strain when approaching plastic loading can be attributed to the nonlinear increase of creep deformation of the alloy when the

applied stress surpasses 400 MPa, which was observed in uniaxial creep-ageing tests at 143 ℃ for this material [129]. The high increase rate of Δd_f and $(M_{load} - M_{end})$ achieved in plastic loading is due to the effects of plastic strain and larger creep strain respectively induced in stages of loading and creep-ageing. Additionally, for this Al-Li alloy, springback is high and can offset the majority of the loading displacement. The lowest springback percentage is 79.5% for 6 mm sheet for CAF of a target curvature of 1/2000 mm^{-1}. It can be noted that due to high strength and creep resistance of the alloy, even for fabricating panels with a small curvature of 1/2000 mm^{-1}, CAF need be conducted with plastic loading state.

7.4.2 Compensation method verification with flexible tool CAF experiment results

Figure 7-8 shows the photos of the CAFed sheets after using the solution-based springback compensation method proposed in this study for 2 mm and 4mm thick sheets. The left side shows the full picture of the deformed sheets and the right side is the enlarged figure for the mid area. As demonstrated in Figure 7-8, the final deflection increases with increasing iteration for both 2 and 4 mm sheets. Within 4 iterations, the final error between the deflection of the experiment obtained and the target one fell in the range of error tolerance Tol_1 of 0.56 mm.



(a) 2 mm

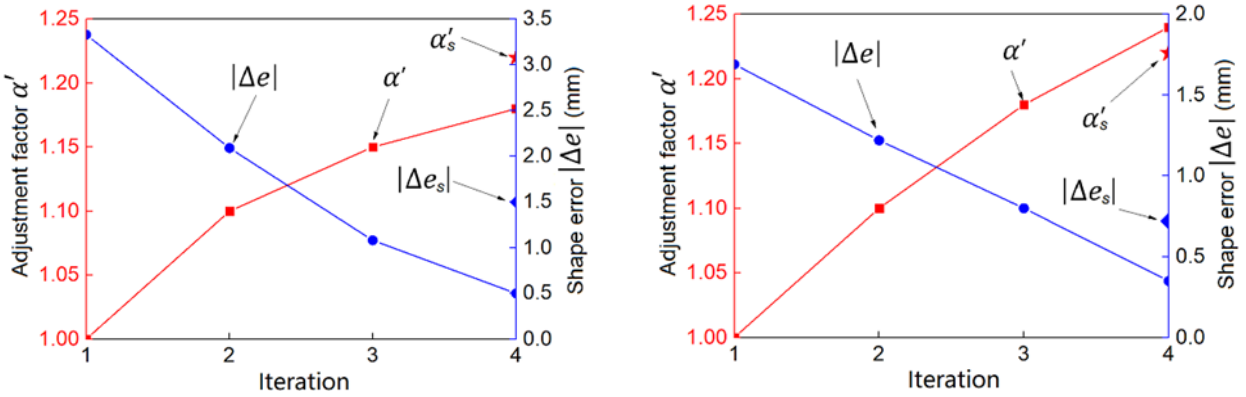


(b) 4 mm

Figure 7-8. Photos of CAF iteration results of sheets with different thickness.

Figure 7-9 presents the corresponding evolution of adjustment factor α' and shape error $|\Delta e|$ with increasing iterations, together with the FE simulation results of adjustment factor (α'_s) and shape error ($|\Delta e_s|$) based on the loaded shape of 4th iteration. As shown in the figure, for 2 and 4 mm sheets, after 4 iterations, the CAFed sheets satisfied the tolerance range of 0.56 mm with shape error of 0.5

mm for 2 mm and 0.38 mm for 4 mm. The adjustment factors were derived with values greater than 1 for both thicknesses, indicating that lower stiffness of the structure was induced for both thicknesses when loading with flexible tool than the proposed uniform stress bending model. With increasing iteration, the adjustment factor increased for both thicknesses, but the increasing rate gradually decreased. This decreasing trend of the rate demonstrated that the factor was converging to an appropriate value to reflect the true relationship between the deflection and the generated moment with the increase of iterations.



(a) 2 mm sheet iterations (b) 4 mm sheet iterations

Figure 7-9. Evolution of adjustment factor and shape error with increased iterations.

In this study, the initial value of adjustment factor was set to 1 to investigate the proposed method. In practical fabrication, the initial value can be set based on FE simulation. As demonstrated in Figure 7-9, the FE simulation results are close to the experimental data. Therefore, by combining FE analysis as preliminary estimation, a more proper initial value greater than 1 can be adopted to decrease the required iterations for the target shape and to improve the cost efficiency when deforming with flexible tool.

7.5 Summary

In this section, a closed-form solution for creep age forming springback prediction covering elastic to plastic behaviours of the material has been proposed. Based on the solution, a springback compensation method for CAF fabrication with complex flexible forming tool has been developed. Both the proposed solution and the compensation method have been verified with corresponding CAF tests including the four-point bending and fabrication with the multipoint flexible tool. The validity

of the proposed closed-form springback prediction solution has been well supported with a maximum error of 0.49 mm compared with the experimental results. Also, successful CAF fabrication of target single-curvature sheet using multipoint flexible tool has been achieved by utilising the proposed springback compensation method within four iterations and with acceptable tolerances. This study shows that the proposed closed-form solution for springback prediction and the springback compensation method are adequate in creep age forming application.

Chapter 8

Conclusions and future work

8.1 Conclusions

As one of the recently introduced 3rd generation Al-Li alloys, AA2060 is characterised by its superior mechanical performances, advanced weight reduction, and balanced synergy of strength and toughness. Due to these advantages, this alloy is being viewed as a potential substitution for its predecessors in aspects of sheet and plate products. However, for the fabrication of large and extra-large panel components, the application of this high strength alloy sheets in CAF has seldom been investigated. Also, the strength of this alloy has significantly increased in the T8 temper which is the most widely adopted finish temper for the Al-Li alloys, the fabrication issue induced by the high strength and increased creep resistance of this alloy requires to be solved. In the purpose of shedding light on the extensive application of the newest 3rd generation Al-Li alloy in CAF via this study, the material behaviour of AA2060-T8 in creep ageing, as well as the corresponding panel fabrication through CAF, have been systematically investigated by adopting the experimental, mathematical modelling, and numerical simulation methods. The creep deformation of AA2060-T8 under the condition of uniaxial loading at 143°C with different applied stresses ranging from 300 to 430 MPa. The microstructural evolution of the material in aspects of precipitation and dislocation density during the creep-ageing process has been studied by conducting TEM and XRD tests. Based on the obtained results of material behaviour and microstructural evolution in creep-ageing, a unified constitutive model adequate to reflect the stress-creep strain relation has been established and its application in the numerical simulation has been demonstrated and verified through additional four-point bending CAF experiments. Finally, an efficient closed-form springback prediction and compensation solution able to effectively combine both the experimental and numerical simulation methods have been established and verified by conducting CAF fabrication of AA2060-T8 with a flexible tool. The following conclusions can be obtained:

1. The creep-ageing tests at 143 °C under the condition of uniaxial loading from 300 to 430 MPa in 20 h demonstrates a wide range of creep deformation from the lowest of 0.02% to the highest of 0.45%. In addition, a nonlinear increase of the creep deformation is observed when the applied stress surpasses 400 MPa, and the creep strain of 430 MPa is 7 times over the 400 MPa with 0.45% under the former stress and 0.06% under the latter.

2. For creep-ageing of the Al–Li alloy at T8 temper at 143 °C, the creep deformation mechanism changes from diffusion creep to dislocation creep with increasing applied stresses. The transition occurs around 400 MPa. The steady state creep strain rate dominated by the dislocation creep mechanism is much higher than that under the diffusion creep. The creep strain rate and stress in logarithmic form have a bilinear relationship with the crossover point around 400 MPa, which is in accordance with the transition of deformation mechanism. The average rate of steady state creep strain rate variation with stress is 2.6×10^{-11} s^{-1} MPa^{-1} for diffusion creep dominated deformation and 1.3×10^{-10} s^{-1} MPa^{-1} for dislocation creep dominated deformation.

3. During creep-ageing at stresses ranging from 300 to 430 MPa, T1 dominates in the precipitate quantity compared with θ'. The applied stress favours T1 precipitates and higher applied stress leads to a higher frequency ratio of T1 to θ′ because of higher dislocation density. The frequency ratio of T1 to θ′ increases from 75% to 25% in the as-received state to 84% to 16%, 93% to 7%, and 97% to 3% under 300, 400, and 430 MPa respectively after creep-ageing for 15 h.

4. A unified mechanism-based constitutive model adequate to reflect the stress-creep strain relation has been established. By combining the work hardening equations to link the loading introduced dislocation density and reduction of the threshold stress, the wide range of creep deformation of T8 tempered Al-Li alloy from 0.02% to 0.45% with corresponding applied stresses ranging from 300 to 430 MPa, as well as the 7 times nonlinear increase of the creep strain when the applied stress increased from 400 to 430 MPa, can be satisfactorily described by the model. Consistent results have been achieved between experimental and modelling results for macro creep-ageing behaviour and microstructural evolutions in aspects of dislocation and precipitation of material in loading and creep-ageing stages. Additional four-point bending CAF tests has demonstrated the applicability and prediction accuracy of the model in numerical simulation.

5. A closed-form springback prediction solution is developed by combining the traditional beam theory and Winkler's theory, for CAF covering deformation from elastic to plastic loadings. Furthermore, an efficient springback compensation method for CAF is proposed based on the developed solution method. Good convergences have been achieved among the results from the developed prediction solution, FE simulation, and experiments for four-point bending CAF tests, conducted in both elastic and plastic loading ranges with different sheet thickness. The validity of the proposed closed-form springback prediction solution has been well supported by the experimental results with a maximum error of 0.49 mm. Also, successful CAF fabrication of target single-curvature sheet using the multipoint flexible tool has been achieved by utilising the proposed springback compensation method within four iterations and with acceptable tolerances.

8.2 Future work

In this study, the fundamental information has been obtained and corresponding methods have been established for applying AA2060-T8 in CAF. However, in this investigation process, more questions have been raised and some of them are to be solved on future work:

1. The creep deformation behaviour of the material was systemically investigated under the condition of uniaxial loading with constant stress, while the stress relaxation behaviour of the material with constant applied strain in creep-ageing has not been carried out. The comparison of the material behaviour under constant stress and strain in creep-ageing still needs to be unveiled, and a further unified constitutive model to integrate these two different conditions can not only significantly promote the theoretical understanding of CAF, but also the efficiency in practical fabrication.

2. This study satisfactorily solved the issues of fabrication difficulty induced by high creep resistance and large amount springback of applying AA2060-T8 in CAF, however only limited in the case of single curvature panels with different thicknesses. With the higher requirements being raised for a more complex contour of CAF fabricated components, further investigation can be carried out on CAF of double curvatures or more complex shape components based on the foundation laid in this study.

3. Though reduced to a much extent when compared to the predecessors of Al-Li alloys, AA2060 still suffers the anisotropy issue which can exert solid effects on the fabrication of components of double curvatures or more complex contours in CAF. Further investigation can be conducted focusing on exploring the effects of the anisotropy issue of the adopted Al-Li alloy in CAF fabrication of components with complex shapes.

References

[1] Munroe J, Wilkins K, Gruber, M, Domack M. Integral airframe structures (IAS): validated feasibility study of integrally stiffened metallic fuselage panels for reducing manufacturing costs. NASA/CR-2000-209337.

[2] Frigo M, Silva E, Barbosa G. Augmented reality in aerospace manufacturing: a review. Journal of Industrial and Intelligent Information. 2016;4:125–30.

[3] NASA. 2017. https://www.nasa.gov/exploration/systems/sls/multimedia/nasa-completes-welding-on-sls-fuel-tank-test-article.html.

[4] Kopp R, Schulz J. Flexible sheet forming technology by double-sided simultaneous shot peen forming. CIRP Annals. 2002;51:195–8.

[5] Montross C, Wei T, Ye L, Clark G, Mai Y. Laser shock processing and its effects on microstructure and properties of metal alloys: a review. International Journal of Fatigue. 2002;24:1021–36.

[6] Gariépy A, Miao H, Levésque M. 3.12-Peen Forming. Comprehensive materials processing; 2014.

[7] Markovina R, Blagojevic B, Ban D. Peen-forming-the possibility of technology transfer from aircraft industry to the production of high-speed ships. Brodgradnja. 2008;59:35–43.

[8] Zhang C, Dong Y, Ye C. Recent developments and novel applications of laser shock peening: a review. Advanced Engineering Materials. 2021;23:2001216.

[9] Holman MC. Autoclave age forming large aluminum aircraft panels. Journal of Mechanical Working Technology. 1989;20:477–88.

[10] Watcham K. Airbus A380 takes creep age-forming to new heights. Materials World. 2004:10–1.

[11] Zhan L, Lin J, Dean TA. A review of the development of creep age forming: Experimentation, modelling and applications. International Journal of Machine Tools and Manufacture. 2011;51:1–17.

[12] Bodily B, Heinimann M, Bray G, Colvin E. et al., Advanced aluminum and aluminum-lithium solutions for derivative and next Generation aerospace structures. SAE Technical Paper 2012-01-1874; 2012

[13] Prasad NE, Gokhale AA, Wanhill RJH, editors. Aluminum-lithium alloys: Processing, properties, and applications. Oxford: Elsevier Butterworth-Heinemann; 2014.

[14] Abd A, Xu Y, Guo X, Zhang S, Ma Y, Chen D. Strengthening mechanisms, deformation behavior, and anisotropic mechanical properties of Al-Li alloys: A review. Journal of advanced research. 2018;10:49–67.

[15] Zhou C, Zhan L, Li H. Improving creep age formability of an Al-Cu-Li alloy by electropulsing. Journal of Alloys and Compounds. 2021;870:159482.

[16] Eberl F, Gardiner S, Campanile G, Surdon G, Venmans M, Prangnell P. Ageformable panels for commercial aircraft. Proceedings of the Institution of Mechanical Engineers, Part G: Journal of Aerospace Engineering. 2008;222(6):873-886.

[17] A380 wing production investment. Aircraft Engineering and Aerospace Technology. 2003.

[18] Bilstein R. Stages to Saturn: A technological history of the apollo/saturn launch vehicle: DIANE Publishing; 1999.

[19] Yang H. Creep age forming investigation on aluminium alloy 2219 and related studies [PhD

thesis]: Imperial College London; 2013.
[20] Sun X, Han X, Dong C, Li X. Applications of aluminum alloys in rail transportation: 9. In: Dobrzański L, editor. Advanced aluminium composites and alloys: IntechOpen; 2021.
[21] Rong Q, Shi Z, Li Y, Lin j. Constitutive modelling and its application to stress-relaxation age forming of AA6082 with elastic and plastic loadings. Journal of Materials Processing Technology. 2021;295:117168.
[22] NASA. 2017. https://www.nasa.gov/exploration/systems/sls/multimedia/gallery/preparing-test-article.html.
[23] Pantelakis S, Kyrsanidi A, Magd E, Dünnwald J, Barbaux Y, Pons G. Creep resistance of aluminium alloys for the next generation supersonic civil transport aircrafts. Theoretical and Applied Fracture Mechanics. 1999;31:31–9.
[24] Nabarro F. Creep at very low rates. Metallurgical and Materials Transactions A. 2002;33:213–8.
[25] Anderson P, Hirth J ,Lothe J. Theory of dislocations. 3rd ed.: Cambridge university press; 2017.
[26] Weertman J. Creep of indium, lead, and some of their alloys with various metals. Trans. Met. Soc. AIME. 1960;Vol: 218.
[27] Kassner ME. Fundamentals of Creep in Metals and Alloys (3rd edition). Butterworth-Heinemann. 2015.
[28] Smallman R, Ngan A. Chapter 15 - Creep, Fatigue and Fracture. In: Smallman R NA, editor. Modern Physical Metallurgy (Eighth Edition). Oxford: Butterworth-Heinemann; 2014. p. 571–616.
[29] Abe F. Development of creep-resistant steels and alloys for use in power plants. In: Shirzad A JS, editor. Structural alloys for power plants: Woodhead Publishing; 2014. p. 250–293.
[30] Huang K, Marthinsen K, Zhao Q, Logé R. The double-edge effect of second-phase particles on the recrystallization behaviour and associated mechanical properties of metallic materials. Progress in Materials Science. 2018;92:284–359.
[31] Rong Q, Li Y, Shi Z, Meng L, Sun X, Lin j. Experimental investigations of stress-relaxation ageing behaviour of AA6082. Materials Science and Engineering: A. 2019;750:108–16.
[32] Yang J, Jiang H, Yao Z, Dong J. Limitations of calculating stress relaxation limit by function-fitting of Inconel718 superalloy. Materials Letters. 2018;221:89–92.
[33] Zhan L, Lin J, Dean TA, Huang M. Experimental studies and constitutive modelling of the hardening of aluminium alloy 7055 under creep age forming conditions. International Journal of Mechanical Sciences. 2011;53:595–605.
[34] Li Y, Shi Z, Lin J. Experimental investigation and modelling of yield strength and work hardening behaviour of artificially aged Al-Cu-Li alloy. Materials & Design. 2019;183:108121.
[35] Mouritz A, editor. Introduction to aerospace materials: Woodhead Publishing; 2012.
[36] Vasudevan AK, Doherty RD. Aluminum alloys--contemporary research and applications. Boston: Academic Press; 1989.
[37] Christian V. Chapter B.6 - The Corrosion Behaviour of Aluminium Alloys. In: Vargel C, editor. Corrosion of Aluminium. Amsterdam: Elsevier; 2004. p. 211–230.
[38] Davis J. Alloying: Understanding the Basics. In: ASM International 2001. p. 351–416.
[39] Buschow KHJ, Cahn RW, Flemings MC, Ilschner B, Kramer EJ, Mahajan S, Veyssière P, editors. Encyclopedia of materials: science and technology. Oxford: Elsevier; 2001.
[40] Mohammadreza Z, Stefania T, Alessandro M, Lorella C, Salem S. Optimisation of heat treatment of Al–Cu–(Mg–Ag) cast alloys. Journal of Thermal Analysis and Calorimetry. 2020;139:3427–40.

[41] David AP, Kenneth EE, Mohamed YS. Phase transformations in metals and alloys: CRC press.
[42] Hiroshi M, Hajime K, Akio I, Shigenobu O. Competing nucleation of single- and double-layer Guinier–Preston zones in Al–Cu alloys. Scientific Reports. 2021;11:4503.
[43] Shen Z, Ding Q, Liu C, Wang J, Tian H, Li J, et al. Atomic-scale mechanism of the θ″ → θ′ phase transformation in Al-Cu alloys. Journal of Materials Science & Technology. 2017;33:1159–64.
[44] Aaronson HI, Enomoto M, Lee JK. Mechanisms of diffusional phase transformations in metals and alloys: CRC press; 2010.
[45] Pierre H, Daniel L, Francis B, Rémi, M, Grant C. Evaluation of the Growth Kinetics of θ′ and θ-Al_2Cu Precipitates in a Binary Al-3.5 Wt Pct Cu Alloy. Metallurgical and Materials Transactions A. 2019;50:3048–60.
[46] Liu H, Bellón B, LLorca J. Multiscale modelling of the morphology and spatial distribution of θ′ precipitates in Al-Cu alloys. Acta Materialia. 2017;132:611–26.
[47] Bakavos D, Prangnell P, Dif R. A comparison of the effects of ageforming on the precipitation behaviour in 2xxx, 6xxx and 7xxx aerospace alloys. Materials Forum. 2004;28:124–31.
[48] Sha G, Marceau R, Gao X, Muddle B, Ringer S. Nanostructure of aluminium alloy 2024: Segregation, clustering and precipitation processes. Acta Materialia. 2011;59:1659–70.
[49] Pierre Villars, Alan Prince, Hiroaki Okamoto. Handbook of Ternary Alloy Phase Diagrams: ASM International; 1995.
[50] Wang S, Starink MJ. Two types of S phase precipitates in Al–Cu–Mg alloys. Acta Materialia. 2007;55:933–41.
[51] Jo H, Hirano K. Precipitation processes in Al-Cu-Li alloy studied by DSC. In: : Trans Tech Publications Ltd; 1987. p. 377–382.
[52] Driver JH, Dubost B, Durand F, Fougeres R, Guyot P, Sainfort P, Suery M, editor. Precipitation and Strengthening in Aluminium Alloys: Trans Tech Publications Ltd; 1996.
[53] Yoshimura R, Konno TJ, Abe E, Hiraga K. Transmission electron microscopy study of the early stage of precipitates in aged Al–Li–Cu alloys. Acta Materialia. 2003;51:2891–903.
[54] Pletcher BA, Wang KG, Glicksman ME. Experimental, computational and theoretical studies of δ′ phase coarsening in Al–Li alloys. Acta Materialia. 2012;60:5803–17.
[55] Wang SC, Starink MJ. Precipitates and intermetallic phases in precipitation hardening Al–Cu–Mg–(Li) based alloys. International Materials Reviews. 2005;50:193–215.
[56] Dorin T, Deschamps A, Geuser F De, Sigli C. Quantification and modelling of the microstructure/strength relationship by tailoring the morphological parameters of the T1 phase in an Al-Cu-Li alloy. Acta Materialia. 2014;Vol 75:134–46.
[57] Decreus B, Deschamps A, Geuser F De, Donnadieu P, Sigli C, Weyland M. The influence of Cu/Li ratio on precipitation in Al–Cu–Li–x alloys. Acta Materialia. 2013;61:2207–18.
[58] Deschamps A, Decreus B, Geuser FD, Dorin T, Weyland M. The influence of precipitation on plastic deformation of Al–Cu–Li alloys. Acta Materialia. 2013;61:4010–21.
[59] Ardell AJ. Precipitation hardening. MTA. 1985;16:2131–65.
[60] Fribourg G. Precipitation and plasticity couplings in a 7xxx aluminium alloy: application to thermomechanical treatments for distortion correction of aerospace component: Institut National Polytechnique de Grenoble - INPG; 2009.
[61] Liu G, Zhang G, Ding X, Sun J, Chen K. Modeling the strengthening response to aging process of heat-treatable aluminum alloys containing plate/disc- or rod/needle-shaped precipitates.

Materials Science and Engineering: A. 2003;344:113–24.
[62] Hazzledine PM, Hirsch PB. A coplanar Orowan loops model for dispersion hardening. Philosophical Magazine. 1974;30:1331–51.
[63] Bahl S, Xiong L, Allard L, Michi R, Poplawsky J, Chuang A, Singh D, Watkins T, Shin D, Haynes J, Shyam A. Aging behavior and strengthening mechanisms of coarsening resistant metastable θ' precipitates in an Al–Cu alloy. Materials & Design. 2021;198:109378.
[64] Shower P, Morris J, Shin D, Radhakrishnan B, Poplawsky J, Shyam A. Mechanisms for stabilizing θ′(Al_2Cu) precipitates at elevated temperatures investigated with phase field modeling. Materialia. 2019;6:100335.
[65] Milligan B, Roy S, Hawkins C, Allard L, Shyam A. Impact of microstructural stability on the creep behavior of cast Al–Cu alloys. Materials Science and Engineering: A. 2020;772:138697.
[66] Dorin T, Geuser F De, Lefebvre W, Sigli C, Deschamps A. Strengthening mechanisms of T1 precipitates and their influence on the plasticity of an Al–Cu–Li alloy. Materials Science and Engineering: A. 2014;605:119–26.
[67] Meng F, Chai Z, Li J, Bian H, Wang Y. Small-angle X-ray scattering study of the δ′ phase growth kinetic in 1420 Al–Li alloy. Materials Characterization. 2001;47:43–6.
[68] Li Y, Shi Z, Lin j, Yang YL, Huang BM, Chung TF, et al. Experimental investigation of tension and compression creep-ageing behaviour of AA2050 with different initial tempers. Materials Science and Engineering: A. 2016;657:299–308.
[69] Marco S, Yan J. Precipitation hardening in Al-Cu-Mg alloys: analysis of precipitates, modelling of kinetics, atrength predictions. Materials Science Forum. 2006;519–521:251–258.
[70] Mihara M, Kobayashi E, Sato T. Effects of the pre-aging period on the formation behavior of nanoclusters in an Al-Mg-Cu alloy. MATERIALS TRANSACTIONS. 2015;56:500–6.
[71] Pelleg J. Mechanical properties of materials: Springer; 2013.
[72] Yang YL, Zhan LH, Xu XL. Constitutive modeling for Al–Cu–Mg alloy in creep aging process. Strength Mater. 2016;48:23–31.
[73] Liu J, Jin Y, Fang X, Chen C, Feng Q, Liu X, et al. Dislocation strengthening without ductility trade-off in metastable austenitic steels. Scientific Reports. 2016;6:35345.
[74] Li Y, Shi Z, Lin J, Yang YL, Rong Q, Huang BM, et al. A unified constitutive model for asymmetric tension and compression creep-ageing behaviour of naturally aged Al-Cu-Li alloy. International Journal of Plasticity. 2017;89:130–49.
[75] Yang Y, Zhan L, Liu C, Wang X, Wang Q, Tang Z, et al. Stress-relaxation ageing behavior and microstructural evolution under varying initial stresses in an Al–Cu alloy: Experiments and modeling. International Journal of Plasticity. 2020;127:102646.
[76] Zheng J, Lin j, Lee j, Pan R, Li C, Davies C. A novel constitutive model for multi-step stress relaxation ageing of a pre-strained 7xxx series alloy. International Journal of Plasticity. 2018;106:31–47.
[77] Liu C, Yang j, Ma P, Ma Z, Zhan L, Chen K, et al. Large creep formability and strength–ductility synergy enabled by engineering dislocations in aluminum alloys. International Journal of Plasticity. 2020;134:102774.
[78] Yang Y, Zhan L, Shen R, Yin X, Li X, Li W, et al. Effect of pre-deformation on creep age forming of 2219 aluminum alloy: Experimental and constitutive modelling. Materials Science and Engineering: A. 2017;683:227–35.

[79] Xu Y, Zhan L, Li W. Effect of pre-strain on creep aging behavior of 2524 aluminum alloy. Journal of Alloys and Compounds. 2017;691:564–71.
[80] Zhan L, Ma Z, Zhang J, Tan J, Yang Z, Li H. Stress relaxation ageing behaviour and constitutive modelling of a 2219 aluminium alloy under the effect of an electric pulse. Journal of Alloys and Compounds. 2016;679:316–23.
[81] Sallah M, Peddieson J, Foroudastan S. A mathematical model of autoclave age forming. Journal of Materials Processing Technology. 1991;28:211–9.
[82] Idem K, Peddieson J. Simulation of the Age Forming Process. Journal of Manufacturing Science and Engineering. 2005;127:165–72.
[83] Guines D, Gavrus A, Ragneau E. Numerical modeling of integrally stiffened structures forming from creep age forming technique. International Journal of Material Forming. 2008;1:1071–4.
[84] Seidman D, Marquis E, Dunand D. Precipitation strengthening at ambient and elevated temperatures of heat-treatable Al(Sc) alloys. Acta Materialia. 2002;50:4021–35.
[85] Zerilli FJ, Armstrong RW. Dislocation-mechanics-based constitutive relations for material dynamics calculations. Journal of Applied Physics. 1987;61:1816–25.
[86] Huang C, Wei M, Lee S. Transient and steady-state nanoindentation creep of polymeric materials. International Journal of Plasticity. 2011;27:1093–102.
[87] Ho KC, Lin J, Dean TA. Constitutive modelling of primary creep for age forming an aluminium alloy. Journal of Materials Processing Teclrnology. 2004;153-154:122–7.
[88] Li Y, Shi Z, Lin J, Yang Y-L, Rong Q. Extended application of a unified creep-ageing constitutive model to multistep heat treatment of aluminium alloys. Materials & Design. 2017;122:422–32.
[89] Lin Y, Lu C, Wei CY, Zheng ZQ. Effect of aging treatment on microstructures, tensile properties and intergranular corrosion behavior of Al–Cu–Li alloy. Materials Characterization. 2018;141:163–8.
[90] Zhao T, Jin L, Xu Y, Zhang SH. Anisotropic yielding stress of 2198 Al-Li alloy sheet and mechanisms. Materials Science and Engineering A. 2020;771.
[91] Zhang J, Wang C, Zhang Y, Deng YL. Effects of creep aging upon Al-Cu-Li alloy: Strength, toughness and microstructure. Journal of Alloys and Compounds. 2018;764:452–9.
[92] Kocks UF. Laws for work-hardening and low-temperature creep. Journal of Engineering Materials and Technology. Jan 1976;98:76–85.
[93] Estrin Y. Dislocation theory based constitutive modelling: foundations and applications. Journal of Materials Processing Technology. 1998;80-81:33–9.
[94] Fribourg G, Brechet Y, Deschamps A, Simar A. Microstructure-based modelling of isotropic and kinematicstrain hardening in a precipitation-hardened aluminium alloy. Acta Materialia. 2011;59:3621–35.
[95] Ashby MF. The deformation of plastically non-homogeneous. The Philosophical Magazine: A Journal of Theoretical Experimental and Applied Physics. 1970;21:399–424.
[96] Zhang J, Deng Y, Zhang X. Constitutive modeling for creep age forming of heat-treatable strengthening aluminum alloys containing plate or rod shaped precipitates. Materials Science and Engineering: A. 2013;563:8–15.
[97] Ma Z, Zhan L, Liu C, Xu L, Xu Y, Ma P, et al. Stress-level-dependency and bimodal precipitation behaviors during creep ageing of Al-Cu alloy: Experiments and modeling. International Journal of Plasticity. 2018;110:183–201.

[98] Nie JF, Muddle BC. Microstructural design of high-strength aluminum alloys. Journal of Phase Equilibria. 1998;19:543–51.
[99] Shercliff HR, Ashby MF. A process model for age hardening of aluminium alloys--1. The model. Acta Metallurgica et Materialia. 1990;38:1789–802.
[100] Labusch R. A Statistical Theory of Solid Solution Hardening. Physica Status Solidi. 1970;41:659–69.
[101] Esmaeili S, Lloyd DJ, Poole WJ. A yield strength model for the Al-Mg-Si-Cu alloy AA6111. Acta Materialia. 2003;51:2243–57.
[102] Rodgers BI, Prangnell PB. Quantification of the influence of increased pre-stretching on microstructure-strength relationships in the Al–Cu–Li alloy AA2195. Acta Materialia. 2016;108:55–67.
[103] Myhr OR, Grong O, Pedersen KO. A combined precipitation, yield strength, and work hardening model for Al-Mg-Si alloys. Metallurgical and Materials Transactions A. 2010;41:2276–89.
[104] Cheng L, Poole WJ, Embury JD, Lloyd DJ. The influence of precipitation on the work-hardening behavior of the aluminum alloys AA6111 and AA7030. Metallurgical and Materials Transactions A. 2003;34:2473–81.
[105] Poole WJ, Wang X, Lloyd DJ, Embury JD. The shearable–non-shearable transition in Al–Mg–Si–Cu precipitation hardening alloys: implications on the distribution of slip, work hardening and fracture. Philosophical Magazine. 2005;85:3113–35.
[106] Lyu F, Li Y, Huang X, Shi Z, Zeng Y, Lin J. An investigation of creep age forming of AA7B04 stiffened plates: Experiment and FE modelling. Journal of Manufacturing Processes. 2019;37:232–41.
[107] Li Y, Shi Z, Lin J, Yang Y-L, Saillard P, Said R. Effect of machining-induced residual stress on springback of creep age formed AA2050 plates with asymmetric creep-ageing behaviour. International Journal of Machine Tools and Manufacture. 2018;132:113–22.
[108] Li Y, Shi Z, Lin J, Yang Y-L, Saillard P, Said R. FE simulation of asymmetric creep-ageing behaviour of AA2050 and its application to creep age forming. International Journal of Mechanical Sciences. 2018;140:228–40.
[109] Lam AC, Shi Z, Lin j, Huang X, Zeng Y, Dean TA. A method for designing lightweight and flexible creep-age forming tools using mechanical splines and sparse controlling points. The International Journal of Advanced Manufacturing Technology. 2015;80:361–72.
[110] Seo Y, Park J, Song W, Kang B, Kim J. Flexible die design and springback compensation based on modified displacement adjustment method. Advances in Mechanical Engineering. 2014;6:131253.
[111] Hwang S, Lee j, Yang Y, Yoo M. Springback adjustment for multi-point forming of thick plates in shipbuilding. Computer-Aided Design. 2010;42:1001–12.
[112] Lyu F, Huang X, Zeng Y, Shi Z, Wang M. Numerical simulation for creep age forming of aluminium alloy 7050 saddle-shaped part. Procedia Engineering. 2017;207:299–304.
[113] Li Y, Shi Z, Yang Y-L, Lin J, Said R. Experimental and numerical study of creep age forming of AA2050 plates with sparse multi-point flexible forming tool. Procedia Manufacturing. 2018;15:1016–23.
[114] Wagoner H, Lim H, Lee MG. Advanced Issues in springback. International Journal of Plasticity.

2013;45:3–20.
[115] Chan KC, Wang SH. Theoretical analysis of springback in bending of integrated circuit leadframes. Journal of Materials Processing Technology. 1999;91:111–5.
[116] Wenner ML. On work hardening and springback in plane strain draw forming. Journal of Applied Metalworking. 1983;2:277–87.
[117] Ma J, Welo T. Analytical springback assessment in flexible stretch bending of complex shapes. International Journal of Machine Tools and Manufacture. 2021;160:103653.
[118] Choi J, Lee j, Bong H, Lee M, Barlat F. Advanced constitutive modeling of advanced high strength steel sheets for springback prediction after double stage U-draw bending. International Journal of Solids and Structures. 2018;151:152–64.
[119] Xue X, Liao J, Vincze G, Gracio J. Modelling of mandrel rotary draw bending for accurate twist springback prediction of an asymmetric thin-walled tube. Journal of Materials Processing Technology. 2015;216:405–17.
[120] Gordan J. On pure bending in non-linear elasticity: A circular closed-form 2D solution for semi-linear orthotropic material. European Journal of Mechanics - A/Solids. 2021;90:104289.
[121] Ma J, Li H, Fu M. Modelling of Springback in Tube Bending: A Generalized Analytical Approach. International Journal of Mechanical Sciences. 2021;204:106516.
[122] Zhang S, Fu M, Wang Z, Fang D, Lin W, Zhou H. Springback prediction model and its compensation method for the variable curvature metal tube bending forming. The International Journal of Advanced Manufacturing Technology. 2021;112:3151–65.
[123] Meng Q, Zhao J, Mu Z, Zhai R, Yu G. Springback prediction of multiple reciprocating bending based on different hardening models. Journal of Manufacturing Processes. 2022;76:251–63.
[124] Narimetla SP, Peddieson J, Buchanan GR, Foroudastan S. A simple unified age forming model. Mechanics Research Communications. 2000;27:631–6.
[125] Jeunechamps P, Ho KC, Lin J, Ponthot J, Dean TA. A closed form technique to predict springback in creep age-forming. International Journal of Mechanical Sciences. 2006;48:621–9.
[126] Li Y, Rong Q, Shi Z, Sun X, Meng L, Lin J. An accelerated springback compensation method for creep age forming. The International Journal of Advanced Manufacturing Technology. 2019;102:121–34.
[127] Gan W, Wagoner RH, Mao K, Price S, Rasouli F. Practical methods for the design of sheet formed components. Journal of Engineering Materials and Technology. 2004;126:360–7.
[128] Yang X, Ruan F. A die design method for springback compensation based on displacement adjustment. International Journal of Mechanical Sciences. 2011;53:399–406.
[129] Wang X, Rong Q, Shi Z, Li Y, Cao J, Chen B, et al. Investigation of stress effect on creep, precipitation and dislocation evolution of Al–Li alloy during creep age forming. Materials Science and Engineering: A. 2022;836:142723.
[130] Lam A. A flexible tool design and integrated modelling techniques for springback compensation in creep-age forming. [PhD]; 2015.
[131] Ashby M. A first report on deformation-mechanism maps. Acta Metallurgica. 1972;20:887–97.
[132] Langdon T. Creep at low stresses: An evaluation of diffusion creep and Harper-Dorn creep as viable creep mechanisms. Metallurgical and Materials Transactions A. 2002;33:249–59.
[133] Chokshi A. Diffusion creep in metals and ceramics: Extension to nanocrystals. Materials Science and Engineering: A. 2008;483-484:485–91.

[134] Hu L, Zhan L, Shen R, Liu Z, Ma Z, Liu j, et al. Effects of uniaxial creep ageing on the mechanical properties and micro precipitates of Al-Li-S4 alloy. Materials Science and Engineering: A. 2017;688:272–9.
[135] Kim JD, Park JK. Effect of stretching on the precipitation kinetics of an Al-2.0Li-2.8Cu-0.5Mg(-0.13Zr) alloy. Metallurgical and Materials Transactions A. 1993;24:2613–21.
[136] Ma P, Zhan L, Liu C, Yang j, Chen K, Huang Z. Strong stress-level dependence of creep-ageing behavior in Al–Cu–Li alloy. Materials Science and Engineering: A. 2020:140381.
[137] Zhang J, Li Z, Xu F, Huang C. Regulating effect of pre-stretching degree on the creep aging process of Al-Cu-Li alloy. Materials Science and Engineering: A. 2019;763:138–57.
[138] Chen X, Zhan L, Ma Z, Xu Y, Zheng Q, Cai Y. Study on tensile/compressive asymmetry in creep ageing behavior of Al–Cu alloy under different stress levels. Journal of Alloys and Compounds. 2020;843:156–7.
[139] Yan Y, Peguet L, Gharbi O, Deschamps A, Hutchinson C, Kairy S, et al. On the corrosion, electrochemistry and microstructure of Al-Cu-Li alloy AA2050 as a function of ageing. Materialia. 2018;1:25–36.
[140] Chung TF, Yang YL, Hsiao CN, Li WC, Huang BM, Tsao CS, et al. Morphological evolution of GP zones and nanometer-sized precipitates in the AA2050 aluminium alloy. International Journal of Lightweight Materials and Manufacture. 2018;1:142–56.
[141] Krug M, Dunand DC. Modeling the creep threshold stress due to climb of a dislocation in the stress field of a misfitting precipitate. Acta Materialia. 2011;59:5125–34.
[142] Wang S, Luo J, Hou L, Zhang J, Zhuang L. Identification of the threshold stress and true activation energy for characterizing the deformation mechanisms during hot working. Materials & Design. 2017;113:27–36.
[143] Dunand DC, Jansen AM. Creep of metals containing high volume fractions of unshearable dispersoids - Part I. Modeling the effect of dislocation pile-ups upon the detachment threshold stress. Acta Materialia. 1997;45:4569–81.
[144] Mordehai D, Clouet E, Fivel M, Verdier M. Introducing dislocation climb by bulk diffusion in discrete dislocation dynamics. Philosophical Magazine. 2008;88:899–925.
[145] Nádai Á, Wahl AM. Plasticity, A Mechanics of the Plastic State of Matter. Journal of Rheology. 1931;2:455–6.
[146] Lin j, Liu Y, Farrugia D, Zhou M. Development of dislocation-based unified material model for simulating microstructure evolution in multipass hot rolling. Philosophical Magazine. 2005;85:1967–87.
[147] Kelly A, Nicholson RB. Precipitation hardening. Progress in Materials Science. 1963;10:149–391.
[148] Reti AM, Flemings MC. Solution kinetics of two wrought aluminum alloys. Metallurgical Transactions. 1972;3:1869–75.
[149] Ho KC, Lin J, Dean TA. Modelling of springback in creep forming thick aluminum sheets. International Journal of Plasticity. 2004;20:733–51.
[150] Li Y, Shi Z, Rong Q, Zhou W, Lin j. Effect of pin arrangement on formed shape with sparse multi-point flexible tool for creep age forming. International Journal of Machine Tools and Manufacture. 2019;140:48–61.
[151] Ye J. Structural and stress analysis theories, tutorials and examples: CRC press; 2015.